UNIVERSITÉ DE GENÈVE
Département d'astronomie

FACULTÉ DES SCIENCES
Professeur T. J.-L. Courvoisier

High Energy Emission from the Galaxy: a Study with *INTEGRAL* and *Chandra*

THÈSE

présentée à la Faculté des sciences de l'Université de Genève
pour obtenir le grade de Docteur ès sciences,
mention astronomie et astrophysique

par

Adamantia PAIZIS

de

Milano (ITALIE)

Thèse N° 3580

GENÈVE
Atelier de reproduction de la Section de physique
2004

.

CETTE THÈSE A FAIT L'OBJET DES PUBLICATIONS SUIVANTES:
voir chapitre 12.

To the INTEGRAL project
and the people involved in it,
for showing me the sky.

Remerciements

La tradition veut que lorsque l'on fait une thèse à l'Université de Genève, l'on doive écrire les remerciements en français. J'aimerais que mon français soit assez bon pour pouvoir exprimer ma gratitude à tous les gens qui m'ont accompagné durant cette thèse. Il n'en est malheureusement rien. Permettez moi donc de faire une petite exception et d'écrire lesdits remerciements dans le langage que j'ai utilisé au cours des dernières années: l'anglais. Ceux-ci se trouvent au chapitre 11.

Tradition has it that the acknowledgments of a Ph. D. made with the University of Geneva are written in french. I wish my french was good enough to really express the gratitude I feel for all the people that have accompanied me during this thesis. Unfortunately it is not. Allow me to make a small exception and to write my acknowledgments in the language I have been using every day in the last years, english. These can be found in chapter 11.

Résumé en Français

Introduction

Tout le travail présenté dans cette thèse a été entièrement effectué à "l'*INTEGRAL* Science Data Centre" (ISDC). Travailler dans un centre collecteur des données scientifiques d'un satellite donne l'opportunité de participer aux événements principaux liés au satellite, être témoin des découvertes, enfin de participer au projet depuis "les coulisses". Comme je le montre au cours de ces pages, cela veut aussi dire être impliquée dans des activités plus spécifiques du projet, ce qui, au final, aboutit à une partie importante du travail de thèse lui-même.

INTEGRAL est une mission de taille moyenne de l'Agence Spatiale Européenne, lancée le 17 octobre 2002. Sa charge utile est constituée de deux principaux instruments sensibles dans le domaine des rayons Gamma, le spectromètre SPI (SPectrometer on board the *INTEGRAL* satellite), et l'imageur IBIS[1] (Imager on board the *INTEGRAL* Satellite), tous deux couvrant le domaine énergétique compris entre 15 keV et 1 MeV. Co-alignés avec ces deux instruments se trouvent deux moniteurs sensibles aux rayons X, JEM-X (Joint European Monitor for X-rays, 4 – 35 keV), et un moniteur sensible dans le domaine visible, OMC (Optical Monitoring Camera, 500 – 600 nm). En plus de ces instruments purement scientifiques, un détecteur de radiation de particules, dont le but est de suivre l'environnement du satellite, est aussi embarqué. En cas de flux important de particules énergétiques ce dernier module éteindra automatiquement les différents télescopes.

Les premiers buts scientifiques d'*INTEGRAL* sont d'obtenir une position précise des sources de rayons X et Gamma du ciel, ainsi que d'en faire la spectroscopie fine. Le ciel Gamma a déjà été observé par de précédentes missions, comme *GRANAT* ou *CGRO*, néanmoins, vu les progrès d'*INTEGRAL* en termes de résolutions angulaires et spectrales, ce dernier est le premier satellite à opérer dans cette région fondamentale du spectre électromagnétique avec une telle précision et une telle sensibilité.

Le sujet principal de cette thèse est l'étude des binaires X de faibles masses (LMXRB pour l'acronyme anglais "Low Mass X-ray Binaries") dans les domaines des rayons X et Gamma avec *INTEGRAL*.

Les binaires X contiennent soit une étoile à neutrons soit un trou noir qui accrète la matière d'une étoile compagnon àtravers la formation d'un disc, dit d'accretion. La classification en termes de faible ou forte masse est basée sur le type spectral du compagnon. dans une LMXRB, le compagnon est une étoile vieille, et il est relativement facile de les identifier et de les classifier. Cependant lorsque l'on cherche à comparer différentes LMXRB, il est intéressant de voir que des systèmes ayant une physique globale similaire (étoile vieille, même objet compact, disque d'accrétion) conduisent à des différences observationnelles parfois très marquées: émission persistente ou transitoire, activité éruptive ou creux de luminosité, pulsations du flux de rayons X, transitions spectrales, éjections, etc...

[1]IBIS est constitué par deux differents detecteurs: ISGRI (*INTEGRAL* Soft Gamma-Ray Instrument, 15 keV – 1 MeV) et PICsIT (Pixellated Imaging Caesium Iodide Telescope, 170 keV – 10 Mev).

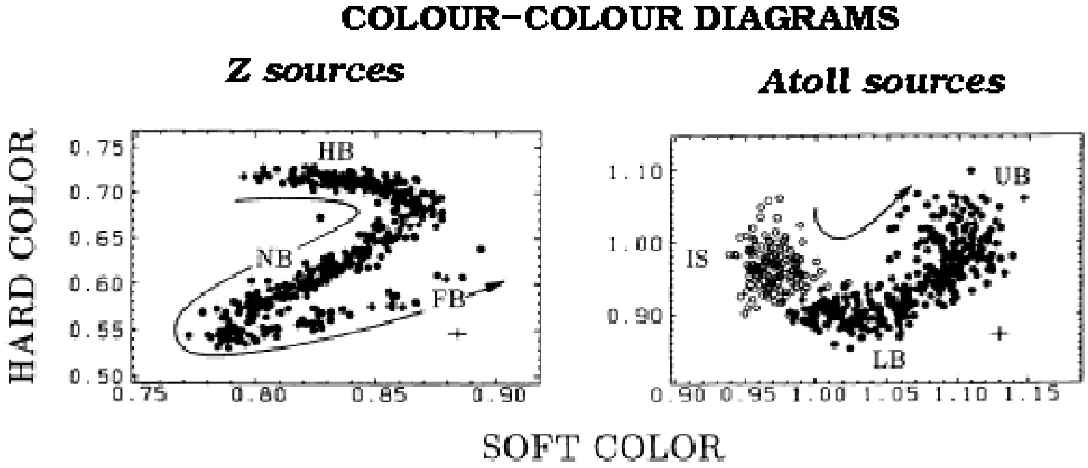

Fig. 1 Le CD typique des sources Z (gauche) et Atoll (droite). Les trois branches crèant le Z sont appelées "Horizontal Branch" (HB), "Normal Branch" (NB) et "Flaring Branch" (FB). des sources Atoll ont deux sortes de branches : le "Island State" (IS) branche et la "Banana State" branche (divisée en branche infèrieure, "Lower Banana", et branche supèrieure, "Upper Banana"). La direction dans laquel le taux d'accrétion $\dot{M}$ augmente est indiqué par les flèches (figure adaptée depuis Hasinger et van der Klis, 1995.)

Nous pourrions penser que ces différences sont liées au type de l'objet compact, mais il semble bien que la réponse ne soit pas aussi simple. Il n'est, en réalité, possible de déterminer la nature de l'objet compact que dans certains cas comme nous le voyons au chapitre 3. En plus, si l'on considère les LMXRB qui contiennent une étoile à neutrons, et qui ont une émission X/Gamma lumineuse et persistente, il est encore possible de trouver des différences notables, comme par exemple les propriétés définissant les classes de sources Atoll et Z.

Depuis la découverte de la première source ponctuelle de rayons X (autre que le Soleil), Scorpius X-1 (Giacconi et al., 1962), l'intérêt pour le ciel X n'a fait qu'augmenter. Les premiers instruments imageurs sensibles aux rayons X furent construit à la fin des années septante. Avec les progrès, notamment au niveau de la sensibilité de ces téléscopes, de nombreuses sources X, de luminosités très différentes, furent identifiées. Ainsi, les binaires X en général furent l'objet d'études aussi nombreuses que rigoureuses, dans la bande dite des "X-mous" (i.e. entre 2 et 10 keV), à partir desquelles les premières classifications furent établies. En fait c'est dans cette bande que les différences observationnelles entre les LMXRB persistentes et brillantes, contenant une étoile à neutrons, ont été découvertes. Hasinger et van der Klis (1989) en étudiant les observations de 16 tels objets, faites avec le satellite *EXOSAT*, et en classifiant les diagrammes "couleur-couleur" (CD)[2], ont montré que pour les six sources les plus brillantes le CD avait la forme d'un "Z" alors que pour les autres le CD était plus fragmenté. Du fait de ces formes, le premier type de source est appelé Z, alors que l'autre est nommé Atoll (Fig. 1).

Les sources Z et Atoll se déplacent le long des branches du CD de manière régulière, et ne sautent jamais de l'une des branches à l'autre. La position d'une source sur le CD est très probablement liée à une quantité physique qui évolue de manière continue, probablement le taux

[2]c'est-à-dire des graphiques où un rapport de dureté entre deux bandes d'énergie (moins énergétiques) est représenté en fonction du rapport de dureté entre d'autres bandes (plus énergétiques)

d'accrétion $\dot{M}$ (Hasinger et al., 1990).

Des études plus récentes (Muno et al. 2002; Gierliński et al 2002; Barret & Olive 2002) ont suggéré que la distinction, pourtant claire, entre les CD des sources Z et Atoll, n'était en fait due qu'à un échantillonage incomplet; si l'on observe les sources Atoll assez longtemps, leur CD ressemblera a un Z. Cependant de nombreuses différences persistent: les Atoll ont un champ magnétique plus faible (environ $1 - 10 \times 10^6$ G contre entre 10 et 100 fois plus pour les Z), elles sont généralement moins lumineuses (d'un facteur 3 à 100), leur spectre est généralement plus dur, elles "accomplissent le Z" pendant un temps plus long, et elles ont un comportement temporel rapide qui évolue avec leur position sur le CD.

Les spectres en rayons X de ces objets (LMXRB à étoile à neutron) sont généralement décomposés en la somme d'une composante "molle", et d'une composante "dure" relativement à la position de leur pic d'émission. Deux modèles concurents sont souvent utilisés pour décrire ce spectre composite: le modèle de l'Est (Mitsuda et al. 1984) et celui de l'Ouest (White et al. 1986). Dans le modèle de l'Est la partie molle du spectre est modélisée par un corps noir multi-couleur, représentant l'émission d'un disque d'accrétion géométriquement fin et optiquement épais. La partie plus haute énergie provient de la Comptonisation thermique des photons émis par la surface de l'étoile à neutrons sur des électrons se trouvant dans la couche dite de bordure, i.e. qui se trouve entre le disque d'accrétion et la surface.

Dans le modèle de l'Ouest la partie basse énergie est modélisée par un simple corps noir représentant l'émission provenant de la surface de l'étoile à neutron + couche de bordure. La partie haute énergie du spectre provient ici encore d'un effet de Comptonisation thermique mais cette fois-ci les photons mous sont comptonisés par des électrons se trouvant dans un milieu type "couronne" situé entre la surface et le disque d'accrétion.

Ces deux modèles représentent bien les spectres sous 20 keV. Les transitions spectrales et les mouvements le long des branches des CD (l'Atoll ou le Z) peuvent être expliqués en terme d'évolution relative des deux composantes. Cependant en étudiant seulement les rayons X mous, il n'est pas possible de distinguer entre ces deux modèles.

Les observations à plus haute énergie sont rendues difficiles par le fait qu'il est extrêmement difficile voire impossible de focaliser les rayons X durs et Gamma. Des techniques plus complexes doivent alors être mises en œuvre pour obtenir des images dans ces domaines d'énergie. La technologie progressant, de plus en plus de missions ont commencé à scruter le ciel dans ces régions spectrales. Ce faisant notre compréhension des binaires X a changé. Un bon exemple de cette évolution est l'étude du type de l'objet compact: on pensait initiallement que les trous noirs accrétants avaient un spectre plus dur que les étoiles à neutrons dans la région 20-500 keV. Un spectre en loi de puissance s'étendant au-delà de 100 keV était même considéré comme une signature de la présence d'un trou noir (Sunyaev et al. 1991). Les observations réalisées avec *GRANAT*/SIGMA, et *CGRO*/BATSE au-delà de 20 keV, ont montré que les sursauteurs X ("X-ray Bursters" qui sont des étoiles à neutrons à faible champ magnétique) pouvaient avoir des spectres durs et lumineux dans la région 20-200 keV (e.g. Barret et Vedrenne 1994; Tavani et Barret 1997). Ensuite, la comparaison des luminosités molles (2-20 keV) et dures (20-200 keV) entre trous noirs et étoiles à neutrons semblait suggérer que les trous noirs avec une queue à haute énergie avaient une luminosité plus élevée que les étoile à neutrons. Ceci fut rapidement démenti par les résultats de *Beppo-Sax*/PDS, qui détecta des queue à haute énergie dans les sources Z brillantes (Di Salvo et Stella 2002). Cinq des six sources Z Galactiques possèdent une telle extension de leur spectre à haute énergie. La seule pour laquelle une telle détection ne pouvait être confirmée avant les travaux présentés dans cette thèse, est GX 5-1 dont la possible émission X dure n'avait jamais pu être séparée de celle du candidat trou noir GRS 1758-258, vu la proximité des deux objets, et le pouvoir de résolution angulaire insuffisant des téléscopes gamma avant *INTEGRAL*.

Il est clair que pour mieux comprendre le comportement et la physique des sources accrétantes, pour distinguer entre étoiles à neutrons et trous noirs, sources Atoll et Z etc, une surveillance du ciel X dur et Gamma couvrant une large plage de luminosité est nécessaire. Dans cette optique, un tiers du temps d'observation d'*INTEGRAL* est dédié au balayage du plan et des régions centrales de la Galaxie (respectivement GPS et GCDE) dans ce qui fait partie du temps garanti. Le suivi régulier des LMXRB au cours de ces observations est au cœur de cette thèse. En préparation de ce suivi nous avons, avant le lancement, réalisé une simulation d'une année de prise de données avec le simulateur d'observations d'*INTEGRAL* OSIM, qui est décrit ci-dessous.

Le simulateur d'observation d'INTEGRAL

Avant la phase d'activité nominale, et bien avant le lancement, une quantité importante de travail de préparation doit être réalisée pour que la mission soit un succès. Dans les phases pré-lancement, j'ai travaillé sur OSIM, le logiciel simulant des observations faites avec *INTEGRAL*. Ses principaux buts sont :

- de générer des données simulées précises pour les instruments de haute énergie d'*INTEGRAL*, dans le but de tester la chaîne de réduction des données (à l'ISDC mais aussi dans les instituts "PI[3]").
- d'aider les observateurs à s'habituer à la structure et l'organisation des données.
- de permettre aux observateurs de simuler des observations pour la préparation de l'AO[4] 1.

La première partie de cette thèse est donc axée sur OSIM, ce qui inclut l'intégration dans le système, les tests, la documentation, et la simulation à but scientifique. La Figure 2 est un zoom sur une simulation du centre Galactique vu par IBIS/ISGRI. Cette simulation montre qu'une centaine de sources peut être détectée par INTEGRAL lors d'une année du temps garanti. La Fig. 3 represente une mosaique de 5.7 Ms obtenue à partir d'observations "temps garanti" réelles de IBIS/ISGRI. Pour une raison de clarté, seules les sources les plus brillantes ont leur nom représenté, mais bien d'autres sources de luminosité plus faible sont aussi visibles. Environ 130 sources ont été détectées durant la première année d'observation du temps garanti, la majorité étant des sources connues, et environ 10% de nouvelles sources. Ces résultats montrent que les simulations étaient réalistes dans le cas des sources brillantes mais assez peu précises pour les sources faibles. Lors de l'utilisation d'un instrument à masque codé, la détermination des fluctuations spatiales et temporelles du bruit de fond est fondamentale. La soustraction d'un bruit de fond simulé, et donc non réaliste, n'influence pas vraiment la détectabilité des sources brillantes mais a, en revanche, une influence dramatique sur la détéctabilité des sources faibles. Un autre point d'importance concerne la modélisation des sources inclues dans le catalogue de référence. Toute inexactitude liée au modèle spectral d'une source résultera en une différence lors de la simulation par rapport à l'observation.

[3]"Principal Investigator"
[4]"Announcement of Opportunity"

Le programme de suivi des LMXRB avec INTEGRAL

Après le lancement, les données scientifiques commencèrent à arriver en grand nombre, et il s'avéra que le temps passé sur le simulateur m'avait apporté une grande expérience utile et nécéssaire pour construire et coordonner la campagne de suivi des LMXRB.

La nature des sources que l'on suit dans ce programme est relativement diverse, puisque l'on s'occupe aussi bien de trous noirs que d'étoiles à neutrons faiblement magnétisées. Dans notre échantillon de 74 sources, il y en a huit qui ont un flux constamment supérieur à 100 mCrab entre 2 et 10 keV. Parmis ces dernières, sept appartiennent soit à la classe des sources Atoll ou Z, cependant qu'un est un trou noir (GRS 1915+105). L'interêt et la force d'un tel suivi réside dans le fait qu'ainsi un grand nombre de sources différentes est régulièrement observé dans les mêmes bandes d'énergie et avec les mêmes instruments. Les résultats sont donc directement comparables, non sujets à extrapolations ni à aucun problème de différences instrumentales. Cette base de données couvrant une longue durée permet et permettra d'étudier de nombreux aspects des LMXRB comme par exemple:

- La dépendance du spectre X sur la luminosité et les différences existant entre LMXRB contenant un trou noir et celles contenant une étoile à neutrons;
- Les propriétés des extensions haute énergie: apparition, corrélation avec les états spectraux, présence ou non de "coupure haute énergie" indiquant si le mécanisme physqiue responsable est d'origine thermique ou non;
- Mesurer le spectre à haute énergie des sources trop faibles pour avoir été détectées avant, ou bien se trouvant dans des régions trop denses (en termes de sources) pour avoir été résolues;
- Etablir de nouveaux CD mais aussi des diagrammes dureté-intensité ("Hardness Intensity Diagram" ou HID) dans les rayons X durs, afin de trouver de nouvelles différences ou similarités entre les différentes classes;
- Etablir des spectres à large bande des sources Atoll ou Z, pour essayer de distinguer entre les différents modèles à travers l'étude des variations spectrales le long des branches du CD.

Construire un telle base de données n'est pas une tâche aisée vu que cela implique de réduire les données d'*INTEGRAL*, ce qui est un processus long et relativement délicat. Vu l'afflux important de données, ne pas être submergée nécessite de développer une infrastructure qui analyse automatiquement les données, en extrait l'information, et la représente de manière efficace. Les résultats d'une telle approche porteront leurs fruits à long terme. Par exemple, comme l'ont montré Muno et al. (2002) et Gierliński et al. (2002), seule l'accumulation de plusieurs années d'observations de *RXTE* a permis de montrer que le CD des Atoll ressemblait aussi à un Z. C'est notre but avec *INTEGRAL*, construire une telle base de donnée mais dans la bande d'énergie des rayons X durs, dans laquelle un tel travail n'a jamais été fait.

À l'heure actuelle, le matériel brut est extrait pour toutes les sources de notre échantillon. La Figure 3 représente la mosaique IBIS/ISGRI de toutes les observations GPS et GCDE de la première année, soit environ 5.3 Ms, alors que la figure 4 représente un exemple de courbe de lumière automatiquement extraite. De nombreuses autres images et courbes de lumière sont représentées au chapitre 6. Les outils d'extraction des données permettent un certain degré d'interaction: il est par exemple possible de sélectionner la source à afficher, le type de diagramme (courbe de lumière, CD, HID,...), le nombre de bandes d'énergie, les échelles des axes, et l'instrument. Il est ainsi possible d'explorer l'archive de manière rapide et efficace.

En utilisant cette infrastructure, nous avons fourni le catalogue des sources brillantes et des cartes du ciel à la NASA et à l'ISDC qui les ont mis à disposition du public peu avant l'AO 3: un scientifique utilisant la page web "HEASARC Browse" afin de trouver des résultats concernant sa source préférée, peut en obtenir des images et courbes de lumière de SPI et IBIS/ISGRI. Les résultats sont encore relativement préliminaires, et ne représentent qu'approximativement les capacités d'*INTEGRAL* en ce qui concerne les sources ponctuelles.

Parmis les sources de notre échantillon, nous avons d'abord sélectionné celles qui sont constamment brillantes; pour celles-ci nous avons approfondi l'analyse scientifique. Ce sous-échantillon comprend les LMXRB avec étoiles à neutrons, appartenant aux classes Atoll et Z (Paizis et al. 2003, 2004a,b, Chapitre 6).

Notre étude de la variabilité montre que les données du temps garanti d'*INTEGRAL* sont suffisantes pour étudier l'historique de l'évolution de ces sources. Les sources de la classe Z sont plus brillantes que les Atoll (comme l'on s'y attendait), et il ne semble pas y avoir d'importantes différences de variabilité entre les différentes classes. Si cela est confirmé par plus de données d'*INTEGRAL* alors ce sera un résultat important: les Atoll et les Z appartiennent à la même famille lorsque l'on considère la variabilité temporelle.

Nos analyses spectrales montrent que les sources de type Z n'ont pas de coupure dans leur spectre à haute énergie, et ce jusqu'à environ 50 keV, cependant qu'elles semblent avoir un spectre plus dur que les Atoll au-delà de 20 keV. Ceci est probablement dû au fait que les Atoll de notre échantillon sont des systèmes brillants se trouvant généralement dans l'état dit "mou".

Nous voyons une indication de durcissement du spectre à haute énergie dans GX 3+1 et de manière plus convaincante dans Sco X-1 (la première étant une Atoll, la seconde une Z). La recherche de telles extensions haute énergie dans les LMXRB et la compréhension des phénomènes physiques associés est l'un des buts principaux de notre campagne. Les différents modèles physiques expliquant l'émission de rayons X et Gamma par les LMXRB sont introduits au chapitre 3.

Après avoir étudié les aspects temporels et spectraux séparemment, nous réunissons ces deux approches, extrayons des spectres selon la position sur le CD, dans l'étude d'une source Z particulière GX 5-1 (Paizis et al. 2004a, Chapitre 7). Dans le passé, les observations en rayons X de GX 5-1 étaient contaminées par l'émission du candidat trou noir GRS 1758-258 qui ne se trouve "qu'à" 40 minutes d'arc. Grâce aux capacités d'*INTEGRAL* en termes d'imagerie et à sa grande sensibilité, nous sommes capables, pour la première fois, d'étudier le spectre de GX 5-1 au-delà de 30 keV, ainsi que ses variations spectrales, sans contamination. La Figure 3 montre comment GX 5-1 et GRS 1758-258 sont clairement séparées par ISGRI. Nous ajustons les spectres moyens ISGRI ($\sim$167 ksec) et JEM-X ($\sim$76 ksec) de GX 5-1 avec les deux modèles concurents discutés plus haut. Ces deux modèles représentent relativement bien les spectres sous 30 keV. Au-delà nous détectons une extension ou queue haute énergie, dont l'origine physique est probablement la même que les queues observées dans les autres sources Z (Di Salvo et Stella 2002, Chapitre 3). Cet excès à haute énergie est bien représenté par le model de l'Est (Fig. 5 et chapitre 7), alors qu'un large écart est visible lorsque l'on utilise le modèle de l'Ouest. Si l'on ajoute une loi de puissance a ce dernier alors seulement l'ajustement devient acceptable. Puisque le modèle de l'Est donne une interprétation physique à la présence de la queue de haute énergie, nous préférons ce modèle pour l'analyse et la discussion de la variabilité spectrale de GX 5-1. La figure 6 représente le HID de GX 5-1. Notre étude spectrale plus fine est ensuite basée sur l'analyse de chaque pointés (d'environ 2000s) d'*INTEGRAL*. Nous pouvons alors interpréter les spectres de GX 5-1 en termes de Comptonisation d'un corps noir (d'environ 2 keV) par un plasma chaud (d'environ 10 keV). Les mouvements de la source le long du Z sont attribués aux variations de la température du corps noir dont l'emission a origine dans la surface de l'étoile à neutrons chauffée par la couche de bordure. Ainsi, lorsque GX 5-1 se déplace vers le bas du Z, la température de la surface de l'étoile à neutrons décroît régulièrement alors que le taux d'accrétion augmente (Fig. 7 droite). Cette anti-corrélation peut être une conséquence de l'expansion graduelle de la couche de bordure, expansion que l'on voit dans nos données (Fig. 7 gauche). Cette interprétation est aussi en bon accord avec les prédictions théoriques (Popham et Sunyaev 2001).

L'étude de GX 5-1 montre que, grâce à *INTEGRAL*, nous pouvons étudier la "météorologie" autour de l'étoile à neutrons. On "voit" en fait la température et la taille de l'aire émettrice changer. Ces travaux n'apportent pas de preuve définitive quant à la présence d'une surface et donc d'une étoile à neutrons dans un système[5]. En fait, le corps noir de température variable pourrait provenir du disque d'accrétion qui est, lui, présent autour des trous noirs, et dans ces derniers cas responsable de la composante basse énergie. Mais cette approche pourrait nous rapprocher dans le futur d'une nouvelle méthode d'identification du type de l'objet compact par la mise en évidence d'une surface solide.

Le balayage fait avec Chandra

Avec *INTEGRAL* nous détectons GX 5-1 à un flux $F_{5-20\mathrm{keV}} \sim 10^{-8}$ erg/cm^2/s, ce qui est très élevé. Les binaires X sont intrinsèquement des objets très brillants, mais leur proximité augmente leur éclat apparent: les objets de notre échantillon sont en effet Galactiques. Si l'on regardait dans une région à priori vide, un temps d'exposition long serait nécessaire pour éventuellement y détecter une population de sources très faibles d'origine Galactique ou bien des sources intrinqèquement brillantes mais situées à une distance plus grande (extra-Galactique). Nous avons réalisé un balayage profond d'une région "vide" du plan Galactique (l,b)$\sim$(28.5°, 0.0°) avec le satellite américain Chandra, qui est sensible entre 0.08 et 10 keV et possède une excellente résolution angulaire (sub-seconde d'arc), ainsi qu'une très grande sensibilité. Grâce à ces observations nous pouvons séparer la contribution des sources faibles de celle du fond diffus Galactique afin d'etudier ces deux composantes séparément. Sous 10 keV, les sources ponctuelles ne contribuent qu'à hauteur de 10% à l'émission totale dans ce champ de vue. Ma contribution à ce travail réside dans l'étude des sources ponctuelles. Les résultats sont reportés par Ebisawa et al. (2004b) et discutés au chapitre 9.

Nous détectons dans ce champ 274 sources ponctuelles (jusquà une significance de 4σ) en plus de l'émission diffuse (Fig. 8). La sensibilité de détection atteinte est de $\sim 3 \times 10^{-15}$ erg/cm^2/s dans la bande 2-10 keV. Aucune de ces sources n'était connue avant. Dans la bande d'énergie la plus faible (0.5-2 keV) nous détectons 182 sources, alors qu'entre 2-10 keV nous en détectons 79. Seules 26 sont détectées dans les deux intervalles, ce qui suggère une certaine dichotomie dans la population de sources.

A partir de ces travaux nous avons construit un catalogue contenant la position des sources, leur flux, leur significativité, leur rapport de dureté et l'identification de la contrepartie infra rouge. Un nouvel acronym, "CXOGPE" ("Galactic Plane Sources reported by Ebisawa et al. 2004b") est enregistré au CDS[6] pour les sources de ce catalogue. Pour identifier la nature des sources ponctuelles nous avons utilisé les informations spectrales de Chandra ainsi que les résultats des suivis multi-longueurs d'onde. La plupart des sources de ce catalogue est très probablement extra-Galactiques, puisque le nombre de sources n'excède pas le nombre de sources extra-Galactique auquel on s'attend (provenant de mesures effectuées à plus haute lattitude).

[5]Dans le cas de GX 5-1, d'autres méthodes nous permette de savoir qu'il s'agit d'une étoile à neutrons

[6]http://vizier.u-strasbg.fr/viz-bin/DicForm

Ceci est aussi confirmé par les résultats des observations en proche infra rouge, puisque seulment le 20% des sources "dures" a une contrepartie. Une partie significative du 80% restant est très probablement extra-Galactique puisque les sources se trouvant derrière le plan Galactique sont très absorbées en proche infra rouge. En revanche, le 20% possédant une contrepartie est très probablement Galactique, des candidats possibles étant des variables cataclysmique en quiescence, objets considérés comme étant très nombreux dans le plan Galactique. Du point de vue des sources "molles" le $\sim 80\%$ a une contrepartie infra rouge. Le spectre X et la contrepartie suggèrent qu'elles sont très probablement des étoiles actives en X. Nous prévoyons d'avoir le même type d'approche dans d'autres régions du plan Galactique afin d'obtenir une carte précise des sources le peuplant.

Le travail à l'ISDC

Outre les travaux précédemment présentés, qui constituent le cœur de ma thèse, d'autres opportunités m'ont été offertes. L'étude systématique des données *INTEGRAL* du temps garanti, et le développement d'OSIM m'ont apporté de nouvelles collaborations. La plupart concernent d'autres sources suivies dans le temps garanti (voire le chapitre 10 pour plus de détails), par exemple le programme de suivi des pulsars émettant en X , le suivi du candidat trou noir 1E 1740.7-2942, ou encore la première étude du spectre large bande de la binaire X de forte masse et candidat trou noir Cyg X-3.

Un autre type d'expérience est venu du fait de se trouver à l'ISDC pour faire cette thèse: "être scientifique de garde" ("SCientist On DutY" SCODY) en salle d'opérations. Le scody est responsable de la surveillance des instruments et des observations en temps dit "presque réel". Sa tâche première est de réagir rapidement en cas de problèmes liés aux instruments ou bien lors de résultats scientifiques inattendus (nouvelle source, éruption, sursaut gamma; voir l'introduction). Outre l'expérience (et parfois les maux de tête) acquise, ces activités ont conduit aussi à des issues inattendues, comme la détection du premier sursaut Gamma d'*INTEGRAL* alors que j'étais de garde (GCN 1706).

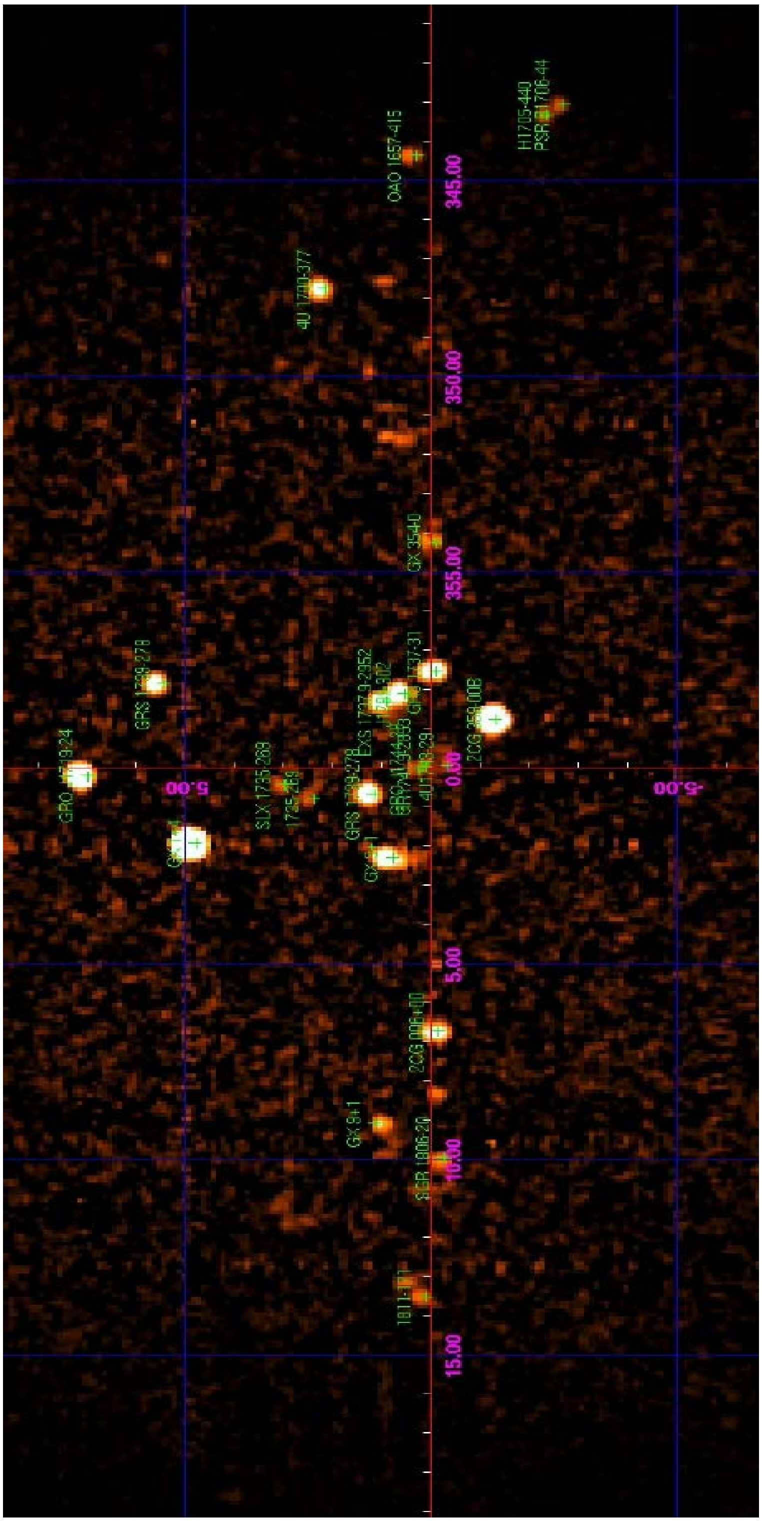

Fig. 2 Simulation del la première année du temps garanti (GPS) avec OSIM/IBIS(ISGRI) (exposition totale:1.8x10^6 sec). Zoom dans le centre Galactique.

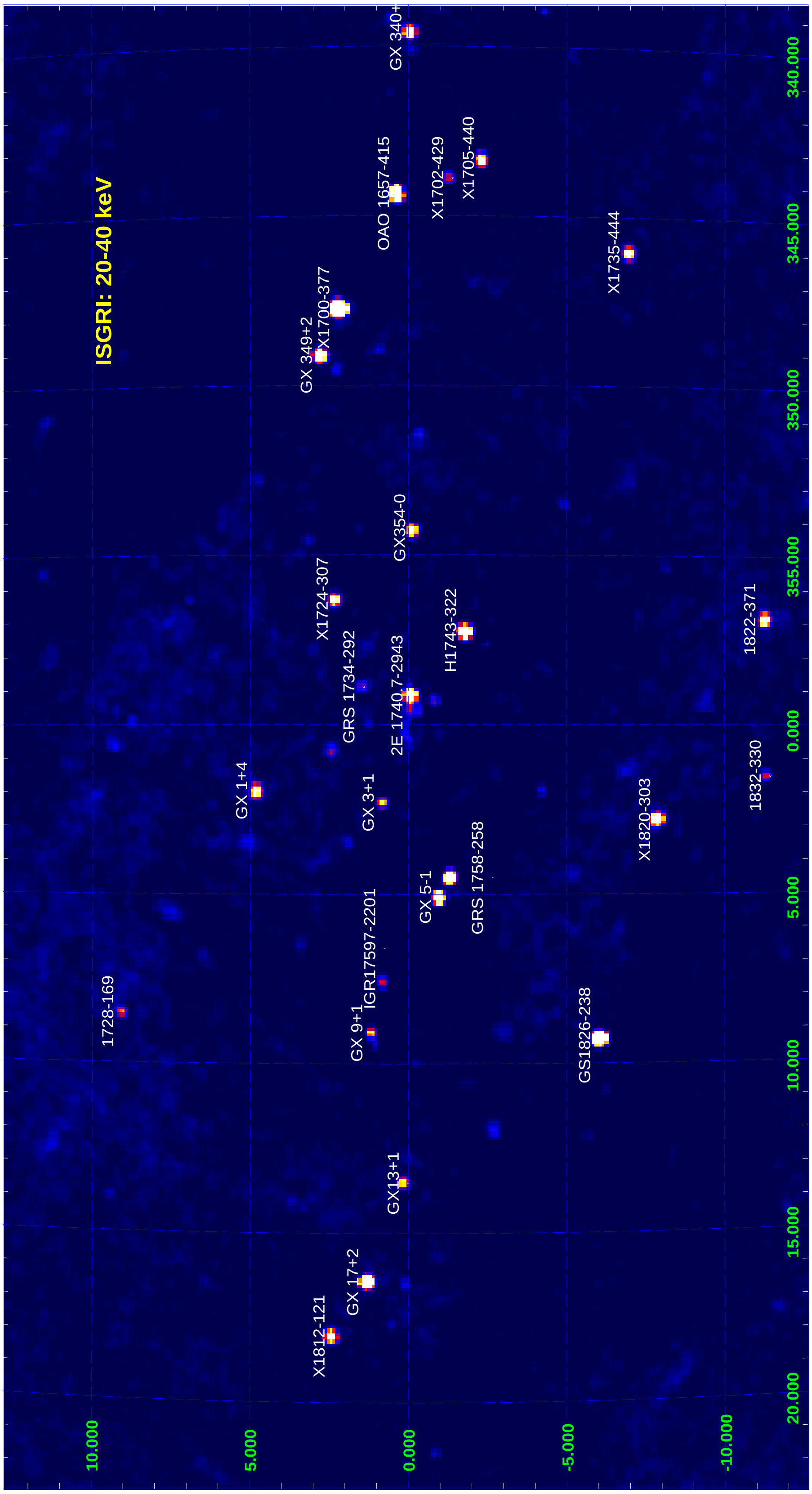

Fig. 3 Mosaique des données de la première année du temps garanti (GPS+GCDE) avec IBIS(ISGRI), ∼5.7Msec

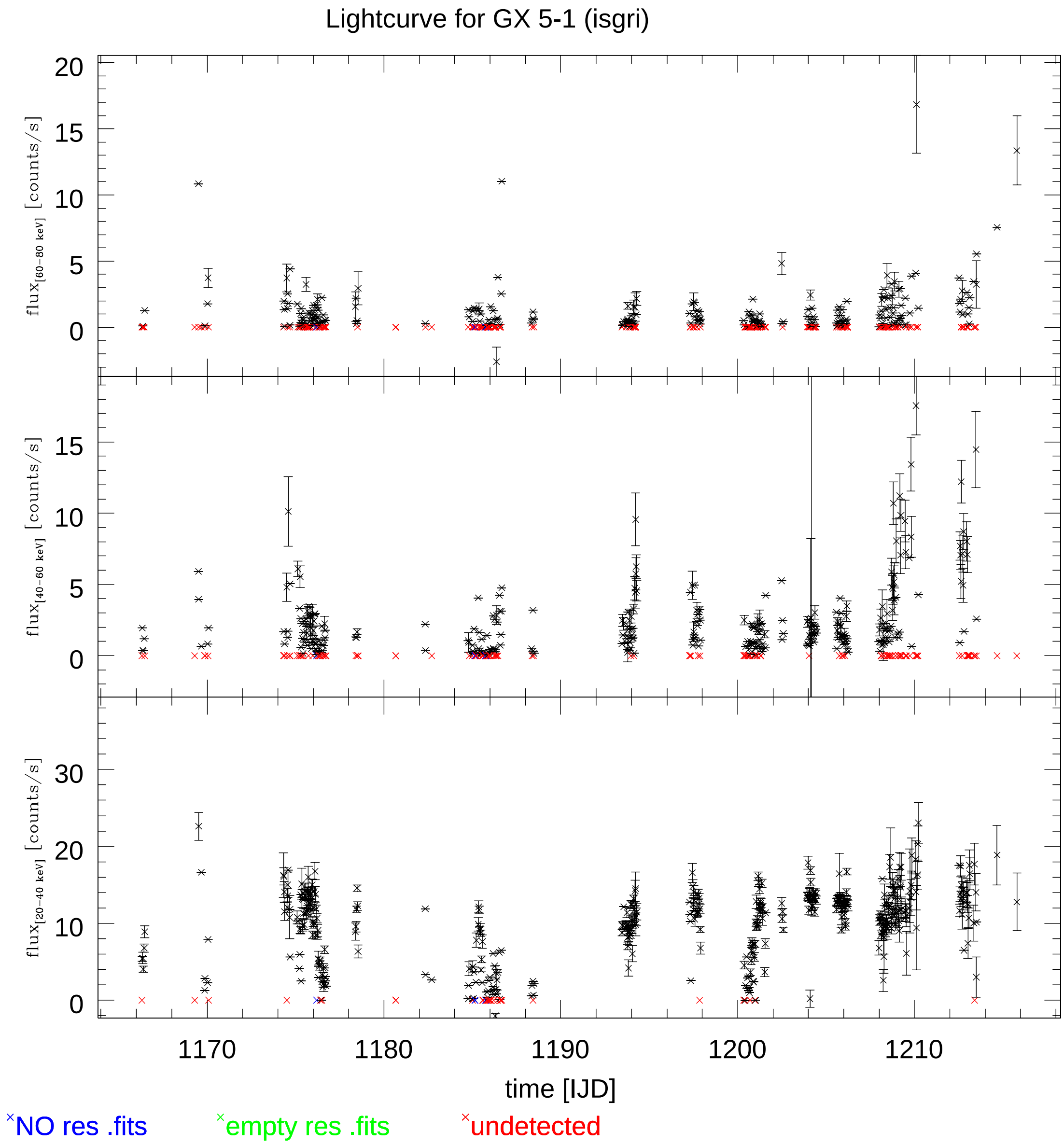

Fig. 4 Coubes de lumière de GX 5–1 dans les bandes d'energie 20–40, 40–60, 60–80 keV. Les barres d'error sont à 1σ. Ces observations ont été effectuées dans la periode entre Janvier 2003 et Julliet 2003 (*INTEGRAL* Julian Day, IJD∼[1160-1220])

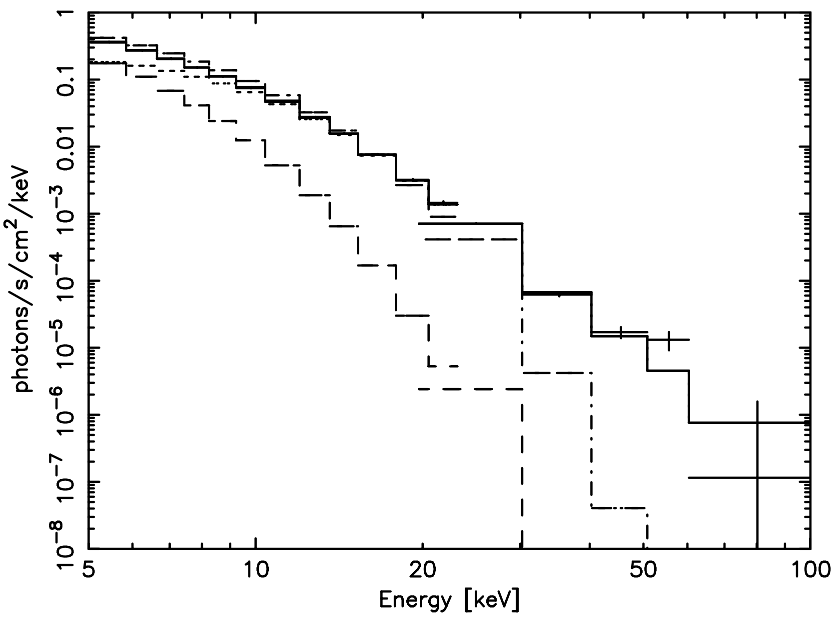

Fig. 5 Spectres de photons de GX 5-1 avec le modèle de l'Est superposé. Les tirets représentent la composante de basse énergie, le disque d'accrétion (1.4 keV). Les tirets-points représentent la composante plus dure, i.e. l'émission thermique de la surface de l'étoile à neutrons sans la composante de Comptonisation (l'épaisseur optique du plasma est fixée à 0). Un excès a haute énergie est relativement évident. Les points (qui se superposent à la ligne continue) représentent la composante dure totale, i.e. l'émission de la surface de l'étoile à neutrons et la composante de Comptonisation (épaisseur optique=0.37). L'excès à haute énergie est bien ajusté. La ligne solide représente le modèle total. L'émission est dominée par la composante haute énergie.

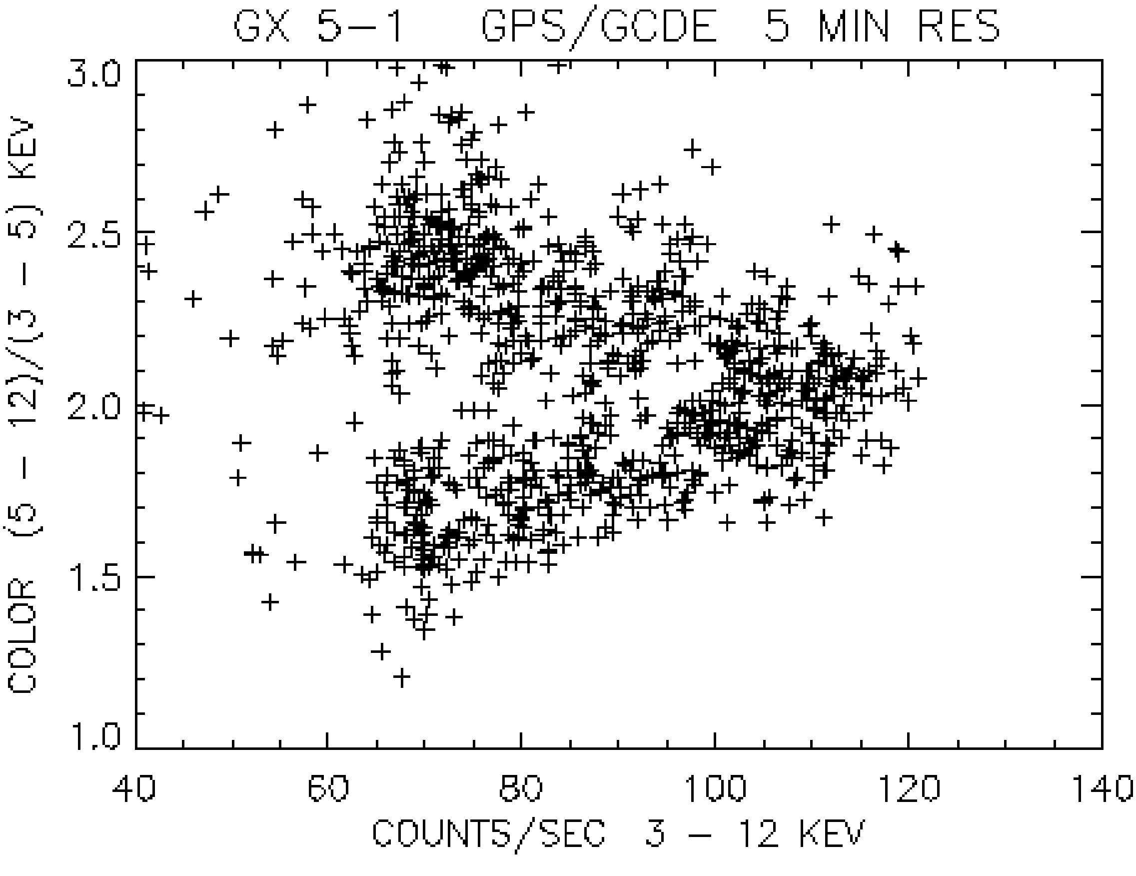

Fig. 6 HID de GX 5-1 obtenu à partir des données de JEM-X. Une partie du Z est clairement visible, à savoir les branches horizontale (supérieure) et normale (inférieure).

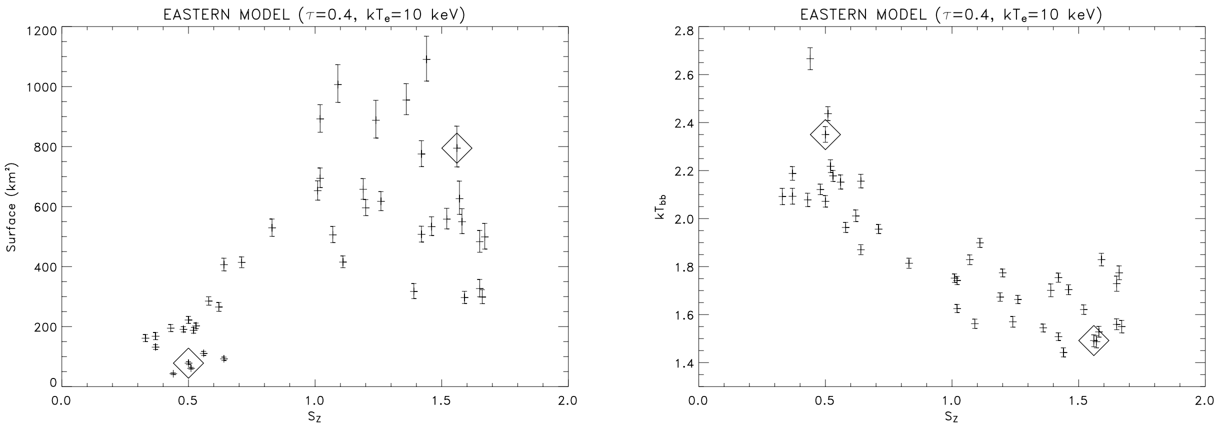

Fig. 7 Relations entre les propriétés des photons thermiques et la position de la source le long du Z. La température du plasma d'électrons est fixée à 10 keV, et l'épaisseur optique à 0.4. Cadre de gauche: évolution de l'aire émettrice du corps noir en fonction du paramètre S_z indiquant la position le long du Z (S_z=0 signifie que la source est au début du Z, i.e. dans le HB où le taux d'accrétion est supposé être plus faible. Lorsque la source se déplace vers le NB, S_Z et le taux d'accrétion augmentent). Cadre de droite: évolution de la température de la surface émettrice de l'étoile à neutrons, kT_{bb} , en fonction de S_Z.

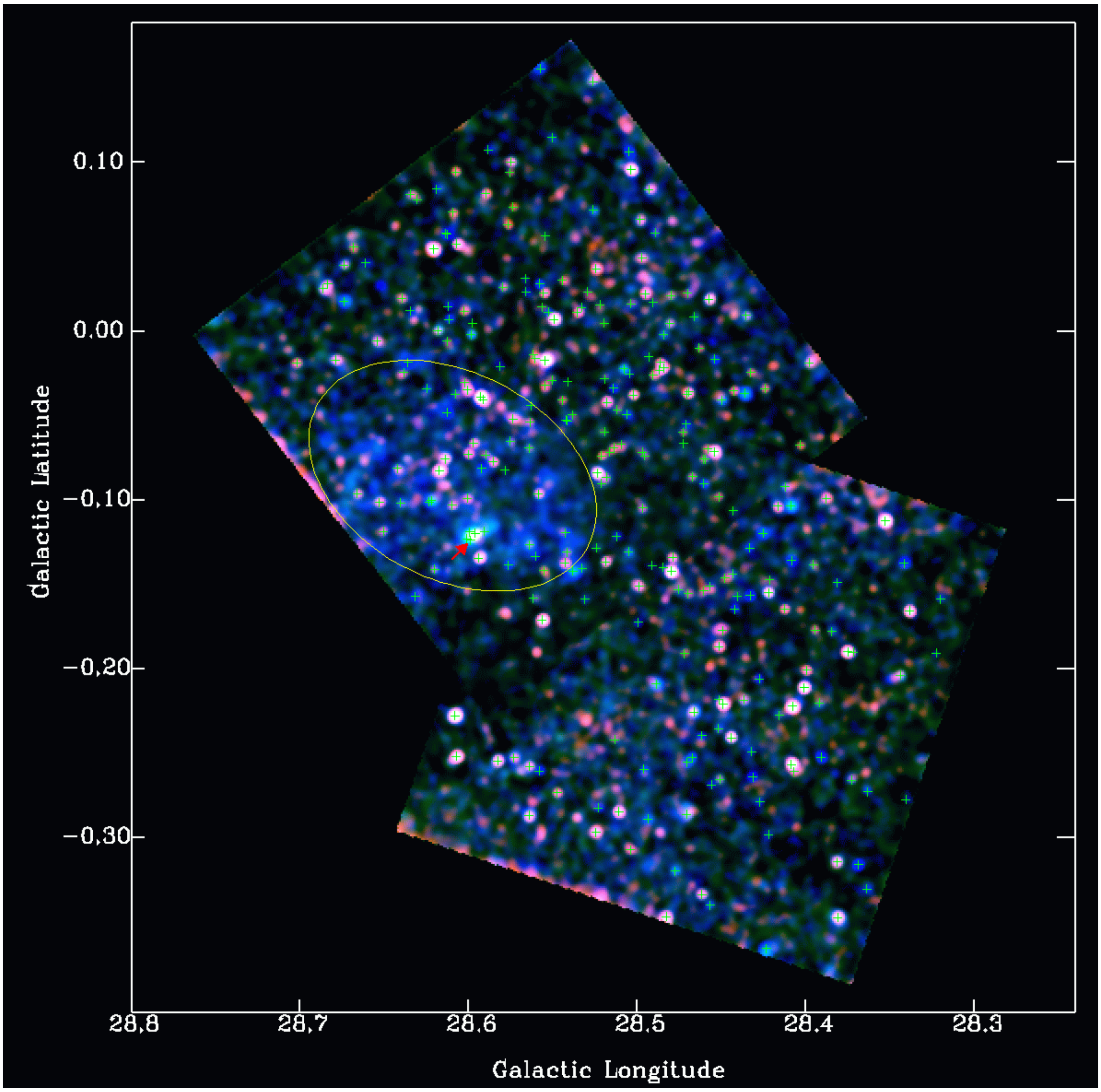

Fig. 8 Les sources detectées dans nos observations Chandra.

Table of contents

List of acronyms

- *ADAF* Advection Dominated Accretion Flow
- *ADC* Accretion Disc Corona
- *AGN* Active Galactic Nucleus
- *ATEL* Astronomer's TELegram
- *AU* Astronomical Unit
- *BH* Black Hole
- *BHC* Black Hole Candidate
- *CONS* CONsolidated
- *CC* Colour-Colour diagram (also CD)
- *CD* Colour-colour Diagram (also CC)
- *CE* Common Envelope
- *CO* Compact Object
- *CV* Cataclysmic Variable
- *DITHERING* In order to improve an instrument with coded mask spatial resolution, it is possible to use the 'dithering' technique. Dithering consists in obtaining multiple images of the same field of view, with an attitude shift between each image.
- *DRP* Dithering Reference Point
- *EOR* End Of Revolution
- *FB* Flaring Branch
- *FCFOV* Fully Coded Field Of View
- *FITS* Flexible Image Transport System, a standard astronomical data format
- *FOV* Field Of View
- *FTOOLS* FITS based software utilities
- *GCDE* Galactic Centre Deep Exposure
- *GCN* Gamma-ray Coordinates Network
- *GOES* Geostationary Operational Environmental Satellites

- *GPS* Galactic Plane Scan
- *GRB* Gamma Ray Burst
- *G/S* Ground Segment
- *GSFC* Goddard Space Flight Center
- *GUI* Graphical User Interface
- *HERC* High Energy Reference Catalogue
- *HB* Horizontal Branch
- *HID* Hardness Intensity Diagram
- *HMXRB* High Mass X-Ray Binary
- *IA* Interactive Analysis
- *IAUC* International Astronomical Union Circulars
- *IBAS* *INTEGRAL* Burst Alert System
- *IBIS* Imager on Board *INTEGRAL* Satellite
- *INTEGRAL* INTErnational Gamma Ray Astrophysics Laboratory
- *IOSM* Interactive Operations Status Monitoring
- *IPN* InterPlanetary Network
- *IQLA* Interactive Quick Look Analysis
- *IREM* *INTEGRAL* Radiation Environment Monitor
- *ISGRI* *INTEGRAL* Soft Gamma Ray Instrument
- *ISDC* *INTEGRAL* Science Data Center
- *ISOC* *INTEGRAL* Science Operations Center
- *JEM-X* Joint European Monitor for X-Rays
- *LMXRB* Low Mass X-Ray Binary
- *MCD* Multi Colour Disc
- *MOC* Mission Operations Center
- *NB* Normal Branch
- *NRT* Near Real Time
- *OSA* Off-line Scientific Analysis
- *OSIM* Observation SIMulator

- *OSM* Operations Status Monitoring
- *OG* Observation Group defined as a collection of Science Window Groups plus observation level results.
- *OMC* Optical Monitoring Camera
- *PCFOV* Partially Coded Field Of View
- *PICsIT* Pixellated Imaging Caesium Iodide Telescope
- *POINTING* A specific commanded location on the Celestial sphere. It is also the period of time during which the spacecraft reference axis (X axis) is held at a commanded location.
- *QLA* Quick Look Analysis
- *RLO* Roche Lobe Overflow
- *RXTE* Rossi X-ray Timing Explorer
- *S/C* SpaceCraft
- *S/W* Software
- *SA* Standard Analysis
- *SCW* Science Window, a unit of continuous observing time used by the ISDC system to archive and process data. It is the basic unit of *INTEGRAL* observations. Under normal dithering operations one science window shall correspond to one S/C pointing or slew manoeuver. In the OSIM it refers only to pointings as slews are not simulated.
- *SLEW* The movement of the S/C between 2 pointings. Also the period of time covered by this.
- *SMBH* Super Massive Black Hole
- *SPI* SPectrometer on board *INTEGRAL* satellite
- *SXT* Soft X-ray Transient
- *TM* TeleMetry
- *TOO* Target Of Opportunity
- *XRB* X-Ray Binary
- *WD* White Dwarf

Chapter 1
INTRODUCTION

This thesis has been entirely done at the *INTEGRAL* Science Data Centre (ISDC). Working at a data centre of a satellite means being given unique opportunities, participating to its main events, witnessing its discoveries, being part of the whole system from "behind the scenes". As it will become clear through these pages, it also means being involved in project activities that end up being an important part the PhD itself.

The main topic of this thesis is the study of low mass X-ray binaries (LMXRBs) in the X-rays and γ-rays with *INTEGRAL*.

X-ray binaries contain either a neutron star or a black hole accreting material from a companion star. The classification as low or high mass X-ray binary is based on the spectral type of the companion. In a LMXRB the companion is an old type star. We are able to define a LMXRB quite easily. Nevertheless, when we look at the observational differences it seems amazing that the same basic "pattern" (old type star - compact object - disc) can give rise to many observational differences: persistent emission, transient behaviour, bursting activity, X-ray pulsations, dips, state transitions, ejections, etc.

We could think that these observational differences are related to the fact that in some systems there is a black hole while in some others there is a neutron star. But actually, this turns out to be a very delicate point. Only in some cases can we actually tell the nature of the compact object.

Digging in further, we see that even when we restrict our attention to LMXRBs with a neutron star and even more, with a persistent and bright emission, still we find observational differences among the objects, the so-called Atoll and Z sources.

Since the discovery of the first non-solar X-ray point source, Sco X-1 (Giacconi et al., 1962), the interest for the X-ray sky grew strong. X-ray imaging instruments were built in the late 1970s allowing a wide range of X-ray luminosity sources to be discovered. LMXRBs, and X-ray binaries in general, have been thoroughly studied in the soft X-ray band (2–10 keV) where they were first observed and classified. Historically, two main spectral states were first observed, the "high-soft" and "low-hard" spectral state, according to the luminosity of the source in the 2-10 keV band (higher for the soft state). Observations performed above the "traditional" energy range showed that the behaviour above 10 keV is different: "a low-hard" state is normally brighter in hard X-rays. Soft X-ray astronomy developed first and many source classifications still hold for historical reasons.

Observations at higher energies were rendered difficult by the very nature of the radiation: hard X-rays and γ-rays cannot be focussed and more difficult techniques are required to have imaging in these energy ranges. With the progress of technology more and more missions started to observe at higher energy and, as a result, our understanding of X-ray binaries changed. A good example can be the study of the nature of the compact object in LMXRBs. A part from some cases in which the nature seems clear, a signature for the presence of a black hole has been always looked for.

Accreting black holes were widely believed to have harder 20–500 keV spectra than accreting neutron stars. A power-law spectrum with a hard tail extending out to several 100 keV was considered a black hole signature (e.g. Sunyaev et al., 1991).

Observations performed with *GRANAT*/SIGMA and *CGRO*/BATSE in the hard X-rays, above 20 keV, showed that X-ray burst sources (low magnetic field neutron stars) can also have hard 20-200 keV spectra (e.g. Barret and Vedrenne, 1994 and Tavani and Barret 1997). Later on, a comparison of hard (20–200 keV) and soft (2–20 keV) luminosities suggested that black hole systems with hard tails have higher (total) luminosity than neutron stars; all neutron star hard tails occured in relatively low accretion rate systems. This was soon proven wrong by *BeppoSAX*/PDS that detected hard tails in bright neutron star binaries belonging to the class of Z sources (Di Salvo and Stella, 2002). Five out of the six Galactic Z sources showed clear hard tails. The only one for which such a detection could not be confirmed prior to the work presented here is GX 5-1 that could never be resolved in the hard X-rays due to the strong contamination from the nearby black hole candidate GRS 1758-258.

An overview of the current knowledge on X-ray binaries is given in the first part of this thesis. It is clear that to better understand the behaviour of accreting sources, neutron star versus black holes, Atoll versus Z etc, a more sensitive survey of the hard X-ray spectra over a wide range of luminosities coupled to imaging capabilities is needed. In this respect, the *INTEGRAL* mission is ideal to study X-ray binaries in a regular and unbiased way in the less explored hard X and γ-ray bands. A regular monitoring of LMXRBs with *INTEGRAL* can play a key role in understanding the physics of these objects.

INTEGRAL was launched in October 2002. Before nominal activity and even long before launch, a lot of work and preparation had to be done for the mission to be successful. In the pre-flight phases, I worked on OSIM, the *INTEGRAL* Observation SIMulator that has been largely used to assess the scientific validitation of the analysis software. A description of the *INTEGRAL* mission and of the work on OSIM is given in Part II.

Working on OSIM has been very useful in order to get familiar with the scientific analysis of *INTEGRAL* data. After launch, data started to come in at a high pace and the time spent on the simulator turned out to be a useful experience to master the means to build and coordinate the *INTEGRAL* LMXRB monitoring program. The first results of this program together with a detailed study of GX 5-1, for the first time disentangled from the nearby black hole candidate, are given in Part III of this thesis.

With *INTEGRAL* we detect a flux of $F_{5-20\,\mathrm{keV}}$ 1.54×10^{-8} erg s^{-1} cm^{-2} from GX 5-1. This is a very intense flux. X-ray binaries are very bright objects but such a high flux is obtained also because this source, as well as the other LMXRBs of our sample, is Galactic.

If we were to look into a region of the sky free from nearby sources then we would need long exposure times before detecting faint Galactic or even extra-Galactic populations that reveal themselves with a flux well below $\lesssim 10^{-8}$ erg s^{-1} cm^{-2}. The Galactic plane survey done by *ASCA* (Sugizaki et al., 2001) reached a sensitivity limit of $\sim 3\times10^{-13}$ erg s^{-1} cm^{-2} in the 2–10 keV band. *ASCA*'s point source sensitivity was limited by the moderate X-ray mirror point spread function ($\sim 1'$). With *Chandra* (sub arcsecond resolution) we have carried a deep survey of the Galactic plane region at (l,b)$\sim$(28.5°, 0.0°), where *ASCA* had detected no point sources. We have detected 274 point sources as well as a clear diffuse emission. With *Chandra* we reach a sensitivity of $\sim 3\times10^{-15}$ erg s^{-1} cm^{-2} in the 2–10 keV band. This *Chandra* survey is presented in Part IV of this thesis.

The *INTEGRAL* and the *Chandra* surveys constitute the main part of this thesis. During my PhD time however, many other opportunities showed up. The systematic study of the *INTEGRAL* data for the LMXRB monitoring as well as working on OSIM brought to several fruitful collaborations that are described in Part V of the thesis.

A somewhat different type of experience came along while being on shift at ISDC, i.e. being a SCientist On DutY in the *INTEGRAL* operations room. Alternatively known as "scody in the barn". The ISDC tasks include running a quick-look analysis of the data within few hours to detect new and unexpected sources, monitoring the instruments and dealing with triggers from the *INTEGRAL* Burst Alert System, IBAS.

These operations are performed by the scientist on duty, a role covered in turn by all the scientists of ISDC. Every shift lasts three days, corresponding to one revolution, about once every month. The scody is primarily responsible for monitoring the scientific output of the *INTEGRAL* instruments and reacting quickly to problems or scientific results. The main tasks are:

- *Interactive Operations Status Monitoring, IOSM*: Six screens in the operations room are dedicated to monitoring the instruments. The scody regularly checks the health all the *INTEGRAL* instruments - JEM-X, SPI, OMC, IBIS (two screens), IREM and the spacecraft itself (the latter two in one screen).

- *Interactive Quick Look Analysis, IQLA*: The results of the QLA analysis are displayed interactively for ISGRI and JEM-X via the Interactive QLA tools developed locally at ISDC. The scody's main task is to continually monitor this output during the day to check for behaviour of sources that may trigger an *INTEGRAL* TOO, new sources or highly variable sources, recently announced sources (such as XTE transients, delivered via e-mail to the operational account). The action to be taken in these cases is carefully defined in the procedures maintained by the two operation managers.

- *Interactive Burst Alert System, IBAS*: The IBAS system provides alerts to the operators in the event of a Gamma-Ray Burst (GRB) being detected by *INTEGRAL*. The response required from the scody depends on the nature of the GRB detection and ranges from immediate action (in the case of a trigger within the IBIS field of view) to low priority monitoring of strong bursts seen in the SPI-Anti Coincidence System. The results of IQLA and IBAS are displayed on four different screens in the operations room adding up to a total of ten screens, shown in Fig. 1.1.

- *End of Revolution, EOR, Report*: The scody is responsible for summarising the scientific performance of *INTEGRAL* during the revolution in the EOR report. Since the reports are publicly accessible via the web, care is taken not to release sensitive information e.g. concerning private observations seen with IQLA.

For a young scientist being on duty is an important experience. We are the first to see images of the high energy sky with *INTEGRAL* discovering new sources or unusual behaviour of well known ones, having the responsibility of triggering a target of opportunity, investigating the GRB alerts. We have the chance to look at regions of the sky and sources that we might not have the opportunity to see otherwise; to build the knowledge of which sources, not necessarily belonging to our field of research, are hard X-ray emitters; to consider an event from different points of view, investigating its nature on the basis of the simultaneous information gathered from many missions (e.g. *INTEGRAL* high energy instruments as well as the radiation environment monitor

Figure *1.1: The ten screens that the scientists on duty use during their shifts. They are continuously updated with housekeeping and scientific data from INTEGRAL. The six on the left are for monitoring the instruments (IOSM), the four on the right include the IQLA screens (shown in the image) and IBAS screens (in a different workspace and thus not visible in the image). The digital clock on the upper left shows the hours, minutes and seconds in the INTEGRAL orbit while the one on the right shows the universal time which is the satellite's time system. In between the revolution number is shown. (Credits: ISDC - A. Paizis).*

IREM, the RXTE All Sky Monitor [7], GOES [8], the missions belonging to the Inter-Planetary Network, IPN [9], etc).

Besides the experience (and sometimes headaches!) gained, the activities linked to the operations led also to unexpected outcomes, as described in Part V of this thesis.

[7] http://heasarc.gsfc.nasa.gov/xte_weather/

[8] Geostationary Operational Environmental Satellites, http://www.sec.noaa.gov/today.html, that report the space weather conditions, an indirect way of monitoring the solar activity to which *INTEGRAL*, and especially JEM-X, is sensitive.

[9] http://gcn.gsfc.nasa.gov/gcn/gcn_main.html, to cross check the occurence of GRBs.

First part

X-RAY BINARIES

Chapter 2
ACCRETION PROCESSES

In this chapter the basic concepts of the accretion processes in astrophysics are given. It is intended as an introduction to this fundamental branch of high energy astrophysics. This part is to be considered as the starting point to understand the emission of X-ray binaries that are described in the next chapter. For more details we refer to the articles of Frank, King and Raine (2002) and Kato, Fukue and Mineshige (1998) which have been used as main references for this chapter.

2.1 Sources of energy in the Universe

The luminosity of the Sun is $L_\odot$=3.83 $\times$ 10^{33} erg s^{-1}. Historically, many candidates were considered as the main energy source for such a luminosity. In the case of gravitational energy, if an object of mass M gravitationally contracts from infinity to a radius R, the gravitational energy released is

$$E_{grav} \simeq GM^2/R \tag{2.1}$$

The efficiency, η_G, of gravitation in releasing mass energy can be estimated by dividing Eq. 2.1 by the rest mass of the object Mc^2 (c being the speed of light and G the gravitational constant). For the Sun we obtain

$$\eta_G \simeq GM/Rc^2 \simeq 2 \times 10^{-6} \tag{2.2}$$

which is well below the efficiency η_N of the hydrogen nuclear fusion

$$\eta_N \simeq 7 \times 10^{-3} \tag{2.3}$$

The main source of energy of the Sun, and of stars in general, is nuclear fusion which takes place in the central regions.

This is not true for all kinds of sources. From the quantities involved in the estimate of η_G above it is clear that the larger the ratio M/R, i.e. the compactness of the accreting object, the greater the efficiency. In fact for a neutron star of radius R=10 km and mass $M \simeq M_\odot$ we have

$$\eta_{G(NS)} \simeq GM/Rc^2 \simeq 0.1 \tag{2.4}$$

Indeed gravitational energy *is* the answer to the energetics involved in the physics of compact objects such as white dwarfs, neutron stars and stellar mass/super massive black holes.

But how is this gravitational energy released?

Since the discovery of quasars in the 1960's many researchers have constructed various models for the enormous amount of energy that these objects were able to release. Quasars emit about 10^{47} erg s^{-1}, which is about a thousand times more luminous than a non-active galaxy, and the engine behind this emission has been a great enigma in astronomy. This was finally solved by the concept of a super massive black hole accreting matter from a surrounding accretion disc.

Accretion discs are rotating gaseous discs that form around objects such as protostars, white dwarfs, neutron stars and black holes. When gas falls onto a massive object gravitational energy of the gas is released. This is the *mass accretion* process in astronomy.

It is important to note that not *all* accretion processes form a disc. In fact matter accreting onto a mass M will form a disc when its specific angular momentum J is too large for it to hit the accreting object (M) directly. We define the circularisation radius

$$R_{circ} = J^2/(GM) \tag{2.5}$$

as the radius at which matter would orbit if it did not loose angular momentum. The condition for disc formation is typically that R_{circ} should be larger than the size of the accretor (King, 1995). In X-ray binaries the accretor is a neutron star or a stellar mass black hole and the condition always holds if accretion is via the Roche lobe overflow (RLO). The outcome is much less clear if the accretion is from a wind, as J is much lower in this case. As we will see in Section 3.3, this means that Low Mass X-ray Binaries (LMXRBs) that are RLO-fed accretion systems, are more likely to form an accretion disc than High Mass X-ray Binaries (HMXRBs) that are generally wind-fed accretion systems.

Roche lobe overflow

In a binary system with a compact star of mass M_1 and a 'normal' star of mass M_2 orbiting around the common centre of mass (CM) with separation a, the shape of the resulting equipotentials is governed entirely by the mass ratio $q = M_2/M_1$. Nevertheless for any value of q the following will happen: matter orbiting at large distance from the system ($r \gg a$) will see only a point mass concentrated in the CM i.e. the equipotentials are circular. The same applies for matter orbiting in the vicinity of one of the two stars ($r \ll a$): it will feel only the gravitational pull of the nearest star. Between these two extreme cases there is a critical case where the equipotential has a figure eight shape (as shown in Fig. 3.1). The part surrounding each star is known as its *Roche lobe*. The two lobes join at the inner Lagrange point, L_1. Material inside of the two lobes in the vicinity of L_1 finds it much easier to pass through L_1 into the other lobe than to escape the critical surface. In the case of LMXRBs, when the 'normal' star fills its Roche lobe matter will overflow through L_1 into the Roche lobe of the companion. The transferred material cannot land on the accreting star until it has gotten rid of most of its angular momentum. This leads to the formation of the accretion disc.

In the case of a conservative accretion with constant binary mass and angular momentum, mass transfer from the less massive to the more massive star, as in a LMXRB, will widen the orbit. Conversely, transfer from the more massive to the less massive star, as in a HMXRB, will shrink the binary separation if the disc is formed.

In a binary system with no accretion going on, the orbit will be circularised and the separation will gradually decrease by gravitational radiation and/or magnetic braking.

2.2 The standard accretion disc model

In 1973 Shakura and Sunyaev proposed a fundamental model for accretion discs. This model is now referred to as the *standard accretion disc model* or the α-disc. According to this model, gravitational energy is eventually transformed into radiation so that a bright disc can be observed. From the early 1980's distinct types of accretion that have low emissivity have also been considered (such as the so-called *advection dominated accretion flow*, ADAF). Currently, multiple branches with different associated variability and luminosity are recognised as the source of the wide behaviour of accreting objects.

2.2.1 The basic picture

An accretion disc consists mainly of hydrogen gas. In the standard model, the disc is flat, i.e. geometrically thin, and opaque, i.e. optically thick. The gas in the disc is rotating around the central object with different velocities at different radii. At each radius r the gravitational force is balanced by the centrifugal force and each annulus of size dr is in circular orbit.

Between the different rings forming the accretion disc there is friction (viscosity). As a result, the gas is heated and begins to emit electromagnetic radiation. The accreting matter liberates *half* of its kinetic energy in the form of heat in the accretion disc. This radiation is believed to be part of the source of luminosity in e.g. X-ray binaries. The accretion is sustained by the companion star that is regularly providing matter.

Through the viscous interaction between the inner and outer layer, the faster inner layer looses angular momentum and falls slightly inwards while the slower outer layer gains angular momentum. The rotating disc gradually falls in, i.e. accretes, towards the centre while angular momentum is transferred towards the outer region.

When in the vicinity of the accreting object, the fate of the accreting matter depends on the nature of the central object. In the case of accretion on a weakly magnetised, i.e. old, neutron star, the magnetic field is so weak ($\lesssim 10^{10}$ G) that it does not influence the accretion flow. The accretion disc can extend very close to the neutron star surface where the remaining half kinetic energy of the accreting matter is released and radiated away as blackbody emission from the neutron star's surface.

In the case of a black hole, in the innermost regions of the disc the gravitational attraction force increases in-wards so strongly that there is no stable circular orbit for a particle at $r<r_{ls}$, r_{ms} being the radius of the marginally stable circular orbit. As a result the standard accretion disc has an inner edge. In the case of a Schwarzschild (non rotating) black hole, for example, the radius r_{in} of the inner edge is

$$r_{in} \simeq r_{ms} = 3r_g \tag{2.6}$$

where r_g is the Schwarzschild radius ($r_g = 2GM/c^2$). For a Kerr (maximally rotating) black hole $r_{in}=r_g/2$.

2.2.2 The basic parameters

The basic parameters of an accretion disc are the mass M of the central object, the mass accretion rate $\dot{M}$ and the viscous parameter α. $\dot{M}$ is the amount of gas that falls onto the central object per unit of time. The viscous parameter represents the magnitude of the friction between the gas layers and is a parameter internal to the disc.

2.2.3 Temperature, spectrum and luminosity

Since the gravitational potential is stronger at the centre of the disc where the rotation speed is faster, the heating rate is also larger in the inner region rather than in the outer region. The gas temperature of the disc is higher in the inner region and decreases with R as

$$T(R) = T_*(R/R_*)^{-3/4} \tag{2.7}$$

R_* being the radius of the accreting star and T_*

$$T_* \propto (M\dot{M}/R_*^3)^{1/4} \tag{2.8}$$

where M is as usual the mass of the compact object, $\dot{M}$ the mass accretion rate. In the standard picture, the disc is assumed to radiate locally as a blackbody. Since the disc has different temperatures at different radii the resulting disc spectrum is a superposition of blackbody spectra with a wide range of effective temperatures. Such a spectrum is called multi-colour disc blackbody (MCD, Mitsuda et al., 1984).

In the inner region of the disc, a hot outer layer affects the emergent spectrum by Comptonisation. This leads to an observed temperature T_{col} which is higher than the effective temperature T_{eff}. The value of this hardening factor is still a matter of debate and is estimated to be about 1.5 for X-ray bursters (Ebisawa et al., 1994 and references therein) and between 1.7-1.9 for black hole candidates (Shimura and Takahara, 1995).

The disc luminosity L_d is given by

$$L_d = (GM\dot{M})/(2r_{in}) = (1/2)L_{acc} \tag{2.9}$$

where r_{in} is the radius of the disc inner edge. This luminosity is just *half* the gravitational energy per unit mass at r_{in} times the accretion rate $\dot{M}$ (see Eq. 2.1) i.e. is half of the luminosity available in the accretion process. This means that half of the energy is radiated while the matter in the disc slowly spirals inwards and, for the case of a neutron star, the rest is available to be radiated from the boundary layer itself which is as important as the disc for the total emission.

In the case of an accretion disc around a Schwarzschild black hole with $r_{in}=3r_g=6GM/c^2$ the disc luminosity becomes

$$L_d = (1/12)\dot{M}c^2 \tag{2.10}$$

which depends only on the mass accretion rate.

The luminosity associated with the mass accretion is generally written as

$$L_{acc} = \eta\dot{M}c^2 \tag{2.11}$$

where η is the efficiency of conversion of the rest mass energy into heat (see Section 2.1). In the above approximation the efficiency of disc accretion onto a Schwarzschild black hole is $\eta\simeq0.08$. For a white dwarf for which $M=M_\odot$ and $R\simeq5\times10^8$ cm, $\eta\simeq3\times10^{-4}$. For a neutron star with $M=M_\odot$ and $R = 1.5\times10^6$ cm $\eta \simeq0.1$. Therefore accretion onto compact objects can be a remarkably powerful source of energy.

2.3 Eddington luminosity

If we consider the inner disc radius r_{in} in units of the Schwarzschild radius r_g then the disc luminosity L_d is only a function of the mass accretion rate $\dot{M}$ and does not depend on the mass of the compact object M (see Eq. 2.11). Nevertheless, M plays an important role when considering the maximum accretion luminosity achievable. As the luminosity becomes larger for a fixed mass, the radiation pressure also increases and eventually overcomes the gravitational force. The gas particle is ultimately blown off and accretion stops. This means basically that an infinitely luminous accretion powered object cannot exist. For a fixed mass there is a maximum possible luminosity obtained via stable accretion onto a compact object. The luminosity at

Table 2.1: Characteristics of the compact objects in various accreting systems. HMXRBs are also accreting systems but in general not via the formation of an accretion disc (see next chapter), therefore they are not listed here. CV: cataclysmic variable; WD: white dwarf; NS: neutron star; BH: black hole; AGN: active galactic nucleus; SMBH: super massive black hole; AU: astronomical unit= 1.5×10^{13} cm; $R_\odot$=6.96×10^{10} cm; $L_\odot$=3.83×10^{33} erg s^{-1}; $M_\odot$=1.99×10^{33} gr; (Kato et al. 1998).

System	Accreting object	Mass	Size
CV	WD	$\sim M_\odot$	$\sim 10^{-2}\ R_\odot$
LMXRB	NS	$\sim M_\odot$	10 km ($\sim$$10^{-5}\ R_\odot$)
	BH	$\gtrsim$3 $M_\odot$	$r_g$$\gtrsim$10 km
AGN	SMBH	$\sim 10^6$-$10^9\ M_\odot$	$r_g \sim$ 0.02-20 AU ($\sim$4-4$\times10^3\ R_\odot$)

which the radiation pressure (on ionised gas) is exactly balanced by the gravitational force is the Eddington luminosity and in the case of a steady and spherically symmetric accretion flow is

$$L_{Edd} \simeq 1.3 \times 10^{38} (M/M_\odot) \mathrm{erg\,s^{-1}} \tag{2.12}$$

This is deduced for the case of a spherically symmetric accretion flow and not for a disc, nevertheless it is a simple way to have a good estimate of the maximum luminosity in stable conditions for any kind of accreting compact object. L_{Edd} depends on the ratio H/He present in the disc. If hydrogen is dominant then L_{Edd} is as given in Eq. 2.12. For an Helium disc, L_{Edd} is about twice as much since more radiation is needed to balance the heavier Helium rich disc.

For accretion on a neutron star, L_{Edd} corresponds to an Eddington mass accretion limit of

$$\dot{M}_{Edd} \simeq 1.5 \times 10^{-8} M_\odot \, \mathrm{yr}^{-1}. \tag{2.13}$$

Typical X-ray luminosities of LMXRBs and HMXRBs are in the range of 10^{35}–10^{38} erg s^{-1} corresponding to mass accretion rates in the range of 10^{-11}–$10^{-8} M_\odot$ yr^{-1}.

It is important to note that the $\dot{M}_{Edd}$ limit is a limit for the *accreted* mass rate. The *mass transfer rate* from the companion towards the neutron star may be considerably larger. Calculations show that mass transfer exceeding $10^{-4} M_\odot$ yr^{-1} may still be dynamically stable (Tauris et al., 2003).

2.4 Accretion disc powered objects

Tables 2.1 and 2.2 summarise the characteristics of the central objects and surrounding accretion discs in various astronomical objects.

AGNs are by far the brightest objects but their emitted radiation is cooler than the case of LMXRBs. In fact the luminosity $L \propto \dot{M}$ (from Eq. 2.11), $L \propto M$ (from Eq. 2.12) and $M \propto R$ for the case of a black hole. All this in Eqs. 2.7 leads to

$$T \propto L^{-1/4}. \tag{2.14}$$

The more luminous the object, the cooler the disc and radiated spectrum.

Accretion onto a stellar mass BH will emit in the X-rays/γ-rays whereas accretion on a SMBH will have a strong emission in the optical and ultraviolet. This indeed corresponds to observational results.

Table 2.2: Accretion disc properties in various systems (10^7K correspond to $\simeq 1$ keV) (Kato et al. 1998).

System	Mass	Size	Temperature	Luminosity
CV	$\ll M_\odot$	$\sim R_\odot$	$\sim 10^4$-10^5 K	10^0-10^2 $L_\odot$
LMXRB	$\ll M_\odot$	$\sim R_\odot$	$\sim 10^4$-10^9 K	10^0-10^5 $L_\odot$
AGN	$\lesssim 10^6$ $M_\odot$	$\sim 10^7 R_\odot$	$\sim 10^5$ K	10^{10}-10^{13} $L_\odot$

2.5 Final remarks

Accretion is the main engine behind the high energy emission of many compact objects. It is important to note though that the radiation emitted from the accretion itself (i.e. the disc and the radiation released on the neutron star surface) is only in some cases directly visible. In most cases it is the fuel for inverse comptonisation by a hot plasma present in the system. The resulting radiation is boosted to higher energies, generally in the X/γ-ray energy range.

If we were to look at the sky in an X-ray survey, e.g. in the direction of the Galactic centre or plane, we would see that (most of) the brightest objects are Galactic X-ray binaries (XRBs). XRBs are accretion powered objects and are so close to us that they appear much brighter than the very distant, extragalactic, AGNs that are intrinsically, by far, the brightest persistent objects (see Tab. 2.2) in the X-ray sky [10] but that appear dim due to their high distance.

The study of the bright-nearby sources and the distant-dim ones requires very different strategies. For the bright nearby sources, regular scans of the regions where they are mostly located (Galactic centre and plane) are an efficient way to look into their variations. For the distant dim objects, deep observations are required with an excellent angular resolution capable of resolving them given that they are much more numerous than the bright nearby ones.

A natural evolution of these strategies resulted in the use of the *INTEGRAL* monitoring programme (5 keV-10 MeV, angular resolution of $12'$ above 20 keV) for the study of the Galactic XRBs and to a CHANDRA deep field survey (0.5-10 keV, angular resolution $< 1''$) for the study of the numerous distant sources.

These two studies are described in part III and IV of this thesis, respectively.

[10]The quasar 3C 273 is at 2.5×10^9 light years from us, to be compared to the $\sim 10^4$ light years for Galactic sources.

Chapter 3
X-RAY BINARIES: AN OVERVIEW

In this chapter an overview of X-Ray binaries is given. The core of this thesis is the hard X-ray emission of LMXRBs hosting a neutron star, in this overview more attention is given to this class of objects. For more details we refer to the book *X-Ray Binaries* (ed. Lewin, van Paradijs and van den Heuvel, 1995, Cambridge) and to the recent review by Tauris and van den Heuvel (2003) that have been mainly used as a reference for this section.

3.1 Introduction

Over 90% of the bright Galactic X-ray sources belong to the wide class of X-ray binaries (XRBs). XRBs are classified into two categories, the low-mass X-ray binaries and high-mass X-ray binaries according to the spectral type of the companion star. These two classes are very different in geometry, origin, evolution and X-ray properties. Figure 3.1 shows a schematic view of a representative HMXRB and LMXRB. We summarise the main characteristics of these two systems in Table 3.1.

HMXRBs can be subdivided in two groups: standard HMXRBs and Be binaries. The standard HMXRBs have a massive giant companion (spectral type O) with $M \gtrsim 20\ M_\odot$. The orbital period of these systems is relatively short, $P_{orb} \simeq 1.4 - 10$ days and the orbit is almost circular. The O-type star generally has a very strong stellar wind and hence the mass accretion can occur mainly through stellar wind capture. In general, these systems are persistent.

On the other hand the Be binaries contain a main-sequence B star with strong emission lines. The orbital period of Be binaries is long, $P_{orb} \gtrsim 15$ days, with eccentric orbits. Many Be systems are (hard) X-ray transients. In fact, normally Be stars have a very strong stellar wind and the X-ray active phase of these objects may correspond to the neutron star passage in the dense wind of the Be star (periastron passage). The observational differences between these two types of systems can be also seen in the P_{spin} - P_{orb} plane, normally known as the "Corbet-diagram" (Corbet 1986).

Like in the case of HMXRBs, LMXRBs can be divided in persistent and transient systems. The transient ones are known as soft X-ray transients (SXTs[11]) due to their spectra that appear softer than in the case of the (hard) HMXRB transients.

In SXTs, the outbursts are likely to be caused by thermal-viscous instability in the accretion disc which occurs if the X-ray luminosity (and average mass transfer rate $\dot{M}$) is below a critical

[11] Historically the first transients detected were very bright, L$\sim 10^{38}$ erg s^{-1}, and had a typical soft to hard spectrum transition. With more observations being performed dimmer, hard transients, L$\sim 10^{38}$ erg s^{-1}, were also detected e.g. GS 2023+338.

value (van Paradijs, 1996). Qualitatively, from equations 2.7 and 2.8, this means also that the accretion disc instability will occur if the temperature, at a certain disc radius, is below a critical value T_c.

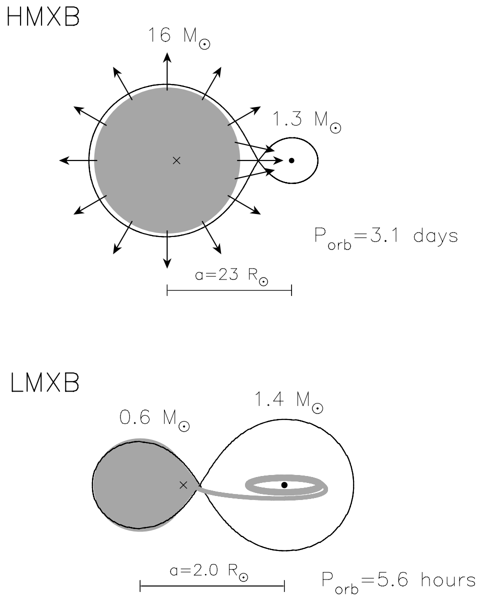

Figure *3.1: Examples of a typical HMXRB (top) and LMXRB (bottom). The compact object in the HMXRB is fed by a strong high-velocity stellar wind and/or by beginning of atmospheric RLO. In the LMXRB the compact object is surrounded by an accretion disc which is fed by RLO. In both cases the Roche lobe equipotential is shown (eight-shaped solid line). (Tauris and van den Heuvel 2003.)*

Observationally, SXTs with neutron stars are relatively rare and almost all LMXRBs with black holes are transients. This would indicate that the accretion disc in black hole systems has a lower mass transfer rate (and temperature) than in the case of neutron stars. Indeed, neutron stars around the same mass companion need to be closer than a black hole for the star to fill its Roche lobe. The disc is smaller and hotter and less likely to trigger the disc instability (Done, 2004 and references therein). The temperature of the disc is also raised via X-ray heating from the central object. This heating, much stronger in LMXRBs than in cataclysmic variables for example, tends to stabilise the accretion flow. This is likely to be the reason why outburst duty cycles of LMXRBs and CVs differ as a class: CVs have shorter quiescent (stable) periods. In their case X-ray heating is not efficient at all to stabilise the flow and outbursts occur more frequently (King and Ritter, 1998).

3.2 The accreting object

In neutron star LMXRBs, the accreting star is very old and weakly magnetised ($B \lesssim 10^{10}$G). In this case, the accretion disc is not influenced by the magnetic field and can extend very close to the neutron star surface where the remaining half kinetic energy of the accreting matter is released and radiated as blackbody emission from the neutron star's surface.

This release of energy from the neutron star surface does not happen always in steady conditions. In general, for lower accretion rates $\dot{M}$, the accreted matter accumulates on the neutron

Table 3.1: Properties of LMXRBs and HMXRBs. (a),(b): see corresponding sections, 3.2 and 3.3 respectively. Adapted from Tauris and van den Heuvel 2003.

	HMXRB	LMXRB
Companion star	Early type (O or B)	Late type (typically G or K)
	$\gtrsim$10 $M_\odot$ (Pop. I)	$\lesssim$1 $M_\odot$ (Pop. II)
L_{opt}/L_X	$\gtrsim$0.1	$\lesssim$0.1
Age	$\lesssim 10^7$yr	$\gtrsim 10^9$yr
Spatial distribution	Galactic plane	Galactic centre and globular clusters
Accreting object$^{(a)}$	high ($\gtrsim 10^{11}$G) B-field NS (or BH)	low ($\lesssim 10^{10}$G) B-field NS (or BH)
Accretion mechanism$^{(b)}$	Wind or atmosph. RLO	RLO
Time scale of accretion	10^5yr	10^7–10^9yr
Orbital period	1–100 d	0.2-200 hr
Orbital separation	$\gtrsim 10^{12}$ cm	$\lesssim 10^{11}$ cm
Type of time variability	regular X-ray pulsations	very few pulsars
	no X-ray burst	often X-ray bursts
	regular X-ray eclipses	few X-ray eclipses
	few X-ray dips	many X-ray dips
X-ray spectrum	kT $\gtrsim$15 keV (hard)	kT $\lesssim$10 keV (soft)

star surface and when the amount of gas is sufficiently high, a runaway nuclear burning takes place and causes *X-ray bursts*.

In few cases, X-ray pulsations have been detected in LMXRBs[12]. Pulsation periods range from about 120 sec for GX 1+4 to about 2.4 msec for SAX J1808.4-3658. The latter is a very important discovery: an accreting millisecond pulsar (i.e. X-ray pulsations) in a LMXRB supports the scenario that LMXRBs are the progenitors of millisecond radio pulsars with a low magnetic field ($\lesssim 10^{10}$ G, see Section 3.5). Spectral features observed in these sources such as a hard spectrum with respect to the average LMXRBs (as e.g. X 1822-371 Parmar, 1986), are better explained by the presence of a high magnetic field pulsar instead of a low magnetic field neutron star.

Accretion onto a highly magnetised (B$\sim 10^{12}$G) young, neutron star (HMXRB) is different. In this case the neutron star is fed by a strong high velocity stellar wind from the companion and in general no accretion disc is formed. The accreted matter is channeled by the strong magnetic field onto the polar caps of the neutron star where it liberates its potential energy. Since in general the magnetic axis does not coincide with the rotation axis, *X-ray pulses* are seen by a distant observer as the neutron star rotates. The confined plasma that produces the X-ray emission decelerates from a few tenths of c to stopping completely on the polar caps and this produces harder spectra than what is produced in LMXRBs from the rotating matter in the accretion disc.

X-ray pulses and bursts are a clear signature of the presence of a surface and are used to discriminate between black holes and neutron stars as the central object. But the lack of such events does not require the presence of a black hole.

3.3 The accretion mechanism

In X-ray binaries the mode of accretion of matter onto the central compact object is determined by the nature of the companion. HMXRBs have evolved (sub)giant companions ($M \gtrsim 10\ M_\odot$). These are massive enough to have a strong stellar wind mass-loss rate ($\dot{M}_{wind} \simeq 10^{-6} M_\odot\ \mathrm{yr}^{-1}$) sufficient to power an X-ray source via an accreting neutron star or black hole for $\sim 10^5$–10^6 yr. Nevertheless, some HMXRBs do have accretion at least partially by Roche lobe overflow and therefore they should have a disc.

LMXRBs are not wind fed X-ray sources as the evolved companion with its $M \lesssim 1\ M_\odot$ does not have a strong wind. These systems undergo mass transfer via RLO from the companion to the compact object. The majority of the transferred material is usually funneled onto the compact object via an accretion disc yielding to accretion rates of $\simeq 10^{-11}$–$10^{-8} M_\odot\ \mathrm{yr}^{-1}$.

Wind-fed accretion is less efficient than RLO as the matter leaves the star in all directions not just towards the accretor and has enough kinetic energy to escape the system except when it passes closely to the accreting star. The total wind mass loss can be high but the fraction of matter that is actually accreted on the companion depends very strongly on the wind velocity V_{wind} ($\dot{M}_{acc} \propto \dot{M}_{wind}/\mathrm{V}^4{}_{wind}$, van den Heuvel 1994) and is in general very small. Conversely, in LMXRBs RLO occurs and almost all the mass is captured by the accreting component.

Another complication to the formation of an accretion disc in HMXRBs is given by the fact that the accreting star is very young and has a significant magnetic field that disrupts any attempt of disc formation at about 100 neutron star radii. This effect is absent in the case of

[12] This is the case of SAX J1808.4-3658, XTE 1751-305, XTE J0929-314, XTE J1807-294, XTE J1814-338, GRO J1744-28, X 1822-371, Her X-1, 4U 1626-67, GX 4+1 (Jonker and van der Klis, 2001 and references therein). The first five systems are accretion-driven millisecond X-ray pulsars (Wijnands 2003).

HMXRBs hosting a black hole for which the formation of accretion disc could occur for very high wind mass loss rates, as e.g. in Cyg X-1. Like in the case of neutrons stars for HMXRBs and LMXRBs harbouring black holes the nature of the companion drives the type of accretion.

LMXRBs have companion stars of $\lesssim$1 $M_{\odot}$ while HMXRBs of $\gtrsim$10 $M_{\odot}$. There must also exist a large number of systems with companion stars masses in the interval of $\sim$1-10 $M_{\odot}$. These are the so-called intermediate mass X-ray binaries (IMXRBs). These systems are not easily observed as a result of simple selection effects. In IMXRBs the companions are not massive enough to produce sufficiently high wind mass-loss rates to power an X-ray source. When they evolve through RLO the relatively large mass ratio between the companion star and neutron star causes this phase to be short lived (only a few 1000 yr). Despite these selection effects against IMXRBs, there are such systems with neutron stars detected: Her X-1 and Cyg X-2. In the latter system the companion has presently a mass $< M_{\odot}$ but is highly overluminous for this mass indicating that it is an evolved star that started out with a mass between 3 and 4 $M_{\odot}$ at the onset of the mass transfer phase (Podsiadlowski et al., 2004), i.e. Cyg X-2 originated from an IMXRB rather than from a LMXRB.

HMXRBs and LMXRBs are naturally selected as X-ray sources fed by a strong stellar wind and RLO.

3.4 Formation and evolution of HMXRBs

The formation of a HMXRB requires two relatively massive stars ($>$12 $M_{\odot}$). Alternatively, the second Main Sequence star (MS) can be less massive initially as long as it gains enough material from the primary star so that it will later end up above the threshold mass for undergoing a supernova explosion like the primary star.

Figure 3.2 shows the formation and evolution of a HMXRB. The more massive MS star evolves faster and transfers most of its envelope to the companion via Roche lobe overflow. Therefore the more massive star becomes less massive just before the supernova explosion. This transfer of matter is very important as it allows the system to remain bound also after the explosion. Once the neutron star is formed the binary system can become an X-ray source if the stellar wind of the companion is strong enough or if the companion starts leaving the main sequence. In either case a HMXRB is born. The orbit of the system is relatively wide and the accretion is mainly wind fed. The difference between a standard HMXRB and a Be-binary could be due to the initial mass of the companion.

All HMXRBs end up in a common envelope phase, as the neutron star (or low mass black hole) is engulfed by the extended envelope of its companion in an orbit which is rapidly shrinking due to heavy loss of orbital angular momentum. The common envelope (CE) can be ejected before the naked core of the giant star explodes to form another neutron star.

This is believed to be the history of systems like PSR 1913+16 (Fig. 3.2). This system consists of two pulsars: the 'recycled' pulsar is the older one that has been 'spun-up' to a $P_{spin}\gtrsim$50 msec during the HMXRB accretion phase. The younger pulsar is born in the second explosion. At this stage there is no more accretion and normally the recycled pulsar is visible as a radio pulsar. The younger pulsar is normally not visible probably as a result of its very short spin-down timescale compared to the old one (a factor of $\simeq$100).

These systems belong to the class of high mass binary radio pulsars (HMBPs). They are charecterised by *eccentric orbits and short orbital periods.* The eccentric orbit is due to the second supernova explosion after which there is no accretion process to circularise the orbit again. The short orbital period is a consequence of the CE phase that can reduce the orbital

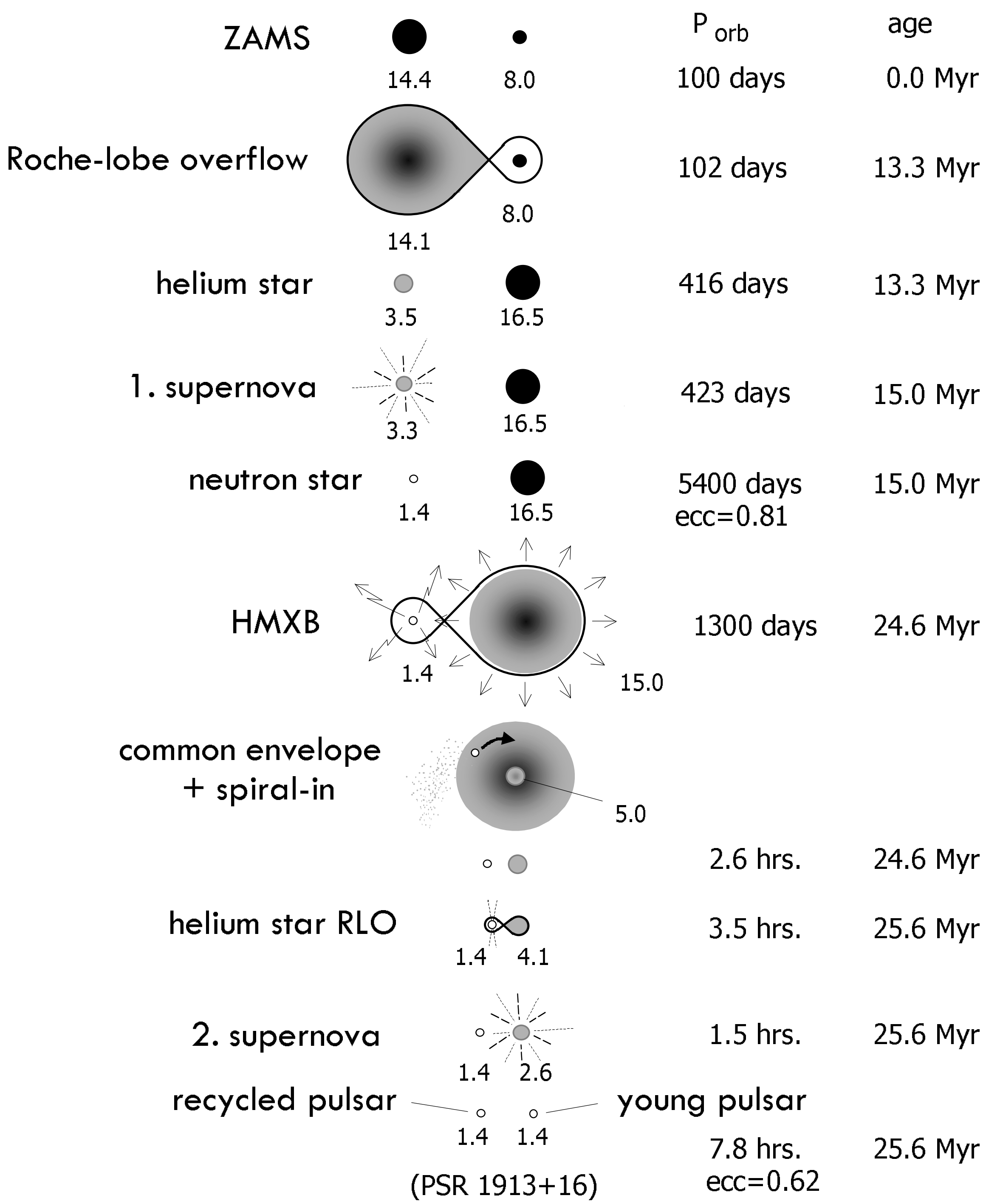

Figure *3.2: Formation and evolution of a HMXRB. Such a binary will experience two supernova explosions. See text. (Tauris and van den Heuvel 2003).*

period also by a factor of ∼100. Indeed without the CE phase we could not end up with two neutron stars being closer than the progenitor radius.

The fate of tight double neutron star systems is to coalesce due to energy loss as a result of gravitational wave radiation. These events could be the progenitors of both short and long duration gamma-ray bursts.

It is important to note that not all HMXRBs will end up as a HMBPs. In fact the ejection of the common envelope will not always occur. The binding energy of the CE to the core depends on the mass of the donor star. A too massive star will not allow the ejection of the CE and the two stellar components will merge within the CE, leading to a so-called Thorne-Zykov object. In this case, a HMBPs will not be born.

3.5 Formation and evolution of LMXRBs

Figure 3.3 shows the formation and evolution of a LMXRB. One MS massive star is required for the formation of a LMXRB, i.e. the star that will eventually become the accreting compact object of the system.

Such a massive star will fill its Roche lobe during its evolution and will engulf the less massive star in a common envelope, similarly to the HMXRB case. The spiral-in will shorten the orbital period of the system due to loss of angular momentum. In this case the CE will be ejected most of the times due to the fact that the overall mass (i.e. CE binding energy) is in this case lower than for a HMXRB. After the ejection of the CE, the more massive star will explode in a supernova event leaving behind a binary system with a neutron star or a black hole and a low mass star.

The explosion will leave a bound system less often than in the HMXRB case due to the fact that here, before the explosion, the to-be-supernova is the most massive object of the two.

Another possible scenario for the formation of a LMXRB is as follows: a massive star of 8-30$M_\odot$ explodes in a supernova and leaves a neutron star. The neutron star has a strong magnetic field (B$\simeq 10^{12}$G at surface) and a rapid rotation period ($\ll$ 1s) at birth. Such a highly magnetised rapidly rotating neutron star can efficiently convert its rotational energy into radiation. This kind of radiation is confined in the radio band and hence the neutron star is observed as a radio pulsar[13]. The rotation powered neutron star gradually looses the rotational energy and slows down and finally the radio pulsar dies. If the neutron star is located in a high density region of stars like the Galactic centre region or in a globular cluster, it may be captured by normal stars to form a binary system. In this case, the newly formed binary system may have a wide separation and eccentric orbit.

Whichever the historical path to create the binary system, what will happen is that the orbit will be circularised and the separation will gradually decrease by gravitational radiation and/or magnetic braking. If the separation becomes small enough (which may take $\sim 10^9$yr) the companion star will fill its Roche lobe and Roche lobe overflow will begin. An accretion disc is formed and X-rays are emitted. This is the birth of the LMXRB.

The companion star determines not only the orbital period of the system but also its evolution.

In the case of a *main sequence companion* (the majority), the two stars of the system (neutron star and main sequence star) are relatively close ($P_{orb} \lesssim 9$ hr, Eq. 3.1). The X-ray active phase is maintained by irradiation of the companion by the X-ray source which causes the companion to

[13] However, in the case of a very young neutron star the conversion of rotational energy into radiation is more efficient in the X-ray or γ-ray bands. A very young neutron star can be a powerful X-ray source. A famous example is the Crab pulsar.

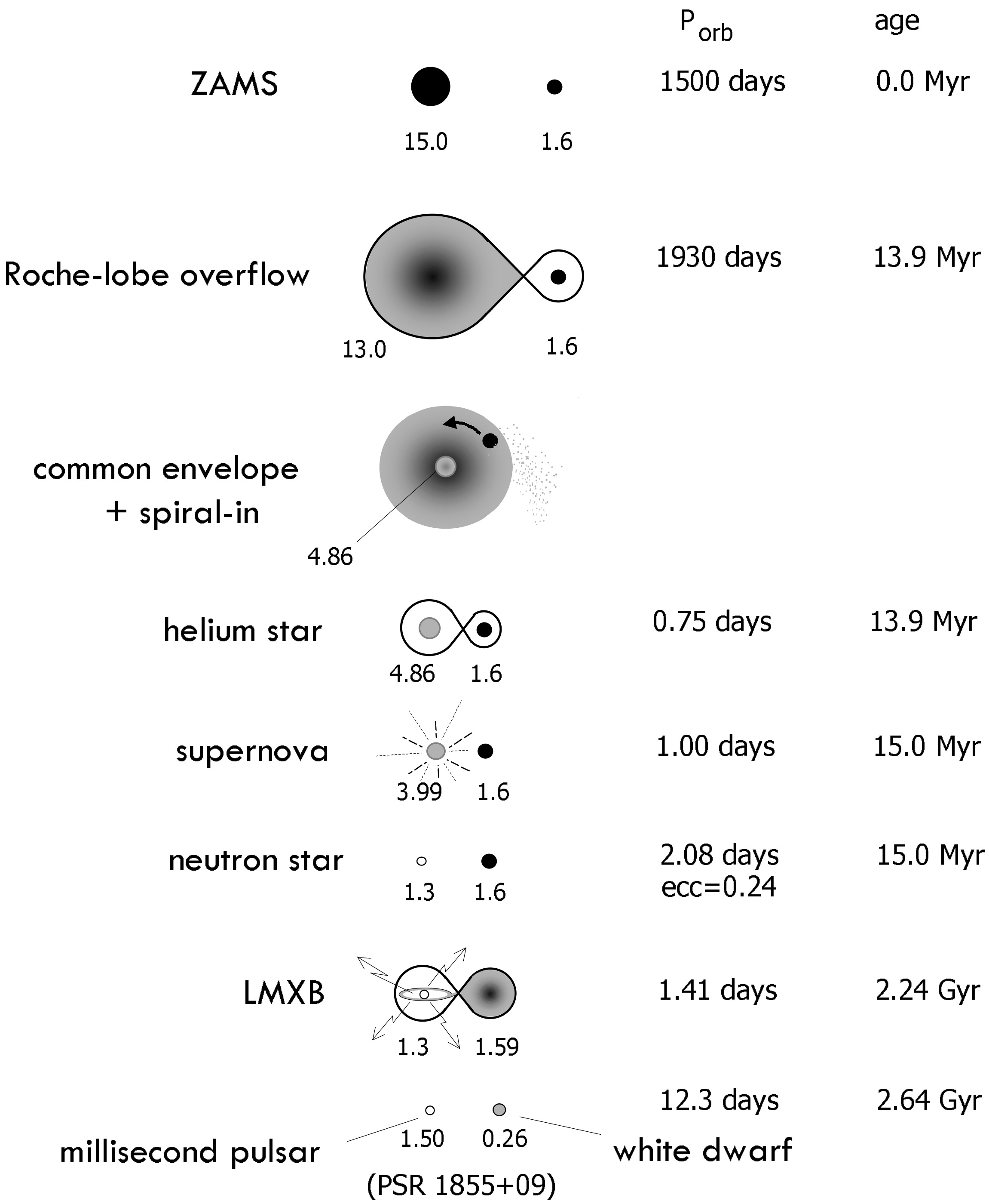

Figure *3.3: Formation and evolution of a LMXRB. This system will experience one supernova explosion, the one of the massive star. (Tauris and van den Heuvel 2003).*

expand and fill its Roche lobe keeping the accretion alive. This phase is expected to continue for about 10^7yr. The companion will not expand forever. When it reaches thermal equilibrium it stops. As a result the RLO will be interrupted, the LMXRB will stop emitting X-rays and will enter a quiescent X-ray phase. This phase will last for about 10^9yr during which the binary orbit will gradually decay due to angular momentum loss via gravitational radiation and/or magnetic braking. In this long period the neutron star may work as a recycled pulsar and a $\lesssim$1day orbital period low mass binary pulsar (LMBP) may occur. When the binary orbit decays to a small enough size, the companion can fill its Roche lobe again. The system enters again its X-ray active phase. These two phases will alternate until the companion becomes too small to fill its Roche lobe ($\lesssim$0.01 $M_\odot$) and ends as a degenerate star. At this point the accretion stops and the neutron star turns into a recycled pulsar. The total mass accreted onto the neutron star by the end of this stage can be close to 0.1 $M_\odot$. This amount of mass accretion is enough to spin up the neutron star to a millisecond period[14] ($\lesssim$10 msec). Indeed this scenario seems to be confirmed by the discovery of millisecond X-ray pulsars in LMXRBs such as SAX 1808.4-3658 (Wijnands & van der Klis 1998). Furthermore, the pulsar wind is expected to evaporate the companion star. The companion will be completely evaporated in $\sim 10^{7-8}$yr and a <u>single recycled millisecond pulsar</u> will remain.

This scenario predicts that the number of potential LMXRBs should be about two orders of magnitude larger than is deduced based on the visible LMXRB detections. The following could solve the birthrate problem: statistically the number of observed LMXRBs and estimated millisecond pulsars does not match (the LMXRBs being $\sim 10^3$ times less than the millisecond pulsars). The active phase of LMXRBs is of the order of $\sim 10^7$yr alternating with quiescent X-ray phases of the order of $\sim 10^9$yr brings the number of existing LMXRBs to be comparable to the estimated number of millisecond pulsars (Bhattacharya, 1995).

In the case of an <u>*evolved companion*</u> (the minority), the X-ray active phase is maintained by the evolutionary expansion of the companion that takes of the order of 10^7yr. The orbit of the system is wider than in the previous case, no evaporation occurs and the companion star evolves in a white dwarf that does not fill its Roche lobe. This system remains a LMBP. LMBPs, unlike HMBPs, are characterised by *circular orbits and long orbital periods*[15] and the orbiting objects are a <u>millisecond pulsar</u> and a <u>white dwarf</u> (as in the case of PSR 1855+09) of Fig. 3.3.

3.6 X-ray modulations in LMXRBs

In this section the different modulations observed in LMXRBs are discussed.

3.6.1 The orbital period

In LMXRBs, while the companion star fills its Roche lobe, the orbital period can be related to the mass and radius of the companion star, M_c and R_c respectively (Asai 1994).

$$P_{orb} = 9\mathrm{hr}(\mathrm{R_c}/\mathrm{R_\odot})^{3/2}(\mathrm{M_\odot}/\mathrm{M_c})^{1/2}. \quad (3.1)$$

This gives $P_{orb} \gtrsim$10 hr for an evolved star and $P_{orb} \lesssim$9 hr for a main sequence star. The majority of the observed LMXRBs have an orbital period of 3-10 hr which corresponds to a main

[14]Neutron stars accreting via stellar wind (HMXRBs) tend to show random fluctuations of $\dot{P}$ while those accreting via Roche lobe (LMXRBs) show steady spin up ($\dot{P}$ <0). RLO is a more efficient process to spin up neutron stars due to the high angular momentum of matter overflowing from the Roche lobe.

[15]Mass transfer from the less massive to the more massive star, as in a LMXRB, will widen the orbit. The resulting LMBP will have a wide orbit.

sequence companion. This is consistent with the fact that stars spend most of their time in the main sequence phase where we have higher chances to observe them.

3.6.2 Bursts

During the X-ray active phase of HMXRBs and LMXRBs hosting a neutron star, the former tend to show X-ray pulsations unlike the latter (see Tab. 3.1).

As discussed in 2.2 this is the effect of the intense magnetic field of the neutron star in a HMXRB that forces accretion onto the polar caps: the rotation of the neutron star makes the light-house effect i.e. the X-ray pulsar that we see. This means that the neutron star rotates with a certain spin period and we are able to see this rotation due to the high magnetic field that mainly generates 'hot spots' at the neutron star's surface.

In the case of LMXRBs, the magnetic field is weak, the accretion disc reaches the neutron star surface in a continuous flow. No hot spots are produced and we are not able to see the rotation of the neutron star. In LMXRBs, the mechanism that can produce a 'hot spot' on the neutron star surface is the already discussed X-ray bursting activity (Section 3.2). X-ray bursts are characterised by a sudden increase of the X-ray flux by more than an order of magnitude. The intensity reaches its maximum in several seconds and decays in times of $\sim$ 10-100 sec. X-ray bursts are naturally divided into two groups, i.e. type I and II (Hoffman et al., 1978 and Strohmayer & Bildsten 2003 for a recent overview). Type I bursts originate from thermonuclear flashes in the surface layers of the accreting neutron stars and are powered by nuclear energy, while type II bursts originate from disc instability and are powered by gravitational energy. The type I bursts are quite a common phenomenon within LMXRBs and have been observed in $\sim$ 60 systems (out of 150, Liu et al., 2001). On the other hand the Rapid Burster (MXB 1730-335) and GRO 1744-28 are the only type II burst sources known. The Rapid Burster is also a type I burster so it is surely a neutron star (Lewin & Joss, 1981). Observationally, type II bursts can be distinguished by type I bursts by the different spectral evolution: the energy spectra of type II burst sources do not show any significant softening during the decay while the type I bursts do (e.g. Lewin et al., 1993), which is interpreted with the neutron star surface cooling down.

The search for neutron star spin periods in X-ray bursts has not proven easy (e.g. Jongert & van der Klis 1995). In type I bursts the accumulated nuclear fuel first ignites at the point of the neutron star surface where it reaches the critical ignition column density and then spreads to all adjacent areas on the surface. When nuclear burning occurs uniformly over the surface, no 'hot spot' is created and the neutron star spin will still be hidden. But in some cases a 'patchy' burning process can occur, making the neutron star spin period visible. Pulsations during bursts (called burst oscillations) have been detected (Strohmayer & Bildsten 2003). With the decrease of the X-ray burst flux, the non-uniformity fades out and so do the pulsations. These bursts are an important tool to infer the nature of the accreting object (neutron star instead of black hole) and, in some cases, to allow the study of the neutron star rotation even if only for the brief duration of the burst.

Type I X-ray bursts can even give insight in the neutron star structure: Cottam et al. (2002) report the discovery of significant absorption lines in the spectra of 28 bursts of the low-mass X-ray binary EXO0748-676. The observed lines correspond to well known spectral transitions with a redshift of z = 0.35. For an astrophysically plausible range of masses (M$\sim$1.3-2.0 $M_{\odot}$), they derive that this value is completely consistent with models of neutron stars composed of normal nuclear matter, excluding some models for which the neutron stars are made of more exotic matter.

Type I X-ray burst theory predicts three different regimes in mass accretion rate $\dot{M}$ for unstable burning (Fujimoto et al. 1981).

1. low $\dot{M}$: 10^{-14} $M_{\odot}$ yr^{-1} $\lesssim \dot{M} \lesssim 2 \times 10^{-10}$ $M_{\odot}$ yr^{-1} . In this regime long ($\gtrsim$10-100 s) bursts are expected.
2. intermediate $\dot{M}$: 2 $\times 10^{-10}$ $M_{\odot}$ yr^{-1} $\lesssim \dot{M} \lesssim$ 4-11 $\times$ 10^{-10} $M_{\odot}$ yr^{-1} producing short bursts.
3. high $\dot{M}$: 4-11 $\times 10^{-10}$ $M_{\odot}$ yr^{-1} $\lesssim \dot{M} \lesssim 2 \times 10^{-8}$ $M_{\odot}$ yr^{-1} producing long bursts.

The different duration of the expected X-ray bursts is given by the kind of environment in which they ignite. In an hydrogen-rich environment the burst will be longer because hydrogen burning in helium has a longer time scale due to the inverse β decay involved in the process. In an helium-rich environment the burst will be shorter. Whether the ignition will happen in an H-rich or He-rich environment depends on the accretion rate and is the result of the balance between the rate at which matter arrives on the neutron star's surface and the rate at which it burns.

The dependence of the burst duration on accretion rate has been used to infer the direction of increase of $\dot{M}$ in the case of the so-called Atoll sources (see Section 3.7).

3.6.3 Eclipses

Another kind of variability found in LMXRBs are the X-ray eclipses. An eclipse occurs when the X-ray emission region is occulted by the companion star. In the case of a total eclipse the ingress and egress are sharply defined and the X-ray flux decreases typically two orders of magnitude or more during the eclipse. The presence of eclipses gives an indication on the angle at which we see the system, i.e. eclipsing objects are viewed at a high inclination angle (edge-on). Eclipses occur at the orbital period and are also common to HMXRBs for which eclipses are more likely and the eclipsing time is much larger (as expected given the larger size of the companion in a high mass binary).

Some of the eclipsing binaries show partial eclipses. Since the partial eclipse would not be observed if the X-ray source were pointlike, the X-ray emission region for these sources is considered to be extended. However, the large potential energy necessary to produce X-ray photons is only available in the region very close to the neutron star. This could be explained if the neutron star is embedded in an X-ray scattering "corona". Such sources are usually referred to as Accretion Disc Corona sources (ADC). The corona is supposed to be produced by X-ray heating of the disc and to be highly ionised having a negligible contribution to the X-ray absorption (White and Holt, 1982). The existence of ADC sources means that even high inclination systems, where the accretion disc completely blocks our line of sight to the central source at all orbital phases, can still be observed just because the corona allows X-rays to be scattered in the line of sight.

Sources with total eclipses as well as sources with partial eclipses have been observed e.g. EXO 0748-676 and X 1822-371, respectively (see Fig. 3.4, left panel).

3.6.4 Dips

In a sample of LMXRBs ($\sim$11 out of $\sim$150, Liu et al., 2001), dips occur. A dip is a temporal decrease of the X-ray intensity. Dips are caused by periodic obscuration of the central X-ray source by a bulge in the accretion disc, where the gas stream from the companion impacts on the outer disc (White and Swank, 1982). The occultation takes place at the orbital period when the line of sight from the central source to the observer is intercepted by the bulge and it is

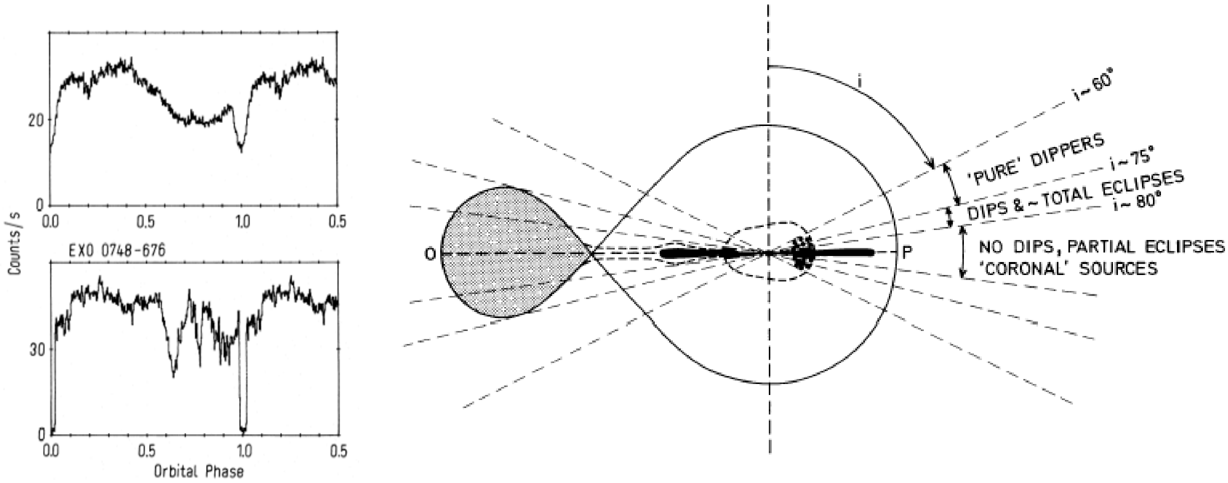

Figure *3.4:* Left panel*: The 1–10 keV lightcurves of the ADC source X 1822-371 (upper panel) and EXO 0748-676 (lower panel) folded with the orbital periods. X 1822-371 shows a partial eclipse and dips. EXO 0748-676 shows a total eclipse and dips. (Parmar et al. 1986)* Right panel*: Different types of orbital modulations in LMXRBs for different inclination angles (Frank et al. 1987).*

independent from the eclipsing due to the companion star orbiting. Unlike the eclipses, the dip depends on the outer structure of the disc and is irregular. Figure 3.4, left panel, shows the dips visible in the lightcurves of EXO 0748-676 and X 1822-371.

An X-ray dip is usually accompanied by a spectral change. As it is caused by a blocking of X-rays in the outer limb of the accretion disc, where most of the metals are in a low ionisation state, the absorption is usually prominent in lower energies ($\lesssim 4\,\mathrm{keV}$) and less clear at higher energies. However, some sources show very little change in the energy spectra during the dips (e.g. the black hole candidate LMXRB 4U 1755-338, White et al., 1984). This could be interpreted as the result of the fact that the intervening material is almost free from metals. The reason for such a low metallicity, a factor of 600 below cosmic values, is not clear.

Another interesting issue in the dipping sources is related to the case of XB 1254-690. This is a binary system with a neutron star as deduced from the presence of X-ray bursts. Courvoisier et al. (1986) reported the discovery of 3.9 hour periodic intensity dips, based on *EXOSAT* observations. Later on, Smale and Wacher 1999 as well as Iaria et al. (2001) reported that the previously observed deep X-ray dipping was not present during their observations of the source. The interesting result was that in both cases the observed 2-10 keV flux was comparable to the intensity observed by Courvoisier et al., i.e. the accretion disc radius and mean mass accretion rate had not changed; the disc just seems to lack the vertical structure usually associated with the impact point of the accretion stream.

Detailed modeling of the disc during active dipping cycles (Motch et al, 1987) has shown that the typical aperture angle of the disc in XB 1254-690 is 9°-13°, with the bulge itself extending to 17°-25°and an inclination of the system restricted to 65°-73°. The absence of regular dips implies that the bulge size has shrunk in angular size from 17°-25° to less than 10°.

But why should this shrinking take place? One would expect that the absence of dipping in XB 1254-690 would imply the presence of a smaller bulge, i.e. smaller mean $\dot{M}$ and therefore luminosity. But this is not the case as the observed luminosity remained unchanged throughout the observations.

An alternative model for the dipping sources was proposed by Church and Baluchinska (1995). In this model the emission consists of two components: a blackbody emission from the compact object plus an extended comptonized emission from the accretion disc corona. During the dip a progressive covering of point-like source by the ADC occurs. The disappeared dipping activity of XB 1254-690 remains a mistery even within this model. It would seem that the corona has disappeared/changed but then the unchanged luminosity level is still not explained.

Dipping sources still remain an intriguing chapter of LMXRBs.

The different modulations (total/partial eclipses, dips) in the X-ray lightcurves are very closely related to the angle at which the system is seen. Figure 3.4, right panel, shows the different types of expected orbital modulations for different inclination angles, i. As soon as i increases, many modulation effects due to intervening matter can occur. Such modulations are absent for small values of i.

3.7 LMXRBs hosting a neutron star

3.7.1 Basic classification of Atoll and Z sources

Although various types of LMXRBs revealed their nature before the 1990's by showing bursts and/or binary orbital phenomena such as eclipses and dips, no such clear systematic behaviour could be found in the brightest persistent LMXRBs.

A useful way to analyse the subtle spectral changes of bright LMXRBs is to divide the spectrum in several broad energy bands and see how the 'colour' (i.e. the ratio of the count rate in two different energy bands) correlates with another colour or with the 'intensity' (i.e. the countrate) of the source. These are the so-called colour-colour diagrams (CD) and hardness intensity diagrams (HID), respectively.

Using *EXOSAT* data for 16 LMXRBs, Hasinger & van der Klis (1989) used the CDs to study their broad-band spectral behaviour. In these diagrams a "soft" colour (ratio of the count rates in the lowest energy bands) is plotted versus a "hard" colour (ratio of the count rates in the highest energy bands). From this study an interesting pattern emerged: the six brightest LMXRBs showed roughly Z-like shaped tracks (or parts of it) while the other sources showed somewhat fragmented CDs (see Fig. 3.5, top). Because of the shape of the tracks the former were called "Z" sources while the latter "Atoll" sources.

The 3 branches building up the Z are called Horizontal Branch (HB), Normal Branch (NB) and Flaring Branch (FB). These names are merely historical and were chosen for the fact that for the first sources studied the HB showed an horizontal orientation, the NB was the branch normally covered by the source, while the FB was characterised by X-ray flares in the source.

Atolls have two kind of branches: the island state (IS) in which the sources generally display no significant state change on time scales of hours to days and the banana branch (divided in lower branch, LB, and upper branch, UB, see Fig. 3.5, top right).

Z sources and Atolls move along the branches of their pattern in a smooth way and never "jump" from one part of the branch to the other. The position of the source on the pattern is likely linked to a physical quantity that evolves in a continuous way, most likely the accretion rate, $\dot{M}$ (Hasinger et al., 1990).

Hasinger et al. (1990) noted that for the Z source Cyg X-2, the UV flux as well as the optical flux increased from the HB to the FB. In LMXRBs, UV and optical emission come mainly from X-rays that are reprocessed by the disc and the X-ray emission is linked to the accretion flow.

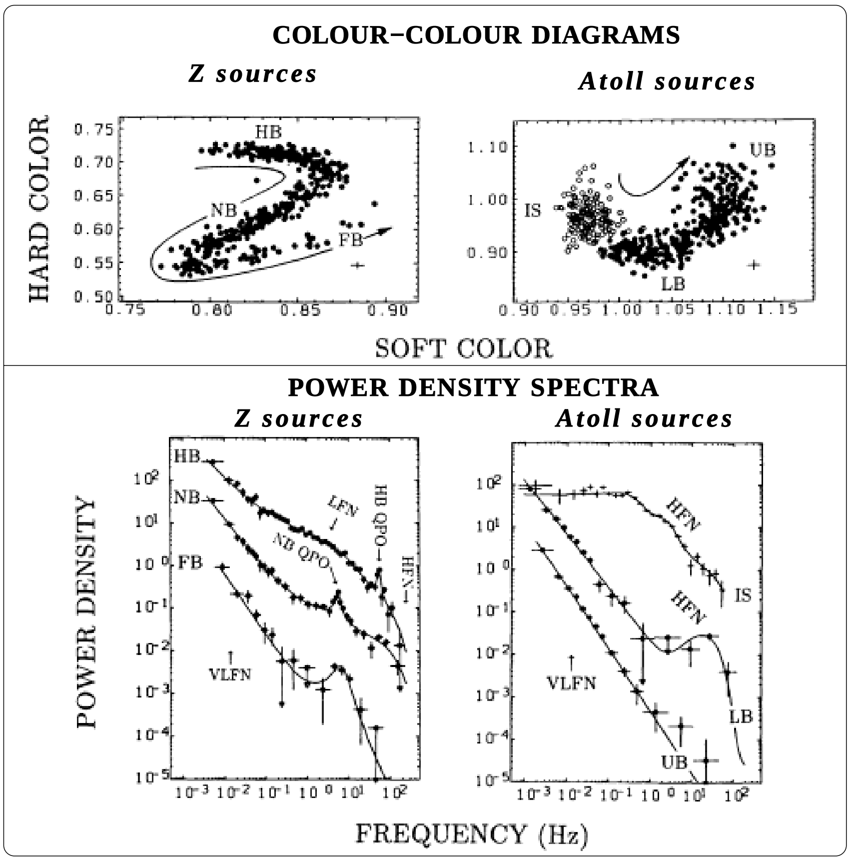

Figure *3.5: X-ray CD (top) and power spectra (bottom) typical of Z sources (left) and Atoll sources (right). The direction in which $\dot{M}$ is inferred to increase is indicated by arrows in the CDs (adapted from Hasinger and van der Klis, 1995.)*

This led to the conclusion that the mass accretion rate increases in the same direction of the reprocessed emission i.e. from HB to FB as shown by the arrow in Fig. 3.5, top-left.

For the Atoll sources, the X-ray intensity is low in the island state which is characterised by regular long X-ray bursts. Less burst activity (with short bursts) is seen in the banana branches. Based on the burst properties such as duration and temperature, van der Klis et al. (1990) reported that the mass accretion rate increases from the IS branch to the UB branch (as shown by the arrow in Fig. 3.5 top-right), consistently with the view that low accretion rates produce long bursts (van Paradijs et al., 1996).

Recent studies (Muno et al. 2002, Gierliński et al., 2002 and Barret & Olive 2002) have suggested that the clear Z/Atoll distinction on the CD is an artifact due to incomplete sampling (Atoll sources, if observed long enough, *do* exhibit a Z shape as well). Nevertheless, many differences remain: Atoll sources have weaker magnetic fields (about 10^6 to 10^7 G versus 10^8-10^9 G of Z sources), are generally fainter ($0.01 - 0.3$ L_{Edd} versus $\sim$L$_{Edd}$), are in general harder, trace out the Z shape on longer time scales than typical Z-sources and have a different correlated timing behaviour along with the position on the Z. Another difference seems to be the orbital period. In Atoll sources the orbital period is in general relatively short ($\lesssim$5 hr) and in the Z sources for which it is known it is long ($\gtrsim$10 hr). This would indicate that Z sources may contain an evolved companion star while Atolls contain a main sequence star (see Eq. 3.1). This might account for the difference in the accretion rate and is consistent with the fact that the number of known Atoll sources (18) is higher than the number of known Z sources (6 confirmed, Liu et al., 2001) since the main sequence phase of a star is much longer than the one of an evolved star making the detection of Atolls more likely. In any case, a larger sample is needed to drive final conclusions.

Another difference that is important to note is that most Atolls show regular bursting activity, unlike Z sources. According to the type I X-ray burst theories (see Section 3.6.2), low $\dot{M}$ (i.e. low luminosity) systems and intermediate $\dot{M}$ systems are expected to show long and short bursts, respectively, which infers the direction of increasing $\dot{M}$ in the case of Atoll sources. Things are not so straightforward when high accretion rate systems are considered, such as the "bright GX Atolls" and Z sources. Z sources have high mass accretion rates of the order of 10^{-8} $M_\odot$ yr^{-1} . For such an $\dot{M}$, long bursts are expected. Instead, the available observations show that most of the Z sources do *not* show any bursting activity, and in two cases (GX 17+2 and Cyg X-2, Kuulkers et al., 2002 and references therein) short bursts have been observed.

Likewise, for the bright "GX Atoll" sources GX 3+1, GX 13+1, GX 9+9, GX 9+1, only the first two infrequently show short X-ray bursts whereas the latter two have not shown bursting activity at all.

This behaviour is not accounted for in the current burst theories and remains an open issue.

It was shown by Hasinger & van der Klis (1989) that each state or branch has a characteristic fast time variability and is therefore an extra diagnostic to identify the source state and to distinguish Z sources from Atolls.

The focus of this thesis is on the spectral properties of the sources. The timing properties of the sources are very briefly mentioned. More details can be found in the references reported below.

3.7.2 Timing variability

Studies of the X-Ray variablility of Z sources (van der Klis, 1995 and van der Klis 2000) revealed two types of quasi-periodic oscillations (QPOs) and three types of rapid flickering ("noise"). See

Fig. 3.5, bottom-left. The two types of QPOs are the ones with frequencies less than 100 Hz (HB oscillations, HBOs, and NB oscillations, NBOs) and the (twin) kHz QPOs. The three noise types are the Very-Low-Frequency-Noise (VLFN), the Low-Frequency-Noise (LFN, appearing and disappearing with the HBO) and the High-Frequency-Noise (HFN). The properties of the noise features and QPOs strongly correlate with the position of the source along the Z pattern (a certain type of noise is more intense in a certain branch and QPOs frequency increases with increasing accretion rate).

The power spectra of the Atoll sources can be described in terms of two rapid variablility components, the Very-Low-Frequency-Noise (VLFN) and the High-Frequency-Noise (HFN). See Fig. 3.5, bottom-right. The properties of VLFN and HFN strongly correlate with the position of the source in the CDs, just like in the case of the Z sources.

Low frequency QPOs ($<$ 100 Hz) are more rare in Atoll sources than in Z sources and kHz QPOs have not been observed in the island or upper banana branch.

3.7.3 Spectra

The X-ray spectra of bright LMXRBs hosting a neutron star are generally described as the sum of a soft and a hard component. Two different models are often adopted to describe this composite emission. They are the so-called *eastern* model (Mitsuda et al., 1984) and *western* model (White et al., 1986).

In the eastern model the softer part of the spectrum is a MCD describing the emission from the optically-thick, geometrically-thin accretion disc (already described in section 2.2.1). The harder part of the spectrum is a higher temperature Comptonised blackbody modelling the emission from the neutron star boundary layer.

In the western model a single temperature blackbody (from the optically thick boundary layer) describes the soft part of the spectrum. Comptonisation of soft seed photons in the innermost region of the accretion disc by a hot corona describes the hard part. Basically, in both models there is a soft component plus a hard Comptonised one. The difference among the two is that in one case the disc is the main contributor to the observed soft component and the neutron star boundary layer is the part that is Comptonised (eastern model) while in the other the situation is reversed: the neutron star boundary layer is mainly producing the soft component while the inner part of the disc is the Comptonised component (western model).

These two models describe equally well the spectra of neutron star LMXRBs below $\lesssim$20 keV. Changes in the interplay of the parameters can explain the changes in the source state from a soft to a hard spectrum. A soft spectrum is a spectrum for which most (more than 80%) of the source flux is radiated below 20 keV. In a hard spectrum about half of the source luminosity is emitted in the hard X-rays, above 20 keV.

Unlike black hole LMXRBs, the spectral changes in the case of neutron star LMXRBs are generally subtle. This is why CDs and HIDs were introduced as they are very sensitive to spectral changes. But in some cases the changes are quite spectacular as shown in Fig 3.6 where the clear soft and hard spectral states for the LMXRB 4U 1705-44 are shown.

Soft spectra

Soft spectra have been observed both in Z and Atoll sources and over a range of luminosity going from $\sim10^{37}$ to $\sim10^{38}$ erg s^{-1} in the soft and hard X-rays (see Barret, 2001, and references therein). These spectra can always be decomposed into the sum of a soft component and a hard Comptonised component in the framework of the previously discussed eastern and western

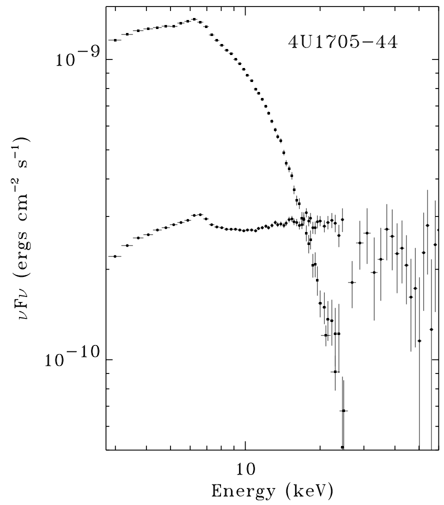

Figure *3.6: Soft and hard spectral states from the LMXRB 4U 1705-44 as observed by RXTE (Barret 2001).*

models. The soft component is described by a single temperature blackbody (BB, western model) or by a multicolour disc blackbody (MCD, eastern model). BB temperatures of less than 1 keV are generally observed. For the MCD, temperatures range between ∼0.5-1.5 keV. The latter MCD model, when corrected for the hardening factor discussed in section 2.2.3, gives plausible values for the effective inner disc radius (e.g. $R_{eff}\sqrt{cosi} \simeq 20$ km in 4U1728-34, Di Salvo et al., 2000, with i being the inclination angle). This value is consistent with the expected value for the neutron star radius, in agreement with the idea that in a weakly magnetised neutron star the disc is expected to reach the neutron star's surface.

For the Comptonised component in the western model a plasma temperature of a few ($\simeq$ 3) keV, i.e. expected cut-off at $\simeq$10 keV, and a relatively large optical depth of $\tau \simeq$5-15 are observed (e.g. GX3+1, kT_e=2.7 keV, τ=6.1, Oosterbroek et al. 2001, GX17+2, kT_e=3.0 keV, $\tau \sim$10, Di Salvo et al. 2000). Seed photon temperatures range from 0.3 to 1.5 keV i.e. in the same range of temperatures for the soft component (Barret, 2001, and references therein).

In the soft and hard X-rays the flux between the soft (BB or MCD) and the hard Comptonised components range between 0.1 and 0.5 indicating that even in the soft spectra, the soft component does not dominate the source luminosity that is basically determined by the Comptonised part.

Soft spectra and hard X-ray tails

Recent broad band studies have shown that many Z sources display a variable hard powerlaw shaped component dominating the spectra above ∼30 keV: Cyg X-2 (Frontera et al. 1998, Di Salvo et al. 2002), GX 17+2 (Di Salvo et al. 2000), GX 349+2 (Di Salvo et al., 2001b) and Sco X-1 (D'Amico et al. 2001).

Such hard tails need an additional power-law component with respect to the two component models previously discussed and contribute up to 10% of the source bolometric luminosity. The parameters of these components, as deduced from recent X-ray observations, are reported in Table 3.2 while an example of a hard tail is shown in Fig. 3.7, left panel.

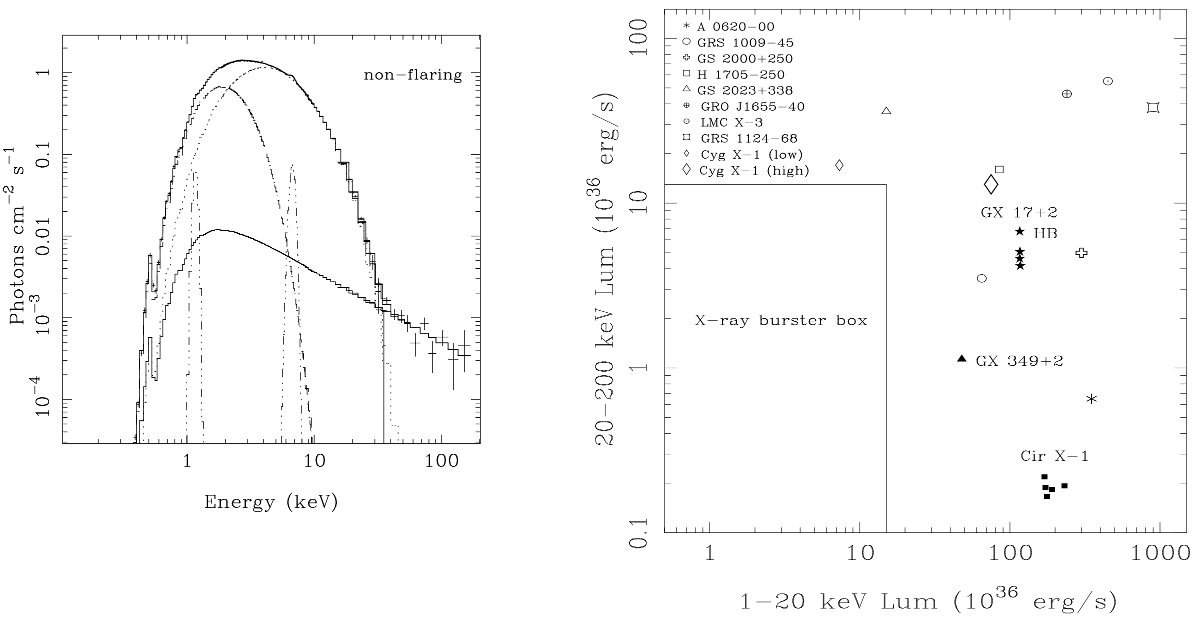

Figure *3.7:* Left panel*: Unfolded spectrum of the GX 349+2 (solid line on top of the BeppoSAX data). The individual model components are also shown, namely the softer component (blackbody), the harder component (Comptonised spectrum), two Gaussian emission lines and the hard tail dominating the spectrum above ∼30 keV (Di Salvo et al., 2001b).* Right panel*: 20-200 keV versus 1-20 keV luminosities of BH binaries (open symbols, from Barret et al. 2000) and NS type-Z binaries (filled symbols). The area covered by X-ray bursters is delimited by the so-called X-ray burster box that is plotted as a solid line. (Di Salvo et al., 2001b).*

Hard spectra

Hard spectra have been observed for luminosities ranging from a few times 10^{36} up to $\sim 3 \times 10^{37}$ erg s^{-1}in the soft and hard X-rays, therefore for lower overall luminosities than in the soft spectra. So far only Atoll sources (and more generally X-ray bursters) have been observed with hard spectra in which about half of the source luminosity is emitted in the hard X-rays (above 20 keV). About 20 LMXRBs have been detected up to 100 keV (Barret and Vedrenne, 1994, Barret et al. 2001, Di Salvo & Stella 2002). Some recent observations of hard X-ray spectra from low-luminosity LMXRBs are reported in Table 3.3.

Like for soft spectra, the broad band hard spectra can be described in terms of the typical two component models with a soft and a Comptonised component. The main differences among the soft and hard spectra reside in the different values of the Comptonised component. The inferred optical depth of the plasma is now about ∼2-3 whereas the electron temperature is typically a few tens of keV (∼30 keV) equivalent to an energy cut-off around 60-80 keV in the spectra.

These temperatures are lower than the ones observed from LMXRBs hosting a black hole (e.g. 100 keV for Cyg X-1, Di Salvo et al., 2001a). The idea that the electron temperature could be used to distinguish between a neutron star and a black hole has already been proposed (Tavani & Barret 1997, Zdziarski et al. 1998 and Barret et al., 2000) and interpreted as the signature

Table 3.2: Recent *BeppoSAX* observations of hard tails in Z sources. *Luminosity* is the (absorbed) luminosity in the 0.1–200 keV energy range; *Hard luminosity* is the luminosity in the power-law component in the 20–200 keV energy range; $E_{\rm max}$ is the maximum energy up to which a source was detected (Di Salvo & Stella 2002).

Source	Branch	Luminosity (10^{38} ergs/s)	Hard Luminosity (10^{36} ergs/s)	Photon index	$E_{\rm max}$ (keV)
GX 17+2[a]	HB	1.2	2.0	2.7 ± 0.3	200
GX 349+2	NB/FB	0.49	0.5	1.9 ± 0.4	200
Cyg X-2	HB	$0.89 - 1.1$	0.8–0.9	$1.8 - 2.1$	200
Sco X-1	HB	–	0.9–1.4	$1.7 - 2.4$	200
	NB	–	0.8	1.6 ± 0.3	200
	FB	–	0.5–1.1	$-1 - 0.1$	200
GX 5-1[b]	NB	~ 3	~ 10	1.8 (fixed)	37

[a] The known, confirmed, Z sources are GX 17+2, GX 340+0, GX 349+2, Cyg X-2, Sco X-1 and GX 5-1.
[b] In this case a contribution from the nearby black hole LMXRB GRS 1758-258 could not be excluded.

Table 3.3: Some recent *BeppoSAX* observations of hard X-ray spectra from low-luminosity LMXRBs. *Luminosity* is the source luminosity calculated in the energy range specified in brackets; kT_e is the inferred electron temperature of the hot Comptonising corona; $E_{\rm max}$ is the maximum energy up to which the source was observed (Di Salvo & Stella 2002).

Source	Luminosity (10^{37} ergs/s)	Photon index	kT_e (keV)	$E_{\rm max}$ (keV)
4U 0614+09	0.5–2.9 (0.1–200 keV)	2.3–2.4	> 150	200
4U 1608–52	0.3–1 (2–60 keV)	1.7–2.2	30–60	200
4U 1705–44	~ 1.5 (1–20 keV)	1.5	~ 25	20
Ter 2 (X 1724-308)	~ 2 (0.1–100 keV)	1.6–1.9	30–90	200
MXB 1728–34 (GX 354-0)	~ 0.7 (35–200 keV)	3.0 ± 0.2	–	200
KS 1731–260	~ 1 (35–150 keV)	2.9 ± 0.8	–	150
Ter 1 (X 1732-304)	$(4.0 \pm 0.8) \times 10^{-2}$ (40–75 keV)	3.2 ± 0.7	20–60	170
SLX 1735–269	~ 1.3 (1–20 keV)	2–3	30–50	200
SAX J1747.0–2853	~ 0.26 (2–10 keV)	1.6–2	30–70	200
SAX J1748.9–2021	~ 1.2 (0.1–200 keV)	1.44 ± 0.5	20–50	100
SAX J1808.4–3658	~ 0.38 (2–200 keV)	1.82 ± 0.04	180^{+120}_{-60}	200
SAX J1810.8–2609	~ 0.12 (1–200 keV)	1.96 ± 0.04	–	200
4U 1820–30	2.3–2.6 (2–50 keV)	2.05 ± 0.05	~ 20	50
GS 1826–238	~ 0.88 (1–20 keV)	~ 1.7	~ 90	150
X 1850–087	~ 0.13 (1–37 keV)	~ 2.3	–	37
4U 1915–05	~ 0.6 (2–50 keV)	1.8–1.95	> 100	200
Aql X-1	~ 0.2 (1–100 keV)	2.2–2.6	–	150

of the neutron star surface acting as a thermostat for the Comptonising region (e.g. Kluzniak 1993).

However, in a few neutron star LMXRBs, no clear cut-offs were observed in the hard X-ray spectra up to about 100-200 keV. This is the so-called "hard state" of Atoll sources (Di Salvo & Stella 2002) and shows that also neutron star LMXRBs can have high plasma temperatures like black holes. Besides, in some cases cut-off energies as low as ∼20 keV have been seen also in black hole LMXRBs, e.g. XTE J1550-564 (Rodriguez et al., 2003). It is very difficult to discriminate the nature of the compact object on the basis on the Comptonising plasma temperature.

3.8 Hard X-ray emission from LMXRBs

Accreting black holes were widely believed to have harder 20-200 keV spectra than accreting low magnetic field neutron stars (e.g. Sunyaev et al., 1991). The SIGMA observations of X-ray burst sources (which are low magnetic field neutron stars) reported by Barret and Vedrenne (1994) showed however that hard 20-200 keV spectra can also occur in neutron stars.

Two new criteria were proposed to distinguish between non-quiescent black holes and neutron stars (Barret et al. 2000). The first one stated that when thermal Comptonisation is responsible for the hard X-ray emission then only black holes have plasma temperatures kT_e larger than ∼50 keV. However, as previously discussed, this criterion is weakened by the fact that there are neutron stars that show non attenuated power-laws until about 200 keV (hard state of Atolls) as well as black holes with very low plasma temperatures. The second criterion was based on the comparison of luminosities in the hard and soft X-rays. Plotting the 1-20 keV luminosity versus the 20-200 keV luminosity for black holes and neutron stars of the Atoll class (mainly bursters), all neutron star systems in which a hard component had been detected lie in the so-called X-ray burster box, while all black hole systems lie outside (see Fig. 3.7, right panel). This seemed to suggest that unlike black holes, neutron star systems are unable to emit hard X-rays when the overall X-ray luminosity (i.e. accretion rate) is high.

With more observations being performed many hard tails have been observed also in the bright systems (Z sources) as previously discussed. Plotting in the same diagram the luminosities of the Z sources GX 17+2 (Di Salvo et al. 2000), GX 349+2 (Di Salvo et al. 2001b) and the peculiar Z source Cir X–1 (Iaria et al. 2001), these data clearly lie outside the X-ray burster box, and there is no clear distinction between Z sources and black holes as far as the 1-20 keV luminosity is concerned (Fig. 3.7, right panel).

This result showed that black holes are not the only sources to have high energy tails when their 1-20 keV luminosity exceeds $\sim 1.5 \times 10^{37}$ erg s^{-1}. Besides, the black hole candidate XTE J1118+480 appears inside the X-ray burster box, making the observational differences among these objects less definite (Farinelli et al., 2003). Nevertheless, it appears to be still true that only black holes can emit bright hard X-ray tails, with a 20-200 keV luminosity $\gtrsim 1.5 \times 10^{37}$ erg s^{-1}. The luminosity in the hard tail observed in Z sources is similar in terms of Eddington luminosity to that seen in black holes. This is further evidence that the same mechanism is probably causing the hard tails in both systems. This would imply that this mechanism does not depend on the presence or absence of a solid surface.

The hard emission from neutron star systems can be explained (at least in the cases in which a cut-off was observed) as thermal Comptonisation of soft photons in a hot region (the corona) perhaps placed between the neutron star and the accretion disc (boundary layer). But in cases where the cut-off has not been observed up to about 100 keV or higher, extremely high electron temperatures are required. This is unlikely given that the bulk of the emission is very soft. Fast radial converging motions are unlikely to be dominant in the innermost region of the accretion flow in such high-luminosity systems, because of the strong radiation pressure emitted from or close to the NS surface. However, power-law tails, dominating the spectra at high energy, can also be produced when the flows are mildly relativistic ($v/c \sim 0.1$). Therefore azimuthal motions around the NS or outflows can be the probable origin of these components, with flatter power laws corresponding to higher optical depth of the scattering medium and/or higher bulk electrons velocities, in a way that is similar to thermal Comptonisation (see Psaltis 2001).

Alternative models have been proposed: X-ray components could originate from the Comptonisation of seed photons by the non thermal high energy-electrons of a jet (e.g. Di Salvo et al., 2000) or via optically thin synchrotron emission or inverse Compton (synchrotron self-Compton and/or external Compton) directly by the jet (Markoff et al., 2001 and Markoff & Nowak 2004).

All the Z sources are detected as variable radio sources, with the highest radio fluxes associated with the HB. The radio emission weakens in the NB, and is not detected any longer in the FB (Fender & Hendry 2000, and references therein). This is in agreement with the behaviour of GX 17+2 and GX 349+2 for which the X-ray hard tail was stronger in the HB but a similar correlation was not observed in the case of Sco X-1 (D'Amico et al. 2001). In this case a hard power-law tail was detected without any clear correlation with the position in the colour-colour diagram. The behaviour of Sco X-1 suggests that there might be a second parameter besides $\dot{M}$ regulating the presence of hard emission in these systems, as already stated for some black hole binaries (e.g. the size of the Comptonising region causing the hard tail, Homan et al., 2001).

3.9 Perspectives with *INTEGRAL*

A survey of the hard X-ray spectra of neutron stars and black holes over a wide range of luminosities would allow to quantify the differences among them in respect to the dependence of the X-ray spectrum over the luminosity. Furthermore, the presence (or absence) of an exponential cut-off in the powerlaw hard tails could help in investigating the origin (thermal or non-thermal) of the hard components.

To accomplish such a study, a good sensitivity in the hard energy domain is not always enough as most of these bright sources are located in the crowded Galactic Centre region. A clear example is the case of the bright Z source GX 5-1 for which the hard emission had never been clearly disentangled from the emission of the nearby ($40'$) black hole candidate GRS 1758-258.

The key to the detection and study of hard emission from these sources is the synergy of high sensitivity and imaging capabilities. The INTEernational Gamma-Ray Astrophysics Laboratory, *INTEGRAL*, has these capabilities: *INTEGRAL*/ISGRI has an excellent angular resolution, $12'$ in the hard-X band (>20 keV) and a good sensitivity (about $\sim$10 times better than the previous hard X-rays imager, SIGMA, on board *GRANAT*). Simultaneous monitoring in the soft X-ray domain (below $\sim$ 20 keV) is provided by the X-ray monitor on-board *INTEGRAL*, JEM-X. All this, combined with the very wide field of view of *INTEGRAL*/IBIS ($30^\circ \times 30^\circ$) makes *INTEGRAL* an ideal mission to study in a regular and unbiased way entire classes of astrophysical objects in the less explored hard X-ra and γ-ray band. All these capabilities are very well exploited in the *INTEGRAL* Core Programme that is devoted to a regular survey of the Galactic plane and centre.

The study of the hard X-ray emission from a sample of Z and Atoll sources during the Core Programme is the main topic of this thesis. After an introduction to the *INTEGRAL* mission and to the pre-flight simulations (Part II), we describe the current results of the *INTEGRAL* LMXRB monitoring programme with special attention to GX 5-1 that we were able for the first time to disentangle from the nearby black hole candidate GRS 1758-258 (Part III).

The study of the hard X-ray emission of a particluar HMXRB, Cyg X-3, is given in Part V of this thesis.

Second part

INTEGRAL AND PRE-FLIGHT SIMULATIONS

Chapter 4
THE MISSION

4.1 Introduction

The INTErnational Gamma-Ray Astrophysics Laboratory, *INTEGRAL* (Winkler et al., 2003), is a medium sized ESA mission successfully launched on October 17th, 2002. Its payload consists of 2 main gamma-ray instruments, the spectrometer SPI (SPectrometer on board *INTEGRAL* satellite, Vedrenne et al. 2003) and the imager IBIS (Imager on Board *INTEGRAL* Satellite, Ubertini et al. 2003), covering the 15 keV – 10 MeV band, co-aligned to two X-ray monitors JEM-X (Joint European Monitor for X-rays, 4 – 35 keV, Lund et al. 2003) and an optical monitor OMC (Optical Monitoring Camera, 500 – 600 nm, Mas-Hesse et al. 2003). In addition, the *INTEGRAL* Radiation Environment Monitor (IREM, Hajdas et al. 2003), a particle radiation detector, monitors the spacecraft orbital environment switching off the instruments in case of a dangerous particle flux increase.

The scientific goals of *INTEGRAL* address the fine spectroscopy and accurate positioning of gamma-ray sources. The gamma-ray sky has already been observed by previous missions like *GRANAT*/SIGMA (Paul et al. 1993) and *CGRO*/CGRO (Zhang et al. 1993) but *INTEGRAL*, with strong improvements in spectral and angular resolution capabilities, is the first high resolution spectral imager to operate in this fundamental region of the electromagnetic spectrum.

As time went by and knowledge deepened, it became more and more evident that a complete understanding of an astrophysical phenomenon could be better achieved via multi-wavelength studies. It is in this frame that the X-ray and optical monitors have been added to the scientific payload. The synergy of *INTEGRAL* instruments is then quite clear: SPI and IBIS have both spectral and angular resolution and are differently optimised in order to complement each other while JEM-X and OMC enable a simultaneous softer band follow-up and source identification.

The spectral and angular resolution capabilities are aimed to the study of the following scientific topics:

1. Compact objects;

2. Extragalactic astronomy;

3. Stellar nucleosynthesis;

4. Galactic plane and centre structure;

5. Particle processes acceleration;

6. Identification of high energy sources.

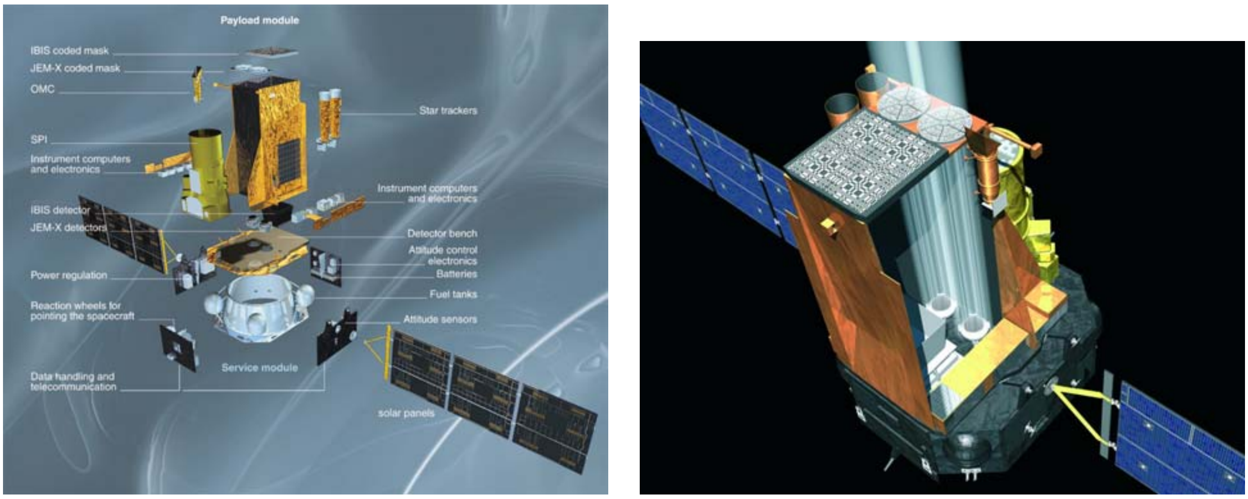

Figure *4.1: The INTEGRAL spacecraft with the payload module on top of the service module (exploded, left). The overall dimensions of the spacecraft (excluding solar arrays that span for 16 m) is ∼5 m x 2.8 m x 3.2 m. The sun direction is along the Z axis (i.e. illuminating IBIS and leaving SPI in the shadow) (Credits: ESA 2002).*

4.2 The spacecraft

The *INTEGRAL* spacecraft consists of 2 main structures: the service module (hosting the whole of the thermal, attitude, orbit and electrical control systems) and the payload module (accomodating the detector assemblies and an empty box supporting at about 3.2 m of height the coded masks, a key feature of *INTEGRAL*'s instruments). Figure 4.1 shows the overall view of *INTEGRAL* service and payload modules.

The *INTEGRAL* satellite was put on its orbit by a Russian PROTON launcher. The orbit is highly eccentric with a revolution period around the Earth of 72 hours, a perigee height of about 9000 km and an apogee height of about 154000 km with an inclination of $\sim 52°$with respect to the equatorial plane. Such an orbit has been chosen to minimise the background noise due to particles trapped in the radiation belts and thus to allow for long uninterrupted observations.

4.2.1 The instruments

Table 4.1 shows the scientific capabilities of the *INTEGRAL* instruments. The high energy instruments (SPI, IBIS[16] and JEM-X) are all coded aperture mask telescopes. Due to the inability to reflect or refract photons of hard X or γ-ray wavelengths, it is not possible to use the conventional focussing techniques used in optical astronomy. At high energies the coded mask technique is the key for imaging, essential to separate and locate sources. Such a technique is now well established in astrophysics and has found widespread applications also in former missions such as *Granat*/SIGMA (Paul et al. 1993), *CGRO*/BATSE (Zhang et al. 1993), *BeppoSAX*/WFC (Scarsi et al. 1993).

[16]IBIS is comprised of 2 distinct layers. The upper layer (ISGRI, *INTEGRAL* Soft Gamma-Ray Instrument, a CdTe detector) is sensitive in the 15 keV – 1 MeV, Lebrun et al. 2003, while the lower layer (PICsIT, Pixellated Imaging Caesium Iodide Telescope) is sensitive in the higher 170 keV – 10 Mev band, Di Cocco et al. 2003.

Parameter	SPI	IBIS
Energy range	18 keV–8 MeV	15 keV–10 MeV
Detector	19 Ge detectors, each (6×7) cm	16384 CdTe dets, each $(4 \times 4 \times 2)$ mm
	cooled @ 85 K	4096 CsI dets, each $(8.4 \times 8.4 \times 30)$ mm
Detector area (cm^2)	500	2600 (CdTe), 2890 (CsI)
Spectral resolution (FWHM)	3 keV @ 1.7 MeV	8 keV @ 100 keV
Continuum sensitivity	5.5×10^{-6} @ 100 keV	6×10^{-7} @ 100 keV
(photons cm^{-2} s^{-1} keV^{-1})	1.2×10^{-6} @ 1 MeV	5×10^{-7} @ 1 MeV
($\Delta E = E/2$, 3σ, 10^6 s)		
Line sensitivity	3.3×10^{-5} @ 100 keV	1.9×10^{-5} @ 100 keV
(photons cm^{-2} s^{-1})	2.4×10^{-5} @ 1 MeV	3.8×10^{-4} @ 1 MeV
(3σ, 10^6 s)		
Field of view (fully coded)	16° (corner to corner)	$9° \times 9°$
Angular resolution (FWHM)	2.5° (point source)	12′
Source location (radius)	≤1.3° (depending on source strength)	≤1′ (for 10σ source)
Absolute timing accuracy (3σ)	≤200 μs	≤200 μs
Mass (kg)	1309	746
Power [max/average] (W)	385/110	240/208

Parameter	JEM−X	OMC
Energy range	4 keV–35 keV	500 nm–600 nm
Detector	Microstrip Xe/CH_4−gas detector (1.5 bar)	CCD + V-filter
Detector area (cm^2)	500 for each of the two JEM-X detectors[a]	CCD: (2061×1056) pixels
		Imaging area (1024×1024) pixels
Spectral resolution (FWHM)	2.0 keV @ 22 keV	–
Continuum sensitivity[b]	1.2×10^{-5} @ 6 keV	–
(photons cm^{-2} s^{-1} keV^{-1})	1.3×10^{-5} @ 30 keV	–
(3σ, 10^6 s)		
Line sensitivity[b]	1.9×10^{-5} @ 6 keV	–
(photons cm^{-2} s^{-1})	8.5×10^{-5} @ 30 keV	–
(3σ, 10^6 s)		
Limiting magnitude (mag)	–	17.8
(3σ, 5000 s)		
Field of view (fully coded)	4.8°	$5° \times 5°$
Angular resolution (FWHM)	3′	25″
10σ source location (radius)	≤30″	6″
Absolute Timing accuracy (3σ)	≤200 μs	≥1 s
Mass (kg)	65	17
Power [max/average] (W)	50/37	20/17

[a] At the moment, only one of the two JEM-X detectors is being operated.
[b] Assumes operation of both detectors.

Table 4.1: *INTEGRAL* payload: key parameters (Winkler et al. 2003)

4.2.2 Coded aperture imaging

In coded aperture imaging systems a mask consisting of an array of opaque and transparent elements to the X and γ radiation is set between the source and the detector. Every source within the field of view projects a shadow of the mask onto the detector plane (shadowgram). In the case of one single bright point source in the field of view, the shadowgram will consist of the mask pattern (or part of it, according to the position of the source with respect to the centre of the mask). For a more complex distribution of sources (e.g. the Galactic centre!) the shadowgram will embody the sum of many such patterns. Given the known mask structure and properties and the detected overall shadowgram, it is possible to disentangle all the single source contributions and finally reconstruct the original sky image (Fenimore & Cannon 1978, Caroli et al. 1987).

Coded mask instruments are thus quite peculiar and the data analysis is complex: the superposition of the shadowgrams leads to the fact that every source contributes to the background of the others and needs to be well disentangled. Likewise, the background's spatial variations need to be accurately determined and removed to be able to detect the weaker sources.

Another main difference with respect to non-coded mask telescopes is that the field of view consists of 2 distinct regions: the Fully Coded Field of View (FCFOV) which is defined as comprising all directions for which the detected flux is completely modulated by the mask and the Partially Coded Field of view (PCFOV) in which only a fraction of the detector plane is illuminated (Fig. 4.2).

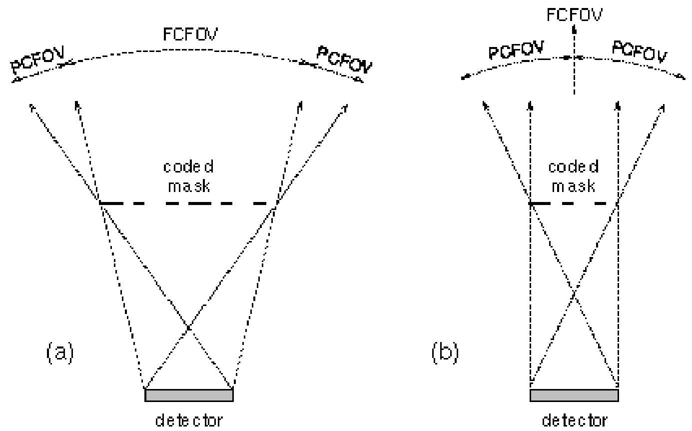

Figure *4.2: Illustration of the fully coded field of view (FCFOV) and a partially coded field of view (PCFOV) for 2 different configurations: mask size bigger than the detector (a) and mask equal to the detector (b). In the latter case only a source on axis is fully coded while in the former there is a bigger FCFOV region. Configuration (a) is used for INTEGRAL coded mask instruments.*

The signal to noise ratio of a source is higher (and constant) in the FCFOV and decreases as the source moves off-axis, into the PCFOV. This leads to the need to have the FCFOV zone as large as possible which is achieved either by a very large detector (heavy and expensive) or choosing a geometrical configuration in which the mask is bigger than the detector area itself (configuration used for *INTEGRAL* instruments). The mask has a base pattern of the same size as the detector and it is made of cyclic repetitions of this base pattern (Fig. 4.3). In this configuration, in the sky image produced by the deconvolution process, a point source does not produce a single narrow peak at its true position but also other spurious ones (ghosts) in well defined offset detector positions. The offset is equal to the base pattern dimensions. It is therefore necessary to discriminate among the produced peaks the real one from the ghosts.

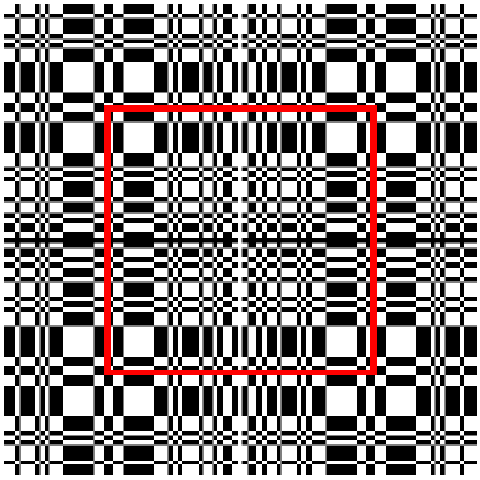

Figure *4.3: The pattern of IBIS mask. The white elements are the ones transparent to the X-γ radiation. The red square shows the basic pattern that is repeated almost 4 times to produce the final complete mask. The "almost" 4 times repetition instead of a complete one simplifies the ghost from source discrimination. In fact, as a result, the real source is generally more significant than the ghosts. See text.*

4.3 The *INTEGRAL* ground segment

The *INTEGRAL* ground segment consists of two major elements, the Operations Ground Segment (OGS) and the Science Ground Segment (SGS). The OGS, consisting of ESA's and NASA's ground segments and the Mission Operations Centre (MOC) at ESOC (see Fig. 4.4), implements the observation plan and performs the standard spacecraft maintenance tasks. The SGS consists of two parties: the *INTEGRAL* Science Operations Centre (ISOC, Much et al. 2003) and the *INTEGRAL* Science Data Centre (ISDC, Courvoisier et al. 2003). ISOC processes the accepted observation proposals and prepares an observation plan which is then implemented by the MOC. The ISDC analyses, archives and distributes the data to the scientific community. It also operates a quick-look analysis of the data within few hours to detect new and unexpected sources, it monitors the instruments and runs a gamma ray burst alert system that provides to the community the position of gamma-ray bursts within seconds (IBASE, Mereghetti et al., 2003a).

This thesis has been entirely developed at the ISDC.

4.4 The observing programme

The first year of *INTEGRAL* science operations time was divided in 2 main parts: the general programme (~65% of the time), opened to the whole scientific community, and the core programme (the remaining ~35%), reserved to the members of the *INTEGRAL* Science Working Team (ISWT). The latter is composed by instrument and data-centre principal investigators, mission scientists and representatives of the US and Russian scientific communities.

The pointing strategy for the two programmes is quite different. In the general programme, there are three possible ways to perform an observation: constantly pointing at a target in the

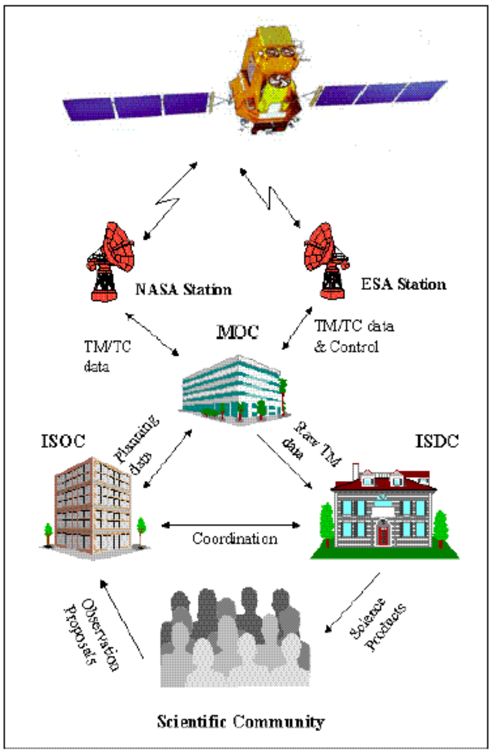

Figure *4.4: INTEGRAL ground segment structure.*

centre of the instruments field of view (so-called staring mode) or performing a small scan around the target (dithering mode). There are two possible dither patterns: the 7-point hexagonal one and the 25-point rectangular one (Fig. 4.5).

The pointing strategy is up to the observer and depends on the scientific aim of the observation i.e. on the driving instrument: a 25-pointing dithering improves the sensitivity of SPI while an hexagonal or staring one would be more appropriate for JEM-X (given its smaller field of view) and *Chandra*.

In the core programme the pointing strategy is different: it consists of regular scans of the Galactic plane (GPS) and of the Galactic centre (Galactic Centre Deep Exposure, GCDE)[17]. The patterns of the GPS (sawtooth pattern) and GCDE for the first year and the SPI FCFOV are shown in Fig. 4.6. Only a few scans and the perimeter of the GCDE are shown for clarity. Both the zones within the GPS and GCDE borders are thoroughly covered during the scans.

The regular analysis and study of *INTEGRAL* core programme data (GPS/GCDE) on a sample of LMXRBs (shown in Fig. 4.6) is one of the main topics of this thesis.

4.5 The first two years in orbit

4.5.1 Space Operations

Immediately after launch (October 17th, 2002), *INTEGRAL* went through its commissioning phase. This phase was split in two parts. The first part was dedicated to instrument activation and configuration optimisation while the second part (Performance Verification, PV) consisted

[17]In addition to specific targets of opportunity.

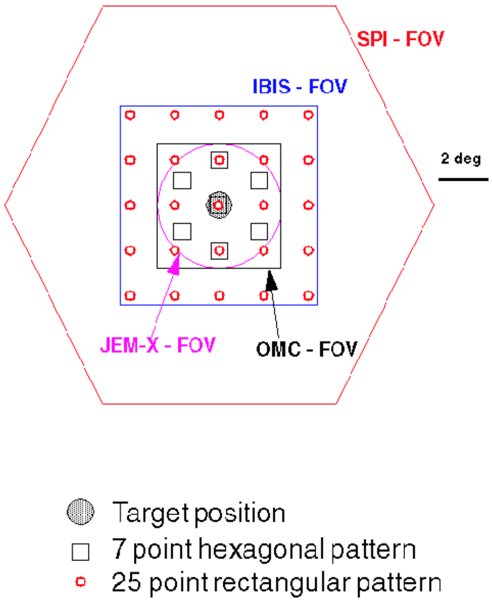

Figure *4.5: INTEGRAL dithering patterns. The fields of view of the instruments are also shown. (Jensen et al., 2003)*

of a set of observations, mainly empty fields and Cygnus region (Fig. 4.7, left pannel).

The instrument calibration activities started on February 2003, i.e. when the main *INTEGRAL* calibration target (the Crab Nebula) became visible (Fig. 4.7, right pannel). The Crab is the calibrator of all high energy missions, due to its high energy brightness and stability, and is used for comparing results from one mission to another.

4.5.2 Science highlights

Nominal *INTEGRAL* operations started on revolution 26 (December 30th, 2002) with the first accepted observations of the first year Announcement of Opportunity (AO1) programme. A special edition of Astronomy and Astrophysics, issued in November 2003, collects about 75 papers with early *INTEGRAL* results.

Galactic compact sources

One of the main strengths of *INTEGRAL* is the accurate positioning of high energy sources. This capability becomes even more powerful when coupled to the size of the field of view of the high energy instruments (IBIS and SPI). The IBIS field of view spans over a square of 30°x 30°. This is a huge portion of the sky (compared for example to the $\sim$15′ x 15′ *Chandra*/HRC and *XMM-Newton*/EPIC field of view, see Fig. 4.8) and it is observed all at once in each *INTEGRAL* pointing ($\sim$2000 secs). These *INTEGRAL* capabilities are mostly exploited during the core programme. The regular scan of the Galactic plane and centre is very valuable as it allows to monitor the poorly studied high energy emission of a large sample of sources. In this frame, the monitoring programme for a sample of LMXRBs was performed, the results of which are given in Part III of this thesis.

Besides offering a great deal of interesting data, a very large field of view increases the chances of catching or discovering a transient or highly variable phenomena in the sky. *INTEGRAL* has already detected at least 46 new strong high energy Galactic sources all of which have been

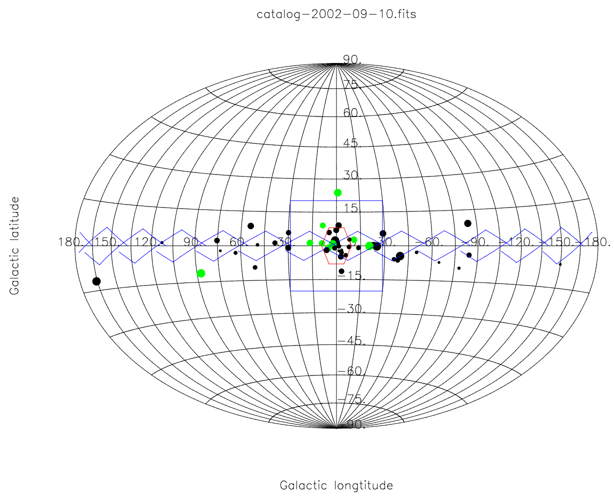

Figure *4.6: GPS and GCDE pattern for INTEGRAL AO1 (in blue). The SPI FCFOV (in red) and the LMXRBs of the monitoring programme are shown: persistently bright ones (green) and transient or highly variable ones (black).*

quickly reported to the astronomical community to enable follow-up observations in different wavebands. This is the case, for example, of IGR J16318-4848, the first new source to be discovered, that revealed an unusual line-rich and strongly absorbed spectrum in an *XMM-Newton* follow-up observation (see Fig. 4.9). This source, together with other similar ones discovered by *INTEGRAL*, suggests the presence of a previously unknown class of highly absorbed objects: these sources either have their bulk energy emission beyond 10–20 keV, or are sources which are so strongly absorbed that they were undetected in earlier soft X-ray surveys such as the *ROSAT* All Sky Survey or the *BeppoSAX* observations of the Galactic center.

Gamma-ray bursts

An important role in the transient event detections with *INTEGRAL* is played by the **I**NTEGRAL **B**urst **A**lert **S**ystem (IBAS, Mereghetti et al. 2003a). Although *INTEGRAL* is a γ-ray astronomy mission not particularly optimised for gamma-ray burst studies, it was soon realised that the IBIS imaging performances and large FOV could offer the possibility of detecting many bursts throughout *INTEGRAL*'s life. Up to now, the estimated rate of about 1 burst per month in IBIS FOV was met. IBAS (based on ISGRI data) has so far obtained the best performance as it is currently able to provide accurate burst positioning (3 $'$ radius error regions) within few tens of seconds from the gamma-ray burst (GRB) itself [18]. Speed and precision are not a matter of competition but are essential to be able to trigger rapid multi-wavelength follow-up to study the nature and origin of these explosions in the sky. In fact, alerts with the coordinates of the gamma-ray burst are distributed via internet to the scientific community within tens of seconds and the hunt for the afterglows starts.
Fig. 4.10 shows the first multiwavelength afterglow of an *INTEGRAL* gamma-ray burst (GRB 030227, Mereghetti et al., 2003c). *XMM-Newton* observed the GRB only 8 hours after its occurrence and detected a fading X-ray counterpart providing a high quality spectrum.

[18]The Inter Planetary Network (IPN, Hurley et al. 2001) can provide error regions of a few tens of square arcmin, but after several hours (or even days). With HETE-2 (Ricker et al. 2003) the gamma-ray burst positions derived on-board at the degree level are available within a few seconds, and later (1-2 hours) refined down to a

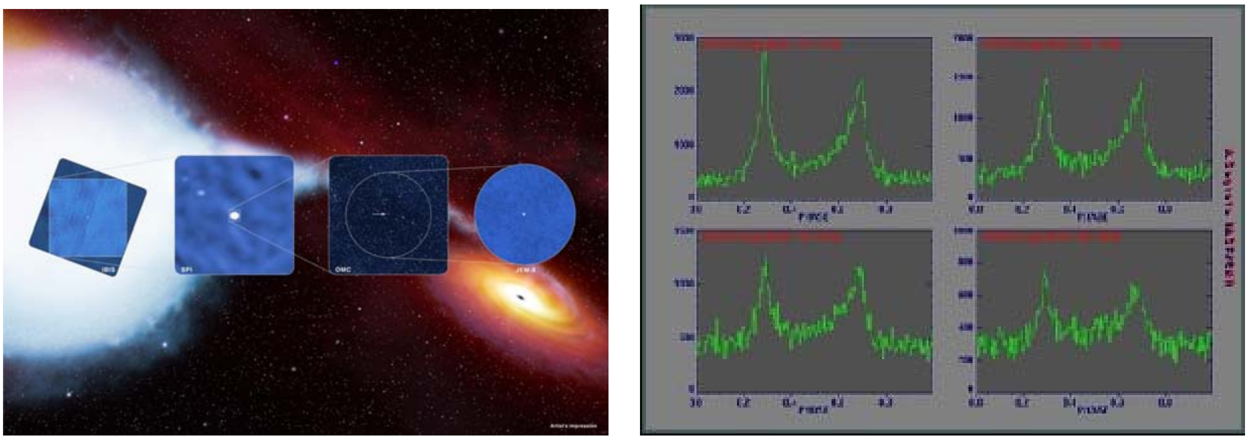

Figure *4.7:* Left*: composite "first-light" image of Cygnus X-1 obtained by the four instruments aboard the INTEGRAL spacecraft overlayed on an artist's view of this binary system (Credits: ESA).* Right*: The pulse profile of the Crab Nebula. Each panel shows the profile in a different energy range as measured by IBIS during the February 2003 observations. (Courtesy: A. Bazzano, G. La Rosa, A. Segreto and the IBIS team).*

Up to now IBAS has detected and distributed in near real time the relevant information for all the GRBs in the IBIS FOV. The only exception to this is the first GRB detected by *INTEGRAL*. Just a few weeks after launch, *INTEGRAL* started the in-orbit calibration observing Cyg X-1. On November 25th, 2002, the satellite was set up for a special observation with IBIS in a non-standard mode which forced IBAS to remain non operational. During this test, a GRB occurred in the PCFOV of IBIS and lasted about 20s. As the *INTEGRAL* scientist on duty that day, I participated in the discovery of this GRB (Bazzano & Paizis 2002) and in the study of its properties (Malaguti et al. 2003).

Similar occasions happened very often during this thesis. Being part of *INTEGRAL* activities and discoveries is one of the most exciting aspects of working at the ISDC especially for a student doing a PhD, during which many unexpected events occur and fruitful collaborations are made. A taste of all this is given in the Part V of this thesis.

Diffuse gamma-ray line emission

The measurement of the properties of line emission from newly formed elements such as ^{26}Al, ^{44}Ti and ^{60}Fe is one of the key goals of *INTEGRAL*. Their detection via the high-resolution spectrometer on board *INTEGRAL* (SPI) will reveal information of the sources and location of such elements through the study of their shape and broadening.

These emission lines are faint and distributed over large regions of our Galaxy and long exposures are required for mapping and studying their properties. Nevertheless, already after a modest exposure time (six months), SPI is able to detect the 1809 keV line produced by the decay of the radioactive isotope ^{26}Al (Fig. 4.11, left pannel) at a resolution comparable to the CGRO performance after its nine year mission. ^{26}Al is probably built in the synthesis of new elements by super-massive stars and this makes it an ideal tracer for historical nucleosynthesis.

The first months of observations already hint at the presence of the 1172 and 1332 keV lines from ^{60}Fe in the direction of the Galactic centre.

few arcmin, with a ground analysis.

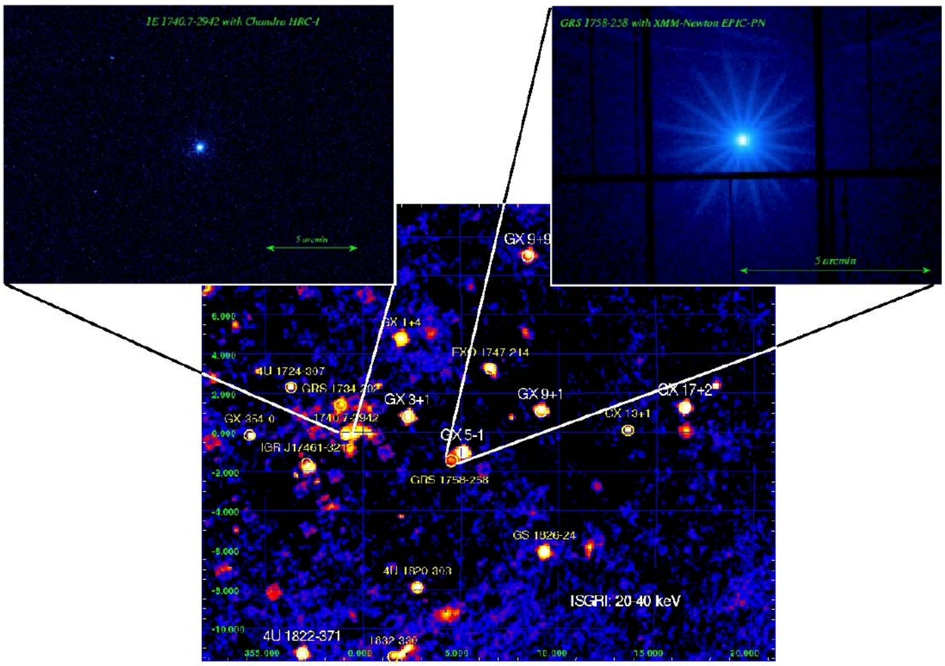

Figure *4.8: IBIS/ISGRI image of the area around the centre of our Galaxy in the 20 – 40 keV range. The image covers a region comparable to the field of view of the instrument. The richness of INTEGRAL data is quite clear (A. Paizis et al. 2003). Each source visible in the image requires its own detailed spectral and timing analysis.For comparison the Chandra/HRC and XMM-Newton/EPIC fields of view (of the size of a few ISGRI pixels!) are shown.*

Another topic of great interest for *INTEGRAL* is the detailed mapping and spectroscopy of the 511 keV electron-positron annihilation feature seen from the central Galactic region (Fig. 4.11, right pannel). The origin of the positrons is unclear and many scenarii have been proposed: neutron stars, black holes, supernovae, novae, gamma-ray bursts, different types of stars, and cosmic-ray interactions with the interstellar medium.

The current SPI preliminary results are very encouraging and suggest that it will be soon possible to have maps of unprecedented spatial/spectral resolutions and sensitivity, approaching to the solution of long standing unanswered questions.

4.6 The Future

Similarly to the two first years, the third year of science operations time is divided into 2 main parts: the general programme (∼75% of the time) and the core programme (∼25% of the time). For the general programme, the third *INTEGRAL* Announcement of Opportunity (AO3) is currently open (13 of September till 29 of October 2004).

In AO2 the total number of proposals received was 142, requesting a total observing time of 144 million seconds. Such an amount of time corresponds to a factor of 8 over-subscription (roughly 18 million seconds are available for the open time programme during the second year).

The AO2 accepted proposals (grade A) integrated up to about 14.7 Msec and cover the

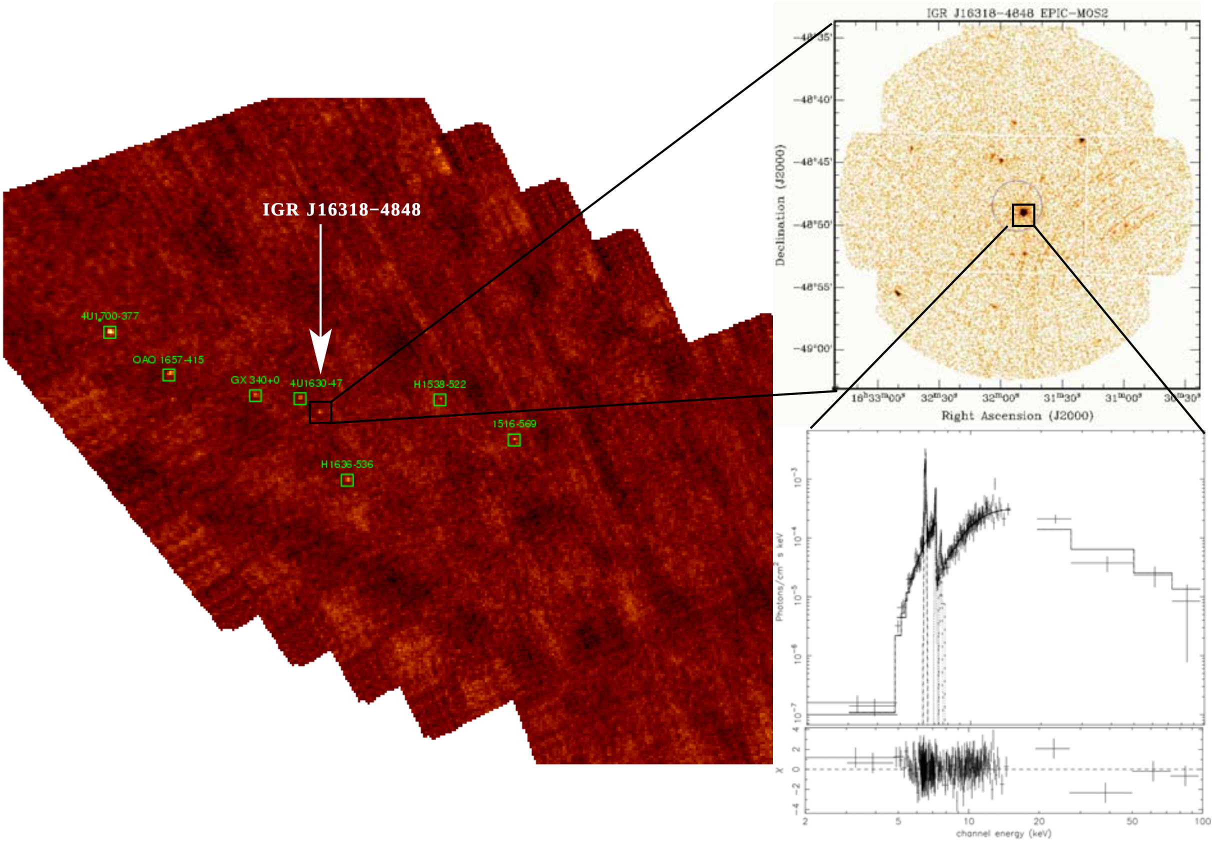

Figure *4.9: ISGRI (20–40 keV) detection of the new source IGR J16318-4848 during a GPS (Courtesy: Rodriguez, Bazzano and the IBIS team). The insets show the XMM-Newton/EPIC follow-up image and the combined EPIC/PN INTEGRAL/ISGRI spectra (Walter et al. 2003).*

following topics:

1. Compact Objects: 7 proposals (for ∼21% of the grade A available time);
2. Extragalactic: 9 proposals (∼24%);
3. Nucleosynthesis: 4 proposals (∼51%);
4. Miscellaneous: 3 proposals (∼4%).

As can be seen, the relative time per proposal was significantly higher for nucleosynthesis, as expected from the discussion on this topic in Section 4.5.2 (diffuse gamma-ray line emission).

The aforementioned grade A time, combined to the accepted Target of Opportunity (ToO) proposals and possible lower (B) grade proposals, build up the *INTEGRAL* general programme which will be executed in parallel to the core programme observations.

All these data (general and core programme) will become public after one year.

In November 2003, the ESA Science Programme Committee (SPC) approved a 4-year rolling extension to *INTEGRAL*'s operations from 17 December 2004 until 16 December 2008. This rolling extension means that towards the end of the first two years the level of resources required

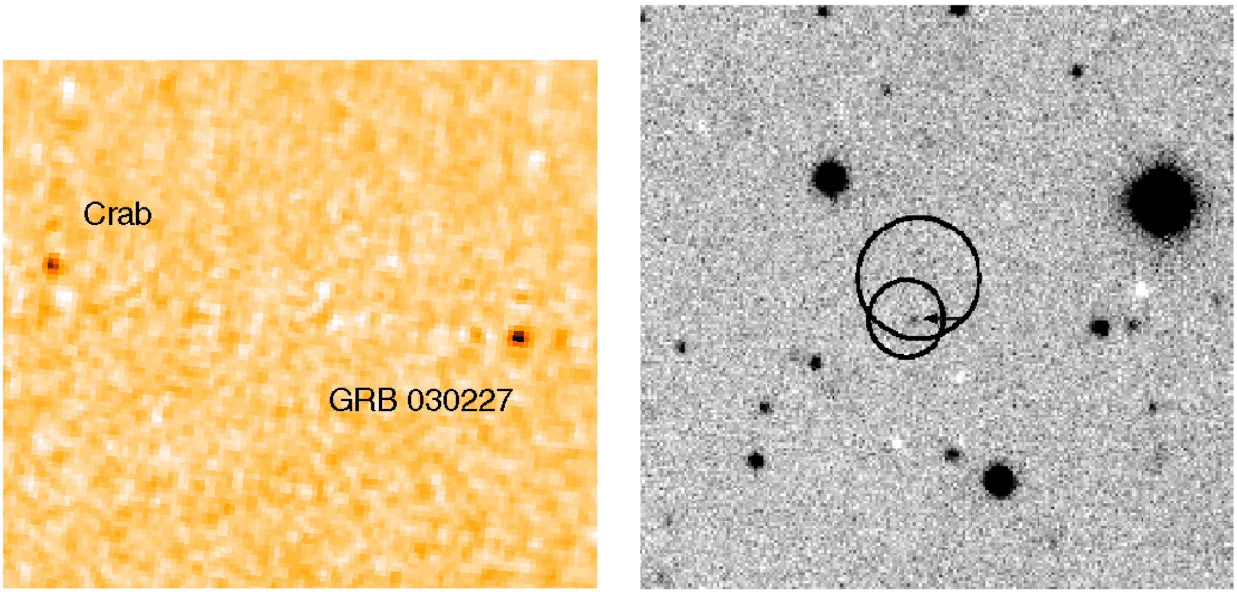

Figure *4.10:* Left*: IBIS/ISGRI image of GRB030227 detected in the Crab field during the calibration phase. The image has been obtained in the 15-200 keV band and was deconvolved using the IBAS software. The distance between the Crab and the GRB is* $\sim 10^{\circ}$ *(Castro-Tirado et al. 2003).* Right*: Optical R band image of the GRB030227 field taken at the 2.5INT. The position of the optical afterglow is indicated by the arrow inside the preliminary and the final XMM-Newton error circles (*$6''$ *and* $4''$ *radii, respectively). The field is* $1'$ *x* $1'$ *. (Castro-Tirado et al. 2003)*

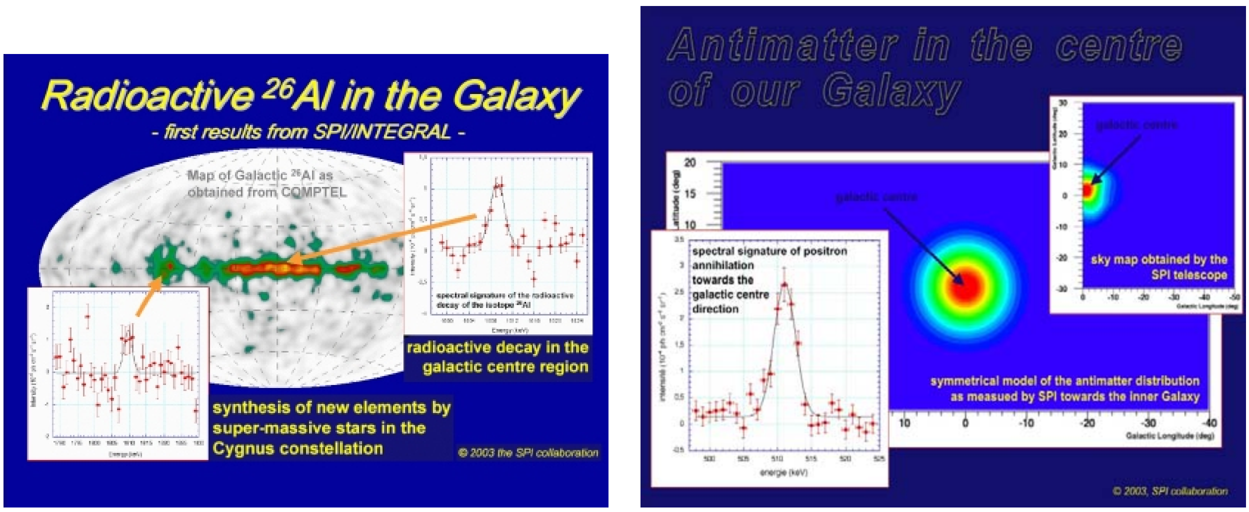

Figure *4.11:* Left*: Map of the Galaxy obtained with CGRO/COMPTEL (1991-2000) in the light of the* ^{26}*Al line. The insets show the SPI detection of this line from the centre of our Galaxy and from the Cygnus area after only several months. (Credits: SPI team).* Right *SPI sky-map and spectrum of the positron-electron annihilation in the centre of the Galaxy based on Core Programme data. (Credits: SPI team).*

for the third and fourth years will be reviewed by the SPC. Should the scientific return remain high and the technical status be appropriate then at the same time the SPC would be asked to approve a further 2 years of *INTEGRAL* operations.

4.7 Final remarks

Already after two years from launch, *INTEGRAL* brings new and exciting results from the high energy universe. Every day more and more data are taken and processed at ISDC in near real time. The scientific community has chosen the targets of interest for *INTEGRAL* to seek and the Core programme keeps scanning the Galactic centre and plane. This is the status now. But before nominal activity and even long before launch, a lot of work and preparation had to be done for the mission to be successful. In this frame, in those pre-flight phases, I took care of OSIM, the *INTEGRAL* **O**bservation **Sim**ulator. OSIM has been largely used to assess the scientific validation of the analysis software as well as to give the scientific community a tool to get familiar with *INTEGRAL* data and capabilities. A description of OSIM and its use is given in the next chapter.

Chapter 5
THE *INTEGRAL* OBSERVATION SIMULATOR

5.1 Introduction

A few years before *INTEGRAL* launch, the instrument specific software for the analysis of *INTEGRAL* data was being developed and some parts were already self consistent. To test those parts, and for the future ones, an observation simulator was built.

This simulator evolved together with the knowledge of the instruments and reached a shape that allowed the distribution to the scientific community to prepare for the *INTEGRAL* AO1 proposals and to get familiar with the complex *INTEGRAL* data structure and analysis.

Once OSIM became solid enough, based on pre-*INTEGRAL* high energy emission knowledge, we carried out a simulation of the first year of *INTEGRAL* Core programme to get the feeling for the potential of such a programme.

5.2 Purpose of the Observation Simulator

One of the roles of ISDC is to process *INTEGRAL* data from the raw telemetry to high-level data products such as sky images, spectra and lightcurves. The high level data products are created by the scientific analysis step which denotes the final step of the ISDC data processing. The Observation SIMulator (OSIM) is a software package that simulates *INTEGRAL* observations. It generates data (at the "corrected" data level, i.e. ready for the analysis tools) in a format very close to the real one. In particular, 2 of the 4 *INTEGRAL* instruments are simulated: IBIS and JEM-X. There is also a SPI simulator but it does not belong to OSIM and it is a software package on its own.
OSIM main purposes were:

- To generate accurate simulated data for the high energy instruments on board *INTEGRAL* to test the scientific analysis pipelines (both within ISDC and at the instrument teams sites).

- To help the *INTEGRAL* guest observers to get acquainted to the peculiar *INTEGRAL* data structure and format.
  In this line, OSIM has been made available to the participants of the "Observing with *INTEGRAL*" School (Les Diablerets, Switzerland, March 2000) for an early taste of *INTEGRAL* data analysis and has been publicly distributed since January 2001 also in view of the AO1 proposal preparation.

These two purposes are quite different and bring two different requirements. For the pipeline developers OSIM had to produce results in a format compatible with the analysis software, to model all the available instrument modes (also the non-scientific ones), to be always up to date with the latest version of the ISDC environment software and libraries and to have the capability of simulating any kind of sky to test the software at many levels: a crowded field to see the angular resolution capabilities, a given brightness ratio among the sources to test the spectral extraction dependency on the nearby sources etc. For the outside users OSIM had to provide realistic results (sensible sources models, instrument description etc) with a user friendly interface.

The first part of this thesis was focussed on the OSIM package, including integrating, testing and documenting the software package for both the aforementioned purposes.

5.3 Overview

OSIM produces a simulated *INTEGRAL* observation. With OSIM, the user chooses the sources to observe, builds them, "observes" them with *INTEGRAL* instruments and finally analyses the results.

It is part of the ISDC Off-Line Scientific Analysis System i.e. the interactive analysis software made available to the users. As such, it is assumed to be run as part of the overall ISDC system.

Fig. 5.1 shows its main structure.

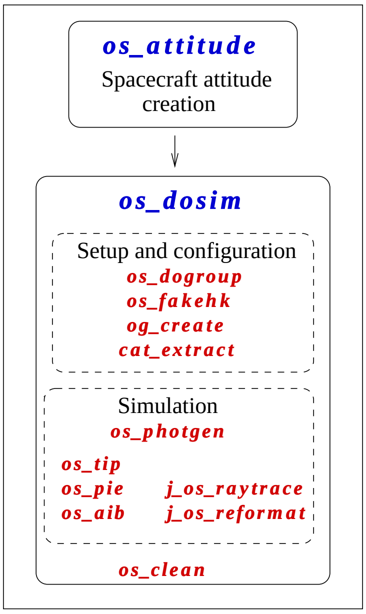

Figure *5.1: Overview of OSIM executables.*

The main components of OSIM (Paizis 2001[19]) are :

1. Pointing Definition: *os_ attitude*, a single executable;

2. Setup, configuration, simulation and cleaning: *os_ dosim*, a script calling other executables.

[19]http://isdc.unige.ch/index.cgi?Soft+download

The user first defines the pointing characteristics (*os_attitude*) and then launches the script that calls one after the other the remaining executables to perform the setup and configuration step and then the simulation (*os_dosim*). According to the instrument chosen, the script will automatically launch the correct instrument simulator (*os_tip,os_pie* and *os_aib* for IBIS or *j_os_raytrace* and *j_os_reformat* for JEM-X).

Once the simulation is done, it is necessary to have analysis software to convert the list of raw events into in high level products.

For JEM-X the instrument specific software was available in a self-consistent shape since the beginning of OSIM so no ad-hoc software was developed. For IBIS, this was not the case and an alternative Prototype for IBIS Scientific Analysis (PISA) was developed.

The latest versions of OSIM were compatible with PISA as well as with the constantly evolving JEM-X and IBIS instrument specific software.

OSIM is the result of the effort of many people from different institutes:

- M. Beck (ISDC, Switzerland): OSIM installation scripts (not described here);
- A. Bird (University of Southampton, Great Britain): IBIS simulation;
- D. Cremonesi (IASF, Italy): attitude, setup and configuration, PISA;
- D. Götz (IASF, Italy): PISA;
- P. Kretschmar (ISDC, Switzerland): overall *os_dosim* script (JEM-X), JEM-X fake housekeeping creator;
- J. Lockley (University of Southampton, Great Britain): source simulation;
- A. Paizis (ISDC, Switzerland/IASF, Italy): software integration, testing, documentation and user support.
- N. Produit (ISDC, Switzerland): attitude, overall *os_dosim* script (IBIS), setup and configuration, PISA;
- N.-J. Westergaard (Danish Space Research Institute, Denmark): JEM-X simulation.

5.4 A more detailed description

In this section the components of OSIM are described.

5.4.1 *os_attitude*

This executable generates the attitude file which contains a sequence of pointings and slews according to the user specifications: sky region, dithering pattern, number of pointings, duration of pointings etc.

5.4.2 *os_dosim*

This script is written in isdcroot which is an ISDC adaptation of ROOT[20], the object oriented data analysis framework developed at CERN.

[20]http://root.cern.ch/

Given the attitude file and interactive user inputs, it performs the whole the chain of the simulation. It returns data ready to be analysed to obtain high-level data products.

The script performs the following steps:

1. Setup and configuration;
   - Directory tree creation: *os_dogroup* ;
   - Housekeeping data creation (only for JEM-X: *os_fakehk*);
   - Data structure creation : *og_create*;
   - Catalogue extraction (extracts from the complete catalogue only the sources that end up being in the field of view of the instruments. This selected catalogue can be changed by the user to best fit his/her needs) : *cat_extract*.
2. Simulation;
   - Source simulation: *os_photgen*;
   - IBIS simulation: *os_tip,os_pie* and *os_aib*;
   - JEM-X simulation: *j_os_raytrace* and *j_os_reformat*
3. Cleaning step (all the non-filled data structures are removed): *os_clean*.

The photon generator (*os_photgen*)

The photon generator takes the output files from the setup stage and uses XSPEC to generate the source spectra. It then starts either the JEM-X or IBIS simulation according to the user's choice. The process of photon creation is started and each individual photon is "posted" to the instrument simulator. Eventually, when all the photon data have been generated and sent, the photon generator closes down. In the case of empty fields only the background photons are saved in the output files (by *os_aib*, see IBIS simulator below). The spectral models supported are all those available in XSPEC. Only point-like sources can be simulated. The source time variability models implemented are constant flux, sinusoidal oscillations, pulses and burst with exponential decay.

IBIS simulator

The IBIS simulator consists of three modular tasks to trace source photons through the IBIS instrument, apply the on-board processing and add a representative background to the source data. Initially, descriptions of source photons are received from the photon generator and are processed by a ray tracer which uses a simplified IBIS geometry and limited physics set to obtain speed gains over a more comprehensive Monte-Carlo simulation.

Those executables -described below- are called automatically (in sequence) by *os_photgen*.

1. *os_tip* (Observation Simulator Trace IBIS Photons).
   The fast photon tracer. For each traced photon which generates one or more valid energy deposits, a data packet is sent to the event processor (next step) with the following information:
   - event time
   - interaction pixel number

- energy deposited in the interaction

2. *os_pie* (Observation Simulator Process IBIS Events).

   Simulates the IBIS detector performance and stores the IBIS data in a format analogous to the one used in real telemetry. Simulation of the on-board processing takes into account the basic detector responses (energy resolution, charge loss, low energy threshold). Instrument dead-times are also applied to the source data. At the end of the event processing, the output data are stored in the data structures created within this step and the Add IBIS Background (next step) is triggered.

3. *os_aib* (Observation Simulator Add IBIS Background).

   A static background model derived from The INTEGRAL Mass Model (TIMM, Ferguson et al. 2003) is added to the source data that are finally re-formatted to generate a realistic ISDC data structure. Two background models may be used with a user defined mix for the two components. This is intended to allow for example interpolation between pure solar-minimum and solar-maximum background models. The background models work and give a sensible answer with no systematic effects for any window length $< 10^4$sec.

JEM-X simulator

The JEM-X simulator performs the same steps as the IBIS simulator. The executable called within *os_photgen* is in this case *j_os_raytrace* (JEM-X Observation Simulator RAY TRACEr). It reads the list of photons provided by the photon generator, ray-traces them through the JEM-X instrument and creates the list of photons recorded in the detector. The only exception is the background treatment: in this case, the background is created at the beginning of the simulation. The cosmic X-ray background is assumed to be uniform and the instrument background constant over the detector surface.

After the ray tracing is done the user has to launch *j_os_reformat* that converts simulated photons into "corrected" ones adding information on event loss and rejection occuring in the telemetry.

No attempt was made to model the JEM-X spectral response.

5.5 Simulation of Vela X-1

In a coded mask instrument each source projects on the detector its own shadow through the mask. The combination of those contributions on the detector builds up the final shadowgram which is the starting point for reconstructing the original sky image.

In presence of one bright source (e.g. the bright high mass X-ray binary Vela X-1) in a non crowded field, the shadowgram shows a clear mask pattern (i.e. the shadow of the bright source dominates over the others) as shown in Fig. 5.2, left panel. For comparison the IBIS/ISGRI mask is visible in Fig. 4.3. For a crowded field with sources of comparable brightness, the shadowgram presents no more a mask pattern as the different contributions are mixed and none dominates over the others (Fig. 5.3, left panel).

The right panels of Fig. 5.2 and Fig. 5.3 show the reconstructed sky. In the case of Fig. 5.2, the ghosts of the source are clearly visible. Among the 9 candidate positions found after the image deconvolution, one is the true one (the source) and the remaining 8 are spurious (ghosts). For IBIS, the ghosts are 10.5 degrees apart (size of the FCFOV) in a fixed pattern, shown in Fig. 5.2.

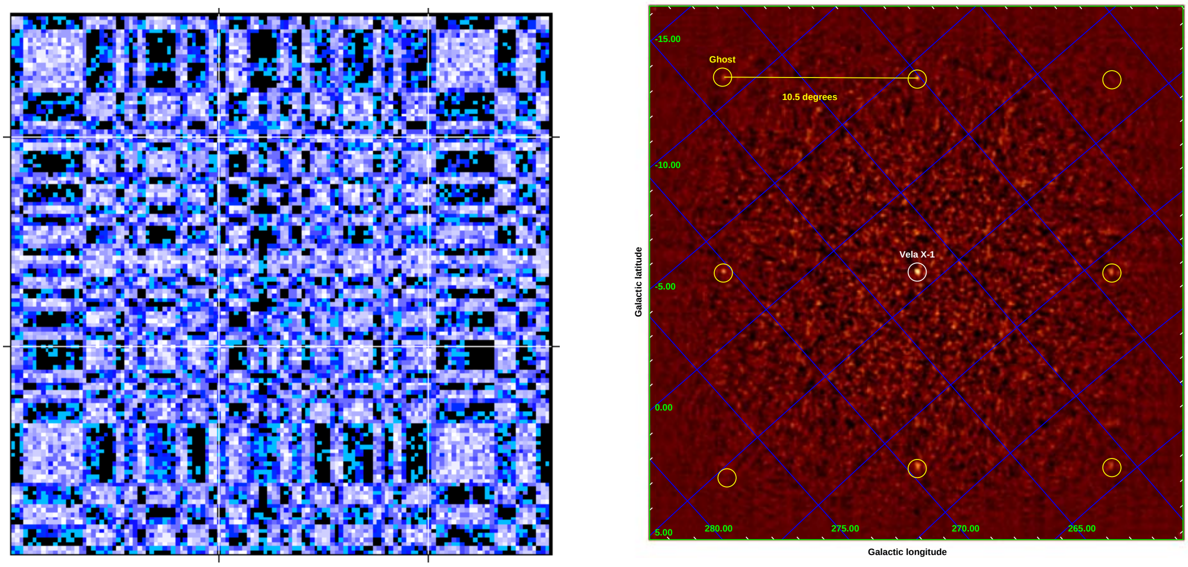

Figure *5.2:* Left: *Shadowgram for an ISGRI 500 second simulation of the Vela X-1 field. Vela X-1 is almost on axis. The mask pattern is clearly visible due to the presence of the bright Vela source.* Right: *The reconstructed sky image. The ghosts of Vela X-1 are visible. See text for details.*

The analysis tools perform an iterative removal of sources which identifies one ghost after the other and removes it from the image, producing a final image with only the sources and no ghosts (as in Fig. 5.3, right).

Fig. 5.4 shows the IBIS/ISGRI spectrum extracted for a 500 sec Vela simulation. The returned photon index and normalization at 1 keV for the powerlaw model used to fit the spectrum are respectively 2.01 +/- 0.04 and 2.3 +/- 0.3 photons s^{-1} cm^{-2} keV^{-1}. Those values are to be compared with the input ones, 2 and 2.41. Such a good agreement is expected for a source as strong as Vela X-1. For weaker sources the flux reconstruction is correct within about a factor of 2.

The final shadowgram and reconstructed sky image for JEM-X1 for this simulation are shown in Fig. 5.5. The first two images are in a skewed system (i.e. we obtain an elliptical field of view) while the latter shows a circular field, i.e the shape of JEM-X field of view. In this case the JEM-X mask pattern is not visible in the shadowgram (as for IBIS/ISGRI) because the background photons have already been included and their effect is to cover the Vela X-1 shadow on the detector. Besides, the JEM-X mask pattern is less easily recognizable than the IBIS one.

The JEM-X spectral response is not modelled in OSIM so no spectrum is available.

Also for JEM-X the mask is larger than the detector but it repeats its basic pattern only partially. Less repetition brings on one side a less smooth reconstruction of the source in the FCFOV, but, on the other, it mostly suppresses ghosts and only sources far off the centre need to be cleaned of artifacts.

5.6 The Galactic Plane Simulation

About a third of *INTEGRAL*'s observing time is devoted to the regular scans of the Galactic plane (GPS) and centre (the Core Programme). In preparation for this, we have made at ISDC some IBIS/ISGRI and JEM-X simulations of 1 year of Core programme observations. I performed

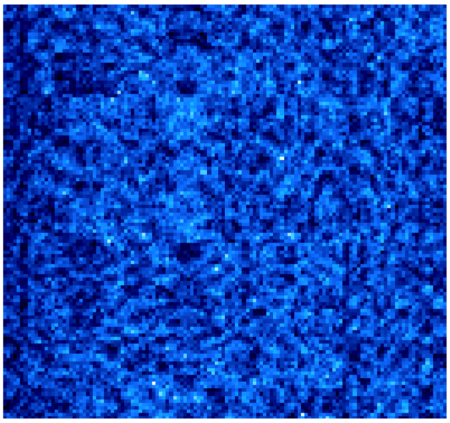

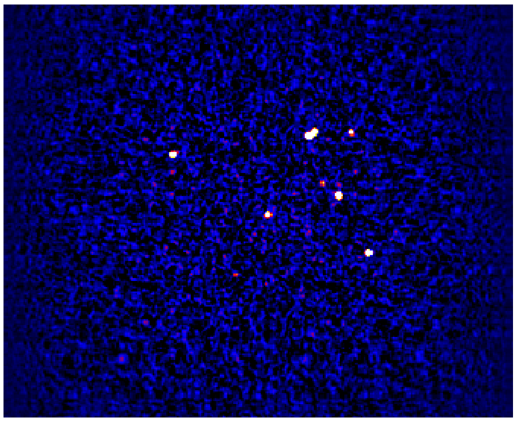

Figure *5.3:* Left: *Shadowgram for and ISGRI 500 second simulation of an artificial crowded field. 10 fake bright sources (of the order of Vela X-1) have been simulated.* Right: *The reconstructed sky image after the ghost cleaning process. See text for details.*

the IBIS/ISGRI simulation and analysis while the JEM-X simulations and the image mosaicking have been performed by ISDC collaborators.

The JEM-X data have then been analysed with the available realistic software while for ISGRI data we have used the PISA software already mentioned.

The simulated sources are the ones present in the ISDC General Reference Catalogue. Such a catalogue is the result of the merging of 9 X-Ray and Gamma Ray catalogues[21]. For more details on the catalogue see Ebisawa et al. 2003.

In the simulation, all the sources in the catalogue have been modelled. A model of the instrument background is also included (see OSIM detailed description) while diffuse emission is not.

The pattern of the first year GPS and GCDE has been shown in Fig. 4.6. For the GPS we simulated 144 saw-teeth patterns (following as close as possible the pointing indications in the AO1 documentation[22]) leading to a total of 1728 pointings (each saw tooth has 12 pointings). The GPS pointing exposure at the time of the simulation was planned to be 1050 sec which lead to a total simulated exposure of 1.8×10^6 sec (instead of the 2.3×10^6 sec advertised exposure). For the GCDE, we simulated 1 of the 2 grid cycles (1074 pointings) for a total of 1.9×10^6 sec (instead of the 2 cycle 4.3×10^6 sec grid).

Fig. 5.6 shows the GPS simulation with a zoom in the Galactic centre. A more detailed description of our work is given in Walter et al. 2003b.

Our simulation showed that about 100 known sources can be detected by *INTEGRAL* in the Galactic plane scans. Given the large IBIS field of view that covers about half of the sky during those scans, we expected also many serendipitous sources to be discovered.

[21] Van Paradjis'-Liu's LMXB catalog, Van Paradjis'Liu's HMXB catalog Macomb & Gehrels' Gamma-Ray source catalog, 4th Uhuru catalog (2-6 keV) HEAO1 A-4 catalog (13-180 keV), BATSE obs. of Piccinotti's AGN sample (20-100 keV), Tartarus ASCA AGN data (0.4-10 keV), IAUC catalog (based on IAU Circulars between 01.2000 and 07.2002), Third EGRET catalogue.

[22] ftp://astro.estec.esa.nl/pub/integral/AO/AODocC.pdf

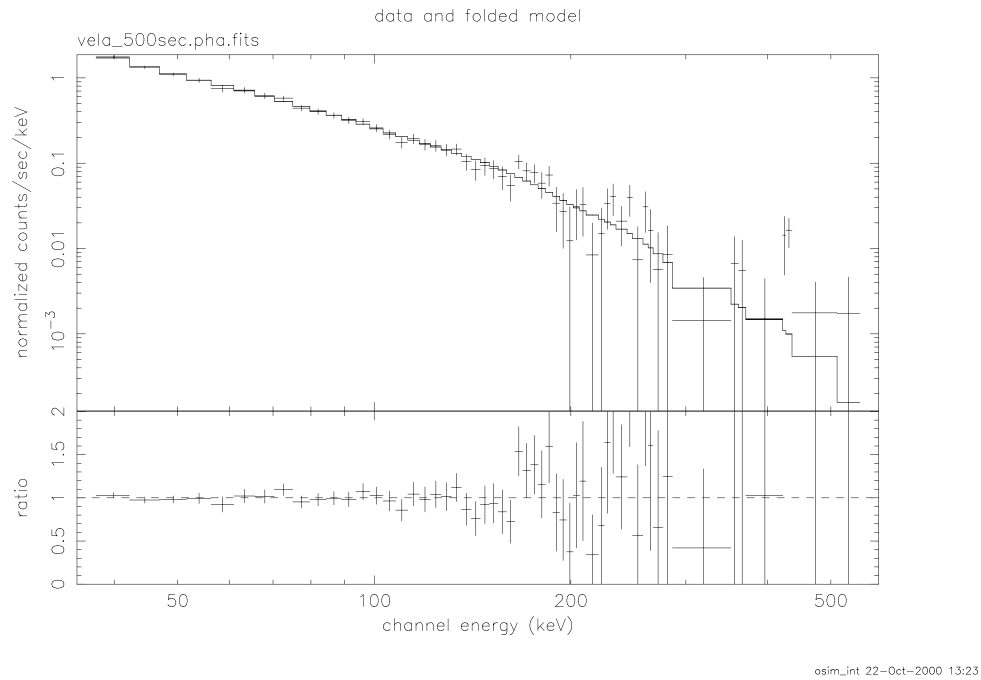

Figure *5.4: Spectrum obtained from a 500 second simulation of VELA X-1 with the IBIS/ISGRI detector.*

5.7 The Galactic Plane Observation

With time, both the pointing exposure and GPS/GCDE scheduling changed. Each GPS pointing lasts 2200 sec instead of 1050 sec and the pointings actually performed are a consequence of solar constraints and Galactic plane and centre visibility.

Fig. 5.7 shows an IBIS/ISGRI mosaic of about 5.7 Msec of real core programme data (GPS and GCDE) which corresponds to about 1 year of observations (December 2002 to January 2004). Only the brightest sources have been labelled for clarity but many more weaker sources are also visible. This image is much cleaner than the simulated one. In the last years there has been an important evolution in the analysis tools. About 130 sources have been detected in the first year of core programme, the vast majority of which are known sources and about a tenth new *INTEGRAL* sources[23].

Those results show that the simulation was indeed realistic for the bright sources but inaccurate for weak ones. In a coded mask instrument the determination of the background fluctuation and spatial variations is fundamental. Subtracting a non realistic background will not influence much the detectability of bright sources, but it can make the difference for dim ones. Unfortunately the determination of the background is very difficult. Many *INTEGRAL* pointings have been dedicated to observing source-free regions to build the correct maps but even now, after two years from launch, a correct determination has not been reached.

Another issue that comes also into play to make the comparison between simulated and real data difficult is the accuracy of the source models included in the catalogue. We used a version

[23] At the time of writing there are 46 *INTEGRAL* sources (IGRJhhmms+-ddm). Some of them are likely to be a contamination of 2 or more CHANDRA/XMM sources; others turned out to be previously detected ASCA sources but indeed there are also some new sources that are heavily absorbed (thus soft X-ray faint and undetected by previous X-ray missions).

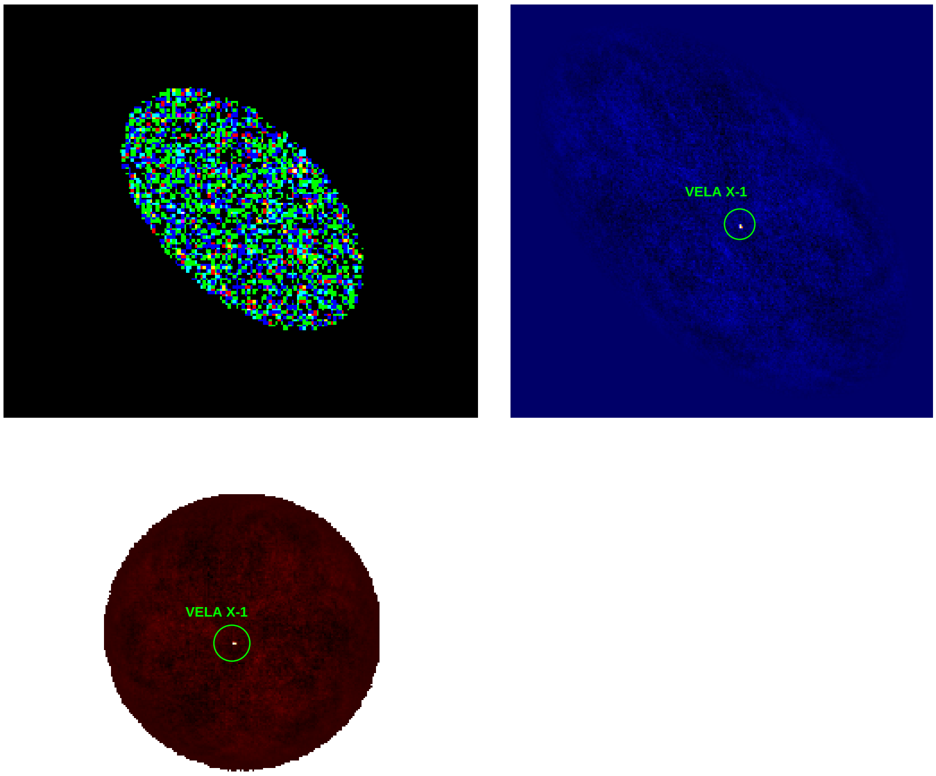

Figure *5.5: Skewed shadowgram (upper left), image (upper right) and real detector coordinates reconstructed image (lower) for the JEM-X simulation of Vela X-1.*

of the general reference catalogue that was available then. This version included some non up to date spectral models as well as some non realistic extrapolations from soft to hard X and γ rays. A simulation of only a portion of the sky would have allowed an update of the catalogue but for the whole Galactic plane we decided to keep the catalogue in the available form as it was solid enough to give a rough estimate of what to expect from a 1 year core programme.

5.8 Final remarks

Since the launch of *INTEGRAL*, ISDC started processing real data and the overall use of OSIM faded away in favour of reality. My work has also followed this path and with the beginning of *INTEGRAL* core programme, I started a systematic analysis of a sample of LMXRBs, coordinating a monitoring programme. This work is the topic of next part.

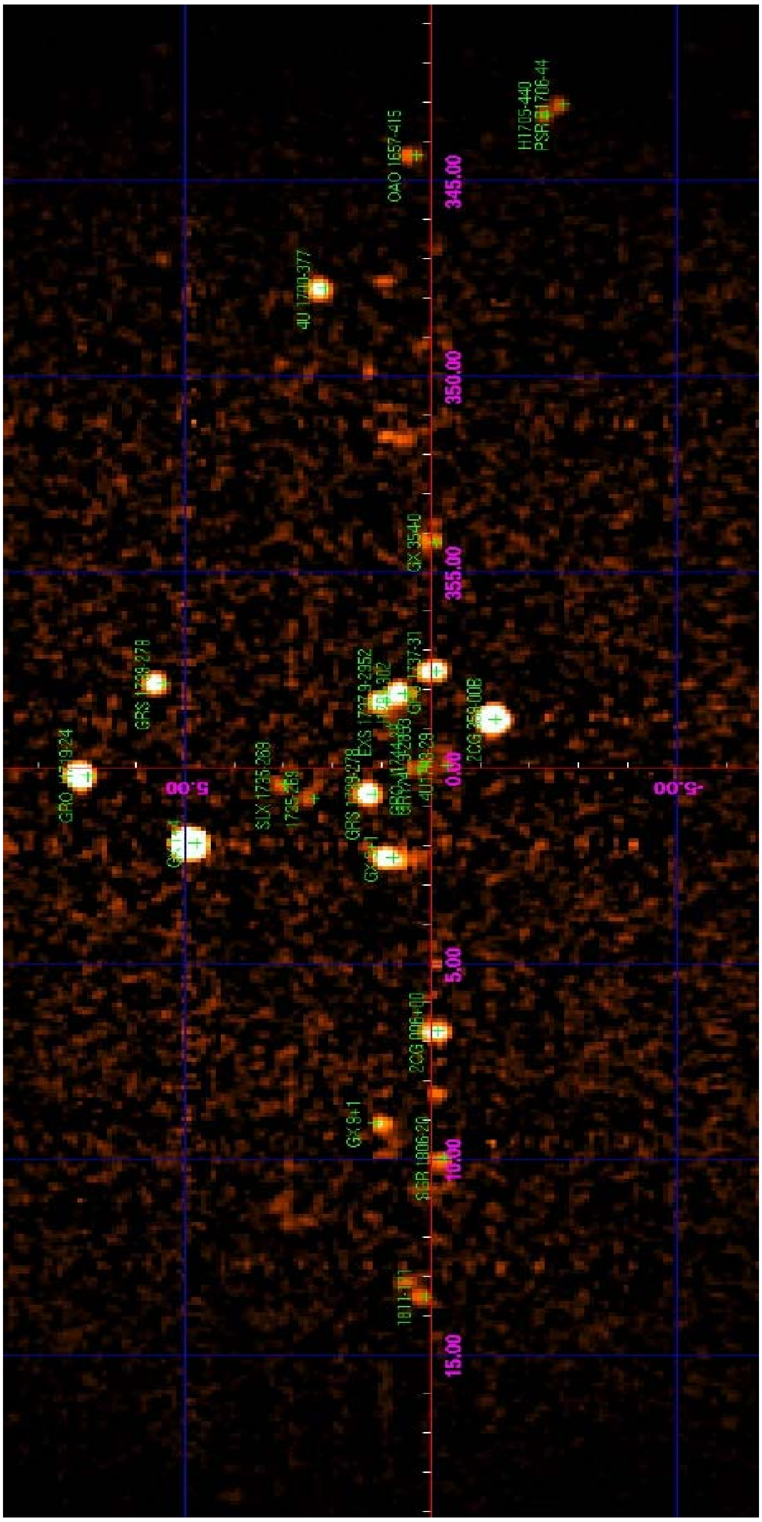

Figure *5.6: Simulation of the first year of Galactic plane scan pointings with OSIM/ISGRI (total exposure: 1.8x10^6 sec). Zoom in the Galactic centre.*

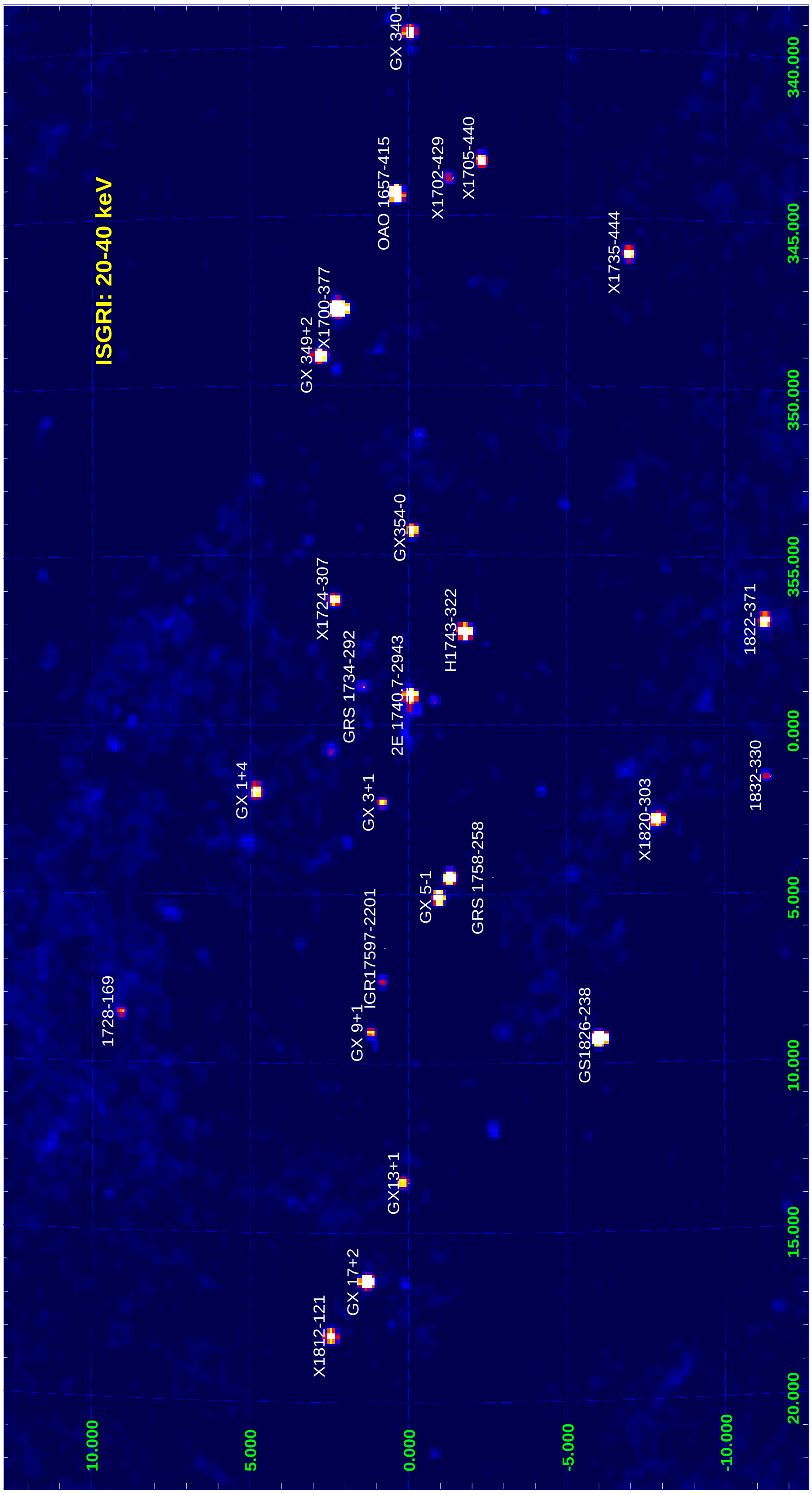

Figure *5.7: IBIS/ISGRI mosaic of the first year of core programme data (5.7 Msec).*

Third part

THE HARD X-RAY EMISSION OF LMXRBS STUDIED WITH *INTEGRAL*

Chapter 6
THE *INTEGRAL* LMXRB MONITORING PROGRAMME

In this chapter we desribe the LMXRB monitoring programme we perform with *INTEGRAL*. This work is still in progress but the main infrastructure has been built. After a brief reminder on the core programme structure and the list of monitored sources, we discuss the coordinated multiwavelength campaign and the status of the programme with the first results.

6.1 The *INTEGRAL* core programme

In the first year of *INTEGRAL* operations, 35% of the observing time of *INTEGRAL* was devoted to a large observing programme that would not have been possible to implement using individual proposals. This *INTEGRAL* Core Programme consists of [24]

- A deep exposure of the Galactic Central Radian (GCDE; 4.74×10^6 s);
- Regular scans of the Galactic Plane (GPS; 1.80×10^6 s);
- Pointed observations of selected sources (1.38×10^6 s).

Only the first two are used for the monitoring programme. The GCDE covers a cross-like pattern covering the area between $l \sim \pm 30.0°$ and $b \sim \pm 20°$ with a dense coverage of the area within about $b = \pm 10°$ and a looser monitoring further out. Each pointing lasts 1800s. The GPS is realised by regular scans of the visible part of the Galactic Plane in a sawtooth pattern ranging up to $b = \pm 6.45°$. Due to the wide FOV of the *INTEGRAL* instruments this means that sources up to $b = \pm 12°$ can be observed in the IBIS FCFOV. The exposure per source depends on its position relative to the scan path and will differ from instrument to instrument due to their different FOVs. Each pointing lasts 2200s.

The schematic patterns of the GPS (sawtooth pattern) and GCDE for the first year are shown in Fig. 6.1.

6.2 Sources of the sample

Table 6.1 shows the LMXRBs that belong to the monitoring programme. From the all known LMXRBs (Liu et al, 2001) we have selected the sources that are in the IBIS FCFOV during the core programme pointings. A further selection on the final list has been imposed, leaving out the sources that are being studied by other *INTEGRAL* collaborations[25]. As the data become

[24] http://astro.estec.esa.nl/SA-general/Projects/Integral/AO1_WWW_core_programme.htm
[25] According to the *INTEGRAL* policies regarding core programme data.

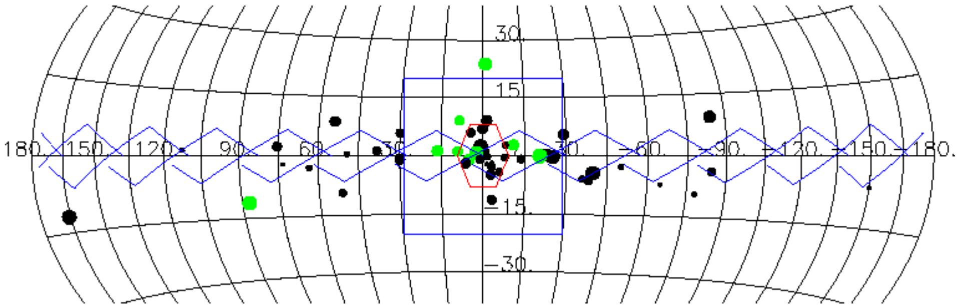

Figure *6.1: GPS and GCDE pattern for INTEGRAL AO1 (in blue). Only a few scans and the frame of the GCDE are shown for clarity. Both the zones within the GPS and GCDE borders will be thoroughly covered during the scans. The SPI FCFOV (in red) and the sources of the monitoring programme are shown: persistently bright ones (green) and transient or highly variable ones (black). The size of the symbol expresses the source IBIS/ISGRI and JEM-X intensity in units of Crab (1 Crab is used as higher limit, see Sco X-1, i.e. the source with highest latitude). In the catalogue used to build this graph, the outburst count rate is assigned to the transient sources.*

public, the sources relevant to our study (e.g. the two bright Z sources GX340+0, GX349+2) will be included to have a better overall picture of the high energy behaviour of LMXRBs.

In Fig. 6.1 the distribution of the sources of Table 6.1 is shown. The sources in green are the 7 bright persistent LMXRBs of our sample to which the remaining two known Z sources (GX 340+0, GX349+2) have been added.

6.3 Aim of the monitoring programme

The nature of the sources in the list is very diverse, containing black hole as well as weakly magnetised neutron star binaries with very different variability and type. All these sources will be regularly observed by *INTEGRAL*.

In the sample of 74 sources, there are eight LMXRBs persistently brighter than 100 mCrab in the 2-10 keV band. Seven belong to the already discussed Atoll and Z classes, i.e. they host a neutron star (see below), while one is a black hole LMXRB (GRS 1915+105). For these sources a more detailed study will be carried out with respect to the dimmer ones (e.g. GX 5-1, see next chapter).

The strength of the monitoring lies in the fact that a large sample of different sources is regularly observed in the same energy bands and with the same instrumentation. The results are directly comparable, free from extrapolations or instrument response differences. The long term database that will be built will give a very interesting view of the Galactic Plane and Centre in the less explored hard X-ray domain ($>$ 10 keV). It will allow the study of many aspects of LMXRBs that have been already discussed in Part I of this thesis such as

- The differences among black hole and neutron star LMXRBs for what concerns the dependence of the X-ray spectrum over the luminosity;
- The properties of the hard tails: occurrences, correlated spectral states, presence or absence of a cut-off that would show if the physical mechanism behind the hard tails is thermal or non-thermal;

Table 6.1: LMXRBs of the monitoring programme. *C.O.*: compact object, black hole or neutron star. The dynamically determined black holes (BH) (i.e. with M_{BH}>3 $M_\odot$) are specified with a *d* (Orosz, 2002). The remaining are believed to contain a BH on the basis of their X-ray spectra and temporal properties (Tanaka & Lewin, 1995); "-" means the C. O. is thought to be a neutron star; *Type*: A=Atoll, B=Burster, D=Dipper, G=Globular cluster, P=Pulsar, T=transient, U=ultra soft, Z=Z source, ADC= accretion disc corona source; f_X=average or minimum observed flux in 2-10 keV in micro Janksy (1 μJy = 2.4×10^{-12} erg s^{-1} cm^{-2} keV^{-1} i.e. about 1 mCrab/keV); f_{max}=maximum observed flux or outburst average flux in micro Jansky, in the 2-10 keV. If f_{max} is present then f_X is the minimum flux; *V[mag]*= apparent visual magnitude (Liu et al, 2001).

Name	l	b	C.O.	Type	f_X	f_{max}	V[mag]
J0422+32 (XN Per 1992)	197.3	-11.9	BH(d)	T	–	3000^a	13.2
0620-003 (N Mon 1975)	210.5	-6.5	BH(d)	T,U	< 0.02	50000	11.2
0918-549	275.9	-3.8	-	-	10	-	21
0921-630	281.8	-9.3	-	D	3	-	15.3
1009-45 (XN Vel 1993)	275.4	9.4	BH(d)	T,U	–	800^b	14.7
1124-684(N Mus 1991)	295.0	-6.1	BH(d)	T,U	< 4	3000	13.6
1354-645 (Cen X-2)	310	-2.8	BH	T,U	5	120	16.9
1516-569 (Cir X-1)	322.1	0.0	-	T,B,A	5	3000	21.4
1524-617 (TrA X-1)	320.3	-4.4	BH	T,U	< 5	950	-
1543-475	330.9	5.4	BH(d)	T,U	<1	15000	14.9
1543-624	321.8	-6.3	-	-	35	-	-
1556-605	324.1	-5.9	-	-	16	-	18.6
1617-155 (Sco X-1)	359.1	23.8	-	Z	14000		12.2
1624-490	334.9	-0.3	-	D	55	-	-
1630-472 (Nor X-1)	336.9	0.3	BH	T,U,D	< 2	1400	-
1632-477	336.9	-0.4	-	-	13	-	-
1705-250 (N Oph 1977)	358.2	9.1	BH(d)	T	2	3600	15.9
1708-408	346.3	-0.9	-	-	32	-	-
1711-339	352.1	2.7	-	T	16	130	-
1716-249 (XN Oph 1993)	359.8	7.6	BH	T	–	1500^c	16.65
1724-356	352.2	-0.5	-	-	32	-	-
1728-169 (GX 9+9)	8.5	9.0	-	A	300	-	16.8
1730-220	4.5	5.9	-	T	< 10	130	-
1730-312	356.3	1.6	BH	T	–	900	-
1732-273	0.16	2.6	-	T,U	< 5	50	-
1734-292	358.8	1.4	-	-	3.4	-	-
1735-28	359.6	1.56	-	T	< 0.4	565	-
1736-297	358.6	0.7	-	-	2	-	-
1737-282	0.01	1.2	-	-	3	-	-
1737-31	357.3	+0.58	BH	T	–	26	-
1739-278	0.66	1.17	BH	T	–	860^d	23.2
1739-304	358.33	-0.3	-	-	9	-	-
1740-294 (GX X-4)	359.36	0.01	-	T(?)	–	30	-
1741-322	357.1	-1.6	BH	T,U	<2	770	-
1741.2-2859	359.8	0.18	-	-	<1.5	300	-
1742-326	356.8	-1.9	-	-	< 2	3	-

Name	l	b	C.O.	Type	fx	fmax	Vmag
1742.2-2857	359.9	0.01	-	-	0.1	-	-
1742.5-2845	0.14	0.06	-	-	0.15	26^e	-
1742.5-2859	359.95	-0.05	-	-	1	5	-
1742.7-2902	359.9	-0.11	-	-	0.2^e	-	-
1742.8-2853	0.06	-0.06	-	-	0.2^e	-	-
1742.9-2849	0.13	-0.06	-	-	0.2^e	-	-
1742.9-2852	0.09	-0.06	-	-	0.2	-	-
1743.1-2843	0.25	-0.03	-	-	0.5	12	-
1743.1-2852	0.11	-0.11	-	-	0.2^e	-	-
1744-265 (GX3+1)	2.3	0.8	-	B,A	400	-	-
1744-299	359.3	-0.89	-	-	6	-	-
1744-361	354.1	-4.2	-	T	< 25	275	-
1745-203	7.7	3.8	-	G,T	< 0.1	180	-
1746-331	356.9	-3.1	BH	U	26	-	-
1746.7-3224	357.5	-2.6	-	-	0.1	-	-
1747-313	358.6	-2.2	-	G,T	1.5	20	-
J1748-288	0.7	-0.21	BH	T	-	640	-
1749-285 (GX+1.1,-1.0)	1.1	-1.1	-	T	–	60	-
J1755-324	358.0	-3.6	BH	T	–	180^f	-
1755-338	357.2	-4.9	BH	D,U,T	–	100	18.5
1758-205 (GX9+1)	9.1	1.2	-	A	700	-	-
1758-250 (GX5-1)	5.1	-1.0	-	Z	1250	-	-
GRS 1758-258	4.5	-1.4	BH	U	20	-	-
1803-245	6.1	-1.9	-	T	< 2	1000	-
1813-140 (GX17+2)	16.4	1.3	-	Z,B	700	-	17.5
1822-000	29.9	5.8	-	-	25	62	22
X 1822-371	356.9	-11.3	-	D,P,ADC	10	25	15.3-16.3
1846-031	29.9	-0.9	BH	T,U	–	300	-
J1856+053	38.27	1.26	BH	T	–	70	-
J1859+226	54.05	8.59	BH(d)	T	–	600	15.31-15.75
GRS 1915+105	54.3	-0.9	BH(d)	T	300	-	-
1918+146	49.3	0.4	-	T	< 5	45	-
1957+115	51.3	-9.3	-	U	30	-	18.7
2000+251 (XN Vul 1988)	63.4	-3.1	BH(d)	T,U	< 0.5	11000	18.9
J2012+381	75.4	2.2	BH	T,U	–	160	21.33
2023+338 (V 404 Cyg)	73.2	-2.2	BH(d)	T,U	0.4	20000	12.7
2142+380 (Cyg X-2)	87.3	-11.3	-	Z,B	450	-	14.7
2318+620	112.6	1.3	-	-	2.4	-	-

a: 20-300 keV; *b*: 1-10 keV; *c*: 20-100 keV; *d*: 2-60 keV; *e*: 0.9-4 keV; f: 2-12 keV.

- The hard X-ray energy spectra of sources that were too faint to be detected by previous missions or in a too crowded field to be disentangled (e.g. GX 5-1);
- New CDs and HIDs in hard X-rays, seeking for new differences/similarities among the different classes;
- The Atoll and Z sources broad band spectra to see if it is possible to favour one of the two competing models (eastern versus western) by studying the hard X-ray spectral variations along the tracks in the CDs;
- The presence of long term variability patterns and the variability of the sources as a class;
- The ”anomalous” bursting activity of some bright "GX" Atolls and Z sources as well as the unexpected "silence" of others;
- The presence of given timing properties also in the hard X-rays (such as pulsations seen e.g. in the ADC source X 1822-371) to build accurate timing models.

6.4 *INTEGRAL* results on the web

In collaboration with the team responsible for the study of accreting pulsars we have agreed that the results of such a work will be made public as soon as they are considered to be reliable. The *INTEGRAL* instruments calibrations are still on-going and specific parts of the software are still to be validated (e.g. the light curve extraction for very short time bins). Nevertheless, a significant amount of work has already been done and the monitoring programme starts to give first results (see Section 6.6).

In winter 2004, ISGRI and JEM-X light-curves and hardness ratios will be put on the web for all the sources belonging to our sample. These web pages will be regularly updated as soon as new observations are performed and the data will be analysed in a similar way to what the *RXTE*/All Sky Monitor team[26] has been doing for the softer energy band (1.2–12 keV). An example of the layout of the pages for the case of X 1822-371 is given in Figs. 6.2 and 6.3. The aim is to give the general information on each source together with the new ISGRI and JEM-X lightcurves. Links to relevant references and to the *RXTE*/ASM data will also be given. These web pages have been developed by members of the collaboration at the Institute for Astronomy and Astrophysics in Tübingen. Populating these pages is a time consuming process and for the LMXRBs the persistent sources will be considered first.

The *INTEGRAL* Bright Source Catalogue

In view of the third *INTEGRAL* announcement of opportunity an *INTEGRAL* bright source catalogue has been made public[27]. This catalogue is a collaborative effort between the ISDC and the Goddard Space Flight Center and is based on publically available data from IBIS and SPI. Sky maps have also been included in the "*INTEGRAL* Public Data Results" which is also public[28]. The results are preliminary and are meant to give only a rough indication of what *INTEGRAL* can do with respect to point sources. Using the infrastructure developed for the LMXRB monitoring program, I provided the IBIS catalogue and data results. These results have

[26] http://xte.mit.edu/ASM_lc.html
[27] http://isdc.unige.ch/index.cgi?Data+sources
[28] http://lheawww.gsfc.nasa.gov/users/beckmann/obslist.html

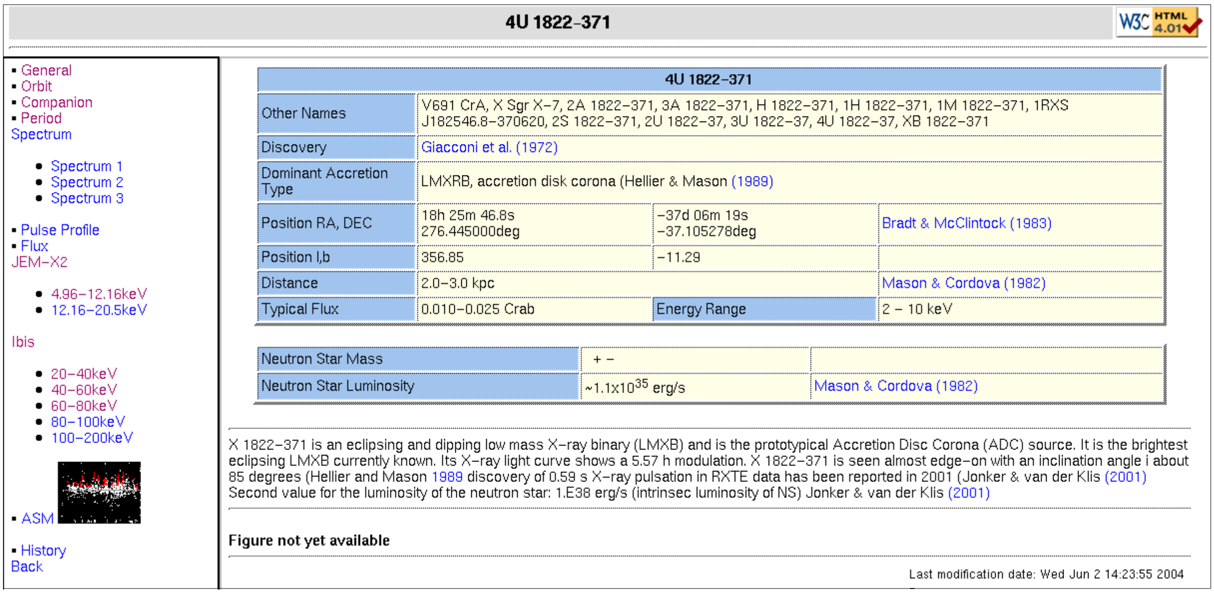

Figure *6.2: Layout of the web pages presenting the monitoring programme results. This is an example for the "General" page with the main information about the system. All the options on the left will be available through links to the references and to other web pages (e.g. RXTE/ASM URL). Fig. 6.3 shows the page that is loaded selecting the IBIS 20-40 keV option on the left.*

been included in the HEASARC archive. In this way, when a scientist uses the main HEASARC Browse[29] to look for results on a given source, also IBIS and SPI data products are extracted.

6.5 Multiwavelength campaigns

Multiwavelength campains are the key to obtain a complete picture of the processes involved in any astronomical event.

Indeed, within the monitoring programme we have widened our attention to energy bands other than the *INTEGRAL* one.

6.5.1 Soft X-rays

While the JEM-X monitors provide simultaneous X-ray data, their lower energy threshold of 4-5 keV limits the ability to perform studies in the soft X-ray energy range in which the soft component of the LMXRB spectra is normally seen ($\sim$ 1 keV). Besides, due to the smaller field of view of JEM-X, sources observed during GPS scans will only be in the field of view of JEM-X for one pointing ($\sim$ 2 ksec), and not for three consecutive pointings as for IBIS. We compensated for these shortcomings by arranging simultaneous *RXTE* observations of the nine brightest LMXRBs in the area covered by the GPS and the GCDE. They are listed in Table 6.2.

The simultaneous observations are being regularly triggered according to the *INTEGRAL* planning and to the *RXTE* availability.

These observations are very important as they provide a wide energy range coverage from about 2 keV up to several 100 keV, making the best use of both missions – the high time resolution

[29]http://heasarc.gsfc.nasa.gov/db-perl/W3Browse/w3browse.pl

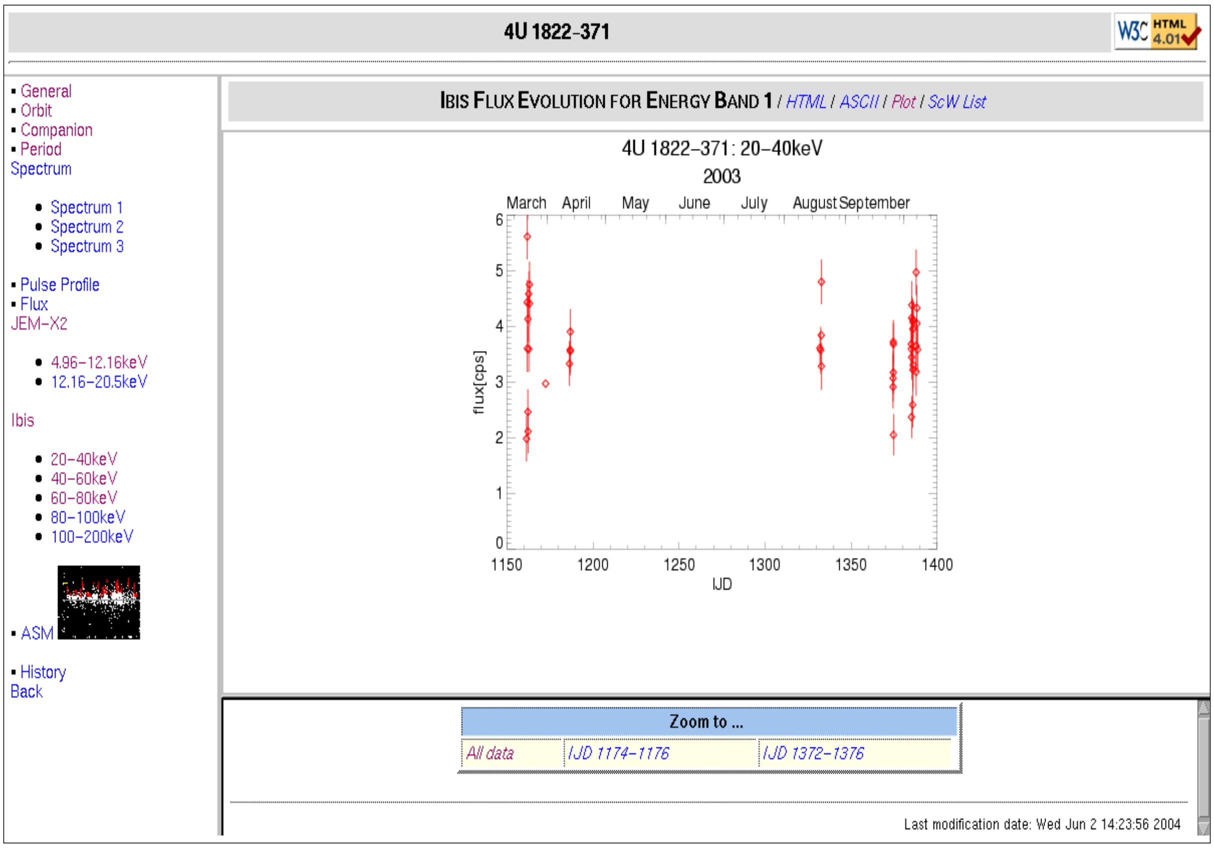

Figure *6.3: Light curve of isgri in the 20-40 keV band. Different zooms as well as time units will be available. It is also possible to download the corresponding ascii file with the relevant information.*

and spectral capabilities of *RXTE* at energies below ~ 50 keV and the hard X/ γ ray coverage of *INTEGRAL*. In fact:

- simultaneous *RXTE*/*INTEGRAL* observations will allow us to have a good coverage of the soft to hard part of the spectra helping to distinguish the currently discussed models for the X-ray spectrum and to obtain insight in the interplay among the concurrent hard and soft part of the spectra. The *RXTE* data are also important for confirming the source position in the CD, while the *INTEGRAL* data will help to determine a very hard color (60–200 keV)/(13–60 keV), constructing a 3 dimensional color map for studying the hard spectrum in greater detail than has been possible before.

- only with *RXTE* will it be possible to measure a detailed power spectrum of the LMXRBs below 20 keV. Such measurements are not possible with JEM-X due to the small area and low exposure time during a GPS pointing. The availability of broad-band X-ray and gamma-ray spectra and the timing information will allow us to study the correlated timing and spectral behaviour of these sources.

- *RXTE* will allow to look for type I bursts in Z sources and in the "bright GX Atolls".

Name	Type	Flux (mCrab) 2-10 keV	*RXTE* time (ksec)
GX340+0	Z	500	36.18
GX349+2	Z	825	25.5
GX9+9	Atoll	300	35.7
GX9+1	Atoll	700	16.92
GX5-1	Z	1250	16.44
GX17+2	Z	700	6.36
GX3+1	Atoll	400	31.68
Cyg X-2	Z	450	0
Sco X-1	Z	14000	29.46

Table 6.2: Neutron star LMXRBs persistently brighter than 100 mCrab in the 2-10 keV band (Liu et al., 2001) for which we have been awarded *RXTE* time in cycle 8 and 9 (Proposal ID 80020, 90022, PI: A. Paizis). For each source we have been granted a series of 6 simultaneous *RXTE* - *INTEGRAL* observations of 6 ksec each for a total of 36 ksec per source. The current status of the *RXTE* observations is also given.

6.5.2 Radio

A striking result reveals itself when we look at the radio emission from persistent X-ray binaries: there seems to be a common observed radio luminosity from the black hole candidate binaries in the low/hard state [30] and the (neutron star) Z sources on the horizontal branch (where hard tails are in general stronger). Unless coincidental, these results imply a physical mechanism for jet formation which is at work with either a black hole event horizon or a neutron star surface.

On the other side, Atolls and X-ray pulsar systems as a class are consistently dimmer at radio wavelengths than BHCs and Z sources by a factor of $\gtrsim$5 and $\gtrsim$10, respectively (Fender & Hendry 2000).

Fig. 6.4 sketches the presence of the radio emission in LMXRBs containing a neutron star.

It is likely that the accretion rate is the reason for these differences. This is supported by the radio detections of the Atoll source GX 13+1 which is believed to be accreting at a higher rate than the other Atolls. Occasional detections of Atoll sources in the radio band could be associated with transient periods of high accretion rates comparable to those continuously occurring in Z sources.

Simultaneous observations in the radio - X-ray domain are very valuable to investigate the correlations among the emission in these energy bands for black hole, Atoll and Z binaries of our sample. Within the monitoring programme, we do have long-standing collaborations with the operators of the Ryle Telescope[31], the Radio Astronomical Telescope Academy Nauk[32] (RATAN, Russia), the Molonglo Observatory Synthesis Telescope[33] (MOST, Australia) and the Very Large Array[34] (VLA, USA).

In October 2003, we performed quasi-simultaneous X-ray/radio observations of the bright Atoll source GX 9+9 using *INTEGRAL*, *RXTE*, RATAN, MOST and the VLA (unpublished

[30] The low hard state for black hole binaries is in general a state in which the bulk of the emission is at about 100 keV.

[31] http://www.mrao.cam.ac.uk/telescopes/ryle/

[32] http://brown.nord.nw.ru/

[33] http://www.physics.usyd.edu.au/astrop/most/

[34] http://www.vla.nrao.edu/

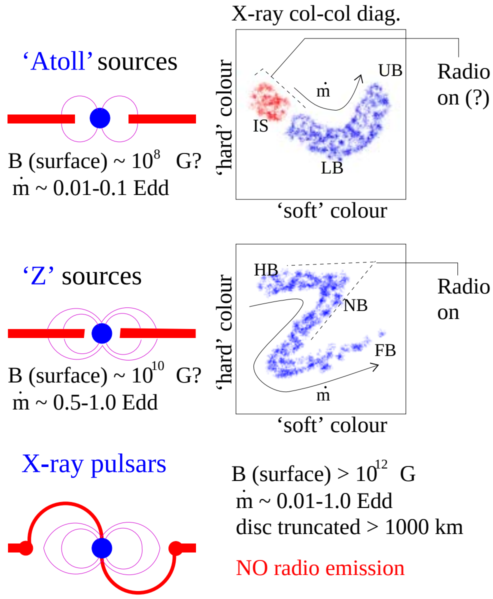

Figure *6.4: A qualititative sketch of the relation of radio emission to accretion in the three 'types' of neutron star XRBs. In the low magnetic field Atoll sources there is marginal evidence that such sources are 'radio on' when in the island state in the X-ray CD. The Z sources, that are believed to be accreting at a much higher rate, are 'radio on' when on the horizontal branch and maybe also, at a lower level, in the normal branch in the CD. Finally, in the high-magnetic field X-ray pulsars no radio synchrotron emission has ever been detected (figure taken from Fender 2001).*

results). In the radio domain very low upper limits were found, comparable to what reported in Fender & Hendry 2000.

6.5.3 Optical

In the case of LMXRBs, the optical emission is commonly thought to originate mainly in reprocessed X-ray emission from the disc as the companion is too faint in the optical to give a definite signature. The disc extends up to 10°-15° viewed from the compact object i.e. intercepts a fourth of the $\sim 10^{37}$ erg s^{-1}radiated by the X-ray source. Thus, much of the disc is intensely heated and it outshines the typical K/M dwarf secondary which has an intrinsic luminosity of $\lesssim 10^{33}$ erg s^{-1}. All the major X-ray events (bursts, outbursts, pulses etc) are expected in the X-ray domain first and then in the optical after a certain time lag. This actually occurs and the measured time lag gives the size of the reprocessing disc region (van Paradijs & McClintock, 1995).

The nature of the optical emission is strongly depending on the disc activity and leads to a natural division among the sources of our sample:

- Transient sources tend to be in quiescence for most of the time. During the quiescent period, X-ray and thus optical emission is very low. Unless the source is in outburst, little or no information can be deduced about the disc. Normally this state is used to compute the mass function of the system to infer the mass and thus the nature of the compact object. This kind of study, although important, does not gain from simultaneous X-ray observations.

- Persistent sources are always observable in the X-rays so there are better chances to see them in the optical although many factors can come into play like apparent size of the reprocessing disc, orientation of the binary, position of the binary with respect to the highly optical absorbed Galactic center etc.

For the simultaneous optical-X-ray observations of the persistent objects for which optical emission has been detected, two kinds of approaches are feasible:

1. Long term observations: a sample of persistent sources can be regularly monitored, building up a long term optical lightcurve to be compared with the X-ray one. In this case the actual simultaneity is not so important although the frequency of the optical observations should be such that we can characterise the source variability. Our collaboration with the Geneva Observatory enables us to use the Geneva photometer at La Palma[35] and the photometer or spectrometer "Coralie" at La Silla[36]. A first feasibility study (Carrier, 2002) showed that for the photometer installed at La Silla, relatively short exposure times, about 500s, are sufficient to achieve a good signal to noise ratio for sources brighter than V=19mag. A regular coverage of the sources on the southern hemisphere with known visual emission (about 15 sources) would give a long term study of the optical properties of these sources to be compared with the X-ray ones.

2. Short term observations: for a selected sample of persistent sources, simultaneous X-ray optical observations can be performed. These observations are aimed to study the correlation of fast X-ray optical variations in order to see if the optical fast variations follow the X-ray ones (like in GRO J1655-40, Hynes et al., 2000) confirming the reprocessing theory or if they are independent (like in GX 339-4, Motch et al, 1981) leading to the interpretation of an original optical source which is then reprocessed in the accretion disc to higher energies (see Merloni et al., 2001 where QPOs detected in the *optical* are discussed). Very few such optical X-ray simultaneous observations have been carried out due to the difficulty of having fast optical photometers. New fast timing detectors are being developed (OPTIMA-MPE project[37], ULTRACAM-Sheffield/Southhampton project[38] and PhoCA-IASF Milano project[39]), compact instruments that can be mounted at different telescopes. The attempt made to observe the Z source Cyg X-2 with PhoCA at the telescope of Asiago (Italy) simultaneously to *INTEGRAL* and *RXTE* observations has not been succesful so far due to bad weather conditions.

Ground based coordinated observations are difficult to plan. *INTEGRAL* gives currently only a two week planning in advance (which often undergoes last minute changes) while ground based telescopes need months of notification in advance given the very tight schedule. Nevertheless, thinking of the goals we can obtain from these coordinated observations is the first step to actually manage to perform them.

On the other side, *RXTE* planning is extremely flexible and capable of a replanning even with a one week notice. The *RXTE* coordinated observations are indeed regularly happening, especially in the last months during which we have optimised the tools for downloading and going through the *INTEGRAL* planned pointings on a daily basis.

[35] http://www.unige.ch/sciences/astro/fr/Recherches/
[36] http://obswww.unige.ch/La_Silla/home/fr/index_no_frame.html
[37] http://www.mpe.mpg.de/gamma/instruments/optima/www/optima.html.
[38] http://www.shef.ac.uk/ phys/people/vdhillon/ultracam/overview.html.
[39] http://zahir.mi.iasf.cnr.it/web/phoca/default.htm

In the frame of the multiwavelength campains and to keep track of all the executed and planned GPS and GCDE pointings I created a web page [40] including all the relevant information. Coverage maps such as the one in Fig.6.5 are given for all the executed and planned observations.

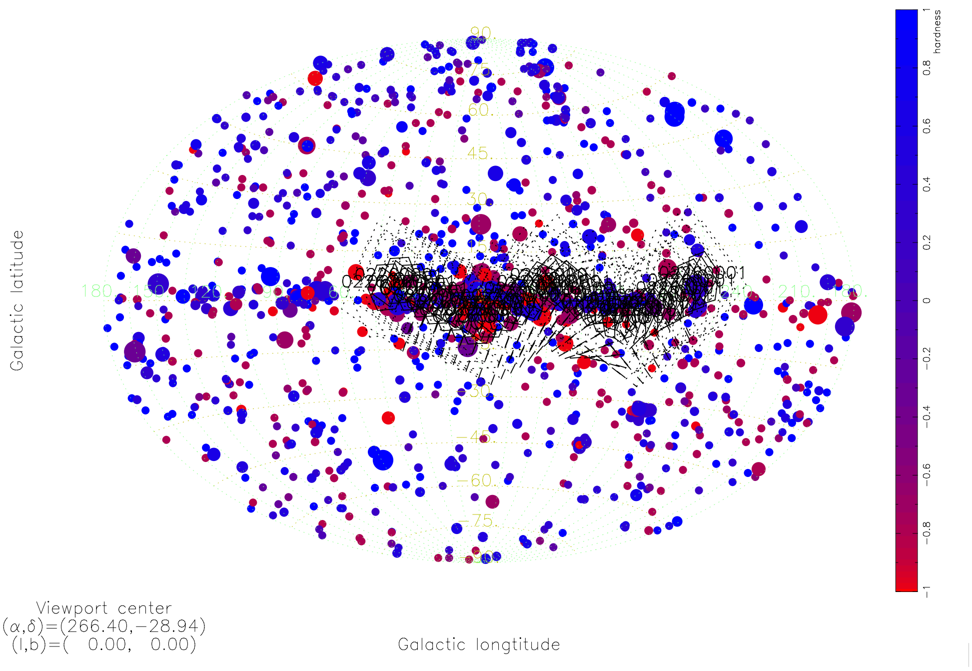

Figure *6.5: Coverage map provided for the currently planned GPS of revolution 226.*

The page is regularly updated and is publicly available in the attempt to ease coordinated observations within our collaboration as well as for external groups.

6.6 First results

We have analysed one year of *INTEGRAL* core programme data with the Off-line Scientific Analysis, OSA 3.0. The first impression from this analysis is that these data constitute a huge data base of information that has to be methodically analysed and studied. Just to give a feeling of the amount of results that can be extracted, we give in Table 6.3 the list of sources of our sample that have been detected at least in five pointings at a significance level of at least 5σ in the 20-40 keV ISGRI energy band.

Each pointing (2000s) can contain interesting variability patterns. All these data have to be carefully checked and fluxes in physical units (or upper limits) have to be given per source and energy band. Automatising the analysis is the only way to be able to analyse such a large data set. Once the results are available, each source has to be closely looked at: in Table 6.3, it is unlikely that all the detections at 5σ in the 200-400 keV band are real. The analysis has been performed in a "forcing mode": the software was asked to extract the flux at the catalogue position. If the source happens to be on the rim of the detector where normally there is a

[40] http://isdc.unige.ch/∼paizis/CP.html

Name	Det1	Det2	Det3	Det4	Det5	Det6	Det7
1516-569	32	2	1	1	1	0	3
1724-356	6	2	3	4	4	2	3
1728-169 (GX 9+9)	28	3	5	3	3	4	3
1730-220	5	7	2	4	5	1	2
1732-273	9	10	8	2	3	2	1
1734-292	19	5	3	2	3	4	5
1736-297	7	4	6	6	5	3	3
1737-282	13	2	5	5	5	3	4
1739-278	5	4	2	6	3	4	1
1739-304	6	4	4	4	1	5	1
1742-326	5	4	5	3	8	1	6
1742.5-2845	11	3	2	3	3	5	3
1742.7-2902	5	1	0	4	4	2	3
1743.1-2843	17	3	2	1	5	0	4
1744-299	18	7	1	3	6	4	2
1744-361	7	0	2	7	4	2	3
1746-331	6	0	4	2	2	4	4
1746.7-3224	21	10	9	3	10	6	1
1747-313	11	6	2	9	10	4	3
1822-371	240	2	3	5	1	1	1
1543-475	9	2	3	2	0	5	1
1630-472	289	240	136	64	33	1	0
Cyg X-2	10	0	0	0	0	0	0
1730-312	7	9	8	5	3	6	3
1734-292	6	2	0	4	6	5	2
GRS 1758-258	388	334	146	71	36	6	2
GRS 1915+105	56	37	14	2	1	1	1
GX 17+2	601	5	2	4	4	3	6
GX 3+1	78	4	2	0	4	5	4
GX 5-1	484	4	5	6	5	2	4
GX 9+1	94	3	6	6	4	0	3
1705-250	6	6	2	2	1	1	2
1745-203	17	1	2	1	5	2	2
1755-338	6	3	5	4	5	2	2
J1748-288	10	8	2	6	3	3	2
J1755-324	6	4	5	6	6	5	5
Sco X-1	132	13	1	0	2	1	2
Crab	20	20	20	20	19	17	4

Table 6.3: Number of pointings per energy band in which each source has been detected by ISGRI with a detection significance higher than 5σ (Det$x$ with x=1,...,7 correspond to 20-40, 40-60, 60-80, 80-100, 100-150, 150-200, 200-400 keV). These numbers do not give information about the relative brightness of the source: the Crab is not dimmer than GX 9+1 but it was covered less often due to its position relative to the dithering pattern. What we intend to show is the amount of data available (each pointing is about 2000s long). The presence of detections in more than one energy band of course denotes a harder source. For comparison, the Crab is included in the last line of the table.

noise pattern, the flux and corresponding signal to noise will be extracted and attributed to the source. This way of extracting the data was chosen for the first analysis of all the available core programme data in order to be able to extract upper limits for each source per pointing. The drawback of the noisy false detections can be minimised by selecting only the pointings in which the source was within a certain off-axis angle from the pointing direction.

The interpretation of the data from the LMXRBs of the sample can be done at many levels. The highest level is to have a fast glance at all the sources via their lightcurves and hardness ratios. These types of results are being put on the web and give the hard X-ray flux history. With more data being added it will be easier to have a glance at the usual behaviour of the source, spotting unusual fluxes i.e. states that need to be further investigated possibly with coordinated multiwavelength observations.

The infrastructure for this step is already existing. We have built tools to regularly analyse the data, extract the results and display them in an efficient way (an example of the final output for X 1822-371 has been shown in Figs. 6.2 and 6.3).

A second level of study will be to seek a synthetic view of all the data. This means selecting some common parameters to characterise the spectra and the lightcurves for each source and then to see how these parameters depend on the source classification. Properties already seen in the soft X-rays determining a class might be confirmed but different classifications might reveal themselves. Examples for such parameters are the long term variability (is there a systematic difference in the hard X-ray variability among the different classes?), the average spectral hardness (would we define black holes, Atolls and Z sources on the basis of the hard X-ray spectra?), and *INTEGRAL* defined colour-colour diagrams (how do these sources move in a hard CD on a long term?). Figure 6.6 shows the combined CD for different types of sources based on a large *RXTE* archive. This long term study shows that portions of the CD have *never* been covered by neutron star systems, possibly due to their boundary layer emission. This kind of comparison requires large sets of data to have better chances to catch the sources in all their possible states. A similar work will be done with the *INTEGRAL* data base, in newly defined, harder energy bands to seek e.g. for the influence of the boundary layer (or event horizon) in the less studied hard X-ray domain.

Results of this kind of study will be collected mainly on the long run. Large amounts of data spanning over a long period have to be gathered. As it has already been shown by Muno et al. (2002) and Gierliński and Done (2002) only after collecting several years of *RXTE* data could it be possible to see that actually Atoll sources, if observed long enough, do display a Z in the CD.

Currently the raw material has been extracted for all the sources of our sample. A few examples of ISGRI sky maps are given in Figs. 6.7, 6.8, 6.9. Each map is the mosaic of one revolution. These sky maps are part of my contribution to the HEASARC archive web pages.

The mosaic of all the revolutions with GPS and GCDE data of the AO1 (about 5.7 Msec) was already given in Fig. 5.7.

A few examples of the lightcurves that are automatically extracted by the existing infrastructure are given in Figs. 6.10 to 6.16. The time covered is IJD$\sim$[1100-1300] which corresponds to the period between January 2003 and July 2003. The source coverage depends on the position of the source with respect to the GPS and GCDE scans (Cyg X-2 and Sco X-1 are less thoroughly covered).

The scientific analysis package used to extract these lightcurves is OSA 3.0, with which 1Crab gives $\sim$100, $\sim$45 and $\sim$20 counts per second in the 20–40, 40–60, 60–80 keV bands respectively.

In the lightcurves each bin corresponds to one pointing (about 2000 sec). The different size

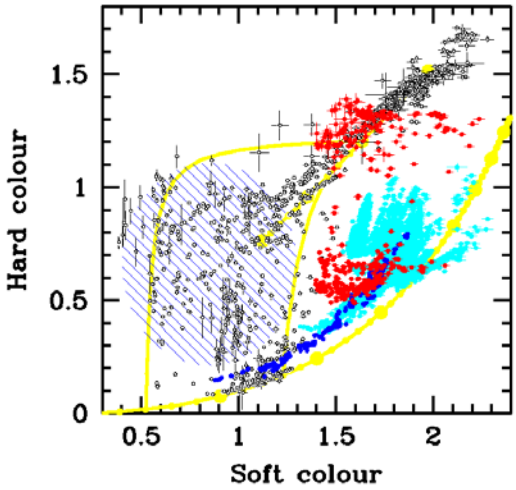

Figure *6.6: Combined colour-colour diagrams for differnt source types. Hard colour is the ratio of fluxes in 9.7–16 and 6.4–9.7 keV bands and soft colour is the ratio of 4–6.4 and 3–4 keV. Open circles represent black hole candidates, red, cyan and blue filled circles neutron star systems i.e. atolls, Z sources and the peculiar Cir X-1, respectively. The hatched region is* inaccessible *to neutron stars due to their boundary layer emission. Spectra with colours falling in this region are seen* only *in black hole candidates (taken from Done & Gierliński 2003).*

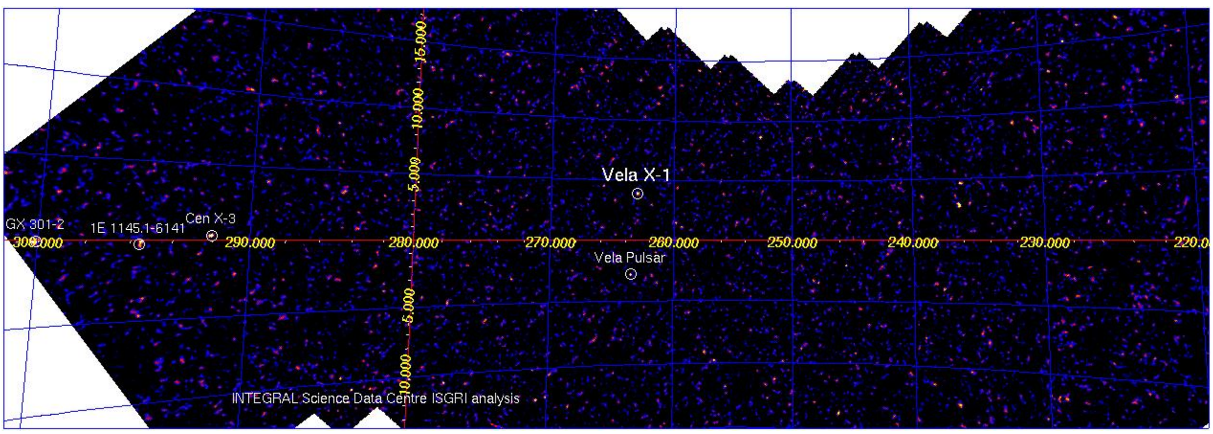

Figure *6.7: ISGRI mosaic of the GPS performed in revolution 66 (about 25 ksec, 20-40 keV).*

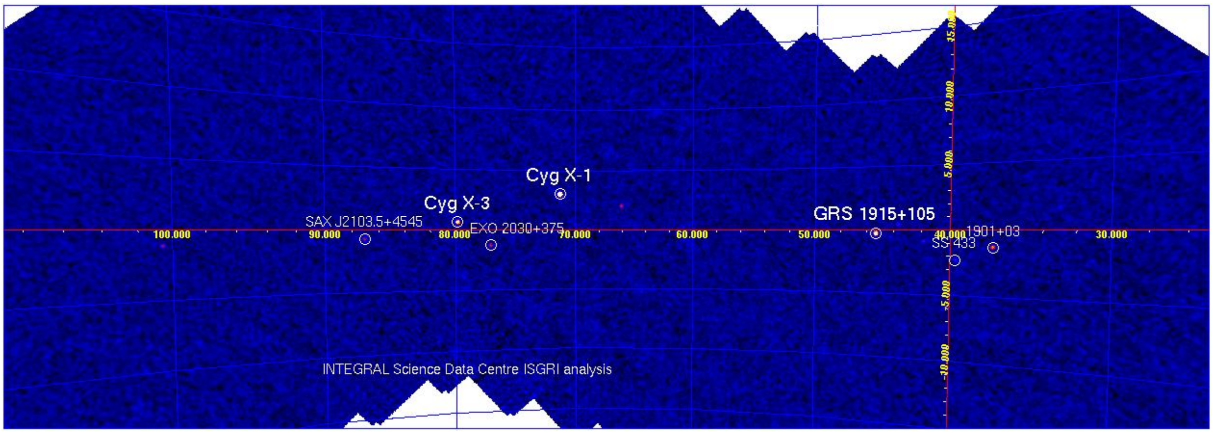

Figure *6.8: ISGRI mosaic of the GPS performed in revolution 67 (about 20 ksec, 20-40 keV).*

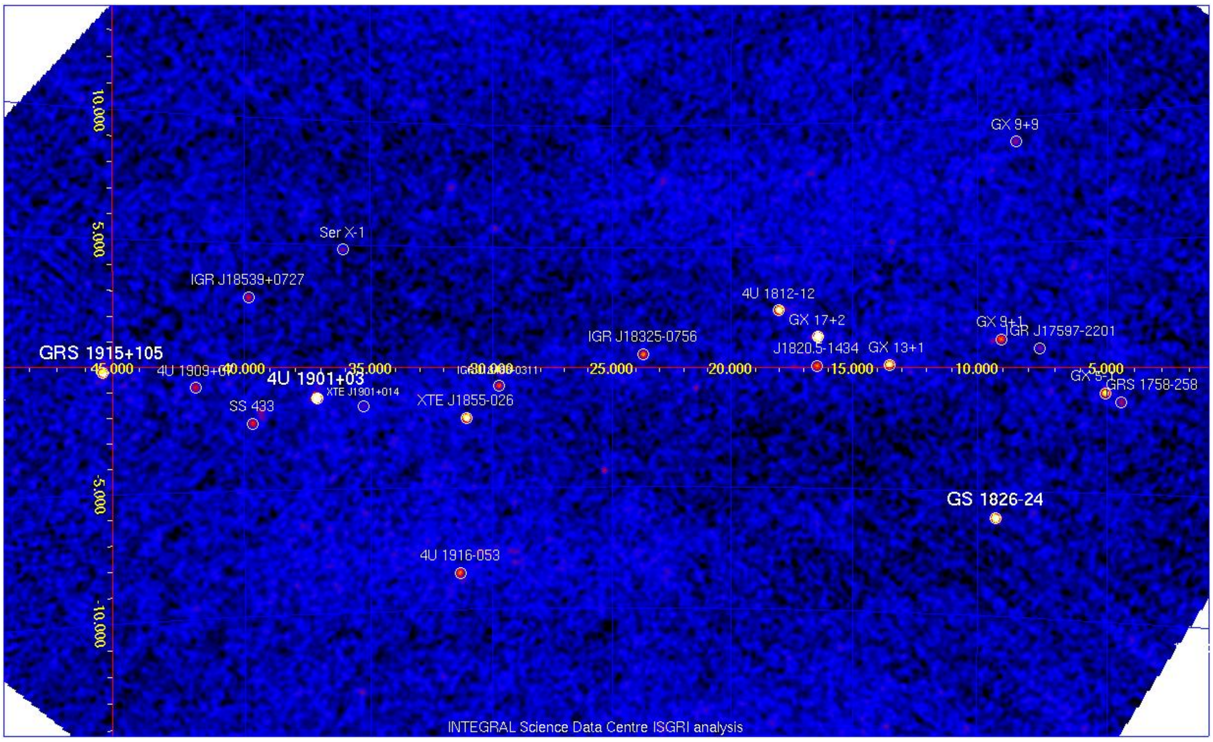

Figure *6.9: ISGRI mosaic of the GCDE performed in revolution 65 (about 200 ksec, 20-40 keV).*

of the error bars within one source is also related to the position of the source with respect to the ISGRI FOV: a source in the FCFOV is detected with a better signal to noise than in the PCFOV (see Section 4.2.2).

The tools available to extract the data allow a certain degree of interaction: it is possible to choose the source to be displayed, the type of diagram (lightcurve, HID, CD etc), the number of energy bands, the axis ranges and the instrument. Other correlations can be also studied on the fly such as the countrate or detection significance as a function of the off-axis angle. In this way it is possible to browse our archive in an efficient and quick way.

We have started a more detailed study on the persistently bright sources for which we had sufficient data. The results are described in the two papers included in this chapter. The first one is the paper prepared for the A&A *INTEGRAL* special issue (Paizis et al., 2003) while the second is the contribution to the 5^{th} *INTEGRAL* Workshop held in Munich (Paizis et al., 2004b). At the time of writing of the first one, many parts of the software had still to be validated and the results obtained to be cross-checked. The instrument calibrations were in a very raw state and this is reflected in the paper where mainly the potential of the monitoring programme is shown. Things evolved until the second paper, for which we had a better knowledge of the instruments and software issues. We went further in the study, starting to look into the variations of the sources as a class, into the average spectra and into the behaviour of the sources in the traditional energy bands.

The third level of study is the most detailed one and consists of taking one source at a time and going through all the available data, in a systematic study of its temporal and spectral properties. In the next chapter such a study for GX 5-1 is given (Paizis et al., 2004a).

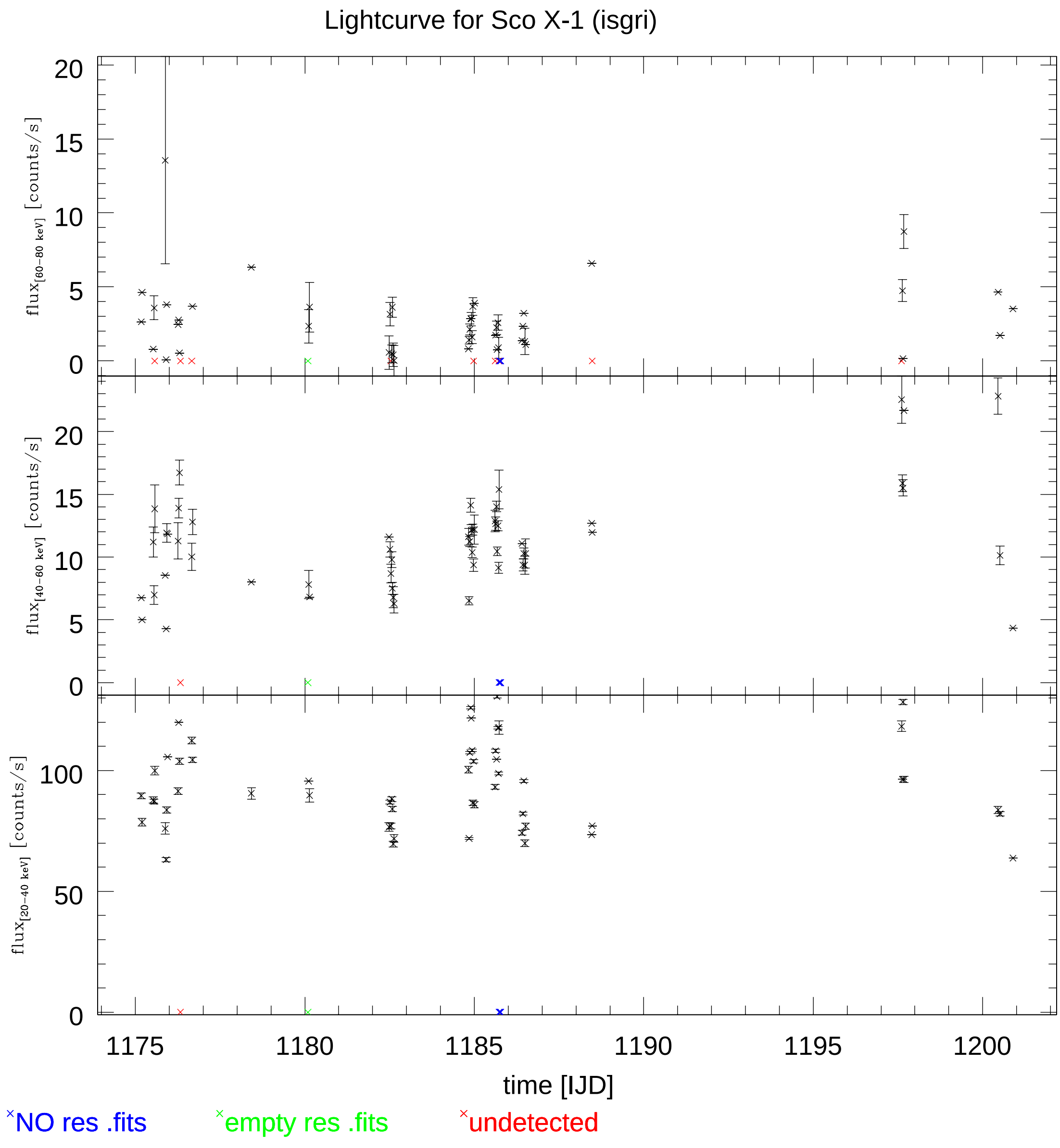

Figure *6.10: ISGRI lightcurves of Sco X-1 in the 20–40, 40–60, 60–80 keV bands. The error bars are at 1σ.*

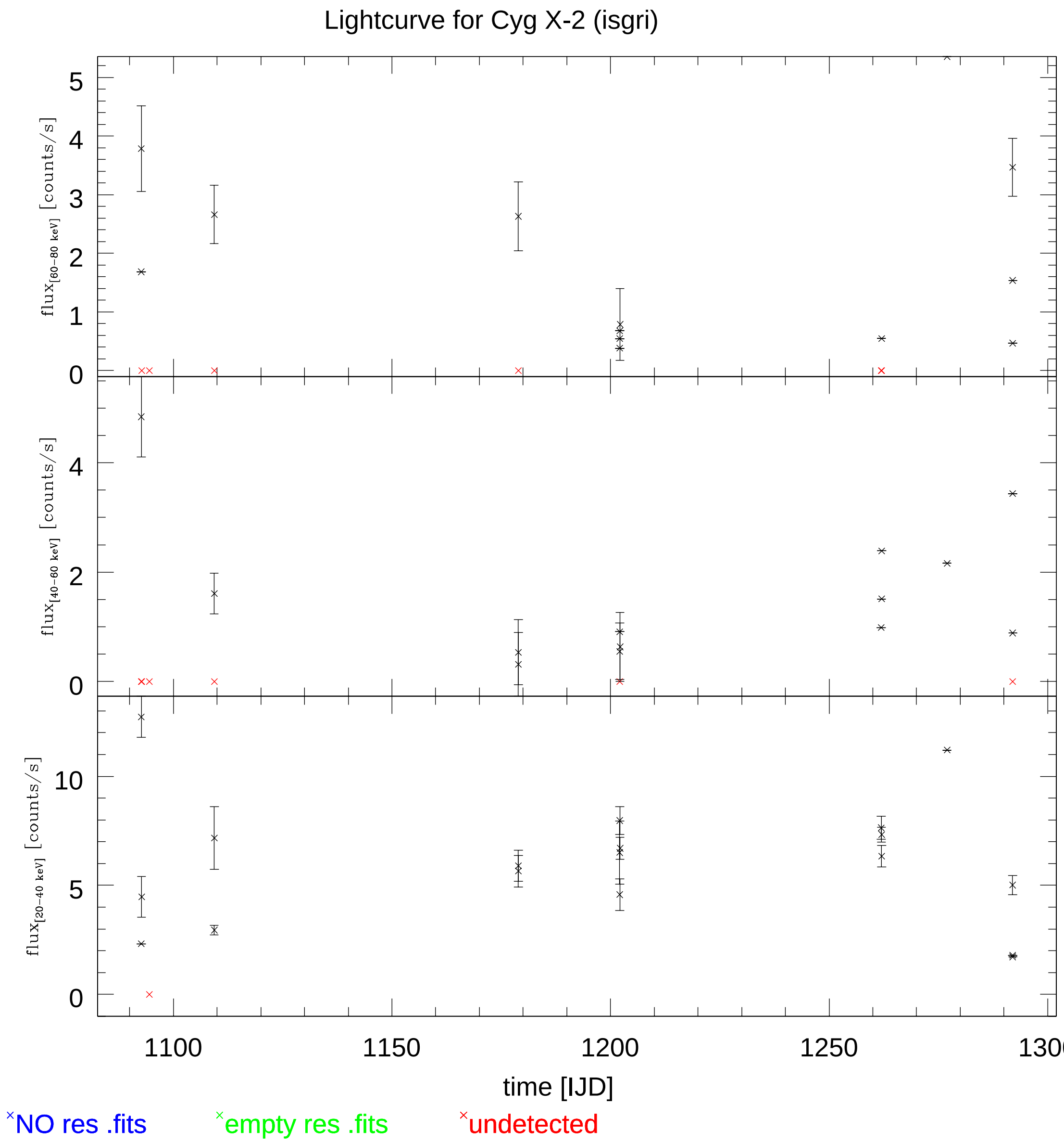

Figure *6.11: ISGRI lightcurves of Cyg X-2 in the 20–40, 40–60, 60–80 keV bands. The error bars are at 1σ.*

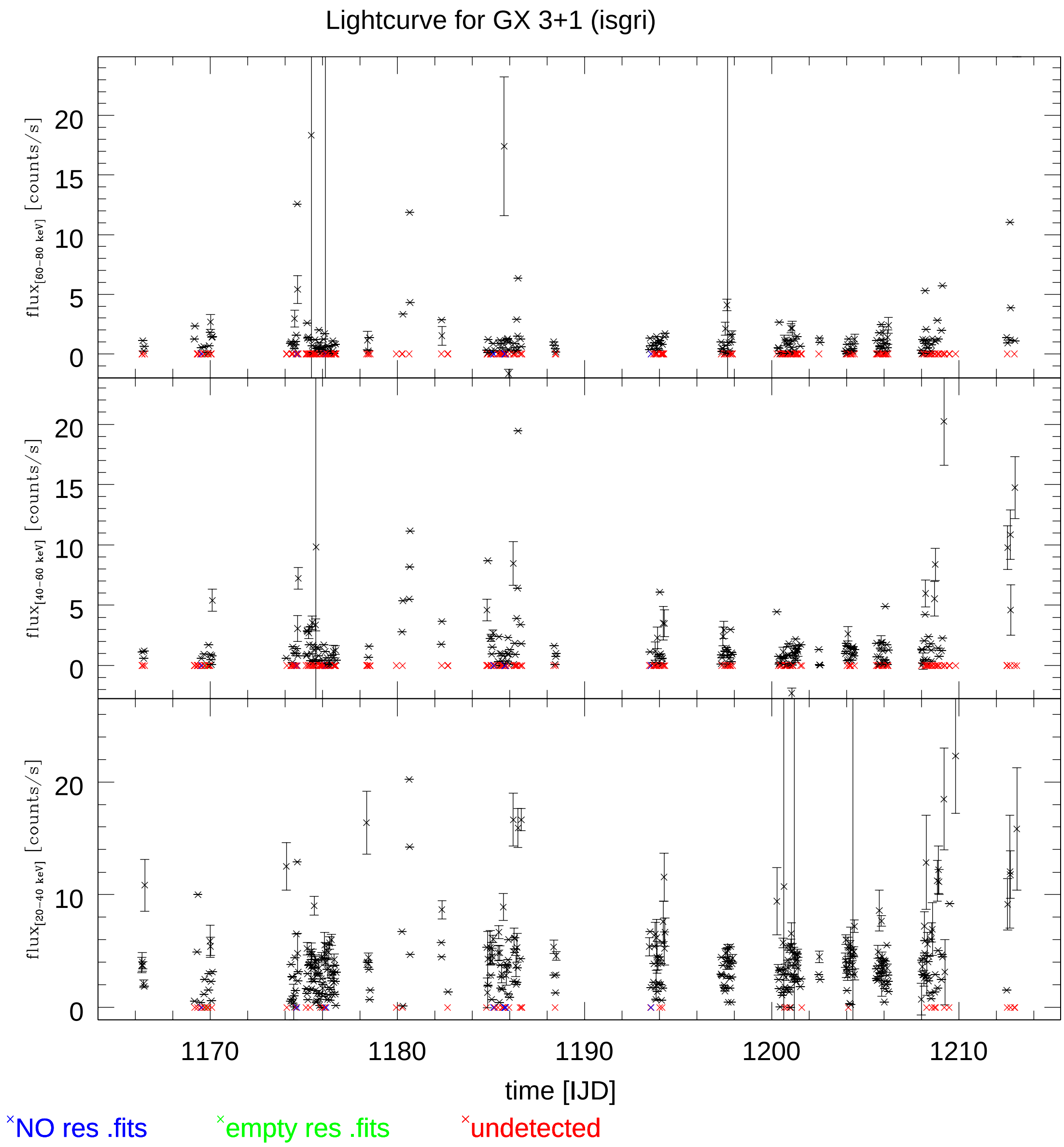

Figure *6.12: ISGRI lightcurves of GX 3+1 in the 20–40, 40–60, 60–80 keV bands. The error bars are at 1σ.*

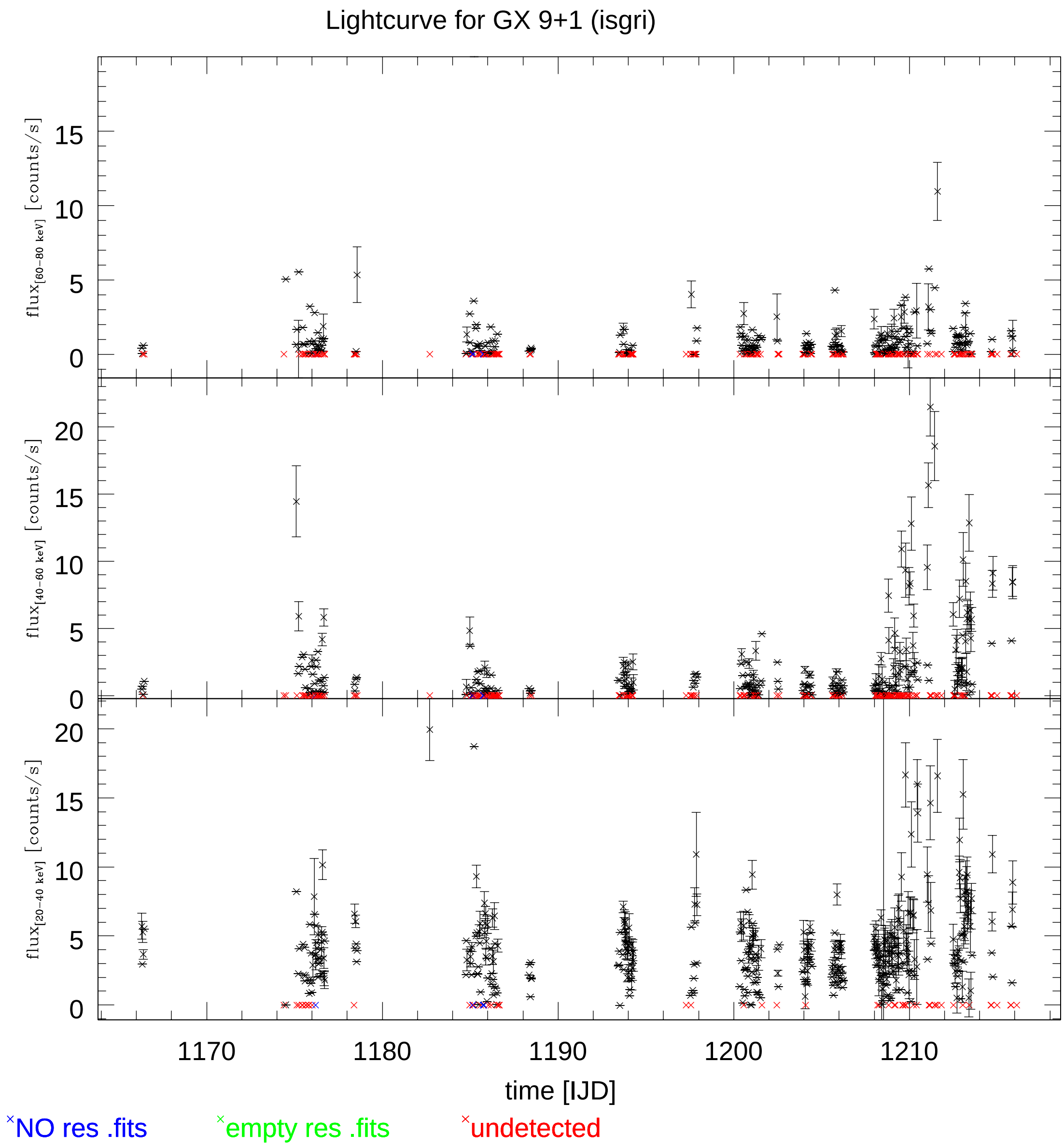

Figure *6.13: ISGRI lightcurves of GX 9+1 in the 20–40, 40–60, 60–80 keV bands. The error bars are at 1σ.*

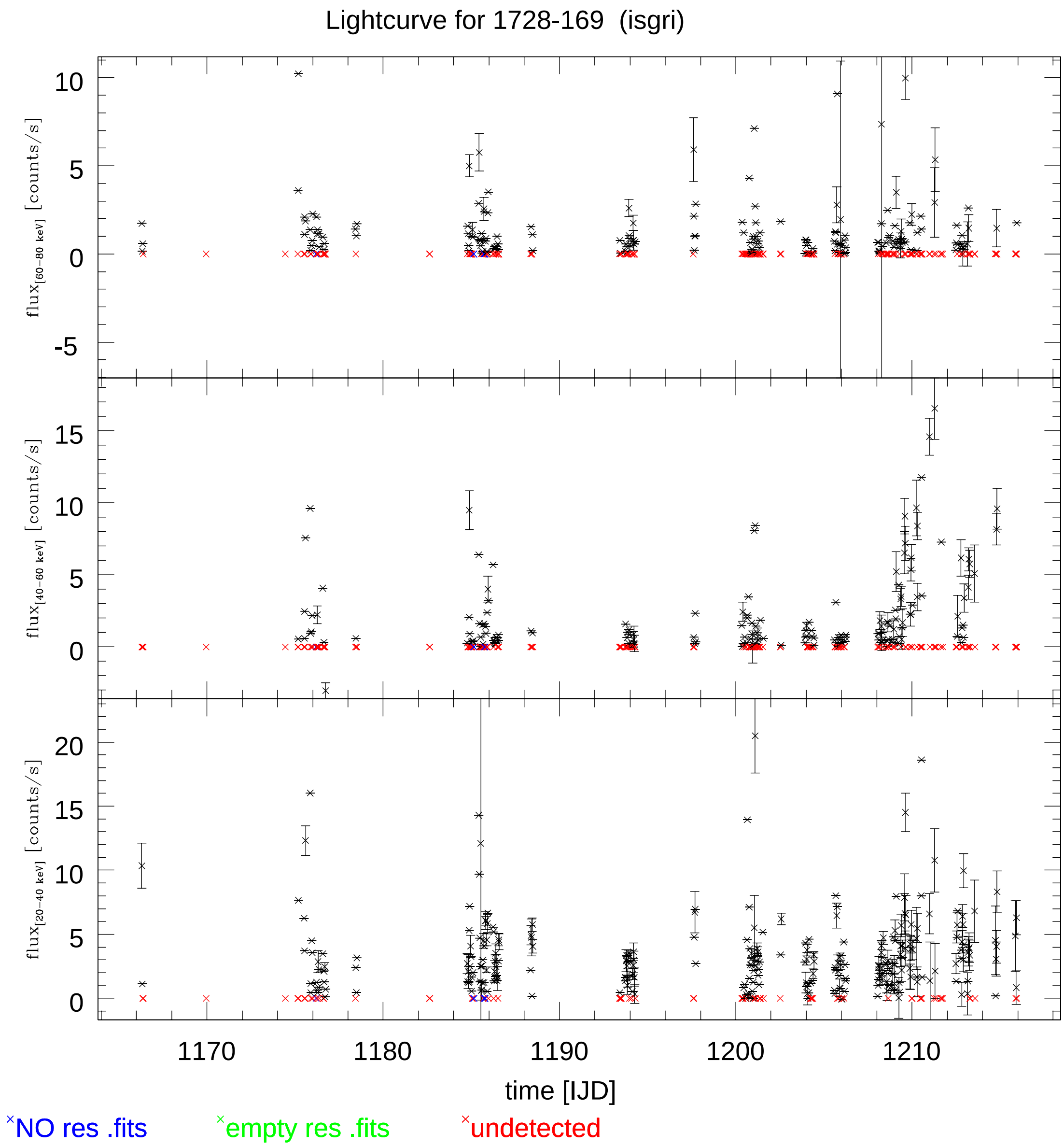

Figure *6.14: ISGRI lightcurves of GX 9+9 in the 20–40, 40–60, 60–80 keV bands. The error bars are at 1σ.*

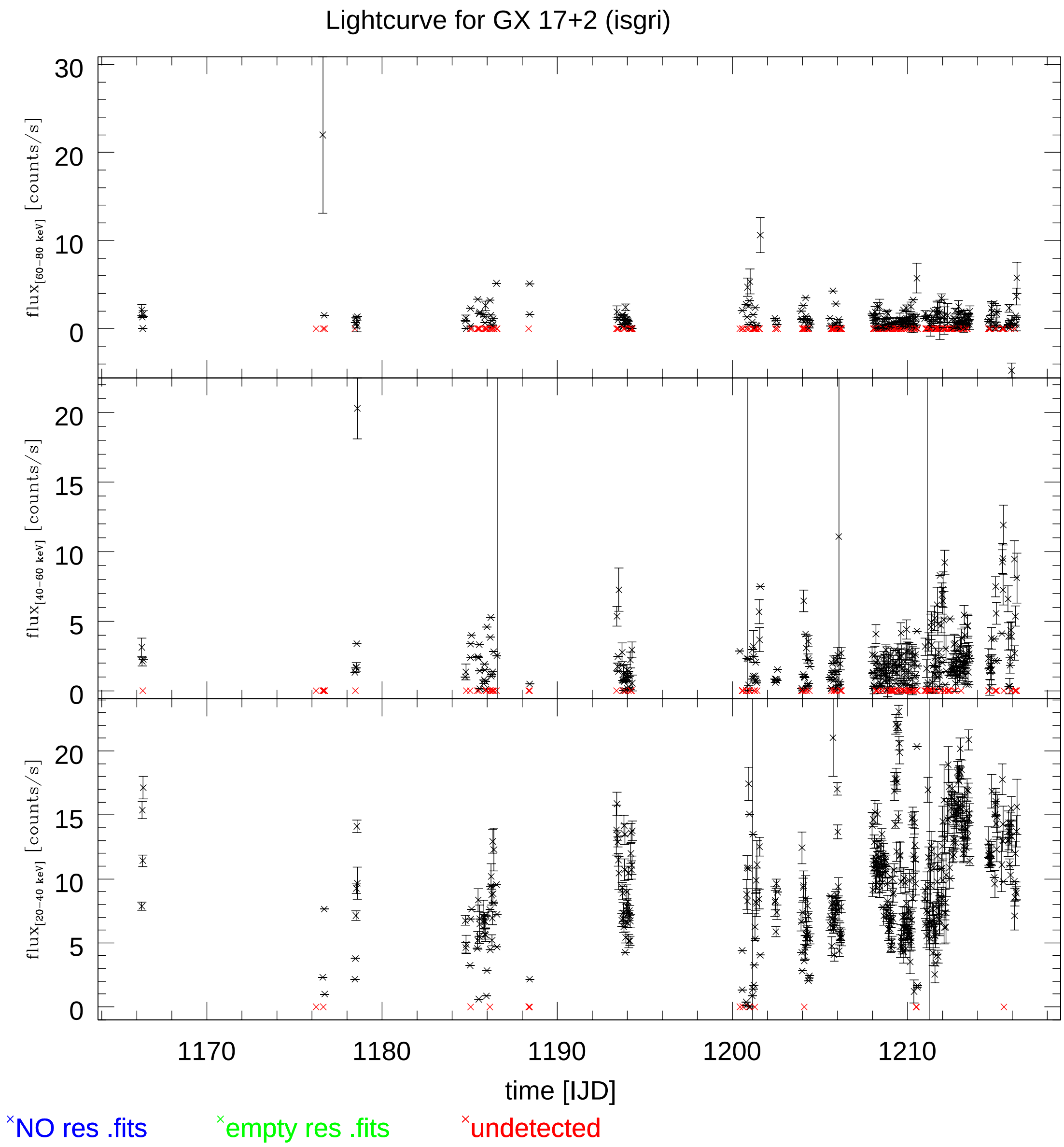

Figure *6.15: ISGRI lightcurves of GX 17+2 in the 20–40, 40–60, 60–80 keV bands. The error bars are at 1σ.*

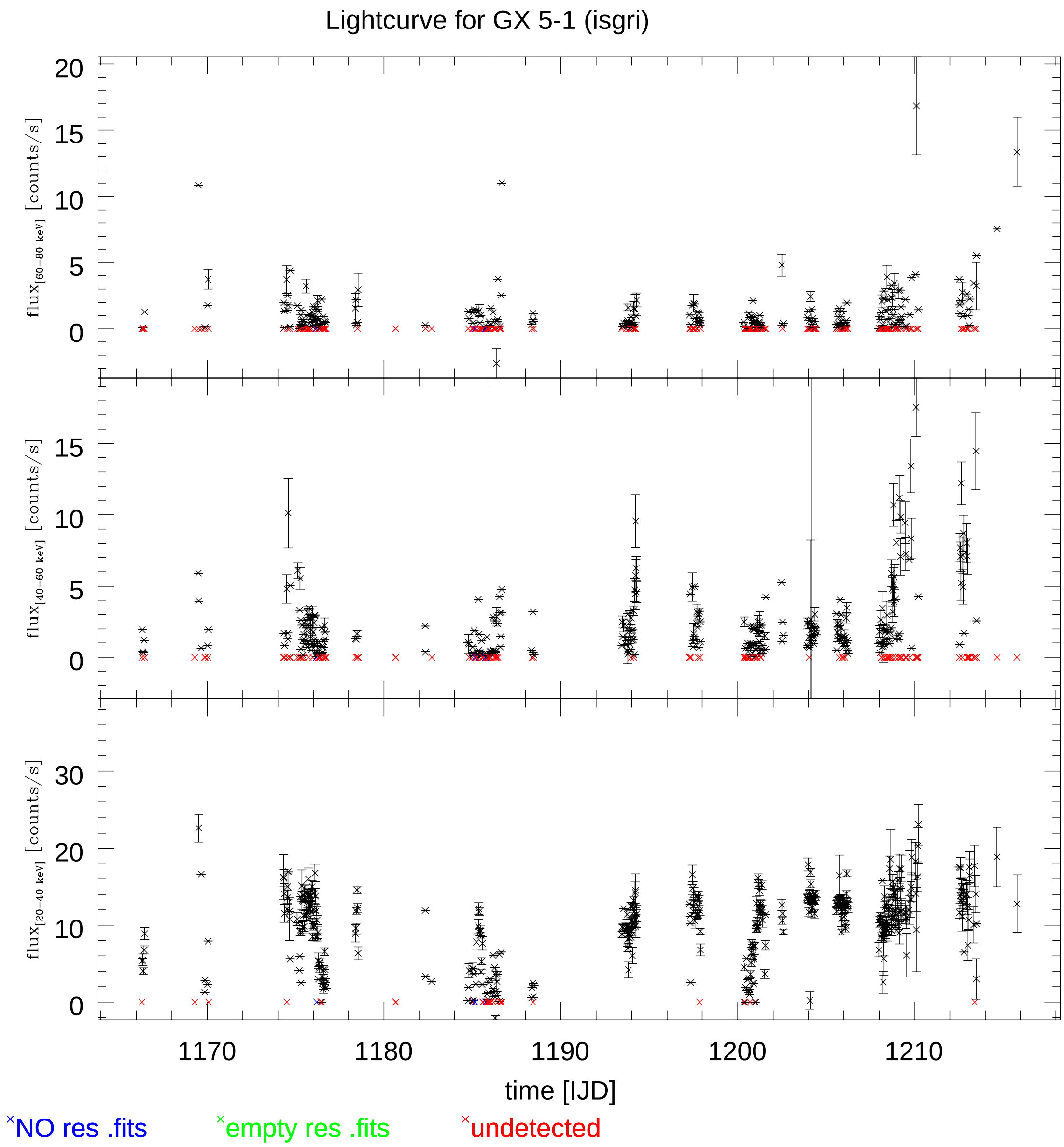

Figure *6.16: ISGRI lightcurves of GX 5-1 in the 20–40, 40–60, 60–80 keV bands based. The error bars are at 1σ.*

A&A 411, L363–L367 (2003)
DOI: 10.1051/0004-6361:20031207

Astronomy & Astrophysics

First *INTEGRAL* observations of eight persistent neutron star low mass X-ray binaries⋆

A. Paizis[1,2], V. Beckmann[1,3], T. J.-L. Courvoisier[1,4], O. Vilhu[5], A. Lutovinov[6], K. Ebisawa[1], D. Hannikainen[5], M. Chernyakova[1], J. A. Zurita Heras[1], J. Rodriguez[7,1], A. A. Zdziarski[8], A. Bazzano[9], E. Kuulkers[10], T. Oosterbroek[10], F. Frontera[11], A. Gimenez[12], P. Goldoni[13], A. Santangelo[14], and G. G. C. Palumbo[15]

1 *INTEGRAL* Science Data Centre, Chemin d'Écogia 16, 1290 Versoix, Switzerland
2 CNR-IASF, Sezione di Milano, via Bassini 15, 20133 Milano, Italy
3 Institut für Astronomie und Astrophysik, Universität Tübingen, Sand 1, 72076 Tübingen, Germany
4 Observatoire de Genève, Chemin des Maillettes 51, 1290 Sauverny, Switzerland
5 Observatory PO Box 14, Tahtitorninmaki, 00014 University of Helsinki, Finland
6 Space Research Institute (IKI), High Energy Department, Ul. Profsojuznaya 84/32,117810 Moscow, Russia
7 CNRS, FRE 2591, CE Saclay DSM/DAPNIA/SAp, 91191 Gif sur Yvette Cedex, France
8 N. Copernicus Astronomical Ctr., Bartycka 18, 00716 Warsaw, Poland
9 CNR-IASF, Sezione di Roma, via del Fosso del Cavaliere 100, 00133 Roma, Italy
10 Research and Scientific Support Department of ESA, ESTEC, PO Box 299, 2200 AG Noordwijk, The Netherlands
11 Dipartimento di Fisica, Università di Ferrara, via Paradiso 12, 44100 Ferrara, Italy
12 Instituto Nacional de Tecnica Aerospacial, Carretera de Ajalvir 4, 28850 Torrejon de Ardoz, Madrid, Spain
13 CEA Saclay, DSM/DAPNIA/SAp, 91191 Gif sur Yvette, France
14 CNR-IASF, Sezione di Palermo, via Ugo La Malfa 153, 90146 Palermo, Italy
15 Università di Bologna, via Ranzani 1, 40127 Bologna, Italy

Received 15 July 2003 / Accepted 1 August 2003

Abstract. Early results from the INTEGRAL Core Program, for a sample of eight persistently bright neutron star low mass X-ray binaries in the energy range from 5 keV to 200 keV, are presented. It is shown that INTEGRAL efficiently detects sources and that spectra may be obtained up to several hundreds of keV by combining data from three of the four INTEGRAL instruments: JEM-X, IBIS and SPI. For the source GX 17+2 it is shown that the spectrum extends well above 100 keV with a flattening above 30 keV. This might suggest a non-thermal comptonisation emission, but uncertainties in the current data reduction and background determination do not allow firm conclusions to be drawn yet.

Key words. stars: neutron – binaries: close – X-rays: binaries – *INTEGRAL* sources

1. Introduction

Since its launch in October 2002, the International Gamma-Ray Astrophysics Laboratory, *INTEGRAL*, has been providing a large amount of interesting data. The combination of the two wide field of view (FoV) instruments, the imager IBIS (15 keV–10 MeV, $29^\circ \times 29^\circ$ partially coded FoV, Ubertini et al. 2003) and the spectrometer SPI (20 keV–8 MeV, $35^\circ \times 35^\circ$ partially coded hexagonal FoV, Vedrenne et al. 2003) coaligned with the JEM–X (Lund et al. 2003) and OMC (Mas-Hesse et al. 2003) monitors, allows large areas of the sky to be observed and monitored in one pointing in a wide frequency range from the optical to the γ-ray domain. Such a capability is fully exploited during the *INTEGRAL* Core Program (a series of successive scans of the Galactic Plane (GPS; Winkler et al. 2003) and Galactic Centre (GCDE)) which is regularly producing large amounts of data, in particular on persistently bright sources.

The aim of this paper is to report preliminary results from early measurements on eight persistent bright Low Mass X-ray binaries (LMXRB) hosting a neutron star. The sample has been selected from a larger set observed during the Core Program Observation scans on the Galactic Plane executed so far. The sources are listed in Table 1. Given the type of sources involved (about hundred of mCrabs in the 2–10 keV band, Liu et al. 2001) and the pointing exposures of about 2000 s,

Send offprint requests to: A. Paizis,
e-mail: `Ada.Paizis@obs.unige.ch`

⋆ Based on observations with *INTEGRAL*, an ESA project with instruments and science data centre funded by ESA member states (especially the PI countries: Denmark, France, Germany, Italy, Spain, and Switzerland), Czech Republic and Poland, and with the participation of Russia and the USA.

for single pointing spectral extraction, JEM–X for soft photons (5–20 keV) and the low energy IBIS detector, ISGRI (Lebrun et al. 2003) for harder photons (20–200 keV) were chosen. PICsIT, the hard photon IBIS detector (Di Cocco et al. 2003), has its peak sensitivity above 200 keV while the LMXRBs are considered to display a rather steep spectrum and consequently have fluxes below PICsIT detectability. The spectrometer SPI has been used to extract the hard energy spectra (20–200 keV) averaged on longer time scales.

The combination of JEM-X, IBIS and SPI data provides a complete soft to hard energy coverage, allowing a regular monitoring of source behaviour. Special attention is given to the hard emission (>50 keV) monitoring for which *INTEGRAL* will give unprecedented continuous coverage.

Section 2 of this paper gives an overview of the state of the art studies on LMXRBs containing a weakly magnetized neutron star and a short description of the *INTEGRAL* Core Program selected sample. Section 3 contains details of the relevant *INTEGRAL* observations and data reduction methods used. Preliminary results are summarised in the last section.

2. Bright LMXRBs in the *INTEGRAL* Core Program

2.1. LMXRBs with weakly magnetised neutron stars

LMXRBs hosting a weakly magnetised neutron star can be broadly classified into two classes (van der Klis 1995): high luminosity/Z sources and Atoll sources covering a much wider range in luminosity. Z sources describe an approximate "Z"-shape (horizontal, normal, and flaring branch) in the colour–colour (CC) and X-ray hardness intensity diagrams while Atoll sources are characterised by an upwardly curved branch. Two recent studies (Muno et al. 2002; Gierliński & Done 2002) suggest that the clear Z/Atoll distinction on the CC diagram is an artifact due to incomplete sampling: Atoll sources, if observed long enough, *do* exhibit a Z shape in the CC as well. Many differences, however, remain: Atoll sources have weaker magnetic fields (about 10^6 to 10^7 G versus 10^8–10^9 G of Z sources), are generally fainter (0.01–0.3 $L_{\rm Edd}$ versus $\sim L_{\rm Edd}$), can exhibit harder spectra, trace out the Z shape on longer time scales than typical Z-sources and have a different correlated timing behaviour along with the position on the Z. Thus the distinction, at least from a practical point of view, still makes sense.

Recent broad band studies, mainly with *BeppoSAX*, have shown that many Z sources display a variable hard power-law shaped component, dominating their spectra at $\gtrsim$30 keV (Di Salvo & Stella 2002; D'Amico et al. 2001; Di Salvo et al. 2000, and references therein). This power-law has been explained as non-thermal Comptonisation. As previously said, lower luminosity systems (Atolls) can display much harder spectra which can be well described with a simple power-law with photon indices of about 1.5–2.5. Hard X-ray components extending up to a few hundred keV have been seen in about 20 neutron star LMXRBs of the Atoll class. These sources usually display an exponential cut-off between many tens and a few hundred keV. This component is interpreted as unsaturated thermal Comptonisation and is known as the "hard state" of Atoll sources.

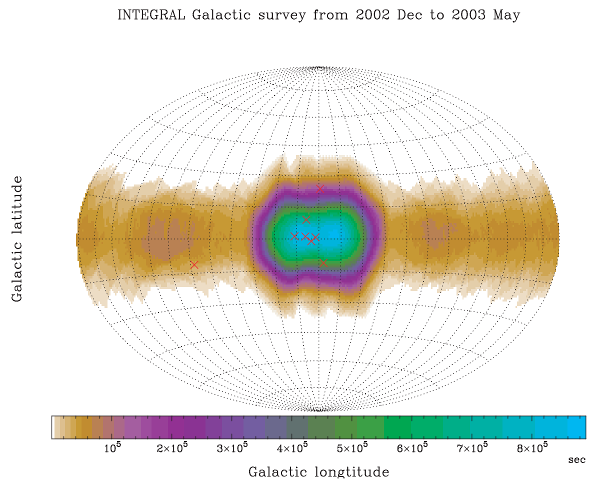

Fig. 1. Exposure map for a total of 6 months of GPS and GCDE data. The spatial distribution of the 8 sources is visible (red crosses).

The long term X-ray variability of those sources has been extensively studied in the 2–12 keV band with the *RXTE* All Sky Monitor, as well as during *RXTE* dedicated pointings till about 40 keV (van der Klis 2000; Swank 2001). On the other side, *BeppoSAX* pointings have shown the presence of the hard tails mentioned above showing that Neutron Star systems, as well as Black Hole ones, are capable of producing such hard photons.

The combination of regular monitoring in the hard X-rays and γ-rays has not been done before and this is where *INTEGRAL* will give a major contribution to understanding the behaviour of bright Low Mass X-ray binaries from 5 keV up to about 200 keV.

2.2. The INTEGRAL Core Program sample

Thirtyfive per cent of *INTEGRAL* observing time, the Core Program, is time reserved for the institutes that developed and delivered the instruments, for the *INTEGRAL* Science Data Centre (ISDC; Courvoisier et al. 2003) and for the Russian scientists in return for providing the Proton rocket which put *INTEGRAL* in orbit.

Figure 1 shows the exposure map for a total of six months of this program. As can be seen, the centre of our Galaxy has been heavily covered, with the total observing time decreasing as we move away from it. From the overall list of about 70 persistent and transient LMXRBs belonging to our monitoring program, the 8 sources detected primarily by IBIS/ISGRI and then by JEM-X in at least 20 pointings, have been selected. At the time of writing OMC data on these sources is still quite sparse and, therefore, will not be included in this paper. The red crosses in Fig. 1 show the position of those sources in the Galaxy while in Table 1 the complete list is presented.

The exposure per source depends on its position relative to the scan path and will differ from instrument to instrument due to their different FoV.

Table 1. Bright persistent LMXRBs regularly monitored by *INTEGRAL*. *Type*: A = Atoll, B = bursting, Z = Z-source, ADC = Accretion Disc Corona; *Flux*: average fluxes (in mCrab) as observed by RXTE/ASM (1.5–12 keV) and by SPI (20–40 keV; about 1 Msec overall exposure). See text.

Name	l	b	Type	$f_{\rm RXTE}$	$f_{\rm SPI}$
Sco X-1	359.09	23.78	Z	11420 ± 1875	439 ± 4.1
1822-371	356.85	−11.29	ADC	25 ± 29	33 ± 2.0
GX 3+1	2.29	0.79	AB	390 ± 64	34 ±1.9
GX 9+9	8.51	9.04	A	265 ± 44	31 ± 2.1
GX 9+1	9.08	1.15	A	495 ± 75	34 ± 3.1
GX 5−1	5.08	−1.02	Z	913 ± 137	77 ± 1.8
GX 17+2	16.43	1.28	ZB	603 ± 104	56 ± 2.9
Cyg X-2	87.33	−11.32	ZB	440 ± 80	35 ±6.9

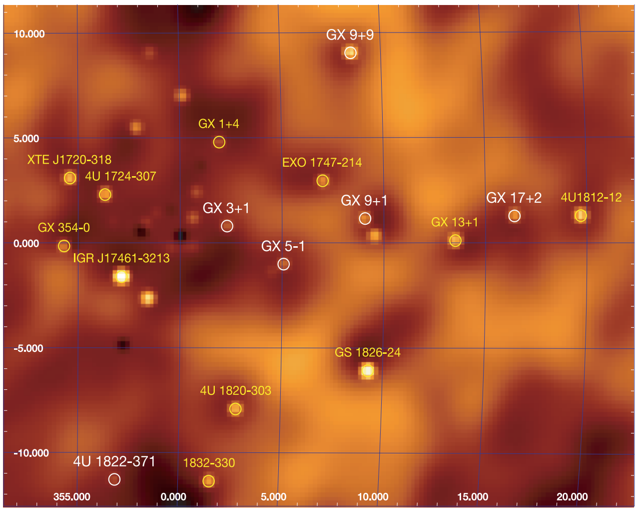

Fig. 2. SPI image of the Galactic Centre in the 40–100 keV band. The sources in white belong to our monitoring program. Other sources are marked in yellow for orientation.

3. Data reduction and analysis

A large fraction of the Galactic Centre Deep Exposure (GCDE) has already been completed. One scan of the GPS is performed every 12 days on average.

We have analysed most of the Core Program data currently available with the standard *INTEGRAL* Data Analysis System (IDAS). The following 3 subsections provide the instrument specific analysis details.

3.1. SPI analysis

The analysis of the SPI data is based on GCDE observations taken from revolution 47 up to 62, i.e. between March 3rd and April 19th, 2003. 544 dithering pointings used in the analysis combine a total exposure time of 958 ksec. As the instrumental resolution of SPI is about 2.5°, source confusion can affect the results. The ISGRI data have been used as a reference to check for sources which might interfere in the SPI data. GX 5-1 is separable by 40 arcmin from the black hole candidate GRS 1758-258. In this case both sources will influence the results of source extraction of each other and fluxes and spectra can only be taken as tentative. In the vicinity of GX 17+2 two sources can be detected, 4U1812-12 and AX J1820.5-1434, at 2.0° and 1.2° angular separation, respectively. In these cases the SPI Iterative Removal Of Sources (SPIROS) program (Skinner & Connell 2003) is able to disentangle the sources fairly well as the closer one is rather faint, though minor effects cannot be excluded.

SAX J1805.5-2031 is located 1.0° away from GX 9+1. As both sources appear to have similar fluxes in the studied energy range, the spectrum of GX 9+1 derived from the SPI data might therefore be affected. In the case of GX 3+1, two faint sources, SLX 1735-269 and SAX J1747.0-2858, are at 2.2 ° and 2.3° angular separation, respectively. As both sources are weak compared to GX 3+1, significant effects on the spectral extraction of GX 3+1 are unlikely. Figure 2 shows an image extracted from the SPI data in the 40–100 keV region. In the very dense region of the Galactic Centre, the extraction of sources seems to fail, while for more isolated sources, like e.g. GS 1826-24 and GX 13+1, the results are consistent with the ISGRI data (see Fig. 3). For the spectral extraction of the source GX 17+2 twenty logarithmic energy bins in the 20–200 keV energy range have been applied to the data (Fig. 4). The instrumental response function used for the analysis has been derived from on-ground-calibration and corrected after the in orbit Crab calibration observation. Source fluxes in the 20–40 keV band have been computed by comparison with results from Crab observation and are therefore given directly in Crab units (see Table 1). Fluxes in the 1.5–12 keV energy band have been extracted from the RXTE/ASM data base. The fluxes have been averaged over the same time period as the SPI data in order to have comparable results. In the case of 4U 1822–371 only the measurements for which the flux added to the 1σ error is larger than 0.0 have been taken into account, so that only reliable data are recognized.

3.2. ISGRI

The analysis of ISGRI data is based on GCDE and GPS data from revolution 30 to 64 i.e. January 11th to April 22nd, 2003. One thousand pointings (for a total of about 2 Msec exposure [1]) have been analysed separately and then combined in the mosaicked image shown in Fig. 3: a zoom in the Centre of the Galaxy in the 20–40 keV and 40–60 keV bands.

Given the ISGRI sensitivity (5σ detection in the 20–40 keV band for a 20 mCrab source in one pointing of 2200 s; Rodriguez et al. 2003, possible systematic errors are not taken into consideration) and the brightness of the sources of our sample, we can extract a source spectrum using (unlike for SPI) only data from one pointing. The ISGRI spectrum for a single pointing from revolution 54 for GX 17+2 is shown in Fig. 4.

[1] This is the total exposure time. The single source (point) exposure is much less as can be seen in Fig. 1.

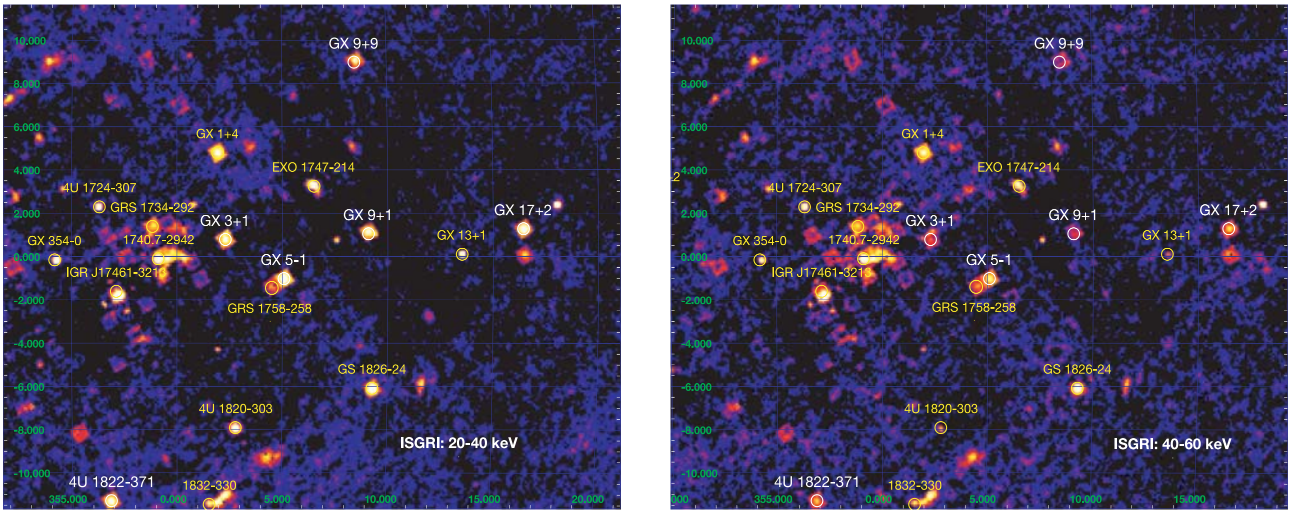

Fig. 3. ISGRI images of the Galactic Centre in 20-40 keV and 40-60 keV respectively. Not all the sources are labeled for clarity. The sources labeled in white belong to our monitoring program.

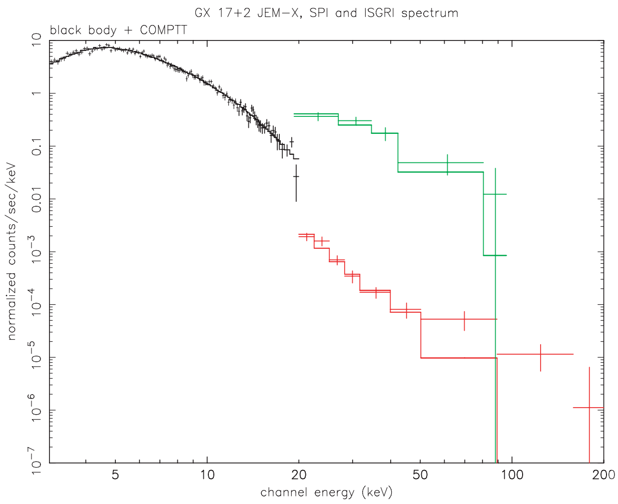

Fig. 4. GX 17+2 combined JEM-X (black), ISGRI (green) and SPI (red) count spectra. The SPI spectrum is based on all GCDE data from March to April 2003, while JEM-X and ISGRI spectra are extracted from one pointing only (about 2.2 ksec). Individual normalisation has been applied to the three instruments in order to compensate for uncertainties in the cross-calibration.

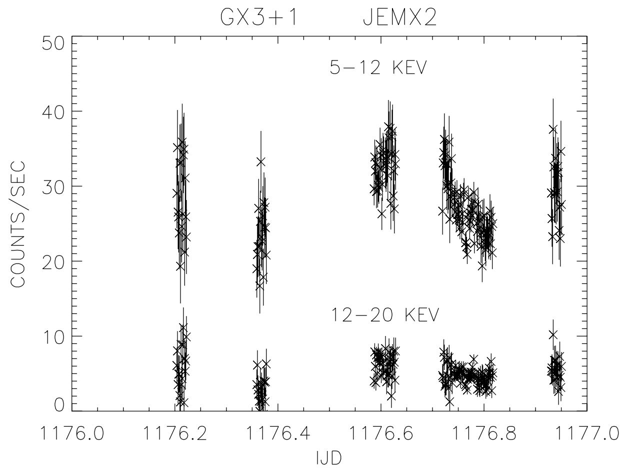

Fig. 5. JEM-X light-curve for GX 3+1 in two energy bands. Each point refers to a 100 second time bin. IJD is the fractional number of days since January 1, 2000 (0 UT). See text for more details.

3.3. JEM-X

The set of data taken from the same position for the same exposure time used for ISGRI has also been analysed for JEM-X using the standard software. Only JEM-X2 data have been available during the observations performed so far. The statistics for a bright LMXRB like GX 17+2 is of course even better than in ISGRI (1 pointing from revolution 54 extraction) and the result is shown in Fig. 4.

Light-curves have also been extracted for each source and for each pointing and a 1 day lightcurve for GX 3+1 is shown as an example in Fig. 5 for two different energy bands (5–12 keV and 12–20 keV). For comparison the Crab pulsar shows a count rate in JEM-X of 70–75 counts s^{-1} and 20–25 counts s^{-1} in the 5–12 keV and 12–20 keV energy band, respectively. Gaps in the data mean that for those periods the source was out of JEM-X FoV, the narrowest of *INTEGRAL* high energy instruments, thus there is no detection.

4. Results

Since its launch, *INTEGRAL* has been producing a huge amount of interesting data. Quite naturally at this early stage of the mission, however, it is not possible to exploit them at best mainly because instrument response functions are still under development and calibrations on-going. More time is required before one can present long and fast time scale variabilities in different energy bands as well as detailed spectral behaviour of the sources. Nonetheless some main conclusions can be already drawn. First of all, the combined spectrum in Fig. 4 shows the *INTEGRAL* mission wide energy band allows the emission of the binary system to be displayed all the way to the hard tail. There seems to be no evidence for a cut-off below 100 keV.

In this case the combined spectrum can be represented by a simple model, including a blackbody plus a comptonisation component. The statistical quality of the fit does not justify adding an additional power law component. However, the present model flux is much below the measured one in the channel centered on 100 keV. This is a possible indication of the presence of a high energy tail on top of the blackbody Comptonised by thermal electrons. Physically, this can be realized if the electrons have a hybrid distribution, with a Maxwellian *and* a high energy tail. This appears to be the case in a number of black hole binaries (e.g., Gierliński et al. 1999; Zdziarski et al. 2001).

Furthermore, based on one pointing only, JEM-X and ISGRI give a significant spectrum up to 100 keV for a source of ~60 mCrab. This will allow the study of the spectral time evolution on a pointing by pointing basis, i.e. monitoring the spectral slope and cut-off on an hourly basis. In this energy region the SPI sensitivity is much lower when compared to ISGRI. The spectrograph can then be used to derive high energy spectra based on longer observations. Though the spectrum is in this case an average over the different stages of the LMXRB cycle, it can reveal high energy tails, as seen in Fig. 4 up to ~150 keV. This capability is also seen in the high energy (40–100 keV) image as shown in Fig. 2.

In addition, note that the ISGRI FoV is about the size of the image in Fig. 3 so the amount of information one can obtain from one ISGRI pointing is evident. Besides, its excellent angular resolution (12′ $FWHM$) allows the emission from close-by sources to be separated. See for instance GX 5-1 and the 40 arcmin distant Black Hole Candidate GRS 1758-258, for which possible SPI source confusion has been pointed out.

Another result of this study is the comparison of the SPI derived fluxes to the RXTE/ASM fluxes as shown in Table 1. As both flux values have been extracted over a long time period of 1.5 months, they represent the mean status of the LMXRBs, i.e. averaged over all positions in the colour-colour diagram. While the Z and Atoll sources of the sample show a steep spectral slope between the 1.5–12 keV and the 20–40 keV band, the 0.59 s pulsar 4U 1822–371 (Jonker & van der Klis 2001) exhibits a comparably flat spectrum with a photon index of $\Gamma \simeq 2$ between the RXTE and SPI data. This hard spectrum has been reported before (e.g. Parmar et al. 2000), but further investigations are necessary in order to understand the nature of this elusive source.

Finally, though the X-ray monitor JEM-X covers a smaller area than the two main instruments (diameter of 13.2°, zero response), Fig. 5 shows that monitoring of the X-ray flux on short (several minutes) and long (days and months) time scale is possible. This will allow, for example, to monitor outburst and the dipping behaviour of 4U 1822-371.

Acknowledgements. We would like to thank Mike Revnivtsev for providing the mosaic tool for the ISGRI images. We also thank P. Laurent and M. Cadolle-Bel for kindly providing preliminary corrected ISGRI response matrices and the SPI colleagues for advice on how to handle SPI data. OV and DH acknowledge the Academy of Finland, TEKES, and the Finnish space research program ANTARES for financial. J.R., acknowledges financial support from the French Space Agency (CNES). A.A.Z., aknowledges KBN grants 5P03D00821, 2P03C00619p1,2, PBZ-054/P03/2001 and the Foundation for Polish Science. AP, AB, FF, AS, & GGCP acknowledge ASI and CNR for financial support.

References

Courvoisier, T. J.-L., Walter, R., Beckmann, V., et al. 2003, A&A, 411, L53
D'Amico, F., Heindl, W. A., Rothschild, R. E., & Gruber, D. E. 2001, ApJ, 547, L147
Di Cocco, G., Caroli, E., Celesti, E., et al. 2003, A&A, 411, L189
Di Salvo, T., Stella, L., Robba, N. R., et al. 2000, ApJ, 544, L119
Di Salvo, T., & Stella, L. 2002, Proc. XXII Moriond Astroph. Meeting, p. 67 [astro-ph/0207219]
Gierliński, M., Zdziarski, A. A., Poutanen, J., et al. 1999, MNRAS, 309, 496
Gierliński, M., & Done, C. 2002, MNRAS, 331, L47
Jonker, P. G., & van der Klis, M. 2001, ApJ, 553, L43
Lebrun, F., Leray, J. P., Lavocat, P., et al. 2003, A&A, 411, L141
Liu, Q. Z., van Paradijs, J., & van den Heuvel, E. P. J. 2001, A&A, 368, 1021
Lund, N., Brandt, S., Budtz-Jorgensen, C., et al. 2003, A&A, 411, L231
Mas-Hesse, J. M., Gimenez, A., Culbane, L., et al. 2003, A&A, 411, L261
Muno, M. P., Remillard, R. A., & Chakrabarty, D. 2002, ApJ, 568, 35
Parmar, A. N., Oosterbroek, T., Del Sordo, S., et al. 2000, A&A, 356, 175
Rodriguez, J., Del Santo, M., Lebrun, F., et al. 2003, A&A, 411, L373
Skinner, G. K., & Connell, P. H. 2003, A&A, 411, L123
Swank, J. H. 2001, AIP Conf. Proc., 575, p. 261
Ubertini, P., Lebrun, F., Di Cocco, G., et al. 2003, A&A, 411, L131
van der Klis, M. 1995, Proc. NATO-ASI Workshop on Neutron Stars
van der Klis, M. 2000, ARA&A, 38, 717
Vedrenne, G., Roques, J.-P., Schönfelder, V., et al. 2003, A&A, 411, L63
Zdziarski, A. A., Grove, J. E., Poutanen, J., et al. 2001, ApJ, 554, L45

THE *INTEGRAL* LMXRB MONITORING PROGRAMME

A. Paizis[1,2], T.J.-L. Courvoisier[1], O. Vilhu[3], M. Chernyakova[1], T. Tikkanen[3], A. Bazzano[4], V. Beckmann[5], J. Chenevez[6], M. Cocchi[4], K. Ebisawa[1], R. Farinelli[7], F. Frontera[7], A. Gimenez[8], P. Goldoni[9], D. Hannikainen[3], E. Kuulkers[10], N. Lund[6], T. Oosterbroek[10], S. Piraino[11], J. Rodriguez[9,1], A. Santangelo[11], R. Walter[1], A. A. Zdziarski[12], and J. A. Zurita Heras[1]

[1]*INTEGRAL* Science Data Centre, Chemin d'Ecogia 16, 1290 Versoix, Switzerland, Ada.Paizis@obs.unige.ch
[2]CNR-IASF, Sezione di Milano, Via Bassini 15, 20133 Milano, Italy
[3]Observatory, P.O.Box 14, Tähtitorninmäki, FI-00014 University of Helsinki, Finland
[4]CNR-IASF, Sezione di Roma, Via del Fosso del Cavaliere 100, 00133 Roma, Italy
[5]NASA Goddard Space Flight Center, Code 661, Greenbelt, MD 20771, USA
[6]Danish Space Research Institute Juliane Maries Vej 30, Copenhagen, Denmark
[7]Dipartimento di Fisica, Università di Ferrara, Via Paradiso 12, I–44100 Ferrara, Italy
[8]Instituto Nacional de Tecnica Aerospacial, Carretera de Ajalvir 4, Torrejon de Ardoz , Madrid, Spain
[9]CEA Saclay, DSM/DAPNIA/SAp, F–91191 Gif sur Yvette, France
[10]Research and Scientific Support Department of ESA, ESTEC, Postbus 299, 2200 AG Noordwijk, The Netherlands
[11]CNR-IASF, Sezione di Palermo, Via Ugo La Malfa 153, 90146 Palermo, Italy
[12]N. Copernicus Astronomical Ctr., Bartycka 18, 00716 Warsaw, Poland

ABSTRACT

Our collaboration is responsible for the study of a sample of 72 low mass X-ray binaries (LMXRB) using the *INTEGRAL* Core Programme data. In this paper we describe the monitoring programme we have started and the current variability and spectral results on a sample of 8 persistently bright LMXRBs hosting a neutron star (Z and Atoll sources). Current results show that among our sample of sources there seems to be no important difference in the variability of Z sources with respect to Atolls and the first colour-colour and hardness intensity diagrams built in the "traditional" energy bands display the expected patterns.
Z sources seem to be harder than the bright Atolls of our sample (above 20 keV) and present no evident cut-off until about 50 keV. A hint of a non-thermal hard tail is seen in Sco X-1 with ISGRI and SPI, similarly to what was previously detected by D'Amico et al. (2001) with *RXTE*. These results, even if preliminary, show the importance of such a programme and the potential underlying it to understand these sources as a class.

Key words: stars: neutron – binaries: close – X-rays: binaries –*INTEGRAL* sources.

1. INTRODUCTION

The International Gamma-Ray Astrophysics Laboratory, *INTEGRAL* (Winkler et al. 2003), has been launched in October 2002. Since then, it has been providing a large amount of interesting data. The combination of two wide field of view (FOV) instruments, the imager IBIS (15 keV – 10 MeV, $29^\circ \times 29^\circ$ partially coded FOV, Ubertini et al. 2003) and the spectrometer SPI (20 keV – 8 MeV, $35^\circ \times 35^\circ$ partially coded hexagonal FOV, Vedrenne et al. 2003) coaligned with the JEM–X (Lund et al. 2003) and OMC (Mas-Hesse et al. 2003) monitors, allows large areas of the sky to be observed and monitored simultaneously in a wide energy range from the optical to the γ-ray domain. Such a capability is fully exploited during the *INTEGRAL* Core Programme (Winkler et al. 2003b), a series of successive scans of the Galactic Plane (GPS) and Galactic Centre (GCDE), which is regularly producing large amounts of data, in particular on persistently bright sources.
Our collaboration is responsible for the monitoring of a sample of low mass X-ray binaries (LMXRBs). In this paper we describe the current results of this programme, showing the importance of this study and the potential underlying such a long term monitoring.
Section 2 of this paper describes the aim of the monitoring programme with a basic overview of the source characteristics. Section 3 contains the data reduction and analysis description while in Section 4 the current results are given. In the last Section we present our conclusions and future plans.

Table 1. Bright persistent NS LMXRBs regularly monitored by INTEGRAL. Type: *A=Atoll, B=bursting, Z=Z source, ADC=Accretion Disc Corona.*

Source Name	l	b	Type
Sco X−1	359.09	23.78	Z
Cyg X−2	87.33	-11.32	ZB
GX 5−1	5.08	-1.02	Z
GX 17+2	16.43	1.28	ZB
GX 3+1	2.29	0.79	AB
GX 9+9	8.51	9.04	A
GX 9+1	9.08	1.15	A
4U1822−371	356.85	-11.29	ADC

2. THE MONITORING PROGRAMME

2.1. The sources of our sample

The nature of the sources in our list is very rich, containing black hole (BH) as well as weakly magnetised neutron star (NS) binaries with very different variability.
Monitoring these sources through the years will give an overview of the hard energy ($>$ 10 keV) behaviour of the Galactic Plane and Centre LMXRBs as a class: outburst frequency, variability level, type I X-ray burst frequency, persitent emission etc, all in the poorly studied hard energy domain.
Among all the sources of our sample, in this paper we focus on the 8 persistently bright LMXRBs listed in Table 1. They all host a neutron star.

2.2. Weakly magnetised neutron star binaries

The current classification of NS LMXRBs is based on the pattern displayed by individual sources in the X-ray colour-colour (CC) and hardness-intensity (HI) diagrams (Hasinger & van der Klis, 1989 and van der Klis, 1995). It comprises the so-called Z sources (that display a ”Z” pattern in the diagrams) and the Atoll sources (that display an upwardly curved branch in the diagrams).
More recent studies (Muno et al. 2002, Gierliński & Done 2002 and Done & Gierliński 2003) suggest that the clear Z/Atoll distinction in the CC diagram is an artifact due to incomplete sampling: Atoll sources, if observed long enough, *do* exhibit a Z shape in the CC as well. Many differences, however, remain: Atoll sources have weaker magnetic fields ($<10^9$–10^{10} G versus $\sim10^9$–10^{10} G of Z sources), are generally fainter (0.01–$0.3L_{Edd}$ versus $\sim L_{Edd}$), can exhibit harder spectra, trace out the Z shape on longer time scales than typical Z sources and have a different correlated timing behaviour along with the position on the Z. Thus the distinction, at least from a practical point of view, still makes sense.
Our sample of sources includes both Z and Atoll sources. Thanks to the *INTEGRAL* monitoring programme we (will) have a long term coverage of all these sources. For the first time they will be studied in a regular and unbiased way in the energy band in which they are poorly known, hard X/γ rays, where they display an interesting behaviour.
Thermal comptonisation is dominant both in soft and hard spectral states of NS LMXRBs and in most cases it is a good representation of the spectra below 20 keV. In this range, LMXRB with a weakly magnetised NS (i.e. non pulsating) can be well described by two competing models. On one side, there is the so-called ”western” model in which the spectrum is composed of the sum of unsaturated Comptonised spectrum (produced by an inner disc corona) plus a blackbody originating from a region close to the neutron star surface or from the boundary layer between the disc and the neutron star (White et al. 1986, 1988). On the other hand, in the ”eastern” model the spectrum consists of the sum of an optically thick multi-temperature disc-model (locally emitting like a pure blackbody) plus a comptonised blackbody again originating from the neutron star or boundary layers (Mitsuda et al., 1984; Mitsuda et al., 1989).
Hard X-ray components extending up to several hundred keV have been revealed in about 20 NS LMXRBs of the Atoll class (Di Salvo & Stella 2002 and references therein). In these systems a power-law like component (with photon index $\Gamma \sim 1.5 - 2.5$) is followed by an exponential cutoff between $\sim$20 and many tens of keV. This is explained in terms of unsaturated thermal Comptonisation. But there are cases in which no evidence for a cutoff is found up to 100-200 keV. This is the so-called ”hard state” of Atoll sources and occurs especially in the lower luminosity systems (note that the Atolls of our sample are among the brightest). On the other hand, broad band studies have shown that also many Z sources display a variable hard power-law ($\Gamma \sim 1.9-3.3$) component dominating the spectra above $\sim 30\,\mathrm{keV}$.
The origin of these hard tails is still debated. Radio observations of some Z sources (Fender & Hendry 2000) seem to show a general trend in which the highest radio fluxes (thought to be originating in jets) are associated to the hardest state of the sources. This could mean that the non thermal, high-energy electrons responsible for the hard tails in Z sources could be accelerated in jets (Di Salvo et al. 2000).

2.3. Aim of the programme

The long term X-ray variability of LMXRBs has been extensively studied in the 2–12 keV band with the *RXTE* All Sky Monitor. At higher energies, the information gathered from the sources has been obtained mainly via dedicated pointings (*RXTE*, *BeppoSAX* etc).
The combination of regular monitoring in the hard X-rays and γ-rays has not been done before and this is where *INTEGRAL* will give a major contribution to understand the behaviour of bright LMXRBs from 5 keV up to $\sim 200\,\mathrm{keV}$ (see also Paizis et al., 2003).
By focusing on the sources presented in this paper, we intend to try to understand the differences between Z and Atoll sources via their (less explored) high-energy emission (hard tails, CC diagrams, different variability, etc).
In collaboration with the accreting pulsars collaboration,

we intend to put the extracted light-curves and hardness intensity diagrams on the web[1]. In this way, the high-energy history of these sources will be easily accessible, enabling also multiwavelength comparisons. In this respect, our collaboration has coordinated *RXTE* observations to the *INTEGRAL* ones in order to have a better coverage of the soft X-ray domain [2]. Similarily, we have access to Radio (RATAN/MOST/VLA) and Optical (La Palma, La Silla) telescopes.

3. DATA REDUCTION AND ANALYSIS

INTEGRAL performs a GPS about every 12 days and the GCDEs are performed according to the Galactic Centre visibility. At the time of writing the first year of core programme has been completed and we have analysed all the data from revolution 26 (January 2003) until revolution 142 (December 2003) for a total of 3078 science windows corresponding to about 5.7 Msec.
Version 3.0 of ISDC's (Courvoisier et al., 2003) Off-line Science Analysis (OSA) software has been used for analysing the data.
Given the type of sources involved (rather steep spectra with about hundred of mCrabs in the 2–10 keV band, Liu et al. 2001) and the pointing exposures of about 2000 s, for the analysis we have chosen JEM–X for soft photons (5–20 keV) and the low energy IBIS detector, ISGRI (Lebrun et al. 2003) for harder photons (20–200 keV). We have not used PICsIT, the hard photon IBIS detector (Di Cocco et al. 2003), as its peak sensitivity is above 200 keV, where LMXRBs have fluxes below PICsIT detectability. The spectrometer SPI and the imager ISGRI have been used to extract the hard energy spectra (20-200 keV) averaged on longer time scales. To increase the signal to noise ratio in the extracted ISGRI spectra, we used an alternative method i.e. we first combined data of different pointings in one single mosaic (weighted combination of the images) and then extracted fluxes in several energy bands.

4. RESULTS

In this section we go through the main results that we have obtained during our monitoring programme up to now. They can be mainly split into two parts: the variability study of our sources and the (average) spectral study.
Fig. 1 shows the distribution in the Galaxy of the sample of sources studied in this paper (with the exception of Sco X-1 and Cyg X-2[3]). The total exposure time is about 5.7 Msec while the final exposure time per source depends on its position with respect to the Galactic Centre: the closer to the Centre the higher the exposure.

[1]The results will thus be publically available, similarly to what the *RXTE*/All Sky Monitor has been doing in the softer X-ray band.

[2]In fact, due to the GPS and GCDE dithering patterns, the sources are very often only in the partially coded FOV of JEM-X and sometimes even not covered at all.

[3]Sco X-1 and Cyg X-2 are far away from the galactic plane and actually are never covered by JEM-X during the scans. This makes our simultaneous *RXTE* coverage even more important.

4.1. Variability study

4.1.1. Light-curves

As already stated, one of the main aims of the monitoring programme is to extract light-curves for the sources in different energy bands. The richness of the light-curve depends on the position of the source in the sky. Fig. 2 (left panel) is an example of an ISGRI light-curve for GX5-1 (quite close to the Centre of the Galaxy). The points with larger error bars correspond to pointings where the source was more off-axis.
For comparison the right panel shows the *RXTE*/ASM light-curve for the same period (7 months). The ASM coverage is of course more extensive (*INTEGRAL* has no all sky monitor programme) but with *INTEGRAL*/ISGRI we will have a coverage of the sources in the harder energy bands, completing the ASM. A hard-energy (20 keV – 1 MeV) sky survey has been performed by the BATSE mission aboard *CGRO* covering the period from April 1991 until June 2000 (Shaw et al., 2004). The *INTEGRAL* high-energy survey will achieve a much better angular resolution and sensitivity[4].
Fig. 3 shows a zoom in a 5-day ISGRI light-curve of GX5-1 and GX17+2.
Light-curves similar to Fig. 2 and Fig. 3 are being extracted also with JEM-X. In this case, due to the smaller size of the FOV, the resulting data set is smaller than for ISGRI. On the other hand, JEM-X covers a softer part of the X-ray spectrum and thus has more statistics. This allows the extraction of smaller time-bin light-curves like the one showed in Fig. 4 where 1 pointing (science window) is further sampled into 100 second bins. Starting from this data base of light-curves (1 pointing bin for ISGRI and 100 seconds bin for JEM-X) we have produced, per source, the count rate distributions in different energy bands. The distributions for GX5-1 (Z source) and GX3+1 (Atoll) are shown in Fig. 5 and Fig. 6 respectively, while Table 2 summarises the results we obtain for all the Z and Atoll sources of our sample. Only the pointings where both ISGRI and JEM-X data were available have been considered. The spread of the distributions is most likely mainly due to the source variability: the poissonian spread accounts for a few % and the vignetting factor (more difficult to quantify) seems to play a minor role since the dependency of the count rate on the off-axis angle has been studied and shows no evident trend for the different sources. What can be seen from the current data set is that Z sources are brighter than Atoll sources (as expected) and there seems to be no important difference in the long-term ($>$ 100 sec) variability of these sources as a class. Apart from GX5-1, that shows an important variability increase when moving from soft to hard range, the remaining Z and Atoll sources do not seem to have evident differences[5].

[4]Integrating over the full nine year database of BATSE observations and over 7 energy channels (25 – 160 keV), the 5σ sensitivity to a persisitent source is $\sim$2mCrab while the angular resolution achieved with BATSE is about half a degree.

[5]The soft (JEM–X) Sco X-1 varibility is missing because JEM-X FOV is too small to cover it during the scans. Our *RXTE* observations of this source will provide a simultaneous soft (*RXTE*) hard (*INTEGRAL*) variability. The same holds for Cyg X-2 (not covered by JEM-X) for which we currently have too few ISGRI points for the count rate distri-

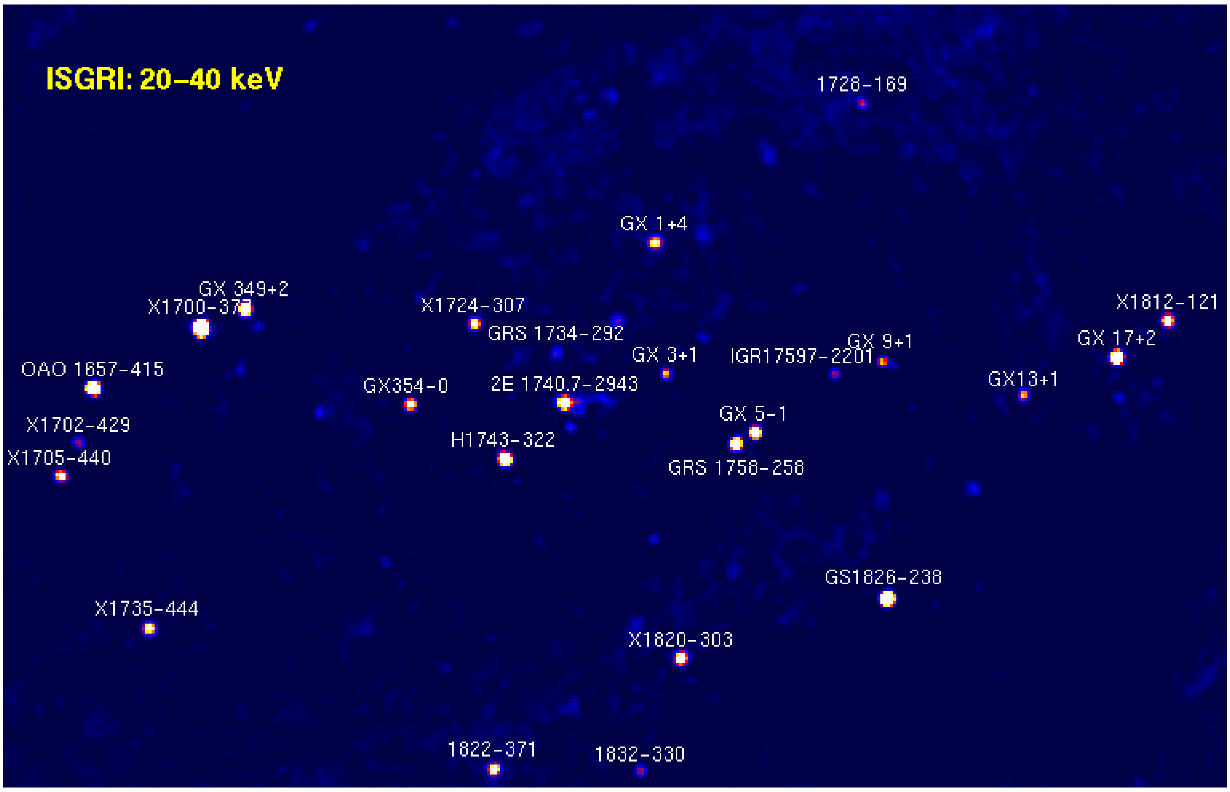

Figure 1. IBIS/ISGRI (20–40 keV) mosaic of the Galactic Centre (5.7 Msec, about 20°x40° centred on the Galactic Centre). Only a few sources are labelled for clarity. Most of the sources of this paper are visible in the image (GX9+9 is labelled here as 1728-169).

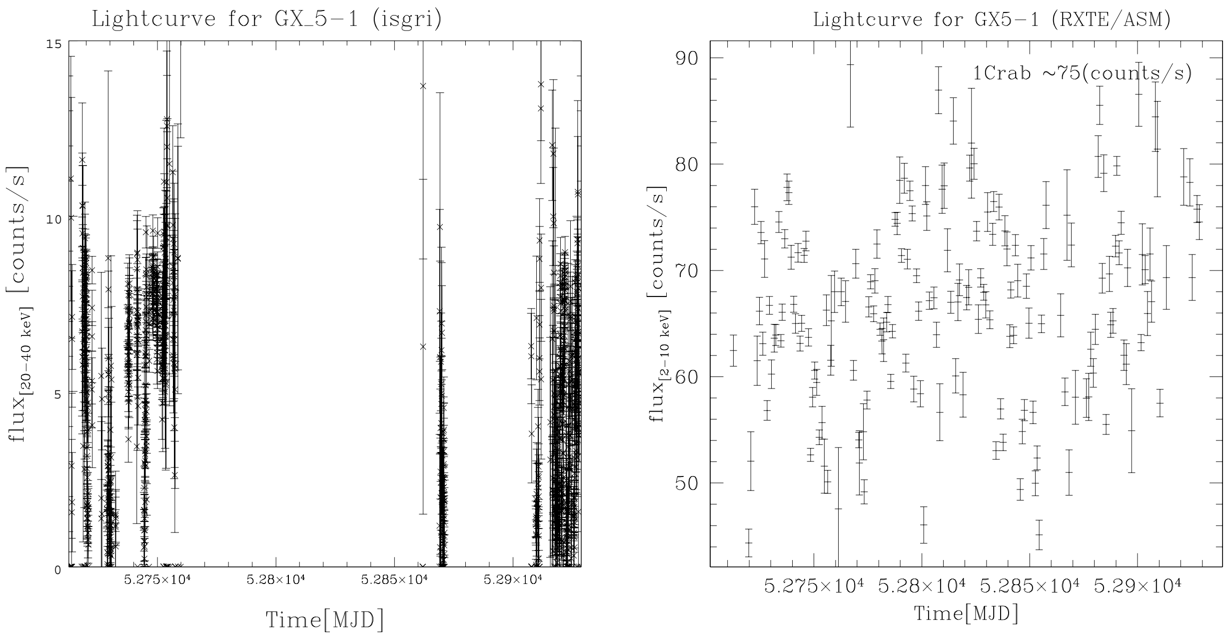

Figure 2. GX5-1 light-curves from March 2003 until October 2003. Left panel*: ISGRI results in the 20-40 keV band (about 2000 sec time-bin). In this energy band 1Crab corresponds to about 100 counts/sec.* Right panel*: quick-look results provided by the RXTE/ASM team in the 2-10 keV band (1 day time-bin).*

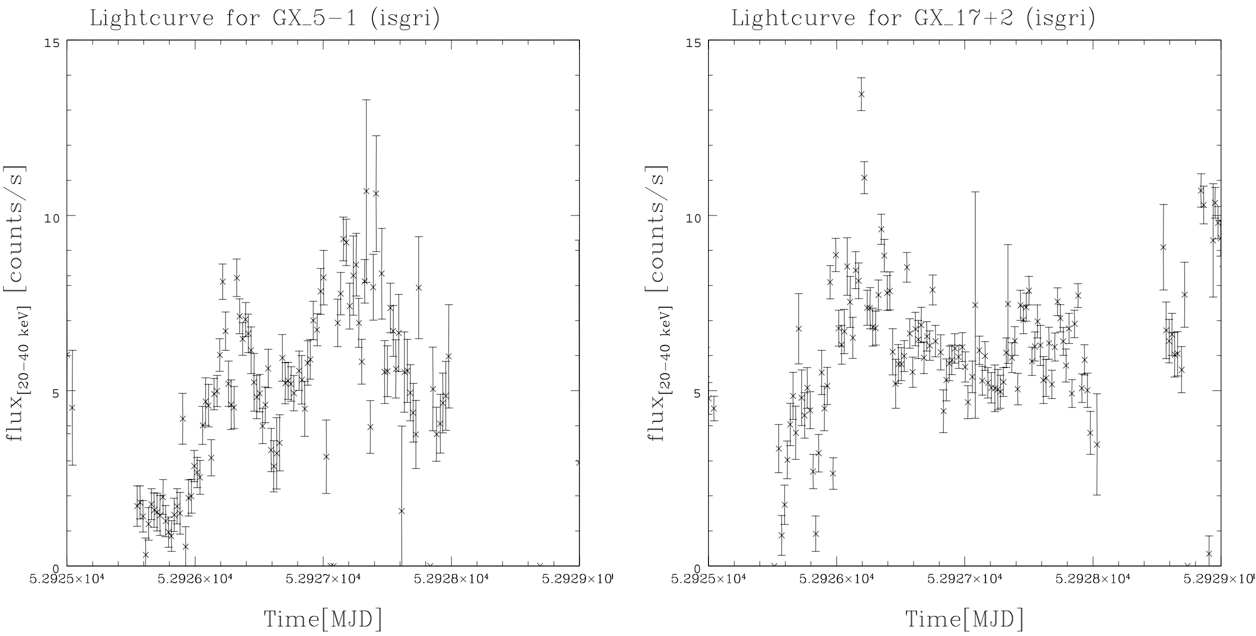

*Figure 3. 5-day ISGRI light-curve for GX5-1 (*left panel*) and GX17+2 (*right panel*)*

Table 2. Variability properties of the sources. J_Mean*: mean counts/sec in the 5–12 keV JEM-X band.* J_Var*: standard deviation of the distribution normalised to the mean in the 5–12 keV JEM-X band in %.* I_Mean*: mean counts/sec in the 20–40 keV ISGRI band.* I_Var*: standard deviation of the distribution normalised to the mean in the 20–40 keV ISGRI band in %.*

Source	J_Mean	J_Var.	I_Mean	I_Var.
Z				
GX 5−1	56.96	39%	4.46	64%
GX 17+2	40.30	35%	5.82	42%
Sco X−1	-	-	78.20	32%
ATOLL				
GX 3+1	23.04	42%	1.65	44%
GX 9+9	14.77	36%	1.35	42%
GX 9+1	32.41	41%	1.72	41%
ADC				
1822−371	1.34	87%	3.35	26%

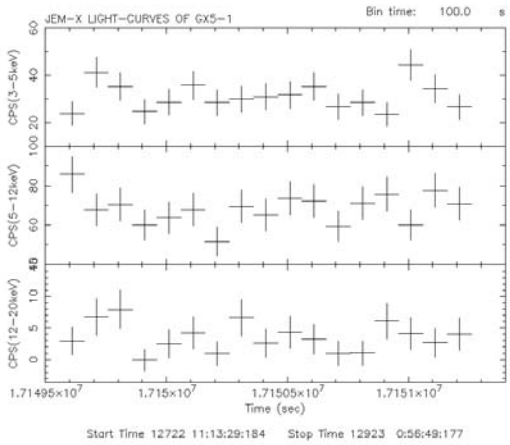

Figure 4. Single pointing JEM-X light-curve of GX5-1 (100 sec bins) in three different energy bands.

On the contrary, the ADC source 4U1822-371 displays a very high flux change in the softer energy range. This result is most likely due to the nature of this source that is known (e.g. Parmar et al. 2000) to display deep variations in the form of regular dips and coronal partial eclipses (hence the name of accretion disc corona source).

4.1.2. Colour-colour and hardness-intensity diagrams

The changes in X-ray spectra of Z and Atoll sources are very subtle and not easy to spot and describe with proper model fitting. Alternative tools are often used to study the spectral variability of these sources and are the al-

bution (the source is covered only in the GPS and not on the GCDE).

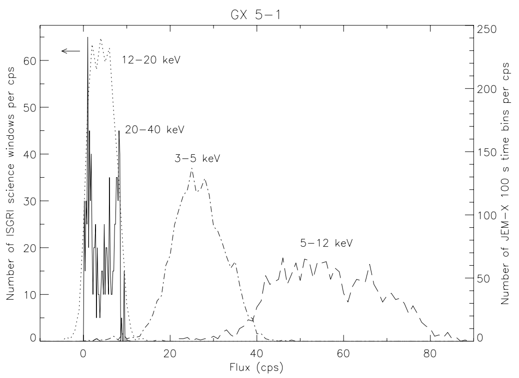

Figure 5. Count rate distribution for GX5-1. The solid line is the 20-40 keV ISGRI distribution while the remaining three curves are the distributions in the three different JEM-X bands used in our analysis.

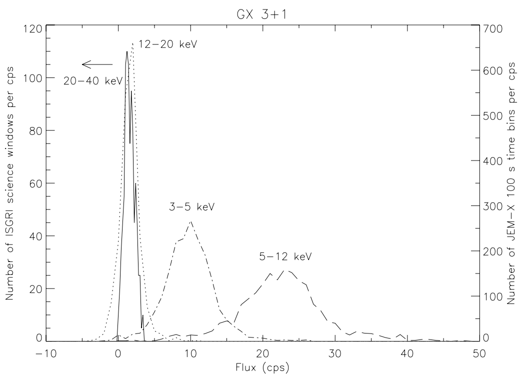

Figure 6. Count rate distribution for GX3+1 in the same energy bands of Fig. 5

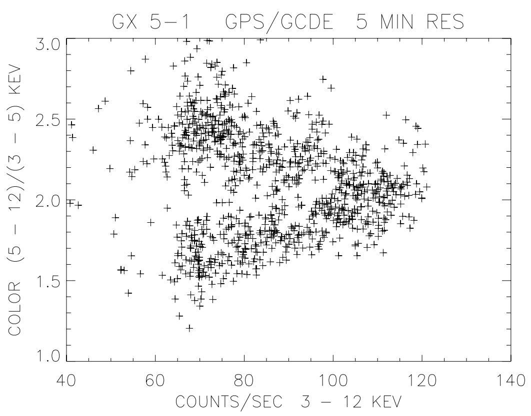

Figure 7. Hardness intensity diagram for GX5-1 obtained with JEM-X (one year data, 5 minute bins).

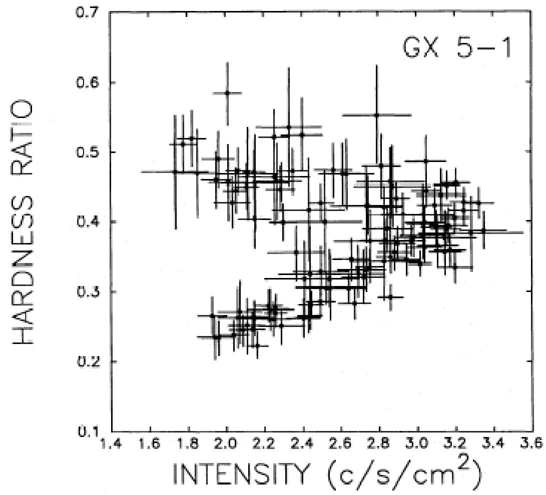

Figure 8. Hardness intensity diagram for GX5-1 obtained with Ginga-All Sky Monitor (three years data). The Ginga-ASM hardness ratio is built with counts in the 6–20 keV/1–6 keV bands while the intensity is the overall count rate in the 1–20 keV band (van der Klis et al., 1991).

ready mentioned colour-colour and hardness-intensity diagrams.
An attempt is made to build these CC and HI diagrams in the same energy bands (i.e. defining the same colours) so that time-distant observations, often performed with different instruments, can still be compared to have a long term view of the source variability. But this is not always possible and normally it is difficult to derive a direct quantitative comparison of CC and HIDs produced with different X-ray detectors. In this respect, the *INTEGRAL* monitoring has the main advantage that the sources (Z and Atolls) will be observed over the years with the same instrumentation and long-term comparisons will be possible.
Besides, based on the huge data base that will be populated with time, it will be possible to search for differences and/or similarities of these sources in new, *INTEGRAL* defined, hard X-ray colour colour diagrams.
The systematic study of CC diagrams in different colours is still on-going and is very closely related to the status of the calibration of *INTEGRAL* instruments. Nevertheless, the first results based on the traditional colour definition seem to show that we indeed obtain the expected pattern for the sources. Fig. 7 shows the JEM-X HID for GX5-1 to be compared to Fig. 8, the *Ginga*-All Sky Monitor HID (van der Klis et al. 1991). The horizontal and normal branches of the Z pattern are clearly visible.

4.2. Spectral study

Starting from the ISGRI imaging results, we have built several mosaics, one per energy band, and then extracted the spectra for each source. Fig. 9 and 10 show the resulting ISGRI (average) spectra. The spectra have been normalised to the Crab spectrum (extracted in the same

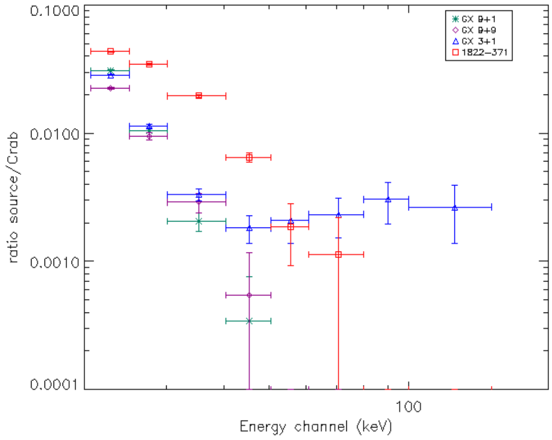

Figure 9. ISGRI spectra extracted from a mosaic of 1 year of core programme data. Atoll sources plus the ADC source.

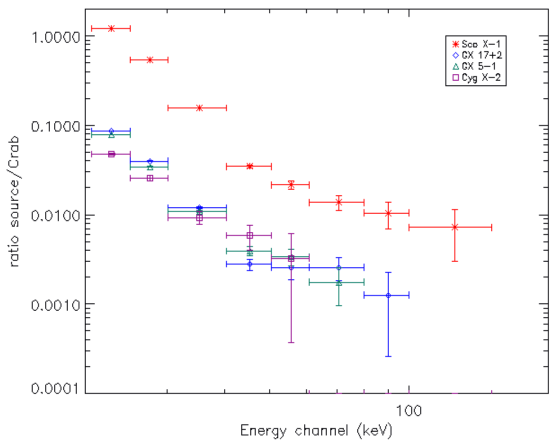

Figure 10. ISGRI spectra extracted from a mosaic of 1 year of core programme data. Z sources. The effective exposure of each source depends on its position (see text). The GX5-1 (close to the Centre of the Galaxy) spectrum exposure is about 1.6 Msec while for Sco X-1 (higher latitude) it is about 260 ksec.

way): a zero slope in the graphs means a source as hard as Crab (i.e effective photon index of 2) while a positive slope means a source softer than Crab.
In Fig. 9 the 3 Atoll sources (GX9+1, GX9+9 and GX3+1) have a similar soft spectrum until about 50 keV. Above 50 keV, GX3+1 shows a hardening comparable to the hardness of the Crab with a 4.5σ significance in the last 3 bins. Such hardening can be described by a comptonised black-body component and (with the current systematics) no additional power-law component (hard tail) is needed. It is also important to note that the source brightness above 60 keV (where the hardening is more evident) is around a few mCrab i.e. comparable to the background fluctuations at these energies (Bodaghee et al. 2004). It is currently difficult to disentangle among source and background contribution and a complete calibration of the instrument is needed to derive more firm conclusions.

Fig. 10 shows the spectra of the Z sources of our sample. Z sources are brighter than Atolls (as expected) and seem also to be harder with no evident cut-off until about 50 keV. Sco X-1 shows a hardening above 50 keV. In this case the hardening is more significant than for GX3+1 (10 σ detection in the 55 keV centred bin and 5.3 σ detection in the 70 keV centred bin) and starts well above the aforementioned background limit. Triggered by this, we have performed a deeper spectral study. Fig. 11 shows ISGRI and SPI spectra of Sco X-1. We fitted the data with the best fit model that D'Amico et al. (2001) used to describe the non-thermal hard tail detected in Sco X-1 with *RXTE*/HEXTE instrument. We get comparable results for the bremsstrahlung component (temperature of about 4.5 keV) and a slightly steeper power-law slope (2.9 instead of their maximum 2.37). In our case the slope of the power-law component is difficult to determine accurately given that it strongly depends on the softer bremsstrahlung component which, in turn, depends on the softer ($<$ 20 keV) part of the spectrum currently missing (the source is not covered by JEM-X and the simultaneous *RXTE* data have not been triggered yet). Our detection confirms the non-thermal hard tail detection of *RXTE*/HEXTE by D'Amico et al. (2001) . Nevertheless,

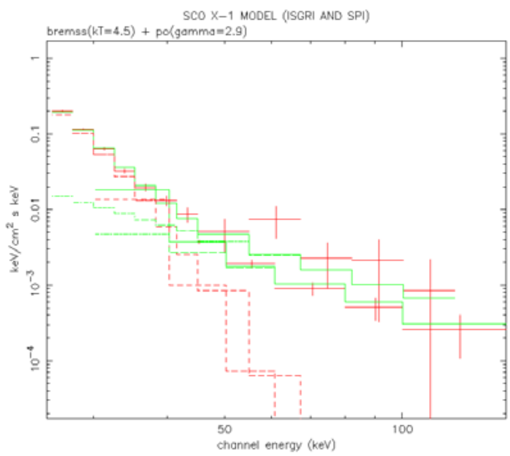

Figure 11. Energy ISGRI and SPI spectra of Sco X-1. The SPI data are the ones with larger error bars. The dotted lines are the bremsstrahlung and power-law models (for the 2 spectra). The solid line is the total model.

such a result should be taken with caution: ISGRI calibration is not optimised yet and a hard tail as the one we detect on a $\sim$260 ksec averaged spectrum would mean that the tail is either steadily there (which does not seem the case from previous observations on Sco X-1) or indeed is variable but very strong when present. The latter could be the case and we will extract spectra at a (few) science window(s) level to have the answer.

5. CONCLUSIONS

We have analysed about 1 year of *INTEGRAL* Core Programme data and built a LMXRB data base that will be made publicly available via the web.
In our monitoring progam we plan to study in a systematic way the high-energy emission of a sample of 72 LMXRBs. Among these are 8 persistently bright neutron star LMXRBs (4 Z sources, 3 Atolls and 1 ADC source). In this paper we have shown the current results from this sample of 8 LMXRBs (all hosting a weakly magnetised neutron star).
The *variability study* (light-curves and CC-HI diagrams) has shown that the *INTEGRAL* core programme coverage is enough to study the high-energy history and evolution of the sources. Z sources are brighter than Atolls (as expected) and, with the current data set, there seems not to be an important difference in the variability of the sources as a class. The CC-HI diagrams built in the "traditional" energy bands already display the expected patterns which is an encouraging result for exploring new, *INTEGRAL* defined, diagram energy bands.
The *spectral study* of the sources of our sample has shown that Z sources seem to be harder than Atolls ($>$ 20 keV) and present no evident cut-off until about 50 keV. Atoll sources in general, as previously stated, can be much harder than Z sources but this is mainly true for the low luminosity ones whereas the Atolls of our sample are soft high state bright systems.
In our averaged ISGRI spectra, a hardening in GX3+1 data is visible (well described by the traditional comptonised black-body model, i.e. no additional power-law component needed) and a hint of a non-thermal hard tail in Sco X-1 ISGRI and SPI data is seen, similarly to what was previously detected by D'Amico et al. (2001) with *RXTE*.
The hunt for such hard tails in NS LMXRBs is a key goal of our monitoring with *INTEGRAL*. They add one more piece to a mosaic that places neutron star binaries next to black holes, for which non-thermal emission was thought to be a prerogative.
In the results presented here, variability and spectral studies have been carried out separately and the next step will be to merge these two aspects, extracting only spectra for a given branch in the CC-HI diagrams, i.e. for well defined spectral states. The coordinated observations will show the presence (or absence) of multiwavelength emission in the different states.
Using all this we are able to build a huge data base that will offer a unique long-term, regular and energy-wide study of a sample of (intrinsically different) LMXRBs. We expect this to be a step forward in the understanding of the physics and geometry of X-ray binaries.

REFERENCES

Bodaghee, A., Walter, R., Lund, N. and Rohlfs, R. 2004, these proceedings

Courvoisier, T.J.-L., Walter, R., Beckmann, V., et al. 2003, *A&A* 411, L53

D'Amico, F., Heindl, W. A., Rothschild, R. E. et al. 2001, *ApJ* 547, 147

Di Cocco, G., Caroli, E., Celesti, E., et al. 2003, *A&A* 411, L189

Di Salvo, T. & Stella, L. 2002, Proc. of the XXXVIIth Rencontres de Moriond, *The Gamma-Ray Universe*, Ed. A. Goldwurm, Doris N. Neumann and Jean Tran Thanh Van, 67

Di Salvo, T., Stella, L., Robba, N. R. et al. 2000, *ApJ* 544, L119

Done, C. & Gierliński. M. 2003, *MNRAS*, 342, 1041

Fender. R. P. & Hendry, M. A. 2000, *MNRAS* 317, 1

Gierliński, M., & Done, C. 2002, *MNRAS* 331, L47

Hasinger, C. & van der Klis, M. 1989, *A&A* 225, 79

Lebrun, F., Leray, J. P., Lavocat, P., et al. 2003, A&A, 411, 141

Liu, Q. Z., van Paradijs, J., van den Heuvel, E. P. J. 2001, A&A 368, 1021

Lund, N., Brandt, S., Budtz-Jorgensen, C., et al. 2003, *A&A* 411, L231

Mas-Hesse, J. M., Gimenez, A., Culbane, L., et al. 2003, *A&A* 411, L261

Mitsuda, K., Inoue, H., Koyama, K. et al. 1984, *PASJ* 36, 741

Mitsuda, K., Inoue, H., N. Nakamura et al. 1989. *PASJ* 41, 97

Muno, M. P., Remillard, R. A., Chakrabarty, D. 2002, *ApJ* 568, 35

Paizis, A., Beckmann, V., Courvoisier, T.J.-L. et al. 2003, *A&A* 411, L363

Parmar, A. N., Oosterbroek T., Del Sordo, S. et al. 2000, *A&A* 365, 175

Shaw, S. E., Westmore, M. J., Hill A. B. et al. 2004, astro-ph/0402587

Ubertini, P., Lebrun, F., Di Cocco, G., et al. 2003, *A&A* 411, L131

van der Klis, M., Kitamoto, S., Tsunemi, H. et al. 1991, *MNRAS*, 248, 751

van der Klis, M. 1995 in: *X-Ray Binaries*, Cambridge University Press, 126

Vedrenne, G., Roques, J.-P., Schönfelder, V., et al. 2003, *A&A* 411, L63

White, N. E., Peacock, A., Hasinger, G. 1986, *MNRAS* 281, 129

White, N. E., Stella, L. and Parmar 1988, *ApJ* 324, 363

Winkler, C., Courvoisier, T.J.-L., Di Cocco, G., et al. 2003, *A&A* 411, L1

Winkler, C., Gehrels, N., Schönfelder, V., et al. 2003b, *A&A* 411, L349

6.7 Future work

The monitoring programme has a lot of potential in unveiling many aspects of LMXRBs as a class.

Much work has still to be done in the coming months. The analysis of all the data will be kept up to date with the evolving software and kowledge of the instruments; light curves and hardness ratios will be regularly populating the web pages; based on the incoming results, main parameters will be selected to characterise the sources; detailed studies will be performed on each source.

In this thesis, a lot of effort has been put in gaining expertise on the *INTEGRAL* data analysis and to build the infrastructure. The up-coming work will also move in other directions: coordinated ground based observations will be intensified; the available simultaneous *RXTE* observations will be analysed. The latter means not only including soft X-ray spectral information but also including in the monitoring programme the timing analysis. Timing and spectral properties are very closely related and their study will help putting constraints on the models describing these systems (see e.g. Rodriguez et al. 2004, where we studied the energy dependence of the QPO amplitudes in GRS 1915+105 with *RXTE*).

Chapter 7
A PARTICULAR LMXRB: GX 5-1

7.1 Introduction

GX 5-1 (4U 1758-250) was first detected in 1968 (Fisher et al., 1968 and Bradt et al., 1968) and is a neutron star LMXRB. It is one of the six currently known Galactic Z sources [41] and displays a complete Z pattern (Kuulkers et al., 1994 and Jonker et al., 2002). Like most of the Z sources, it is located near the Galactic centre, which has rendered difficult its study due to source confusion and optical obscuration. Like all Z sources, it is a radio source and the determination of the radio counterpart allowed for extremely accurate position measurement which have led to a most likely candidate for an infra-red companion (Jonker et al. 2000).

The high persistent soft X-ray flux of GX 5-1 has enabled a thorough study of the source through many years and missions (e.g. Vaughan et al. 1994, Kuulkers et al. 1994, Jonker et al. 2002, Asai et al. 1994).

In the X-ray domain, neither pulsations nor bursts have been detected (Vaughan et al., 1994). The presence of a neutron star is inferred by the fact that this source has a typical Z-source spectral and temporal behaviour like other known neutron star LMXRBs for which bursts have been detected (e.g. Cyg X-2 and GX 17+2).

GX 5-1 displays secular shifts of the “Z” and intensity dips in the FB. As such, together with Cyg X-2 and GX 340+0 that show similar properties, it is thought to be a high inclination system, i.e. viewed “edge on”, for which obscuration from the disc can be important. The remaining three known Z sources, GX 349+2, GX 17+2 and Sco X–1, do not show such properties and thus are thought to be seen at a low inclination angle, i.e. ”face-on” (Kuulkers et al., 1994).

Timing properties typical for Z sources have been detected also in GX 5-1 i.e. the two types of quasi-periodic oscillations (HBO-NBO and twin kHz GPO peaks) and the three types of rapid flickering (LFN, VLFN and HFN) shown in Fig. 3.5, bottom-left (Kuulkers et al. 1994 and Jonker et al. 2002).

Also in the case of GX 5-1 the X-ray spectra can be well described in terms of the already introduced eastern and western model (Section 3.7.3). A sometimes complex interplay of the parameters of these models reproduces the spectral variability along the Z pattern (Asai et al. 1994).

The same richness of results is not present in the hard-X rays (> 30 keV). In this domain the detection of GX 5-1 has been much more difficult. Here the emission from GX 5-1 is dominated by the nearby LMXRB GRS1758-258. The missions before *INTEGRAL* were either not able to disentangle it from the black hole (e.g. *BeppoSAX*, *RXTE*) or with sufficient imaging capabilities

[41] The other known Galactic Z sources are the already mentioned GX340+0, GX349+2, Cyg X-2, GX 17+2 and Sco X-1.

but not sensitive enough to detect it (*GRANAT*/SIGMA).

7.2 Resolving the hard X-ray emission of GX 5-1 with *INTEGRAL*

With *INTEGRAL*, we were able for the first time to look into the hard X-ray emission of GX 5-1 free from contamination and with enough sensitivity to be able to study the spectral variations of the source along the Z pattern. The results of this work which is reproduced in this chapter, are presented in Paizis et al., 2004a. GX 5-1 has a clear hard emission, like the other Z sources, and its variability along the "Z" can be described in terms of the hot neutron star surface properties alone. We can study the "weather" around the neutron star "seeing" the temperature and size of the emitting surface change. This study does not bring to a spectral "proof" of the presence of a surface and therefore of a neutron star[42]. The soft varying seed photons culd be coming also from the accretion disc (western model). But indeed this kind of analysis of the poorly known hard X-ray spectral variations could bring us one step closer to finding a signature of the presence of a solid surface in the accreting object and/or closer to finding new differences/similarities among the sources traditionally classified on the basis of the soft X-rays (<20 keV).

It is interesting to see where GX 5-1 places itself in the wider frame of LMXRBs, i.e. in the soft to hard X-ray luminosity graph already introduced in Fig. 3.7, right panel. Using the average JEM-X and ISGRI spectra with the eastern model best fit shown in Fig. 8 of the paper, and extrapolating the *INTEGRAL* flux down to 1 keV, we obtain the new updated graph shown in Fig. 7.1,

Like in the case of GX 17+2 and GX 349+2, GX 5-1 lies outside the burster box but it is still in the neutron star binary zone, i.e. with $L_{20-200\,\mathrm{keV}} \lesssim 1.5 \times 10^{37}$ erg s^{-1}.

[42]For GX 5–1, we know that it is a neutron star LMXRB because it displays spectral and timing properties similar to known neutron star binaries where type I X-ray bursts were detected (e.g. GX 17+2).

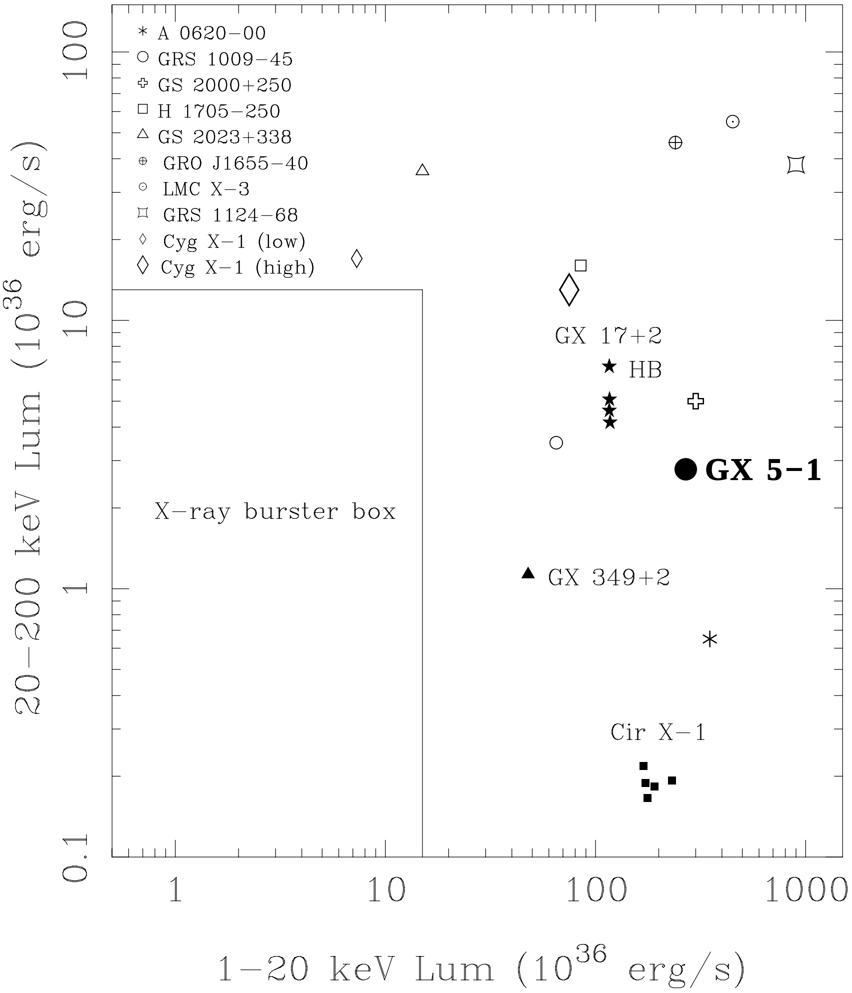

Figure *7.1: 20-200 keV versus 1-20 keV luminosities of BH binaries (open symbols, from Barret et al. 2000) and NS type-Z binaries (filled symbols). The so-called X-ray burster box is plotted as a solid line. This figure is taken from Di Salvo et al., 2001b to which we added GX 5-1 based on our INTEGRAL observations.*

Astronomy & Astrophysics manuscript no. GX5-1 July 12, 2004
(DOI: will be inserted by hand later)

Resolving the hard X-ray emission of GX 5-1 with *INTEGRAL*⋆

A. Paizis[1,2], K. Ebisawa[3,1], T. Tikkanen[4], J. Rodriguez[5,1], J. Chenevez[6], E. Kuulkers[7], O. Vilhu[4] and T.J.-L. Courvoisier[1,8]

[1] *INTEGRAL* Science Data Centre, Chemin d'Ecogia 16, 1290 Versoix, Switzerland
[2] CNR-IASF, Sezione di Milano, Via Bassini 15, I–20133 Milano, Italy
[3] NASA Goddard Space Flight Center, Code 662, Greenbelt, MD 20771, USA
[4] Observatory, P.O.Box 14, Tähtitorninmäki, Fi–00014 University of Helsinki, Finland
[5] CNRS, FRE 2591, CE Saclay DSM/DAPNIA/SAp, F–91191 Gif sur Yvette Cedex, France
[6] Danish Space Research Institute, Juliane Maries Vej 30, DK–2100 Copenhagen, Denmark
[7] Research and Scientific Support Department of ESA, ESTEC, P.O. Box 299, NL–2200 AG Noordwijk, The Netherlands
[8] Observatoire de Genève, 51 chemin des Mailletes, CH–1290 Sauverny, Switzerland

Received / Accepted

Abstract. We present the study of one year of *INTEGRAL* data on the neutron star low mass X-ray binary GX 5–1. Thanks to the excellent angular resolution and sensitivity of *INTEGRAL*, we are able for the first time to obtain a high quality energy spectrum of GX 5–1 from $\sim$5 keV to $\sim$100 keV without contamination from the nearby black hole candidate GRS 1758-258. During our observations GX 5–1 is mostly found in the horizontal and normal branch of its hardness intensity diagram. A clear hard X-ray emission is observed above $\sim$ 30 keV which exceeds the exponential cut-off spectrum expected from lower energies. The hard excess is explained by introducing Compton up-scattering of soft photons from the neutron star surface due to a thin hot plasma expected in the boundary layer. The spectral changes of GX 5–1 downward along the "Z" pattern in the hardness intensity diagram can be well described in terms of monotonical decrease of the blackbody surface temperature. This may be a consequence of the gradual expansion of the boundary layer as the mass accretion rate increases.

Key words. X-rays: binaries – binaries: close – stars: neutron – stars: individual:GX 5-1

1. Introduction

Low-mass X-ray binaries (LMXRBs) are systems where the compact object, either a neutron star (NS) or a black hole candidate (BHC), accretes matter from a companion with a mass $M \lesssim 1M_{\odot}$. LMXRBs hosting a weakly magnetised neutron star can be broadly classified in two classes (Hasinger & van der Klis 1989): high luminosity/Z sources and low luminosity/Atoll sources. In the colour-colour (CC) and X-ray hardness intensity diagrams (HID), Atoll sources display an upwardly curved branch while Z sources describe an approximate "Z" shape. The study of these sources in the hard X-ray domain has proven important especially in the recent years, in the light of the discovery of hard tails extending up to a few hundred keV in NS LMXRBs. This kind of hard emission was thought to be a prerogative of BHCs and had been proposed as a possible signature for the presence of a BH. Hard tails discovered in about 20 NS LMXRBs of the Atoll class as well as in some Z sources showed that NS binaries as well can power such an emission. In all these cases, an additional power-law component had to be introduced to describe the hard emission dominating the spectra above $\sim$30 keV (Barret & Vedrenne (1994); Di Salvo & Stella (2002) and references therein).

GX 5–1 (4U 1758-25) is a Z source and displays a complete Z pattern in the CC and HIDs (Kuulkers et al. 1994; Jonker et al. 2002) showing secular shifts of the "Z". Previous GX 5-1 hard X-ray data were almost always contaminated by the nearby (40′) BHC LMXRB GRS 1758-258. The first mission to clearly resolve GX5-1 from GRS 1758-258 in the high energy domain was SIGMA on board *GRANAT* (Paul et al. 1991). SIGMA observations showed that GX 5–1 was $\sim$30-50 times brighter than GRS 1758-258 below 30 keV, but above 30 keV the emission from the region was mostly to be attributed to GRS 1758-258 (Sunyaev et al. 1991; Gilfanov et al. 1993).

In this paper we report the results of one year of monitoring of GX 5–1 with the INTErnational Gamma-Ray Astrophysics Laboratory, *INTEGRAL* (Winkler et al. 2003). *INTEGRAL* is an ideal mission to study the hard X-ray emission of sources in the crowded Galactic Centre region. *INTEGRAL*/IBIS (Ubertini et al. 2003) has high sensitivity, about $\sim$10 times better than SIGMA, coupled to imaging capability with 12′ angu-

Send offprint requests to: Ada.Paizis@obs.unige.ch
⋆ Based on observations with *INTEGRAL*, an ESA project with instruments and science data centre funded by ESA member states (especially the PI countries: Denmark, France, Germany, Italy, Spain, and Switzerland), Czech Republic and Poland, and with the participation of Russia and the USA.

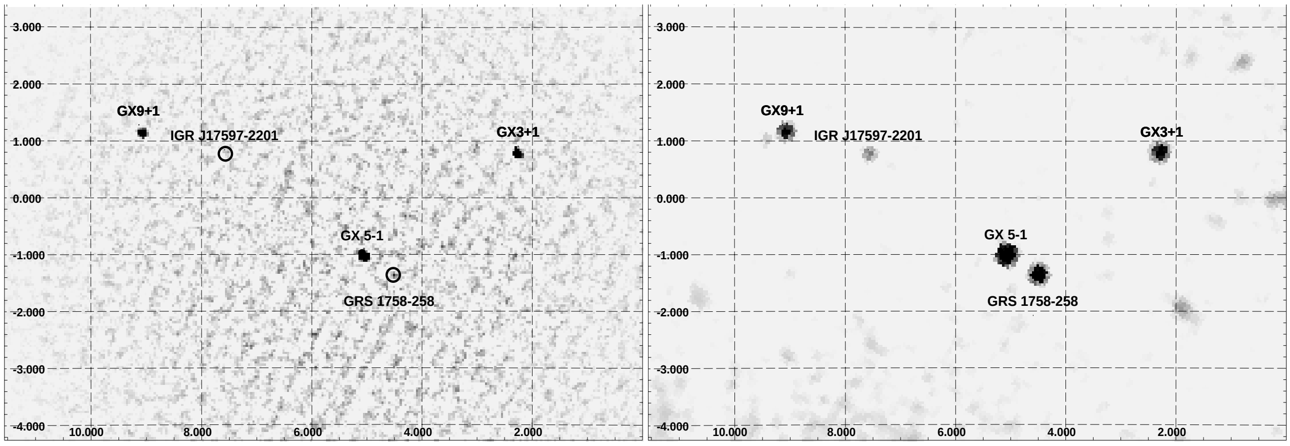

Fig. 1. *Left panel*: JEM–X mosaic image of GX 5–1 in the 5–10 keV band (44 ScWs, ∼76 ksec). *Right panel*: IBIS/ISGRI mosaic image of GX5–1 in the 20–30 keV band (90 ScWs, ∼167 ksec).

lar resolution above 20 keV. In addition, two X-ray monitors, JEM–X1 and JEM–X2 (Lund et al. 2003), provide the soft-X ray simultaneous coverage (3–35 keV, $3'$ angular resolution). Effectiveness of *INTEGRAL* in the study of Galactic bulge bright LMXRBs has been demonstrated in Paizis et al. (2003, 2004) using only initial data.

Thanks to *INTEGRAL*'s imaging capabilities in combination with its high sensitivity, we are able for the first time to study the energy spectrum of GX 5–1 above ∼30 keV and its spectral variations, free from contamination.

2. Observations and data analysis

INTEGRAL performs a Galactic Plane Scan (GPS) about every 12 days and Galactic Centre Deep Exposures (GCDEs) according to the Galactic Centre visibility. Among these observation programs, GX 5–1 has been continuously in the *INTEGRAL* field of view around two distinct periods, April 2003 (*INTEGRAL* Julian Date[1], IJD$\simeq 1200$, hereafter data set 1) and October 2003 (IJD$\simeq 1380$, hereafter data set 2).

For the analysis we used the available X-ray monitor, JEM–X2 (hereafter JEM–X), for soft photons (3–20 keV) and the low energy IBIS detector, ISGRI (Lebrun et al. 2003) for harder photons (20–200 keV).

JEM–X and IBIS/ISGRI data were reduced using the latest available Off-line Scientific Analysis (OSA) package, pre-OSA 4.0. The description of the algorithms used in the scientific analysis can be found in Westergaard et al. (2003) and Goldwurm et al. (2003) for JEM–X and IBIS/ISGRI respectively.

XSPEC 11.3.0 was used for the spectral analysis. The Comptonisation model by Nishimura et al. (1986) (COMPBB) was updated so that the cutoff energy of the model, originally at 70 keV, would suit ISGRI spectra (i.e. moved up to 300 keV).

We used JEM–X to build the HIDs. This was done using all the JEM–X data available with off-axis angle $< 5°$ which led to 113 science windows (hereafter ScWs[2]) each of about 2000 sec exposure. We extracted individual images from each ScW in 3 energy bands (3–5, 5–12 and 12–20 keV). A mosaicking tool by Chenevez et al. (2004) was used to obtain the final JEM–X mosaic image. Within each ScW we extracted 100 s bin light-curves and used one ScW and 100 s data bins to build the HID. For the spectral fitting of JEM–X data it is preferable to have the source within $3°$ off-axis (better vignetting correction and signal-to-noise ratio). This led to 44 JEM–X ScWs. Spectra were grouped so that each new energy bin contained at least 200 counts. Based on Crab calibration results, 3% systematics have been applied between 5 and 22 keV were the spectral analysis has been performed.

In the case of ISGRI we selected the data within the totally coded field of view (FOV, $<4.5°$), resulting in a total of 90 ScWs (44 of which are in common with JEM–X). We extracted individual ScW images in 10 energy ranges with the boundaries 20, 30, 40, 50, 60, 80, 100, 150, 300, 500 and 1000 keV. The fluxes extracted in each image and energy band were used to build the light-curves of GX 5–1. Images from each ScW were combined in a final mosaic from which an overall ISGRI spectrum was extracted. Spectra were also extracted from each ScW with the Least Square Method and were further grouped so that each new energy bin had a minimum of 20 counts. 5% systematics have been applied to all channels. For the spectral fitting we used the newly (December 2003) available, pre-OSA 4.0, ancillary response file (ARF) and redistribution matrix (RMF) re-binned to 16 spectral channels between 20 and 120 keV.

Simultaneous ISGRI and JEM–X fitting was carried out for the 44 JEM–X ScWs. The remaining 46 ISGRI ScWs were not analysed separately because there was not enough statistics to study ISGRI spectra alone on a ScW basis. In the JEM–X - ISGRI simultaneous fit a cross-calibration factor was let free to vary.

[1] The *INTEGRAL* Julian Date is defined as the fractional number of days since January 1, 2000 (TT). IJD=MJD-51544.

[2] A science window is the basic unit of an *INTEGRAL* observation. Under normal operations one ScW will correspond to one pointing or one slew. In our case we considered 113 pointings.

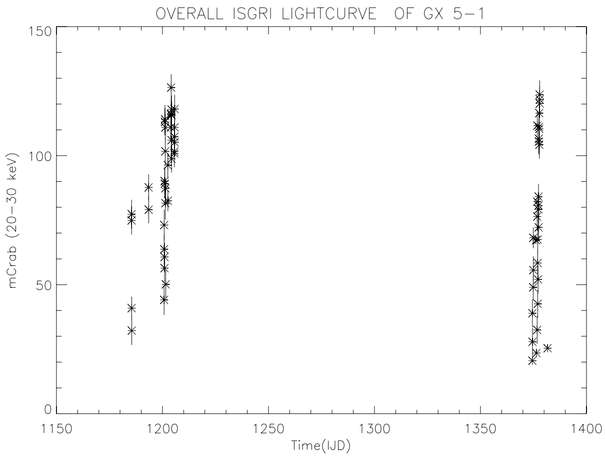

Fig. 2. IBIS/ISGRI light curve of GX 5–1 in the 20–30 keV band in units of mCrab. Each point is one ScW (about 2000 s). In the softer band (i.e. in JEM–X) the source is much brighter, around 1 Crab.

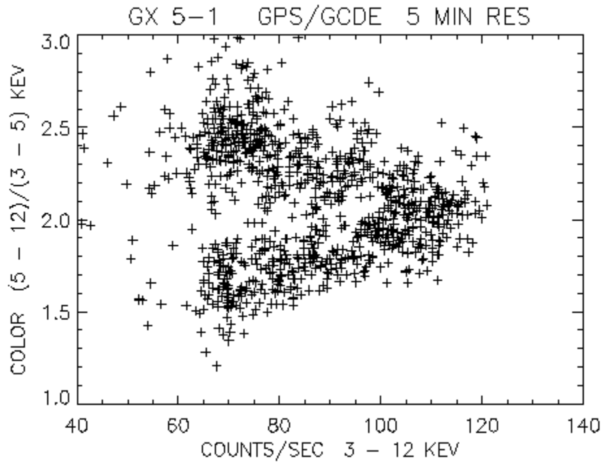

Fig. 3. HID of GX5–1 with JEM–X (data set 1). The soft colour is the (5–12 keV) to (3–5 keV) flux ratio. The graph was built using 100 s time bins that were smoothed with a three bin box-car: this means that each 100 s data value is replaced by the mean of the three neighbouring values. The smoothing was chosen for visualisation purposes as it makes the ”Z” more evident. The horizontal branch (upper part, soft colour > 2) and normal branch (lower part, soft colour < 2) are clearly visible.

3. Results

3.1. Overview of the data

Figure 1 shows the JEM–X, 5–10 keV, and IBIS/ISGRI, 20–30 keV, mosaic image of the region of GX 5–1. The nearby BHC GRS 1758-258 is rather dim in the softer energy range (JEM–X) and becomes much brighter in the harder range (ISGRI) where it is clearly disentangled from GX 5–1. In Fig. 2 the overall (90 ScWs) ISGRI 20–30 keV light curve of GX 5–1 is shown.

3.2. The hardness intensity diagrams

In order to build the HID of GX 5–1 we used the JEM–X soft colour, defined as the (5–12 keV) to (3–5 keV) flux ratio, plotted versus the JEM–X intensity (defined as the 3–12 keV flux).

Figure 3 shows the HID we obtained for the first data set (April 2003). The graph was built starting from the 100 s bins that were smoothed to a 5 minute final bin. The horizontal branch, HB, and normal branch, NB, are quite evident while the flaring branch, FB the last part of the ”Z”, is missing. Note the similarity with the HID derived from *GINGA*/ASM data (van der Klis et al. 1991) and *Mir/Kvant* TTM data (Blom et al. 1993).

Figure 4 shows the ”raw”, i.e. non-smoothed, HIDs obtained for the two data sets (April 2003 and October 2003 respectively). In the first data set the HB-NB vertex was set to (118,2.15) judging from the overall distribution of the data points. Then the slopes of the ”Z” were calculated so that an equal number of data points were left on either side of the line. The deduced slopes are shown in Fig. 4 with a solid line. As the first data set has a cleaner ”Z” pattern, we used this one as the ”true” one to which the second ”Z” was forced to bend. This was done shifting the HB-NB vertex of the second data set until the slopes of HB and NB became equal to those of the first data set. This led to a vertex in the second set at (115.1, 2.4) which resulted in a clear secular shift from 2.15 to 2.4 in the soft colour of the vertex.

Hint for a FB and Dipping FB (DFB) is also seen in the second data set, Fig. 4 right panel, where the low intensity data points correspond to two ScWs where a FB/DFB behaviour was seen. The two ScWs are next to each other in time and immediately after the last NB ScW in what seems a short deviation from the HB/NB tracks. The deduced slope for these points is indicated by the dashed line in Fig. 4, right panel. The FB and DFB have already been detected in GX 5–1 with *EXOSAT*, *GINGA* (Kuulkers et al. 1994) and *RXTE* (Jonker et al. 2002). In these cases the FBs showed different orientations in the HIDs. This is mainly due to the combination of different energy bands. In fact in all cases the flux in the 6–10 keV band increases in the FB and this is consistent with the orientation of the FB we find based on our JEM–X soft colour definition.
Since the current data have an almost continuous coverage from the HB through the NB while coverage of the FB is very poor, in this paper we focus on the HB and NB.

3.3. The S_Z parameter

In order to investigate the correlation between the source position in the ”Z” pattern of the HID and the spectral behaviour, we introduced a one dimensional parameter that measures the position on the ”Z”: S_Z (Dieters & van der Klis (2000) and references therein). Strong evidence shows that the mass accretion rate $\dot{M}$ of individual Z sources increases from the top-left to the bottom-right of the ”Z” pattern (Hasinger et al. 1990), i.e. along the HB, NB and FB. Hence, the S_Z parameter is supposed to be monotonically related to the mass accretion rate.

For each JEM–X data point (100 s bin and one ScW bin) in the HIDs, the two projections onto both branches and the distance to each branch were computed. The branch at the shortest

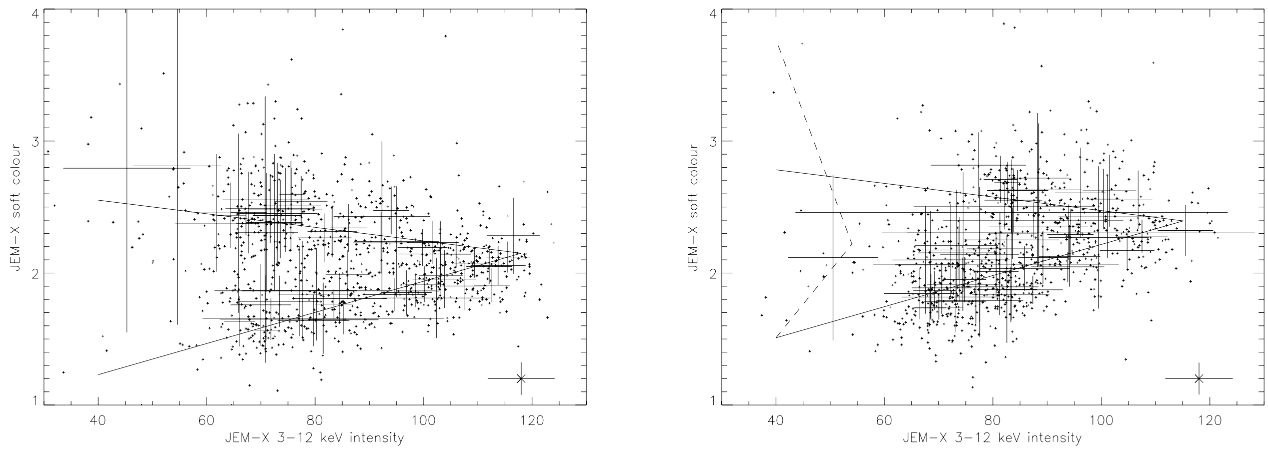

Fig. 4. HID of GX5–1 with JEM–X for the two data sets. The soft colour is the (5–12 keV) to (3–5 keV) flux ratio. The scattered data points are 100 s bins while the points with error bars are one ScW bins. The average statistical error of the 100 s bins is shown in the bottom right of the graphs. The ScW bin values are computed as average of 100 s bins and the associated error is not the statistical one but a measure of how much the source moved along the "Z" track within the ScW. The solid line shows the deduced "Z" for the two data sets. *Left panel*: data set 1 (April 2003). *Right panel*: data set 2 (October 2003). The "Z" shape is less evident in this data set with respect to the left panel. This change could be intrinsic to the source as the exposure time in the two data sets is comparable (58 ScWs in data set 1 and 55 ScWs in data set 2). The dashed line indicates the path of data points that correspond to ScWs where a FB/DFB behaviour was seen.

distance was chosen and after confirmation via visual inspection, to ensure that data points did not jump from branch to branch outside the vertex area, the value of S_Z was assigned. The scale was set so that the HB-NB vertex was at $S_Z = 1$ while $S_Z = 0$ and $S_Z = 2$ were assigned at a 3–12 keV intensity of 40 counts/s (beginning of HB and end of NB respectively). In this frame, $S_Z<1$ means the source is on the HB (lower $\dot{M}$) and $1<S_Z<2$ means that the source is on the NB (higher $\dot{M}$). $S_Z>2$ corresponds to the two possible FB ScWs.

3.4. Energy Spectral Modeling

We averaged all the ISGRI and JEM–X data to achieve the best statistics and tried to find the most physically reasonable spectral model to fit the entire data set. The ISGRI (average) spectrum was obtained from the mosaic image shown in Fig. 1, right panel, and the JEM–X total spectrum by averaging the 44 JEM–X ScW spectra. In this case, the JEM-X spectrum was further grouped to have a number of energy bins comparable to ISGRI.

The X-ray spectra of bright LMXRBs hosting a NS are generally described as the sum of a soft and a hard component. Two different models are often adopted to describe this composite emission. They are the so-called *eastern* model (Mitsuda et al. 1984) and *western* model (White et al. 1986).

In the eastern model the softer part of the spectrum is a multi-colour disc describing the emission from the optically-thick, geometrically-thin accretion disc (XSPEC DISKBB model, Mitsuda et al. (1984)). The temperature at the inner disc radius kT_{in} and the normalisation, linked to the inner disc radius itself, are the parameters of the model. The harder part of the spectrum is a higher temperature Comptonised blackbody describing the emission from the NS boundary layer (COMPBB model, Nishimura et al. (1986)). Photons from the NS surface at a temperature kT_{bb} are up-scattered by a plasma of temperature kT_e and optical depth τ. In this case the normalisation is linked to the seed photon emitting area.

In the western model a single temperature blackbody (from the optically thick boundary layer) describes the soft part of the spectrum (BB model in XSPEC). Comptonisation of soft seed photons (kT_0) in the innermost region of the accretion disc by a corona of given temperature kT_e and optical depth τ describes the hard part (e.g. COMPTT model, Titarchuk (1994)). We used the eastern and western model to fit the average JEM–X and ISGRI spectra simultaneously, and compared the results. In both cases a galactic absorption by a fixed hydrogen equivalent column density of $N_H = 3\times10^{22}$ cm^{-2} (Asai et al. 1994) was added. The results of the fit are given in Table 1 and Fig. 5.

Table 1. Best fit parameters for the average ISGRI and JEM–X spectra of GX 5–1. $F_{5-20\,\mathrm{keV}}$ and $F_{20-100\,\mathrm{keV}}$ are the unabsorbed fluxes in the 5-20 keV and 20-100 keV range respectively in units of erg s^{-1} cm^{-2}; d.o.f. = degrees of freedom. The indicated errors are at 1σ. No error means the parameter was fixed to the indicated value. The cross-calibration factor was frozen to 0.9 for ISGRI with respect to JEM-X.

	Eastern model	Western model
kT_{in} or kT	1.4 keV	1.7 keV
kT_{bb} or kT_0	1.93±0.01 keV	0.87±0.02 keV
kT_e	10 keV	3.02±0.02 keV
τ	0.37±0.01	4.15±0.06 keV
Red. χ^2	1.12 (14 d.o.f.)	6.21(13 d.o.f.)
$F_{5-20\,\mathrm{keV}}$	1.54×10^{-8}	1.54×10^{-8}
$F_{20-100\,\mathrm{keV}}$	3.41×10^{-10}	3.10×10^{-10}

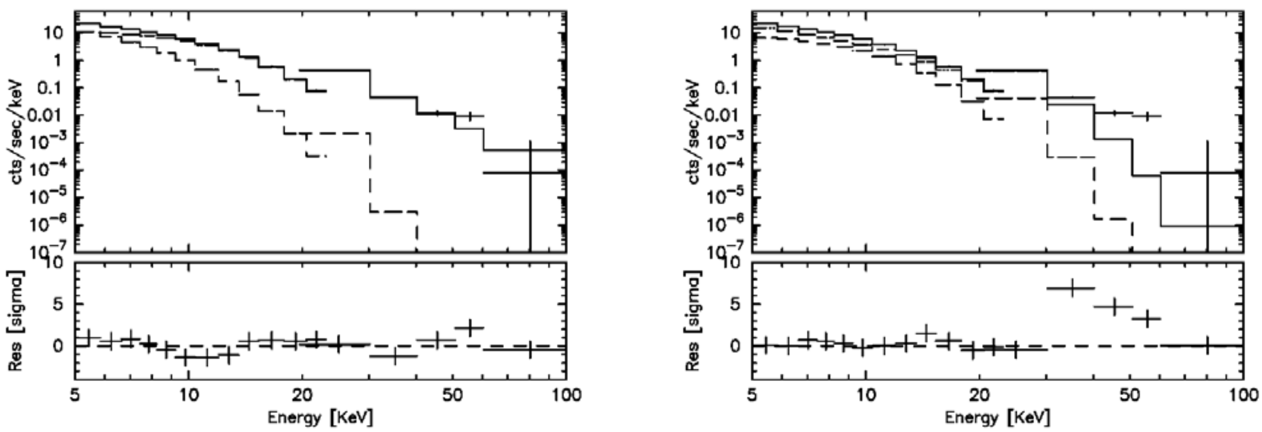

Fig. 5. *Left panel*: best fit of the average ISGRI and JEM–X spectra using the eastern model. The parameters of the fit are given in Table 1. Residuals in terms of σ and the single spectral components are shown. *Right panel*: best fit of the average ISGRI and JEM–X spectra using the western model. Residuals in terms of σ and the single spectral components are shown. A hard excess above $\sim$30 keV is visible. The parameters of the fit are given in Table 1.

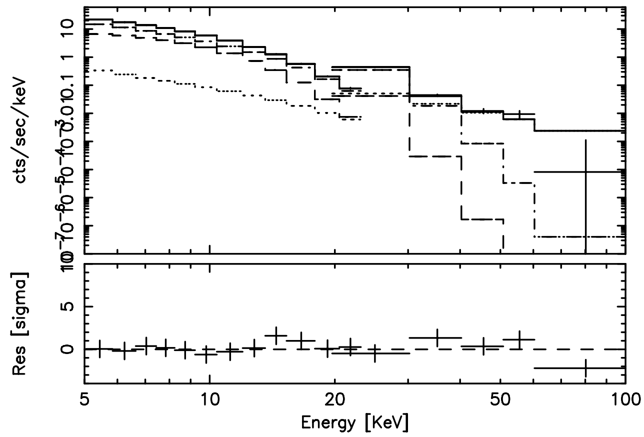

Fig. 6. Best fit of the average ISGRI and JEM–X spectra using the western model to which a power-law with fixed photon index γ=2.5 was added. Red. χ^2=1.2 (12 d.o.f.). Residuals in terms of σ and the single spectral components are shown.

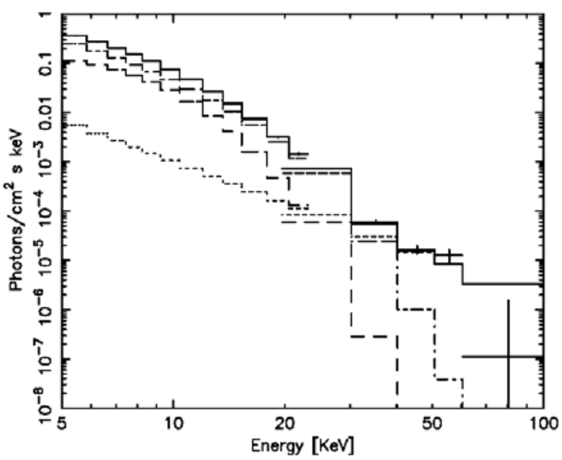

Fig. 7. Photon spectrum of GX 5–1 obtained with the western plus additional power-law model of Fig.6. *Dash*: NS boundary layer emission (BB). *Dot-dash*: Comptonisation of innermost region of the accretion disc (COMPTT). *Dot*: additional power-law. *Solid*: total spectrum.

Both models can describe the spectral shape below $\sim$30 keV equally well. However, in the western model, there is a significant residual in the ISGRI data above $\sim$30 keV. In the eastern model this excess is reasonably well described. This is because the western model predicts an exponential cut-off above $\sim$10 keV, while the eastern model describes the spectral "flattening" above $\sim$20 keV as a Comptonised hard-tail emission. Probably, this spectral flattening, or hard-excess, has the same origin of what has been observed in other NS LMXRBs (Barret & Vedrenne (1994); Di Salvo & Stella (2002)). In fact, adding a power-law component with fixed photon index γ=2.5 in the western model results in a good fit of the observed hard-excess as shown in Fig. 6, count spectrum and residuals, and Fig. 7, photon spectrum. In the 5–100 keV band the power-law component alone contributes to about 1.5% of the total luminosity. Figure 8 shows the photon spectrum obtained with the eastern model parameters shown in Table 1. Since the eastern model provides a physical interpretation for the hard tail, we focus on this model for the analysis and discussion of the spectral changes of GX 5–1.

3.5. Spectral variability along the "Z"

We studied the spectral variation of GX 5–1 over the S_Z parameter using the eastern model. The soft component (DISKBB) was frozen to the average spectra values. The plasma temperature kT_e was fixed at a value of 10 keV, since this parame-

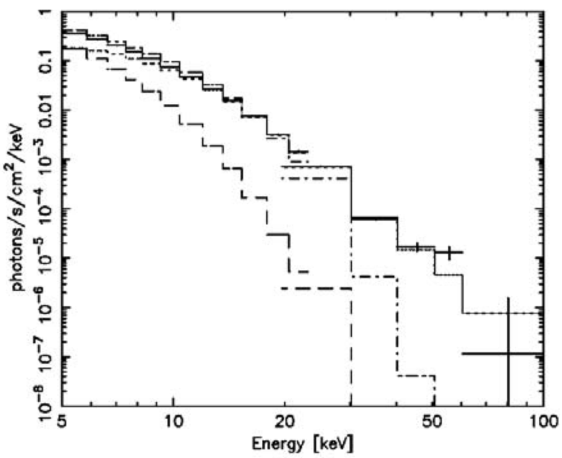

Fig. 8. Photon spectrum of GX 5–1 obtained with the eastern model described in Table 1. *Dash*: soft, disc blackbody component. *Dot-dash*: hard, NS surface blackbody component *without* Comptonisation (τ=0). A hard excess is evident. *Dot* (basically overlapping with the solid line): NS blackbody component to which Comptonisation from a 10 keV, τ=0.37 plasma was added. In the eastern model, Comptonisation from a hot thin plasma gives a reasonable fit of the hard excess. In the western model this was achieved adding a power-law to the model. *Solid*: total spectrum (disc component and NS Comptonised component). The latter two are basically overlapping above 10 keV i.e. almost all the emission is coming from Comptonisation of the NS surface photons.

ter is strongly correlated with τ. The normalisation of the hard component, kT$_{bb}$ and τ were let free to vary as well as the instrument cross-calibration factor. An average value of reduced $\chi^2\simeq$1.2 was obtained. We found a clear relation between the S$_Z$ value and the deduced kT$_{bb}$ for all the ScWs. We proceeded fitting the data letting in one case kT$_{bb}$ vary (τ =0.4) and in the other τ vary (kT$_{bb}$=2.0 keV). In both cases the normalisation was let free as well. Fixing kT$_{bb}$ resulted in a much worse fit (average reduced $\chi^2\simeq$2.5) while fixing τ gave an equally acceptable fit (average reduced $\chi^2\simeq$1.3).
The combined JEM–X and ISGRI spectral fitting for two ScWs, one for the HB and the other one for the NB, are shown in Fig. 9, left and right respectively. The HB case is significantly harder than the NB. With *INTEGRAL*, within one ScW we are able to study the spectral state of GX 5–1 and to see the source variability above 20 keV that has never been studied before. On the other hand, the softer part of the spectrum dominated by the disc emission cannot be constrained and thus we fixed it to the value found from the JEM-X average spectrum.

Fixing the disc component as well as the Comptonising plasma parameters gave a good description of the data. Spectral changes of GX 5–1 along the "Z" were described by variation of the properties of the seed photons alone i.e. of the blackbody emission from the NS surface heated by the boundary layer (hereafter hot NS surface). These are the emitting hot NS surface size, linked to the normalisation, and its temperature kT$_{bb}$.

Figure 10 shows the variation of the emitting hot NS surface area and temperature kT$_{bb}$ along the "Z" (left and right panel respectively). While GX 5–1 moves from the HB to the NB (left to right in Fig. 10), the size of the emitting surface increases while its temperature decreases.

4. Discussion

Our observations constitute the first opportunity in which the Z source GX 5–1 could be monitored in a long term in the hard X-ray domain without contamination from the nearby BHC GRS 1758-258.
The source was thoroughly covered by *INTEGRAL* mainly during two periods (April and October 2003). The HIDs of GX 5–1 for the two periods show a clear secular shift. This is consistent with previous observations of GX 5–1 itself as well as of other Z sources (Kuulkers et al. (1994); Kuulkers & van der Klis (1995) and references therein) for which a secular shift was detected.

In our data GX 5–1 covers widely the HB and NB while very poor coverage of the FB is seen.

4.1. Hard X-ray Emission

The ISGRI and JEM–X average spectra show that GX 5–1 has a clear hard X-ray emission. This "flattening" above 20 keV is well explained within the eastern model in terms of Comptonisation of soft seed photons by a hot optically thin plasma. This spectral flattening has probably the same origin as the hard tails observed in other NS LMXRBs (Barret & Vedrenne 1994; Di Salvo & Stella 2002). In fact, in these cases the spectrum can be well described in the frame of the western model to which an extra powerl-law component has to be added to account for the hard excess. The Comptonising component has generally a temperature kT$_e$ of a few keV and an optical depth τ>1. The photon index of the additional power-law for the different sources is between 1.6 and 2.7. These values are consistent with what we found for GX 5–1. This model is phenomenologically close to the eastern model that we favoured here for the physical interpretation that it allows us to give to the various spectral components. The softer part of the spectrum is dominated by the accretion disc emission that we modelled with DISKBB in the XSPEC terminology. The normalisation of this component led to an inner disc radius of R$_{in}$(cosθ)$^{1/2}$ $\simeq$14(cosθ)$^{1/2}$ km for an assumed source distance of 8 kpc. θ is the angle between the normal to the disc and the line of sight. In the inner region of the disc, a hot outer layer affects the emergent spectra by Comptonisation. This leads to an observed temperature T$_{col}$ which is higher than the effective temperature T$_{eff}$. As a consequence the observed inner disc radius is underestimated by a factor of (T$_{col}$/T$_{eff}$)^2. With this hardening factor correction (= 1.5, Shimura & Takahara (1995)) we obtained an inner disc of about R$_{eff}$ (cosθ) $^{1/2}$ $\simeq$30(cosθ)$^{1/2}$ km. The harder part of the spectrum is dominated by a Compton component in which the soft seed photons are a varying blackbody emission that we associate to the surface of the NS heated by the boundary layer (hot NS surface).

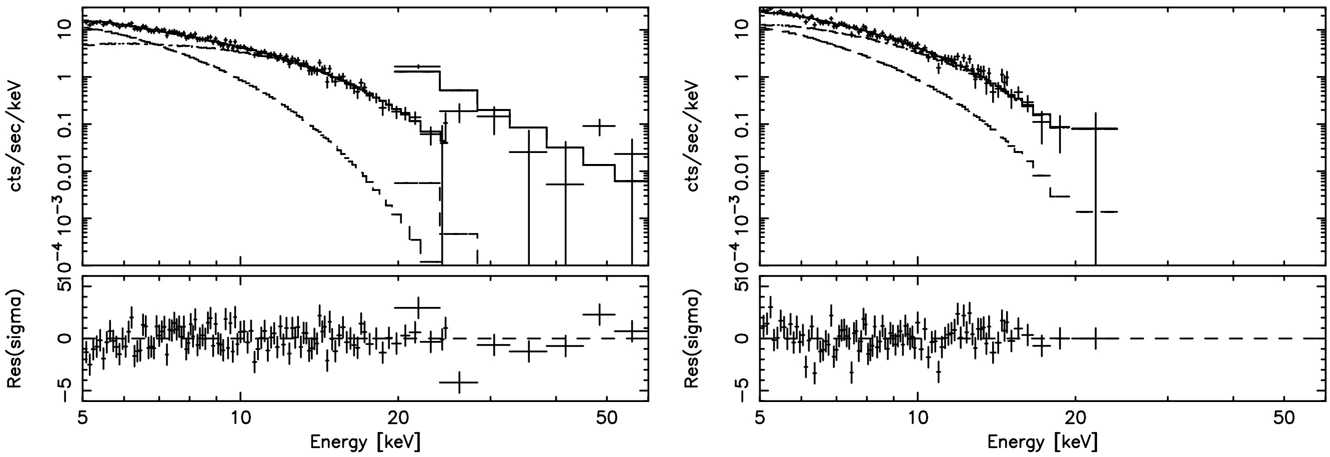

Fig. 9. ISGRI and JEM–X spectra for GX 5–1 in two different ScWs. The best fit and residuals in terms of σ are shown. The two components of the model (DISKBB and COMPBB) are also shown (dashed lines). The Comptonising component is frozen to kT$_e$=10 keV and τ=0.4. *Left panel*: ScW 012000950010 (IJD=1377.57, UTC=2003-10-09). For this ScW S$_Z$=0.50, i.e. GX 5–1 is in the HB. kT$_{bb}$=2.35 keV, red. χ^2=1.4 (112 d.o.f.). (The residuals obtained in the two ISGRI bins between 20–30 keV are not significant as they are due to known ISGRI systematics).*Right panel*: ScW 012200110010 (IJD=1381.63, UTC=2003-10-13). S$_Z$=1.56 i.e. GX 5–1 is in the NB. The spectrum is softer, only one ISGRI ($>$ 20 keV) data point met the requirement of a minimum of 20 counts per bin. kT$_{bb}$=1.49 keV, red. χ^2=1.5 (89 d.o.f.)

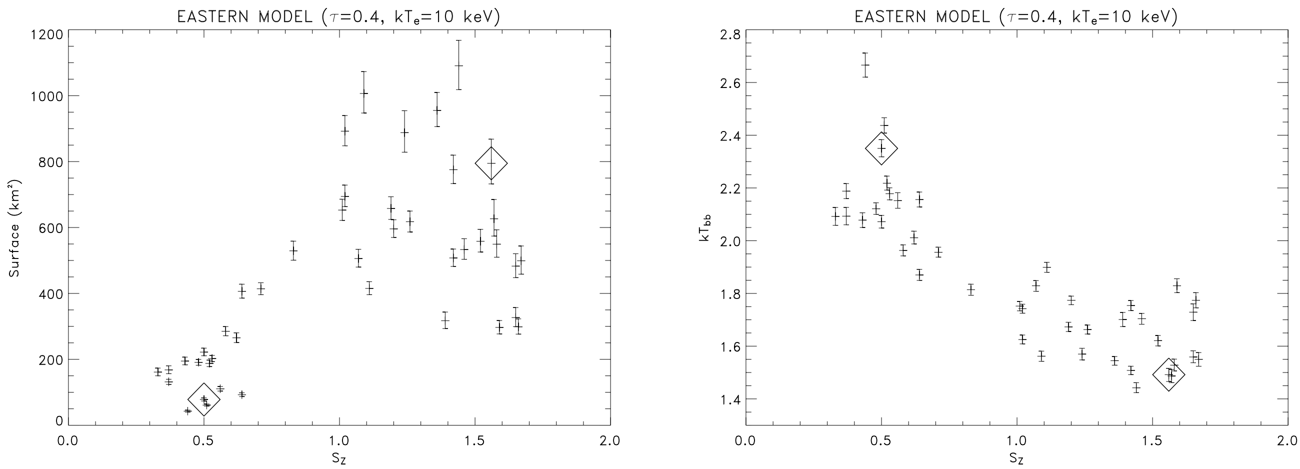

Fig. 10. Relations among the seed photons' properties and position of the source in the "Z". The electron plasma temperature kT$_e$ and the optical depth were frozen to 10 keV and 0.4 respectively. In both panels the two ScWs of Fig. 9 are highlighted. *Left panel*: relation between the blackbody emitting surface and S$_Z$. The surface is in units of km^2 and is computed as $\pi \times d^2 \times$normalisation, where d is the distance of the source in units of 10 kpc, assumed to be 0.8. This relation has a correlation coefficient of R=0.54 in Spearman statistics with a probability of having the same correlation with a randomly distributed sample of P$_{rand}\simeq$10^{-4}. *Right panel*: relation between the derived blackbody temperature kT$_{bb}$ and S$_Z$. In this case the correlation coefficient was of R=$-$0.81 with P$_{rand}\simeq$10^{-11}.

The Comptonising medium is a 10 keV, τ=0.4 medium and it is not seen to vary in our data set.

4.2. Spectral Variation

The spectral changes of GX 5–1 along the "Z" can be explained by the smooth variation of the physical properties of the seed photons originating from the hot NS surface: the surface area increases, the temperature decreases, the spectrum becomes softer, GX 5–1 moves along the HB towards the NB.

This scenario is different from the ones that e.g. Hasinger et al. (1990) and Hoshi & Mitsuda (1991) proposed to explain *GINGA* data of Cyg X–2 and GX 5–1 respectively. Hasinger et al. (1990) studied the spectral variations of Cyg X-2 using both the eastern and western model. The temperature and the luminosity of both components (soft and hard) were let free to vary in both models and a rather complicate interplay of the parameters of both components was describing the spectral variations of the source along the "Z" pattern. Hoshi & Mitsuda (1991) used the eastern model for GX 5–1 and the spectral changes were also in this case due to the variation of different parameters: in the NB the inner disc radius temperature kT$_{in}$ and the NS boundary layer temperature kT$_{bb}$ remained constant and spectral shape changes were explained by an increase of the emission area (from lower left to upper right NB). While the spectrum became harder, in the HB, an additional parameter, kT_{in}, was let free to reproduce the trend of the data. Unlike *GINGA*, with *INTEGRAL* data we can not constrain the variability of the disc component and thus we fixed it to the values found from the average spectra. But, for the first time, we can study the variability of GX 5–1 above 20 keV. The clear result given by the data is that we are able to describe the spectral variations of the source along the whole detected "Z" pattern (NB to HB) with smooth variations of parameters of a single physical component, the hot NS surface. In our data the Comptonising component is not seen to vary.

A common trend to all the scenarios is the fact that the source spectrum becomes harder from the NB to the HB, i.e. for a lower value of mass accretion rate. In LMXRBs there seems to be a global anti-correlation between the mass accretion rate and spectral hardness (Barret & Vedrenne 1994). Theoretical interpretations for this general trend have already been discussed (Inogamov & Sunyaev 1999; Popham & Sunyaev 2001; Kluzniak & Wagoner 1985).

Popham & Sunyaev (2001) have computed the boundary layer structure and its evolution with mass accretion rate $\dot{M}$. They found a significant dependence of the boundary layer size (both height and radial extension) with $\dot{M}$. Matter falls on a portion of the NS surface that is touched by the boundary layer. This part of the NS surface is thermalised and emits blackbody emission. As $\dot{M}$ increases, the area covered by the boundary layer will increase and so will the NS surface responsible of the blackbody emission. This is the same trend we found in the case of GX 5–1 (Fig. 10, left): S_Z, i.e. $\dot{M}$, increases and the emitting NS surface increases. The resulting blackbody luminosity of the NS surface did not undergo important variations. The 5–100 keV observed luminosity reached a maximum variation of a factor of $\sim$3, unabsorbed $L_{5-100\,\mathrm{keV}}$[3]$\simeq$(0.6-1.7)$\times 10^{38}$ erg s^{-1}. This is small compared to the NS emitting surface variation, Fig. 10 left. $L_{5-100\,\mathrm{keV}}$ is the total luminosity obtained from the composition of soft and hard component between 5–100 keV but the variation in $L_{5-100\,\mathrm{keV}}$ is to be attributed to the changes in the hot NS surface properties alone. In fact in our study the emission from the disc as well as the parameters of the Comptonising plasma were kept fixed. In our interpretation, any variation in $L_{5-100\,\mathrm{keV}}$ is a consequence of changes in the properties of the hot NS surface that we modelled with a blackbody emission. Its luminosity is proportional to the emitting surface and temperature, $L_{bb} \propto R^2 \times T_{bb}{}^4$. So, if the luminosity stays nearly constant while the emitting surface increases, then the temperature of the emitting surface will decrease. Thus, the anti-correlation that we found between S_Z and the blackbody temperature kT_{bb} (Fig. 10, right) may be qualitatively understood. The variation of $R^2 \times T_{bb}{}^4$ over S_Z is shown in Fig. 11. The same trend is found for $L_{5-100\,\mathrm{keV}}$ over S_Z (not shown here). L_{bb} as well as $L_{5-100\,\mathrm{keV}}$ changes by a factor of $\sim$3 consistently with the fact that the changes in the overall luminosity, $L_{5-100\,\mathrm{keV}}$, are indeed changes in the blackbody luminosity L_{bb}.

[3] This range includes the 10% uncertainty due to the current calibration status

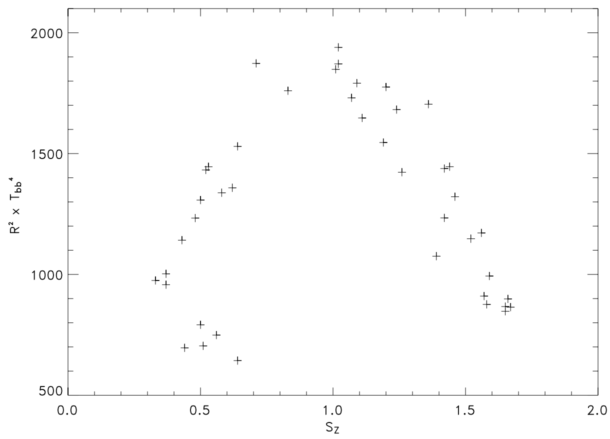

Fig. 11. Variation of $R^2 \times T_{bb}{}^4$, proportional to L_{bb}, over S_Z. The variation of the emitting surface ($\propto R^2$) and T_{bb}, alone, with S_Z is shown in Fig. 10, left and right respectively.

5. Conclusions

A clear hard emission above $\sim$30 keV is detected in GX 5–1. This spectral flattening has probably the same origin of the hard tails observed in other Z sources.

We studied the spectral changes of GX 5–1 along the "Z" pattern in the hardness intensity diagram in terms of Comptonisation of varying soft photons ($\sim$2 keV) by a hot plasma (10 keV). The soft photons are interpreted as blackbody emission from the part of the NS surface that is heated by the boundary layer. The Comptonising plasma is the boundary layer optically thin plasma. When GX 5–1 moves downwards in the "Z", the temperature and optical depth of the Comptonising plasma do not change. What changes along the "Z" is the temperature of the optically thick emission from the hot NS surface that shows a steady decrease with increasing mass accretion rate. This may be a consequence of the gradual expansion of the boundary layer that we detect in the data. This trend is in agreement with theoretical studies (Popham & Sunyaev 2001) that indeed predict the expansion of the boundary layer surface with increasing mass accretion rate.

We will extend the analysis to the new incoming observations to see if our scenario is confirmed. With the long term monitoring we will also have higher chances to catch GX 5–1 in the FB. This is important to test if also along the FB our description of GX 5–1 still holds.

The synergy of a long term monitoring and a multi-wavelength study should be the best way to understand the physics of hard-X ray emission of LMXRBs. Our collaboration is moving in this direction: regular coordinated *INTEGRAL-RXTE* observations of a sample of Atoll and Z sources (including GX 5–1) are being performed and simultaneous radio and optical observations are attempted.

Acknowledgements. A.P. acknowledges V. Beckmann and L. Foschini for careful reading of the manuscript and useful discussion. J.R. acknowledges financial support from the French Space Agency (CNES) and M. Cadolle-Bel for great help with ISGRI spectral responses.

References

Asai, K., Dotani, T., Mitsuda, K., et al. 1994, PASJ, 46, 479

Barret, D. & Vedrenne, G. 1994, ApJS, 92, 505

Blom, J. J., Int-Zand, J. J. M., Heise, J., et al. 1993, A&A, 277, 77

Chenevez, J., Lund, N., Westergaard, N. J., et al. 2004, in Proc. of The 5th INTEGRAL Workshop, *The INTEGRAL Universe*, in press

Di Salvo, T. & Stella, L. 2002, in Proc. of the XXXVIIth Rencontres de Moriond, *The Gamma-Ray Universe*, Ed. A. Goldwurm, Doris N. Neumann and Jean Tran Thanh Van, 67

Dieters, S. W. & van der Klis, M. 2000, MNRAS, 311, 201

Gilfanov, M., Churazov, E., Sunyaev, R., et al. 1993, ApJ, 418, 844

Goldwurm, A., David, P., Foschini, L., et al. 2003, A&A, 411, L223

Hasinger, G. & van der Klis, M. 1989, A&A, 225, 79

Hasinger, G., van der Klis, M., Ebisawa, K., et al. 1990, A&A, 235, 131

Hoshi, R. & Mitsuda, K. 1991, PASJ, 43, 485

Inogamov, N. A. & Sunyaev, R. A. 1999, Astronomy Letters, 25, 269

Jonker, P. G., van der Klis, M., Homan, J., et al. 2002, MNRAS, 333, 665

Kluzniak, W. & Wagoner, R. V. 1985, ApJ, 297, 548

Kuulkers, E. & van der Klis, M. 1995, A&A, 303, 801

Kuulkers, E., van der Klis, M., Oosterbroek, T., et al. 1994, A&A, 289, 795

Lebrun, F., Leray, J. P., Lavocat, P., et al. 2003, A&A, 411, L141

Lund, N., Budtz-Jørgensen, C., Westergaard, N. J., et al. 2003, A&A, 411, L231

Mitsuda, K., Inoue, H., Koyama, K., et al. 1984, PASJ, 36, 741

Nishimura, J., Mitsuda, K., & Itoh, M. 1986, PASJ, 38, 819

Paizis, A., Beckmann, V., Courvoisier, T. J.-L., et al. 2003, A&A, 411, L363

Paizis, A., Courvoisier, T. J.-L., Vilhu, O., et al. 2004, in Proc. of The 5th INTEGRAL Workshop, *The INTEGRAL Universe*, in press (astro-ph/0405376)

Paul, J., Ballet, J., Cantin, M., et al. 1991, Advances in Space Research, 11, 289

Popham, R. & Sunyaev, R. 2001, ApJ, 547, 355

Shimura, T. & Takahara, F. 1995, ApJ, 445, 780

Sunyaev, R., Churazov, E., Gilfanov, M., et al. 1991, A&A, 247, L29

Titarchuk, L. 1994, ApJ, 434, 570

Ubertini, P., Lebrun, F., Di Cocco, G., et al. 2003, A&A, 411, L131

van der Klis, M., Kitamoto, S., Tsunemi, H., & Miyamoto, S. 1991, MNRAS, 248, 751

Westergaard, N. J., Kretschmar, P., Oxborrow, C. A., et al. 2003, A&A, 411, L257

White, N. E., Peacock, A., Hasinger, G., et al. 1986, MNRAS, 218, 129

Winkler, C., Courvoisier, T. J.-L., Di Cocco, G., et al. 2003, A&A, 411, L1

7.3 Future work

The study performed for GX 5-1 will also be done for the remaining bright sources of the sample to see if indeed a common trend can be found. The opportunity to study the hard X-ray emission of all these sources as a class is unique and will be included in the wider frame of the multiwavelength campain. In fact, as it emerged from the presented work, with *INTEGRAL* data alone we can not constrain the variability of the soft component which will be possible with our simultaneous *RXTE* - *INTEGRAL* observations. *RXTE* will also give the opportunity to investigate the temporal properties of GX 5-1 simultaneously to its hard X-ray emission and constrain better the physics underlying the emission processes.

In this part of the thesis we have shown the current results of the survey of Galactic LMXRBs with *INTEGRAL*. These sources are known sources for which the soft X-ray properties had already been thoroughly studied. In our *INTEGRAL* survey we look into the "known" but with new eyes, to discover the hard X-ray emission properties.

In the next part of this thesis we look into a region in the Galactic plane that is free from known sources. In this case, we look deep into the unknown: the number of sources as well as their nature is still to be discovered. We scan no more a wide region of the sky but we look deeply in a very narrow region of the Galactic plane, this time with the soft X-ray eyes of CHANDRA.

Fourth part

THE *Chandra* GALACTIC PLANE DEEP FIELD

Chapter 8
THE MISSION

8.1 Introduction

The *Chandra* X-Ray Observatory (CXO), formerly known as the Advanced X-Ray Astrophysics Facility (AXAF), was launched on 1999 July 23. Managed by NASA's Marshall Space Flight Center, it was designed to provide significant advances over previous X-ray astronomy missions with regards to spatial and spectral resolution over the 0.08-10 keV band. Indeed the X-ray imaging capability of the High Resolution Mirror Assembly (HRMA) is the key to the scientific power of the *Chandra* observatory. Imaging to $0.5''$ (Full Width Half Maximum, FWHM, of the final Point Spread Function, PSF), in contrast to the $\sim 5''$ imaging capability of the previous *Einstein* and *ROSAT* X-ray missions, is truly a significant improvement.

The *XMM-Newton* mission is about ten times more sensitive than *Chandra* to diffuse emission extended over the field of view. Nevertheless its $\sim 30''$ spatial resolution could lead to source confusion. For this reason *Chandra* was first chosen to perform the deep survey of the Galactic plane. The use of *XMM-Newton* for this survey is discussed at the end of next chapter.

The sub-arcsecond spatial resolution enabled *Chandra* to study jets and outflows in quasars and active galaxies which had previously been considered as "point" sources, to reveal structure and interactions within clusters of galaxies for which the distribution of hot gas had previously been considered smooth and symmetric, and to allow point source detection to fluxes 100 times fainter due to the reduction of the detector area which accumulates background. For a complete overview of the mission and of the scientific output of *Chandra* we refer to Weisskopf et al. (2003) and Schwartz (2004). In this chapter only the basics of the *Chandra* mission is given as a complement to the work presented in the next chapter.

8.2 Overview

The Observatory has three major parts written in bold in Fig. 8.1:

- *the telescope system* which focuses X-rays from celestial objects;
- *the Integrated Science Instrument Module, ISIM* which hosts the science instruments;
- *the spacecraft module* which provides the environment necessary for the telescope and the instruments to work.

The telescope system consists of the High Resolution Mirror Assembly (HRMA), a nested set of four grazing-incidence X-ray mirror pairs, with the largest having a diameter of 1.2 m and a 10 m focal length. Together with the instruments it achieves the astonishing PSF of $0.5''$

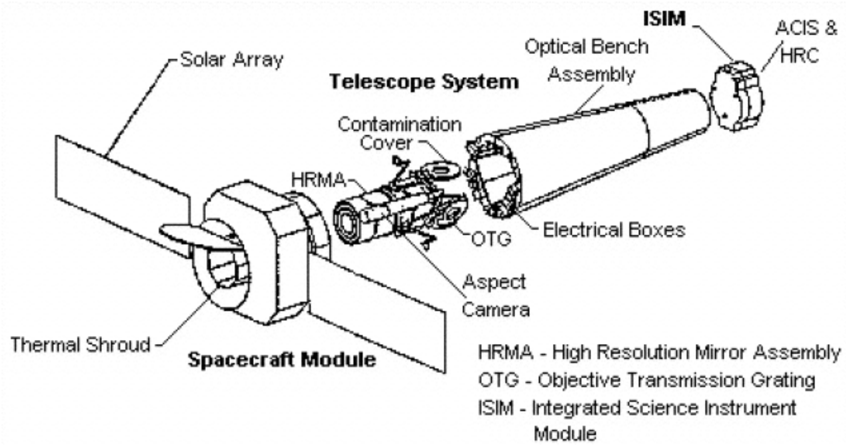

Figure *8.1: Expanded view of the Chandra flight system, showing several subsystems. (Weisskopf et al. 2003.)*

(FWHM). This value is to be compared to $\sim 30''$ of XMM-Newton (similar energy range) and $\sim 12'$ of *INTEGRAL* ($\gtrsim 20$ keV).

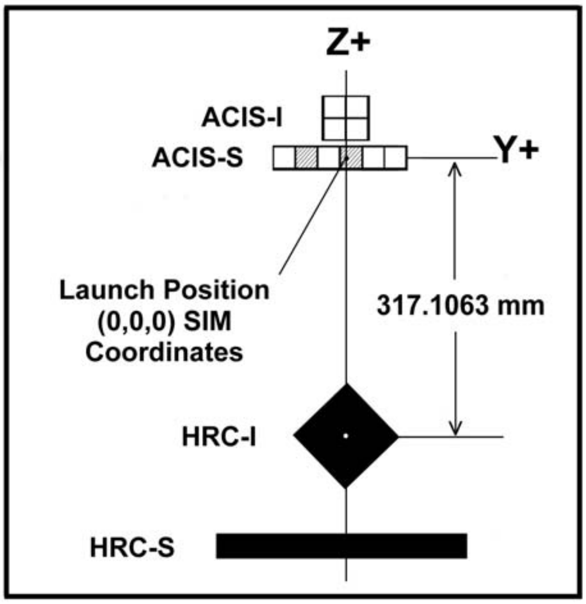

Figure *8.2: Arrangement of the ACIS and the HRC in the focal plane. The view is along the axis of the telescope from the direction of the mirrors (X-axis). The ISIM moves in both the X-axis (focus) and the Z-axis. The Y-axis is parallel to the dispersion direction of the gratings (see text).*

The ISIM houses *Chandra*'s two focal plane imaging science instruments: the High-Resolution Camera (HRC) and the Advanced CCD Imaging Spectrometer (ACIS). One of these two instruments can be moved into the telescope focal plane at any time. The HRC uses micro channel plates (MCP) to convert X-rays, and to amplify the resulting electrons. An incoming photon is located by determining the centroid of the resulting electron cloud. The ACIS uses charge coupled devices (CCD) to convert X-rays into a number of electrons directly proportional to the photon energy, and reads them out in a fixed pattern which preserves the incoming X-ray photon position.

Both the instruments (ACIS and HRC) provide an imaging detector (I) as well as a spectroscopy detector (S). The latter is designed to serve as a readout for the photons dispersed by the transmission gratings that, if desired, can be inserted into the optical path. The focal plane instrument layout is shown in Fig. 8.2. The ISIM moves in both the X-axis (focus) and the Z-axis.

Behind the mirrors, there are two transmission grating spectrometers that can be optionally used. One is optimised for low energies (Low Energy Transmisison Grating, LETG, 0.08-0.2 keV) and the other for high energies (High Energy Transmission Grating, HETG, 0.4-10.0 keV). Only one grating at a time can be used. Spectral resolving power (E/ΔE) in the range 100 to over 1000 can be achieved with good efficiency. These produce spectra dispersed in space at the focal plane. Either the ACIS array or the HRC can be used to record data. In Fig. 8.2 the Y-axis is parallel to the dispersion direction of the gratings, hence the elongated form of the -S arrays that are designed to serve as a readout for the HETG (ACIS-S) and LETG (HRC-S).

The main characteristics of the different components of the *Chandra* Observatory are given in Table 8.1. We refer to e.g. http://cxc.harvard.edu/ and the documents therein for more detailed information on this mission.

8.3 *Chandra* and *INTEGRAL*

Chandra and *INTEGRAL* are two fundamental missions for high energy astrophysics currently operating. They are a big step forward in imaging and spectral performances with respect to the previous missions observing in similar energy bands.

The *INTEGRAL* angular resolution of 12′ seems poor compared to the $\lesssim$1″ of *Chandra*. But the energy range in which such a resolution is achieved makes the difference. Soft X-rays ($\lesssim$10 keV) can be focused by grazing-incidence mirrors, hard X-rays and γ-rays would go through such mirrors and in order to stop, i.e. observe, them alternative methods are to be used like the coded mask technology which makes imaging a very difficult task[43].

A good source location accuracy, roughly $\sim$(angular resolution)/(source significance), is not important just for the sake of precision. It is fundamental to understand the physical processes involved in an object. In fact it allows to attribute the emission in different energy ranges, as given from different missions, to the correct source, especially in the case of crowded regions (e.g. the already discussed case of GX 5-1). It also enables follow-ups at different energy ranges essential to understand the nature of newly detected sources: *INTEGRAL* with its few arcminute position location accuracy is sharp enough to allow for a follow-up observation in the *Chandra* field of view (of the order of tens of arcminutes). Then *Chandra*, with its sub-arcsec position accuracy will in turn restrict the number of optical candidates allowing follow-up observations at optical or radio wavelengths.

In the frame of the monitoring program described in this thesis we observe sources that have been extensively studied and identified in soft X-rays. What we focus on is the poorly known hard

[43]Note that the terms "soft-X" and "hard-X" rays are used differently in this chapter with respect to the *INTEGRAL* related ones. In fact, in the case of *Chandra* (energy range 0.08-10 keV) a 2–10 keV emission is considered "hard". For *INTEGRAL* standards (similarly to *BeppoSAX* and *RXTE*) a hard emission is $\gtrsim$20 keV and $\lesssim$10 keV is normally considered soft. Care was taken to make clear from the context what band is actually being discussed.

Table 8.1: Main characteristics of the *Chandra* instruments and gratings

HRMA	
Focal length	10.066 m
Plate scale	48.8 $\mu/''$
PSF FWHM (with detector)	0.5$''$
ACIS	
I-array (ACIS-I)	4 CCDs used for imaging
S-array (ACIS-S)	6 CCDs used for either imaging or as a grating readout
CCD format	1024 by 1024 pixels
Pixel size	24.0 μ (0.492 $\pm$ 0.0001 $''$)
ACIS-I array size	16.9 by 16.9 $'$
ACIS-S array size	8.3 by 50.6 $'$
Point-source sensitivity	4 X 10^{-15} ergs/cm^2/s in 10^4 s (0.4 to 6.0 keV)
HRC	
HRC-I and HRC-S	CsI-coated microchannel plate pairs
HRC-I field of view	30X30$'$
HRC-S field of view	6 X 99$'$
Spatial resolution, FWHM	$\sim$20μ, $\sim$0.4$''$
Energy range	0.08 - 10.0 keV
Spectral resolution (E/ΔE)	$\sim$1 at 1 keV
Time resolution	16 μs
Point-source sensitivity	9 X 10^{-16}erg/cm^2/s (3σ in 3 X 10^5 s)
HETGS (HETG and ACIS-S)	
HETGS range	0.4 - 10.0 keV
High Energy Grating (HEG) range	0.8 - 10.0 keV
Medium Energy Grating (MEG) range	0.4 - 5.0 keV
HEG resolving power (E/ΔE)	1000 at 1 keV
MEG resolving power	660 at 0.826 keV
LETG	
HRC-S energy range	0.07 - 7.29 keV
ACIS-S energy range	0.20 - 8.86 keV
Resolving power (E/ΔE)	$\gtrsim$1000

X-ray emission. But when *INTEGRAL* discovers a new source things are the other way round. We come to know the source from its hard-X ray part of the spectrum first and then we try to look for it in softer energy bands. The importance of observing such sources in the soft X-ray domain with *Chandra* relies also in the fact that the measurement of the spectral continuum in the soft X-rays ($\lesssim$10 keV) gives information on the physics of the components that are expected as e.g. thermal emission from accretion discs in LMXRBs and from the hot surface of weakly magnetised neutron stars. It also allows one to determine the Galactic absorption towards the source (which might constrain the source distance), to detect the presence of absorbing material intrinsic to the source (e.g., for wind accreters, where short term N_H variations can be observed). For bright sources, discrete features in the soft X-ray spectrum provide further information on the matter surrounding the source, including its temperature and ionisation state.

It is in this frame that we have submitted two proposals[44] to investigate new bright *INTEGRAL* sources with *Chandra*. In order to obtain a good quality spectrum we have chosen to use the *Chandra* high energy grating, HETGS (HETG and ACIS-S) on a bright, ~50 mCrab, source in ISGRI 20–40 keV band. The proposals have been awarded 20 ksecs each but, unfortunately, at the time of writing we have not had the opportunity to trigger the *Chandra* observations.

[44] *Chandra* AO5 and AO6, Proposal number: 05400648 and 06400243, PI: A. Paizis.

Chapter 9
A *Chandra* DEEP SURVEY IN THE GALACTIC PLANE

9.1 Introduction

In this chapter we report the study performed on a typical Galactic plane region with *Chandra*. The observed field is at (l,b)$\sim$ (28.5°, 0.0°) which is along the Galactic plane and has been throughly covered during the *INTEGRAL* core programme scans.

In Fig. 9.1 a map of the Galaxy with the *INTEGRAL*/IBIS field of view centred on (l,b)$\sim$ (28.5°, 0.0°) is shown. An image from IBIS/ISGRI in 20–40 keV is also plotted. In the 30°$\times$ 30° IBIS field, four sources (shown in the image) were detected by IBIS/ISGRI (the LMXRBs 4U 1901+03, GRS 1915+105, 4U 1812-12, GX 17+2). In the ISGRI image the size of the *Chandra* field of view is also shown (yellow square). Zooming in further, the third inset, we can see the superimposed image of our two *Chandra* fields. In the *Chandra* field of view, corresponding to only a few pixels of the IBIS detector, we found 274 point sources.

Thanks to the excellent angular resolution of *Chandra* we were able to disentangle the diffuse emission from the point source contribution and to study them separately. This work is presented in Ebisawa et al. (2004b), and is reproduced at the end of this chapter. The main results are reported below. My contribution has been mainly in the frame of the analysis and study of the *Chandra* point sources.

9.2 Point sources

We have detected 274 point sources in the two *Chandra* deep field observations shown in Fig. 9.1. The complete catalogue of such newly discovered sources is given in Ebisawa et al. (2004b). To identify their nature we used the information given by the *Chandra* X-ray spectrum together with follow-up observations performed in the Near Infra Red (NIR) band which is much less absorbed than the optical. The NIR follow-up observation was performed at the European Southern Observatory (ESO) using the New Technology Telescope (NTT) with the SOFI camera[45].

We found that most of the hard X-ray point sources of the sample are presumably extragalactic since the number of sources does not significantly exceed the number of expected extragalactic ones (as taken from higher latitute measurements). This conclusion is also confirmed by the NIR results: only ~20% of the hard X-ray sources have NIR counterparts. A significant part of hard sources with no NIR counterpart are likely extragalactic since such sources are behind the Galactic plane and will therefore be completely absorbed also in the NIR band. The fewer hard

[45]http://www.eso.org/toc/

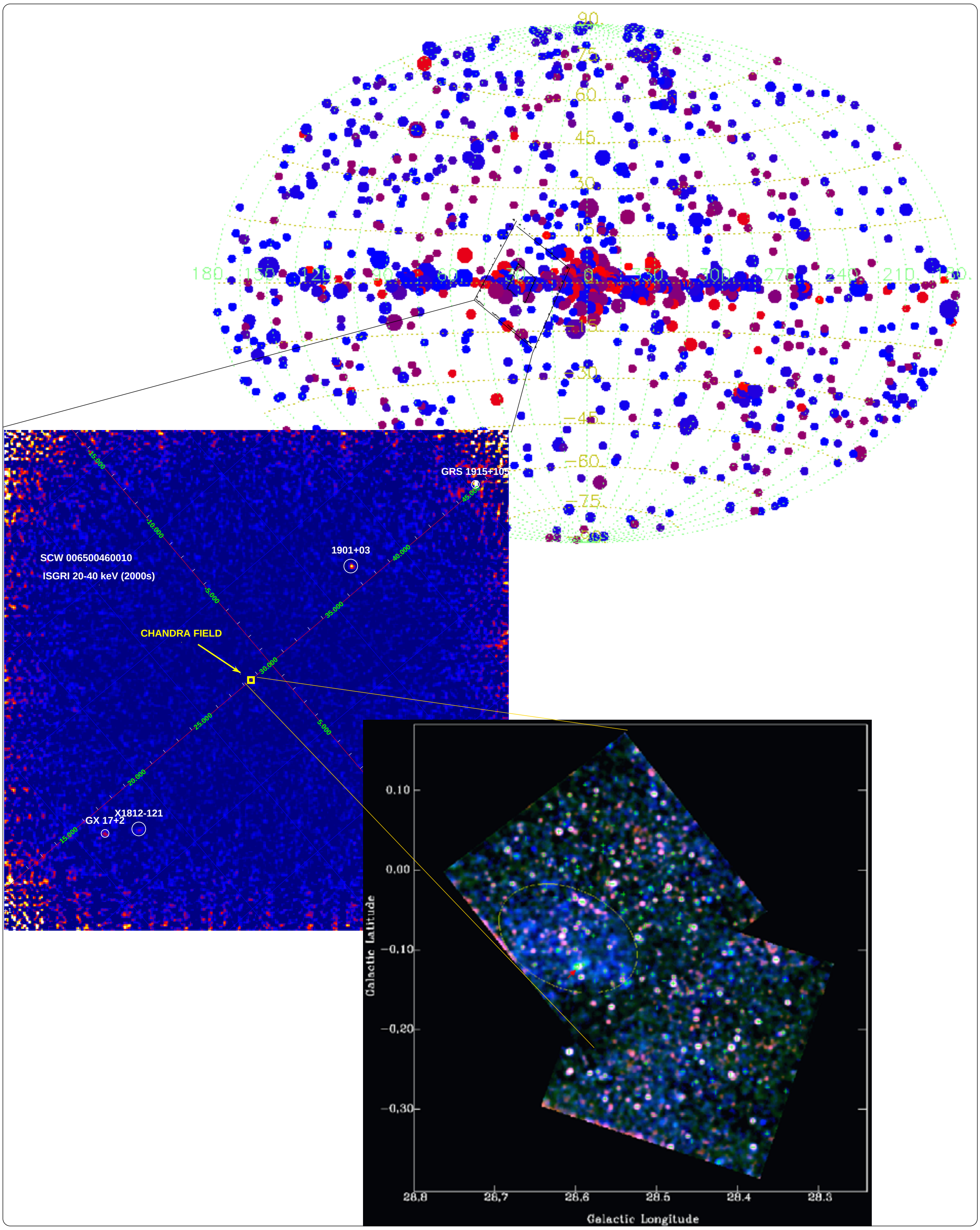

Figure *9.1: View of the field around (l,b)=(28.5°, 0.0°) starting from the map of the whole Galaxy (upper image), INTEGRAL/IBIS single pointing (in the middle) and Chandra superimposed images (100 ksec each, lower image, Ebisawa 2004b).*

sources with NIR counterparts are likely to be Galactic and most likely candidates are quiescent cataclysmic variables that are considered to be numerous in the Galactic plane.

Among the soft sources, ~80% have NIR counterpart. Their X-ray spectrum together with the presence of the NIR counterparts suggest that most of the soft sources are probably nearby active X-ray stars.

9.3 The diffuse emission

The Galactic plane has been known to be a strong hard X-ray (2-10 keV) emitter for over 20 years (e.g. Worrall et al., 1982). The emission forms a narrow continuous ridge, thus it is often called Galactic Ridge X-ray Emission (GRXE). GRXE exhibits emission lines from highly ionised heavy elements such as Si, S and Fe. This suggests that is is originated from thin hot plasmas with a temperature of several keV (Koyama et al., 1986). However whether the GRXE is composed of numerous point sources or truly diffuse emission has been an unresolved problem until recently.

Ebisawa et al. (2001 and 2004b) using *Chandra* ACIS-I data on the two aforementioned overlapping fields, showed that point sources account only for ~10% of the total observed X-ray flux in the field of view and that the rest is truly diffuse emission. A similar study performed in the Galactic centre made by Muno et al. (2004) concludes that the Galactic centre diffuse emission is either truly diffuse or accounted for by a completely new population of faint sources ($\lesssim 10^{31}$ erg s^{-1}) that are ten times more numerous than any known population. The source possibility was kept in consideration because there might be such a numerous and exotic population inhabiting locally the Galactic centre region. However, the observations by Ebisawa et al. (2001, 2004b), were performed on a typical galactic region. This indicates the omnipresence of the X-ray emitting hot plasma along the Galactic plane.

In order to explain the observed spectrum above 2 keV a plasma temperature of 5-10 keV is needed. This temperature is much higher than that of matter which can be bound by Galactic gravity (Warwick et al., 1985). Also the energy density of the GRXE, ~10 eV/cm^3, is one or two orders of magnitude higher than that of other consituents in the interstellar space such as cosmic rays, Galactic magnetic fields, or ordinary interstellar medium (Koyama et al., 1986). The interstellar magnetic field could play an important role to heat and confine the hot plasma. The main source could be also the interaction of low energy cosmic ray electrons or heavy ions with the interstellar medium. But basically there is currently no common agreement on how such a plasma could be heated and why it is held within the Galactic plane.

A recent study by Lebrun et al. (2004) based on *INTEGRAL*/IBIS data from the Galactic centre has shown that in the 20–40 keV band the main contribution from the Galactic centre was made by point sources. It is important to stress that this result is not contradicting our *Chandra* results. We have observed a (small) region in which no bright sources have been observed. The sources we observe are of the order of 0.1μCrab. IBIS looked at the Galactic centre with a (30×30)°field fo view where the bulk of bright Galactic sources lies. Comparing the two results could be misleading. The two regions are different in nature and size. The IBIS results show that the observed region is populated by point sources and that there is room for diffuse emission. This is in agreement with previous results that have shown that a diffuse γ-ray emission is observed from the Galactic plane and region (e.g. Strong et al., 2004). This diffuse emission is suggested to have a non thermal origin as the energy spectrum is presented by a power-law without a thermal cut-off. The Galactic centre and plane diffuse hard X-ray components seem to be smoothly connected to the γ-ray components although their physical relation has not been understood yet.

9.4 Final remarks

This work is an example of the importance of multiwavelength observations in astronomy. Combining information from different wavelengths is indeed a powerful tool to understand the nature of what we observe. We intend to continue this study in other regions of the Galactic plane to map the populations of sources along the plane. Besides, we have proposed for *XMM-Newton* time (AO4) to observe the same *Chandra* fields. *XMM-Newton* is about ten times more sensitive than *Chandra* to diffuse emission extended over the field of view not only because of the larger effective area but also due to the larger field of view. We proposed to observe the same region deeply with *XMM-Newton* to elucidate the origin of the point sources and diffuse X-ray emission through precise X-ray spectral study of the iron K-emission lines. The *XMM-Newton* point spread function (with $\sim 30''$ spatial resolution) may suffer from source confusion. The degree of the source confusion will be estimated using our *Chandra* data (sub-arcsec spatial resolution). This is the reason why it is important to observe with *XMM-Newton* the same field of *Chandra* and not a new one. An example of the richness of the results that can be obtained with the synergy of different missions.

9.5 The paper

In this section the paper Ebisawa et al. (2004b), submitted to ApJ, is reproduced.

Submitted on November 4, 2004

Chandra Deep X-ray Observation of a Typical Galactic Plane Region and Near-Infrared Identification

K. Ebisawa[1,2,3], M. Tsujimoto[4], A. Paizis[2,5], K. Hamaguchi[1], A. Bamba[6], R. Cutri[7], H. Kaneda[8], Y. Maeda[8], G. Sato[8], A. Senda[9], M. Ueno[9], S. Yamauchi[10], V. Beckmann[1], T. J.-L. Courvoisier[2,11], P. Dubath[2,11], & E. Nishihara[12]

ebisawa@subaru.gsfc.nasa.gov

ABSTRACT

Using the *Chandra* Advanced CCD Imaging Spectrometer Imaging array (ACIS-I), we have carried out a deep hard X-ray observation of the Galactic plane region at $(l, b) \approx (28.^\circ5, 0.^\circ0)$, where no discrete X-ray source has been reported previously. We have detected 274 new point X-ray sources (4 σ confidence) as well as strong Galactic diffuse emission within two partially overlapping ACIS-I fields (~ 250 arcmin^2 in total). The point source sensitivity was $\sim 3 \times 10^{-15}$ ergs s^{-1} cm^{-2} in the hard X-ray band (2 – 10 keV) and $\sim 2 \times 10^{-16}$ ergs s^{-1} cm^{-2} in the soft band (0.5 – 2 keV). Sum of all the detected point source fluxes account for only ~ 10 % of the total X-ray fluxes in the field of view. In order to explain the total X-ray fluxes by a superposition of fainter point sources, an extremely rapid increase of the source population is required below our sensitivity limit, which is hardly reconciled with any source distribution in

[1]code 662, NASA/GSFC, Greenbelt, MD 20771

[2]INTEGRAL Science Data Centre, Chemin d'Écogia 16, 1290, Versoix, Switzerland

[3]Universities Space Research Association

[4]Department of Astronomy and Astrophysics, Pennsylvania State University, University Park, PA 16802

[5]IASF, Sezione de Milano, via Bassini 15, I-20133, Milano, Italy

[6]Cosmic Radiation Laboratory, RIKEN (The Institute of Physical and Chemical Research), 2–1, Hirosawa, Wako, Saitama 351-0198, Japan

[7]IPAC, California Institute of Technology, Mail Code 100-22, 770 South Wilson Avenue, Pasadena, CA 91125

[8]Institute of Space and Astronautical Science/JAXA, Yoshinodai, Sagamihara, Kanagawa, 229-8510 Japan

[9]Department of Physics, Kyoto University, Kitashirakawa Oiwake-cho, Sakyo-ku, Kyoto, 606-8502, Japan

[10]Faculty of Humanities and Social Sciences, Iwate University, Iwate, 020-8550, Japan

[11]Observatory of Geneva, 51 chemin des Maillettes, 1290 Sauverny, Switzerland

[12]Gunma Astronomical Observatory, 6860-86 Nakayama Takayama-mura Agatsuma-gun Gunma, 377-0702, Japan

the Galactic plane. Therefore, we conclude that X-ray emission from the Galactic plane has truly diffuse origin. Only 26 point sources were detected both in the soft and hard bands, indicating that there are two distinct classes of the X-ray sources distinguished by the spectral hardness ratio. Surface number density of the hard sources is only slightly higher than observed at the high Galactic latitude regions, strongly suggesting that majority of the hard X-ray sources are active galaxies seen through the Galactic plane. Following the *Chandra* observation, we have performed a near-infrared (NIR) survey with SOFI at ESO/NTT to identify these new X-ray sources. Since the Galactic plane is opaque in NIR, we did not see the background extragalactic sources in NIR. In fact, only 22 % of the hard sources had NIR counterparts which are most likely to be Galactic origin. Composite X-ray energy spectrum of those hard X-ray sources having NIR counterparts exhibits a narrow $\sim$ 6.7 keV iron emission line, which is a signature of Galactic quiescent cataclysmic variables (CVs). We were able to carry out a precise spectral study of the Galactic diffuse X-ray emission without point source contamination, thanks to the superb *Chandra* spatial resolution. Confirming previous results, we have detected prominent emission lines from highly ionized heavy elements in the diffuse emission. In particular, the central energy of the iron emission line was determined as $6.52^{+0.08}_{-0.14}$ keV, which is significantly lower than what is expected from a plasma in thermal equilibrium. The downward shift of the iron line central energy may be explained either by a plasma in non-equilibrium ionization state, or hybrid of the 6.4 keV fluorescent line from non-thermal process and the 6.67 keV line from thermally equilibrium plasma.

Subject headings: Missions: *Chandra* – Galaxy: milky way – X-rays: Star: Galactic diffuse emission

1. INTRODUCTION

The Galactic X-ray source population has been studied from the very beginning of X-ray astronomy. The *Uhuru* satellite detected 339 X-ray sources all over the sky brighter than $\sim 2\times10^{-12}$ ergs s^{-1} cm^{-2} in 2 – 10 keV (Forman et al. 1978). Most bright X-ray sources are concentrated near the Galactic bulge or distributed along the Galactic plane, indicating their Galactic origin. A high sensitive X-ray observation with direct imaging was made for the first time with the *Einstein* satellite (Hertz and Grindlay 1984) in the soft X-rays below $\sim$ 4 keV. The *ROSAT* Galactic Plane Survey (Motch et al. 1991) was made as a part of the *ROSAT* all sky survey, but the energy range was again limited to below $\sim$ 2 keV. These soft X-ray surveys were not able to penetrate the Galactic heavy absorption ($N_H \approx 10^{23}$ cm^{-2}), hence did not allow us to observe those X-ray sources located deepest in the Galactic plane or behind.

In order to observe completely through the Galactic plane and to determine the Galactic source population, hard X-ray ($\gtrsim$ 2 keV) observation is indispensable. This was made possible with *ASCA*, the first imaging satellite in the hard X-ray energy band (Tanaka, Inoue, & Holt 1994). *ASCA* carried out systematic surveys on the Galactic plane (Sugizaki et al. 2001) and the center region (Sakano et al. 2002) down to the sensitivity limit $\sim 3 \times 10^{-13}$ ergs s^{-1} cm^{-2} in 2 – 10 keV. *ASCA*'s point source sensitivity was limited by source confusion due to its moderate X-ray mirror point spread function ($\sim 1'$). *ASCA* discovered more than two hundreds new X-ray sources on the Galactic plane region within the longitudes of $|l| \leq 45^\circ$ (Yamauchi et al. 2002; Ebisawa et al. 2003). Many of them are heavily absorbed and not detected in soft X-ray bands. ASCA suggested an intriguing possibility that there may be still more dimmer, undetected hard X-ray sources in the Galactic plane. *How many Galactic hard X-ray sources are there in the Galactic plane? What are the origins of those dimmest Galactic hard X-ray sources?* Using *Chandra*, the most sensitive hard X-ray telescope in the history, we want to answer to these fundamental questions.

Besides the discrete Galactic X-ray sources, the Galactic plane itself has been known to emit hard X-rays (e.g., Worrall et al. 1982; Warwick et al. 1985; Koyama et al. 1986). The emission forms a narrow continuous Galactic ridge, thus it is called the Galactic Ridge X-ray Emission (GRXE). GRXE exhibits emission lines from highly ionized heavy elements such as Si, S and Fe, which suggests that GRXE originates in thin hot plasmas with a temperature of several keV (Koyama et al. 1986; Yamauchi and Koyama 1993; Kaneda et al. 1997). Whether GRXE is composed of numerous point sources or truly diffuse emission has been a big problem for a long time. *ASCA* was expected to answer this crucial question, but it was not powerful enough to separate numerous dim point sources and diffuse emission (Yamauchi et al. 1996; Kaneda et al. 1997; Sugizaki et al. 2001). The origin of GRXE remained unresolved with *ASCA*.

Chandra is an ideal satellite that is able to resolve GRXE into point sources with a superb spatial resolution of $\sim 0.''6$ (Weisskopf et al. 2002). For this purpose, using the *Chandra* Advanced CCD Imaging Spectrometer Imaging array (ACIS-I), we have carried out a deep hard X-ray observation of the Galactic plane region at $(l, b) \approx (28.^\circ5, 0.^\circ0)$, where extensive observation had already been made but no discrete X-ray source detected with *ASCA*. Our first result was presented in Ebisawa et al. (2001); we have found that only $\sim$ 10 % of the hard X-ray flux (2 – 10 keV) in the *Chandra* field is explained by the point sources brighter than $\sim 3 \times 10^{-15}$ ergs s^{-1} cm^{-2}. Also, by comparing the observed source number density with those measured at high Galactic regions, we have concluded that most of these hard X-ray point sources on the Galactic plane are background AGNs. Therefore, GRXE is truly diffuse emission.

We have made two slightly overlapping *Chandra* deep observations for our project, only the first of which was analyzed in Ebisawa et al. (2001). In Ueno et al. (2003), using both observations, we have made detailed spatial and spectral study of the peculiar supernova remnant candidate AX J1843.8-0352 in the field. In this paper, we will present full analysis of our two *Chandra* observations. The purpose of this paper is two-fold; (1) to study nature of the dimmest X-ray point sources in more detail with an aid of the near-infrared (NIR) follow-up observation using the New Technology Telescope (NTT) at the European Southern Observation (ESO), and (2) to investigate for the origin of the Galactic diffuse emission through precise spectral analysis completely free from the contamination of point sources. Clean separation of the diffuse emission and point sources is great gift of the superb *Chandra* spatial resolution.

2. OBSERVATION AND DATA REDUCTION

2.1. X-ray Observation and Data Reduction

We observed the "empty" Galactic plane region at around $(l, b) \approx (+28^\circ.5, 0^\circ.0)$ in order to study the Galactic diffuse X-ray emission and dim point X-ray sources. This direction is toward the Scutum arm and is known to have strong diffuse emission, thus already extensively observed with *ASCA* (Yamauchi et al. 1996; Kaneda et al. 1997). *ASCA* did not detect any point source brighter than $\sim 2\times10^{-13}$ ergs s^{-1} cm^{-2} (2 – 10 keV), while it found an intriguing hard X-ray diffuse feature (AX J1843.8–0352; Bamba et al. 2001), which was another motivation for our *Chandra* observation in this region. We carried out each 100 ksec pointing on February 25, 2000 (AO1) and May 20, 2001 (AO2), respectively, with slightly overlapping fields. The total area of the observed field is ~ 250 arcmin^2.

In this paper, we have used the event data processed by the *Chandra* X-ray Center with the latest processing system in early 2003. Furthermore, we have applied position and energy calibration (CTI correction) using the CIAO package (version 3.0.1). The Two Micron All Sky Survey (2MASS)[13] was adopted for the position reference for *Chandra* as well as NTT/SOFI data (see the next subsection). Using the positions of those *Chandra* sources that have obvious NIR counterparts, we estimate our *Chandra* position accuracy as $\sim 0.''6$ (see also Section 3.4). Often the *Chandra* position accuracy is dominated by statistical error, in particular for the sources off-axis.

2.2. X-ray Point Source Extraction

First, we made exposure and vignetting corrected images in 0.5 –2 keV, 2 – 4 keV and 4 – 8 keV, and superposed them by assigning red, green and blue color respectively, followed by adaptive smoothing to enhance visibility (Fig. 1). We can clearly see many point sources as well as strong diffuse emission. We carried out point source search using the "wavdetect" program in the CIAO data analysis package. We searched for sources in the 0.5 – 3 keV (soft band), 3 – 8 keV (hard band) and 0.5 – 8 keV (total band) independently. We did not use data below 0.5 keV and above 8 keV in order to avoid high background in both energy ends. Sources that exceed 4 σ significance in any of the three energy bands were considered to be true detections. On the AO1 and AO2 overlapping field, we searched for the sources in the AO1 and AO2 data separately, and combined

[13] http://www.ipac.caltech.edu/2mass

the two significances quadratically if detected in both observations. We have detected 274 point sources within the total field of view. Source position and significance in each energy band, as well as distinction of AO1 or AO2, are given in Table 1. Position errors are the statistical ones calculated by wavdetect, not including any systematic errors.

None of these point sources has been reported in X-rays before. In the soft band, 182 sources have been detected, while in the hard band 79 sources. Only 26 sources are detected both in the soft and hard bands, suggesting an intriguing dichotomy in the source population (see Sections 3.3 and 3.4 for more details). Our sensitivity corresponds to $\sim 3 \times 10^{-15}$ ergs s^{-1} cm^{-2} (2 – 10 keV) and $\sim 2 \times 10^{-16}$ ergs s^{-1} cm^{-2} (0.5 – 2 keV). A new acronym "CXOGPE" (Galactic Plane sources reported by Ebisawa et al. 2004) is registered at CDS for the sources in Table 1 (See http://vizier.u-strasbg.fr/viz-bin/DicForm for detail). Hence, the first source in Table 1 at (18:42:51.77, $-3°51'11.''2$) may be formally designated as "CXOGPE J184251.7−035111", and so on. In this paper, however, the sources in Table 1 are referred as Source 1, 2, etc. for simplicity.

Sources 208, 210, 213, and 216, detected at around (R.A., Decl.)= $(18:43:57, -3°54'48'')$ seem to be parts of a single extended feature, which is designated as CXOU J184357-035441 by Ueno et al. (2003). This extended feature has a characteristic thermal spectrum (Ueno et al. 2003), and is probably a blob associated with the supernova remnant AX J 1843.8–0352/G28.6–0.1 (Bamba et al. 2001). All the other sources are consistent with the *Chandra* point spread function, thus they are considered as point sources.

2.3. NIR Observation and NTT/SOFI Data Reduction

Because of the heavy Galactic absorption, the NIR band has a great advantage over the optical waveband to identify dim X-ray sources on the Galactic plane. In fact, radio observation toward our field has been made (Dickey and Lockman 1990; Dame, Hartman and Thaddeus 2001; Minter et al. 2001), and the total hydrogen column density was estimated not less than $\sim 6 \times 10^{22}$ cm^{-2} (Ebisawa et al. 2001). This corresponds to $A_V \approx 33$ mag using the standard extinction formula ($N_H/A_V \approx 1.8 \times 10^{21}$ cm^{-2} mag^{-1}; Predehl and Schmitt 1995), so that there is hardly any hope to identify extragalactic sources or the most distant Galactic sources in the optical band. On the other hand, NIR extinction formulas $N_H/A_J \approx 5.6 \times 10^{21}$ cm^{-2} mag^{-1} (Vuong et al. 2003) and $N_H/E(J-K) \approx 10^{22}$ cm^{-2} mag^{-1} (Harjunpaeae and Mattila 1996) lead to $A_J \approx 11$ mag and $A_K \approx 5$ mag, hence NIR extinction is much smaller, and NIR observation will allow us to probe deeper into the Galactic plane.

The 2MASS database covers all the sky, and its Point Source Catalog gives the accurate positions and J, H and K_S magnitudes of all the major stars in our *Chandra* field of view (Fig. 2). In order to study more deeply than 2MASS, we have carried out a NIR follow-up observation at ESO using NTT (Tarenghi and Wilson 1989) with the SOFI infrared camera during the nights of 2002 July 28th and 29th. SOFI has 1024×1024 HgCdTe pixels with a moderately large field of view ($4.'94 \times 4.'94$). The pixel size is $0.''2884$ pixel^{-1}, which is comparable to the *Chandra* one ($\sim 0.''5$ pixel^{-1}), thus very suitable to identify *Chandra* X-ray sources. We performed a mosaic observation composed of the 16 pointings slightly-overlapping each other to cover the central region of the two *Chandra* fields (Fig. 3). We defined seven central "A" fields and nine surrounding "B" fields to cover $\sim$ 75 % of the total *Chandra* field. The total exposure times for J, H and K_S bands for each A-field are 10, 10, and 14 minutes, respectively, and those for each B-field are 5, 5, and 7.47 minutes respectively. According to the standard SOFI observation procedure, we carried out a dithering observation, such that each field is covered by 5 (J and H band in B-field), 8 (K_S band in B-field), 10 (J and H band in A-field) or 15 (K_S band in A-field) sequential "frames", each jittered by $\sim 40''$. Exposure time for each frame was 60 (J and H bands) or 56 seconds (K_S band), and each frame was furthermore divided into 6 (J and H bands) or 8 (K_S band) read-out segments in order to avoid saturation. Thus, each frame was the average of the 6 (J and H bands) or 8 (K_S band) snap-shot images. The seeing was best in the first night ($\sim 0.''6$) when we observed fields A1 through A6 (only H and K_S bands for A6), whereas in the second night when we observed the remaining fields, the seeing was worse ($\sim 1.''5$).

IRAF[14] was mainly used to reduce the data following the standard procedure, i.e., subtraction of the dark current, flat-fielding using the dome flat, subtraction of sky using the median-sky technique, removal of bad pixels and cosmic-ray events, and trimming the frame edges. SExtractor (Bertin & Arnouts 1996) was used to extract sources. We searched for sources in each J, H and K_S band separately, and detected 16,890, 26,285 and 27,174 sources (with the DETECT_MINAREA, DETECT_THRESH, and ANALYSIS_THRESH parameter values 5, 1.5, and 1.5, respectively) in J, H and K_S bands, respectively. After removing the overlapping sources, 32,398 sources have been detected at least in one of the three bands (Table 2).

Using the 2MASS database as a reference, we have carried out astrometric correction and absolute magnitude calibration. In Fig. 4, we compare 2MASS and SOFI positions after the astrometric correction. The standard deviation of the shifts between 2MASS and SOFI is $0.''2$ in R.A. and Decl., which is smaller than the SOFI pixel size ($0.''2884$), and may be taken as a typical 2MASS and/or SOFI positional uncertainty. Considering the 2MASS source within $0.''2884$ radius as a counterpart, 8,655 SOFI sources are identified in 2MASS (Table 2).

In Fig. 5 we show correlation of the 2MASS and SOFI J, H and K_S magnitudes after the photometric correction. SOFI magnitudes tend to be larger than those of 2MASS for sources brighter than $\sim$ 10 mag, where SOFI starts to saturate. Also, there is increasing confusion in the 2MASS-SOFI correlation for stars fainter than $J \approx 14$, $H \approx 13$ and $K_S \approx 12$, because of the relatively large 2MASS pixels. This leads to the increasing scatter in the 2MASS-SOFI photometric comparison. For the cleanest samples between 10 and 12 mag, the standard deviations of the 2MASS

[14]IRAF (Image Reduction and Analysis Facility) is distributed by the National Optical Astronomy Observatories, which are operated by Association of Universities for Research in Astronomy, Inc., under cooperative agreement with the National Science Foundation.

– SOFI magnitude differences are 0.08, 0.10, and 0.12 mag in J, H, and K_S bands, respectively (for comparison, the 2MASS measurement precision for bright, non-saturated sources is ∼0.01 to 0.02 mags). These values may be considered as our typical photometric uncertainties.

Finally, in Fig. 6 we show cumulative histograms of the SOFI and 2MASS sources as a function of the SOFI magnitudes. We can see that our sample is almost complete down to ∼18, 17 or 16 mag in J, H, or K_S bands, respectively, if we assume extrapolation of the power-law source distribution at the brighter counts. The depletion of the sources dimmer than these limiting magnitudes may be due to our sensitivity limit and/or depletion of the intrinsic source population. We can also see the depth of our SOFI observation relative to 2MASS which saturates at around ∼16, 15 or 14 mag in J, H, or K_S bands, respectively.

3. DATA ANALYSIS AND RESULTS

3.1. Separation of the Diffuse Emission and Point Sources

One of the main purposes of the present observation is to cleanly separate the diffuse X-ray emission from the point sources, and to study the diffuse emission spectrum free from point source contamination. We have extracted an energy spectrum from both AO1 and AO2 data excluding the AX J 1843.8–0352/G28.6–0.1 region (marked in Fig. 1). Using the background database provided by *Chandra* X-ray Center (CXC), we have subtracted the background spectrum. The CXC background database is constructed from a set of blank sky observations at high Galactic latitudes excluding recognized celestial sources, thus it consists of particle background events and a small contribution from the dim extragalactic sources below the detection limit, as well as galactic or extragalactic diffuse emission at high Galactic latitudes (if any). Hence, after subtracting the background, our spectrum includes only point X-ray sources (Galactic and extragalactic) and Galactic plane diffuse emission, while uncertainty of the background subtraction may not be avoided (see also Section 3.6.2). In addition, we made an energy spectrum combining all the point sources in Table 1, subtracting the same background. In Fig. 7, we show the total energy spectrum and the combined point source spectrum, as well as difference between the two. We can see that only $\sim$ 10 % of the total X-ray emission in the *Chandra* field of view is explained by the sum of all the detected point sources. Even by extrapolating our $\log N - \log S$ curve downward, contribution of the point sources is rather minor (see Section 3.3). Therefore, the difference spectrum, explaining $\sim$ 90 % of the total flux, is considered to be mostly the Galactic diffuse emission (GRXE). We can see that emission lines from highly ionized heavy elements are associated with the diffuse emission. Although the presence of various emission lines in GRXE has been known for a long time (e.g., Koyama et al. 1986; Yamauchi and Koyama 1993; Kaneda et al. 1997), it is for the first time that the pure diffuse spectrum is extracted without point source contamination. More detailed diffuse emission spectral analysis is presented in Section 3.6.

3.2. Spectral Hardness-ratio and Source Fluxes

In order to study spectral characteristics of these new point sources, we computed energy flux and spectral hardness ratio (HR) for each source. The detected raw source counts do not represent the correct source intensities, since they are affected by positional dependence of the detector response (mostly mirror vignetting). Hence, we define and calculate the "normalized count rate" for each energy band, that is the count rate expected when the source is located on the ACIS-I aim point (on-axis direction) and observed for 100 ksec exposure. We define the spectral hardness ratio as $HR \equiv (H - S)/(H + S)$, where H is the normalized count rate in the hard energy band (3 – 8 keV), and S is that in the soft energy band (0.5 – 2 keV). The normalized count rates and HR are also shown in Table 1. Also, we plot the locations of the *Chandra* sources on the 2MASS image with different colors for soft, medium and hard sources (Fig. 2).

To determine source energy fluxes, we need to assume spectral models, but most sources are too dim to determine their energy spectra individually. Therefore, we took the following approach: first, energy spectra are extracted for all the sources (though most spectral bins have null counts), and corresponding instrumental responses were calculated. We categorized the sources into four spectral groups according to the hardness ratio; $HR < -0.8$, $-0.8 \leq HR < -0.2$, $-0.2 \leq HR < 0.6$ and $0.6 \leq HR$. For each spectral group, all the source spectra and responses were averaged. The background spectrum was extracted in the blank detector field for AO1 and AO2 separately, and subtracted from the average spectra after normalizing with the extraction area (thus, the Galactic diffuse emission is subtracted). Then, we fitted these four average spectra with an absorbed power-law model, and determined the average hydrogen column density and power-law index for each spectral group. Finally, each source in the same spectral group was "fitted" with the average spectral model only by adjusting the normalization. From the spectral model thus determined for each source, we calculated the 0.5 – 2 keV and 2 – 10 keV energy fluxes, which are shown in Table 1.

3.3. $\log N - \log S$ and Source Population

We study the point source number densities with the $\log N - \log S$ analysis in the hard band (2 – 10 keV) and soft band (0.5 – 2 keV) separately (Fig. 8). The $\log N - \log S$ curve in the hard band using only the AO1 data was already presented in Ebisawa et al. (2001). We take energy fluxes in Table 1, but our sample is not complete at the lowest flux ends. Therefore we set the lower flux limits at 3×10^{-15} ergs s^{-1} cm^{-2} in the hard band and 2×10^{-16} ergs s^{-1} cm^{-2} in the soft band, respectively, below which we do not discuss source populations. In Fig. 8, we also show the number of the hypothetical point sources below our sensitivity limit whose sum would account for the 100 % of the total X-ray fluxes observed in our field of view. We can clearly see that the actual observed source population is far below the number of point sources required to account for the total GRXE (see also discussion in Section 4.2).

We compare our Galactic plane $\log N - \log S$ curves with those of bright *ASCA* Galactic sources (Sugizaki et al. 2001), extragalactic point sources detected with *ASCA* (Ueda et al. 1999), *ROSAT* and *Chandra* (Giacconi et al. 2001). In addition, we have analyzed the *Chandra* Galactic center Sgr B2 region data (observed in 2000 March 29 for 100 ksec, obsID=944; Murakami, Koyama and Maeda 2001) in a similar manner to our Galactic plane data analysis, and made $\log N - \log S$ curves for both energy bands. The $\log N - \log S$ curves in the Sgr A region are also plotted (mathematical formulas taken from Muno et al. 2003). The extragalactic sources are significantly absorbed on the Galactic plane with a hydrogen column density of $N_H \approx 6 \times 10^{22}$ cm^{-2} (Section 2.3). Assuming a typical photon index of 1.7, we took into account the flux reduction due to the Galactic absorption, and made $\log N - \log S$ curves of the extragalactic sources expected to be seen through the Galactic plane (dashed lines in Fig. 8).

Let's compare our Galactic plane $\log N - \log S$ curves with those for extragalactic sources. In the soft energy band, number of the *Chandra* sources detected above the lowest flux limit is more than 20 times higher than that expected from the extragalactic sources through the Galactic plane (dashed line). Therefore, it is no doubt that most of the soft sources are Galactic. On the other hand in the hard energy band, the situation is quite different; the extragalactic $\log N - \log S$ curve explains most of the observed sources on the Galactic plane. Hence, the observed dichotomy of the source population (Section 2.2) may be naturally explained in that most of the soft X-ray sources have the Galactic origin, while most hard X-ray sources are extragalactic.

Comparison of the source populations in the Galactic plane ($l \approx 28.^\circ 5$), Sgr A ($l \approx 0^\circ$) and Sgr B2 ($l \approx 0^\circ.5$) is also interesting. In the hard energy band, the source number density increases dramatically toward the Galactic center, significantly exceeding that on the Galactic plane and extragalactic one. This indicates that there are much more Galactic point sources in the Galactic center region than in the Galactic plane. In the soft band, on the other hand, the source number density at the lowest flux level is not so different on the Galactic plane and at the Galactic center regions. This is probably because the faintest observable soft sources are mostly located in our neighborhood, so that the direction toward the Galactic center or Galactic plane will not make a big difference. In fact, such dim soft sources at the Galactic *center* will be more significantly absorbed ($N_H \approx 10^{23}$ cm^{-2}) than those *extragalactic* sources in our Galactic *plane* field ($N_H \approx 6 \times 10^{22}$ cm^{-2}) , and are thus hardly detected.

3.4. NIR Identification and Source Classification

We may classify the new X-ray sources according to the HR. We define the "soft" sources whose HR are equal or less than the median $HR = -0.60$. For the rest, the median is $HR = 0.11$, so the "medium" and the "hard" sources are defined as those with $-0.59 < HR \leq 0.10$ and $0.1 < HR$, respectively. Excluding the sources obviously associated to an extended structure, number of the soft, medium and hard sources we have detected is 136, 65 and 69, respectively (Table 3).

Our *Chandra* position accuracy is mostly limited by photon statistics and distortion of the point spread function. We may expect an error of $\sim 1''$ for dim sources far from the aim points. We consider the NIR sources found within $\sim 1''$ of the *Chandra* positions as counterparts. For the *Chandra* sources in the SOFI fields ($\sim$ 75 % of all the *Chandra* sources; Table 3), we show SOFI counterparts in Table 1. 2MASS counterparts are given in Table 1 for the *Chandra* sources outside of the SOFI fields.

In Fig. 9, for each of the *Chandra* sources in the SOFI fields, we plot the relative positional difference to the nearest SOFI source. It is easily seen that most of the soft sources have the NIR counterparts, while medium and hard sources are less likely to have counterparts. In fact, the percentage of the *Chandra* sources having the SOFI counterparts is 83, 53, and 22 % for soft, medium, and hard sources, respectively (Table 3). For all the *Chandra* sources, the percentage with 2MASS counterparts is 45, 26 and 12 %, respectively (Table 3). The fact that the detectability of the NIR counterparts decreases with HR is consistent with the conclusion in the previous section that most soft sources are Galactic, while most hard sources are extragalactic. In fact, if these hard X-ray sources are background AGNs, assuming a typical X-ray/NIR luminosity ratio and the significant Galactic extinction, they are too dim to be detected in the NIR band (see discussion in Section 4.1).

In Fig. 10 (top), we show histograms of the number of sources as a function of HR. It is curious to see that the softest sources are most numerous, and that the number of sources first decreases with HR till $HR \sim 0.5$ and then increases again. On the other hand, number of the sources having NIR counterparts decreases monotonically with increasing HR. This also suggests that our source population is composed of the numerous Galactic soft sources and the less numerous extragalactic hard sources.

The bottom panel of Fig. 10 shows the normalized X-ray counting rates (Section 3.2) versus HR, as well as the presence or absence of the NIR counterpart for each source. We see that almost all the soft sources have NIR counterparts, except several of the dimmest ones. On the other hand for the hard sources, the presence or absence of the NIR counterparts is not related to the X-ray brightness. These facts are also seen in the $\log N - \log S$ curves (Fig. 8) made only from the X-ray sources identified with NIR (either by SOFI or 2MASS). These results suggest that hard X-ray sources without NIR counterparts are mostly extragalactic AGN whose X-ray intensities are widely distributed. In fact, the brightest hard source (Source 200) is not identified in NIR, thus considered to be a strong AGN candidate. Most bright soft X-ray sources are presumably nearby stars and thus they are identified in NIR. On the other hand, those unidentified soft X-ray sources are presumably intrinsically dim in NIR compared to soft X-ray fluxes (see discussion in Section 3.5.2). A small number of the hard sources with NIR counterpart are considered to be Galactic CVs, as we shall see below from detailed X-ray (Section 3.5.2) and NIR analysis (Section 4.1).

3.5. X-ray Characteristics of the Point Sources

3.5.1. X-ray Spectra/Hardness

Since most X-ray sources are too dim (as low as ∼10 counts) to make individual spectra, we combined the sources having similar spectral hardness and made average energy spectra to investigate the spectral characteristics as a class. We categorized all the point sources into six groups, three ranges of the X-ray spectral hardness (Section 3.4), and further grouped according to the presence or absence of the NIR counterparts. We made an averaged energy spectrum for each group.

In Table 4, we show the spectral parameters of the six spectra fitted with a simple absorbed power-law model. When the number of sources combined is small, the power-law photon-index is not constrained tightly. In such cases, for a given spectral hardness, the photon index was determined from the group having more sources, either with or without NIR counterpart, and fixed for the other group. This also helps to clarify the difference of the hydrogen column densities and normalizations between the two groups. Since the hydrogen column density is a measure of the distance to the sources, this suggests that the medium and the hard sources are more likely to be located further than the soft sources. Also, the medium and hard sources without NIR counterparts show clear excess of the hydrogen column densities compared to those with the counterparts, which implies that the medium and hard sources without the counterparts tend to locate further (primarily extragalactic), than those with the counterparts which are more likely to be Galactic. On the other hand, if we compare the soft sources with NIR counterpart and those without counterpart, the average X-ray energy flux of the formers is ~ 40 % smaller than the latter. This suggests that the soft X-ray sources without NIR counterpart are further than and/or intrinsically dimmer than those with NIR counterpart. It is remarkable that the hydrogen column densities are almost the same for both groups of the soft sources, suggesting that the distance is not the main factor to distinguish the two groups. On the other hand, for medium and hard sources, those without the NIR counterparts are *brighter* in both the observed fluxes and the intrinsic fluxes (Table 4). This is considered that significant parts of the hard and medium sources without NIR counterparts are extragalactic, and that they are X-ray bright AGNs which cannot be seen in NIR. A small number of the hard sources having NIR counterpart is likely to be Galactic. Quiescent CVs are strong candidates for these faint Galactic hard X-ray sources (e.g., Mukai and Shiokawa 1993; Watson 1999). A schematic view of explaining the situation is shown in Fig. 11.

3.5.2. Spectral Fitting

In the previous section, we used a simple absorbed power-law model to study the difference of the six average spectra (Table 4). Here, we fit the average source spectra with more physically meaningful models, and also study the iron line feature more carefully.

The X-ray energy spectrum of an active stars is characterized by a two temperature plasma model. Therefore, we used a two temperature MEKAL model in XSPEC (version 11.3.1) for the soft spectrum with NIR counterparts. The spectrum is well fitted with a two temperature plasma at 0.2 keV and 2.0 keV (Table 5). An ionized iron emission line is expected from the high temperature plasma, and indeed there is an evidence of iron emission line though not very strong (Fig. 12, top left). Assuming that the soft sources without NIR counterpart have the same X-ray spectral properties, we tried exactly the same spectral model (including N_H) and allowed only the overall normalization to be a free parameter. We found the fit is reasonably well, with 52 % of the normalization of the soft sources with NIR counterpart (Fig. 12, top right). As we shall see later (Section 4.1; Fig. 19 top), there is a general trend of correlation between NIR fluxes and soft X-rays, primarily accounted for by the distance, while NIR fluxes show large intrinsic scattering (several magnitudes) for a given soft X-ray flux. Reduction of the flux to 52 % corresponds to only ~ 0.7 mag change, which does not explain the non-detection in NIR. Therefore, we conclude that those soft X-ray sources without NIR counterpart are intrinsically dim in NIR relative to the soft X-ray luminosity.

Average energy spectrum of the hard sources with NIR counterparts exhibits a conspicuous narrow iron emission line (Fig. 12, bottom left). The line center energy is 6.67 keV and the equivalent width is 540 eV (Table 5), which is expected in thermal emission from faint CVs (e.g., Ezuka and Ishida 1999). These iron line parameters and the flat spectrum (photon-index = 1.47) correspond to a plasma temperature of $kT \sim 8$ keV. On the other hand, the hard sources without NIR counterparts do not show a narrow iron emission line, but have a broad line and an edge feature which may be modeled with a neutral iron edge (at 7.11 keV) and a broad emission line (at 6.67 keV, EW = 340 eV). These iron features as well as the flat spectrum (photon-index = 0.77) are reminiscent of the disk reflection spectrum often seen in Type II AGN.

The average spectrum of medium sources with NIR counterpart can be fitted with two temperature plasma model, in which the soft component temperature (0.2 keV) is similar to that of the soft spectrum but the hard component temperature is higher (2.9 keV), suggesting a mixture of the relatively hot stars and soft CVs. The average spectrum of medium source without NIR counterpart can be fitted with a power-law which is steeper and less absorbed than the hard sources, presumably indicating a composite of faint hot stars and soft AGNs.

3.5.3. Time Variation

We study time variation of the point sources. For each source, we have made two light curves with bin-widths of 3,000 sec and 10,000 sec. We performed the Kolmogorov-Smirnov test, and if both light curves show variations above 99.9 % significance level, we consider the source to be significantly variable. In our sample, 17 sources are found to be variable, which are marked in Table 1 ("T" in the first column). The distribution of the hardness ratio for these variable sources is shown in Fig. 10 (blue circles). We may not find a clear correlation between the spectral hardness and source variability, besides that there are no variable sources harder than $HR = 0.43$. This might imply that in our sample the soft Galactic sources are more variable than the hard AGNs, but this is not conclusive being limited by the number statistics. Besides, several soft sources exhibit characteristic flare-like variations, such as rapid rise and/or exponential decay, as shown in Fig. 13. The average HR is -0.51 for these seven sources. The flare-like activity and spectral softness are considered to be a signature for the X-ray active flare stars.

3.6. Spectral Study of the Diffuse X-ray Emission

3.6.1. Line Emission

At first, we concentrate on the iron and other emission lines. We fit the iron energy band (5.5 – 7.2 keV) and soft energy band (0.8 – 3.5 keV) separately with a simple power-law plus gaussian model, and determine the line parameters.

We point out that ACIS-I iron line measurement has a significant merit in that contaminating instrumental iron line, which was problematic in *ASCA* and *XMM-Newton* diffuse spectral study, is almost fully negligible. In the iron energy band, a single narrow gaussian model is successful (Table 6; Fig. 14, top). The central line energy is $6.52^{+0.08}_{-0.14}$ keV (90 % error), which is consistent with Kaneda et al. (1997; 6.61 ± 0.02 keV), and significantly lower than what expected from He-like iron in a thermally equilibrium plasma (6.67 keV). A possible explanation of the line energy shift is that the plasma is in non-equilibrium ionization (NEI) state (Yamauchi and Koyama 1993; Kaneda et al. 1997), or the line is composed of a fluorescent 6.4 keV line and a thermal 6.67 keV line (Valinia et al. 2000b). Considering the latter possibility, we fit the same spectrum with a multiple line model. In addition to these two lines, if the charge exchange takes place between the cosmic-ray iron nuclei and interstellar hydrogen atoms (Tanaka, Miyaji, & Hasinger 1999; Tanaka 2002), a hydrogenic iron line at 6.97 keV is expected. Thus, we fit the observed spectrum with the three lines with fixed energies (Table 6; Fig. 14, bottom). The fit is acceptable, though slightly worse than with the single line model. The cosmic-ray charge exchange model predicts significantly broadened emission lines due to the energetic cosmic-ray bulk motion (Tanaka, Miyaji, & Hasinger 1999; Tanaka 2002), but from our statistics we could not constrain the intrinsic iron line width.

We point out that the iron line equivalent width in GRXE is significantly dependent on the spectral model, and difficult to be determined uniquely both in *Chandra* and *ASCA* observations. With a single narrow line model we obtained $EW = 170 \pm 120$ eV, which is smaller than the *ASCA* value with the same model and same sky region, 405 ± 80 eV (Kaneda et al. 1997). Contamination of the point sources with strong iron emission in the *ASCA* spectrum might explain the different at least to some extent. On the other hand, with the three line model, our equivalent width values are $100\pm^{50}_{100}$ eV, $180\pm^{360}_{140}$, and $160\pm^{260}_{160}$ eV, which are consistent with the *ASCA* result using the same three line model on the same sky, < 70 eV, 280 ± 70 and 120 ± 70 eV (Tanaka 2002), though errors are large.

Similarly, the soft band energy spectrum was fitted with a power-law continuum and eleven gaussians (Table 7; Fig. 15). These are the same lines detected in *ASCA* (Kaneda et al. 1997), with the additional Si XIII $K\beta$ line at at 2.18 keV. Equivalent width values are consistent with those in Table 4 in Kaneda et al. (1997), except that we find much weaker 1.74 keV (low ionized Si) and 2.00 keV (Si XIV,Lyα) lines.

3.6.2. Fit with Non-Equilibrium Ionization Plasma Model

We now try to fit the observed diffuse spectrum with a more physically reasonable model. As a working hypothesis, we adopt the same spectral model used by Kaneda et al. (1997), which is a two temperature NEI model (Masai 1984), such that there are soft and hard NEI components which have different temperatures, normalizations, ionization parameters and are affected by different amounts of interstellar absorption.

First, we fix the element abundances for the soft component and hard component, respectively (Table 8 left; Fig. 16 top). The fit is not satisfactory (reduced $\chi^2 = 1.97$), and in particular, the observed iron and neon emission lines are not explained. Next, we adjust abundances of Ne, Mg, and Si in the soft component, and Fe abundance in the hard component (Table 8 right; Fig. 16 bottom). Now the fit is better (reduced $\chi^2 = 1.52$), though artificial adjustment of the abundances is unexplained. Still, we notice a hint of high energy excess above iron line energy, which may be related to the non-thermal component reported above $\sim$ 10 keV (Yamasaki et al. 1997; Valinia et al. 2000b), though this range of the spectrum is subject to the background uncertainty.

With the two component model fit, we have determined the observed flux from the soft and hard component as 2.6×10^{-8} and 2.1×10^{-7} ergs cm^{-2} s^{-1} str^{-1} (0.7 – 10 keV), respectively. If the absorption is removed, the intrinsic fluxes are 1.1×10^{-7} and 7.6×10^{-7} ergs cm^{-2} s^{-1} str^{-1} (0.7 – 10 keV), respectively. Note that the observed flux and spectral shape are significantly affected by the heavy interstellar absorption (Fig. 17). Although the soft component is dominant in the observed flux below 2 keV, the hard component is more dominant over the entire energy band if absorption is removed. Using the same two component model, Kaneda et al. (1997) gave the intrinsic (= absorption removed) soft and hard component fluxes 1.9×10^{-6} and 5.3×10^{-7} ergs cm^{-2} s^{-1} str^{-1} (0.5 – 10 keV), respectively. We remark that, in the NEI models we assume, strong oxygen lines are expected between 0.5 keV and 0.7 keV (Fig. 17), which are hardly observable below the low energy thresholds of both *ASCA* and *Chandra*. Therefore, it will be more reasonable to compare the fluxes in 0.7 – 10 keV, not in 0.5 – 10 keV. Calculated from the NEI model parameters by Kaneda et al. (1997), the observed soft and hard component fluxes with *ASCA* are 5.3×10^{-8} and 1.2×10^{-7} ergs cm^{-2} s^{-1} str^{-1} (0.7 – 10 keV), respectively, and the intrinsic soft and hard component fluxes are 1.9×10^{-7} and 4.3×10^{-7} ergs cm^{-2} s^{-1} str^{-1} (0.7 – 10 keV), respectively. Compared to the *ASCA* result, the *Chandra* flux in 0.7 – 10 keV is $\sim$ 40 % higher, while the soft component flux is $\sim$ 50 % smaller and the hard flux is $\sim$ 80 % higher. The difference is presumably caused by systematics such as slight difference of the sky, uncertainty of the background, and mirror responses, etc. For example, we have subtracted the background taken at high Galactic latitudes, which might include soft photons from AGNs below detection threshold. Also, local soft diffuse emission surrounding the solar system is presumably higher at high Galactic latitudes. Since these photons are completely absorbed in our Galactic plane field, we may have over-subtracted soft X-ray background, which might explain the smaller soft component flux compared to *ASCA*. In any case, our *Chandra* GRXE measurement is considered to be most precise in the sense that it is free from the point source and stray-light contamination which significantly affected the *ASCA* GRXE measurement.

4. Discussion

4.1. Origin of the Point Sources

We have detected 270 point X-ray sources (above 4 σ significance) on a typical Galactic plane field at around $(l, b) \approx (28.^\circ5, 0.^\circ0)$ within $\sim$250 arcmin^2, down to the flux limits $\sim 3 \times 10^{-15}$ erg s^{-1} cm^{-2} (2 – 10 keV) or $\sim 2 \times 10^{-16}$ erg s^{-1} cm^{-2} (0.5 – 2 keV). Thus, we were able to extend the Galactic X-ray source $\log N - \log S$ curves to much dimmer levels compared to the previous observations. In the brightest end, our $\log N - \log S$ curves match well with those made by *XMM-Newton* (Hands et al. 2004) and *ASCA* (Sugizaki et al. 2001) on much larger Galactic plane region.

Based on the X-ray spectral properties and presence or absence of the NIR counterparts, we have presented a schematic view of the origin of point X-ray sources (Fig. 11). Namely, hard X-ray sources without NIR counterpart are extragalactic, those with counterpart are Galactic CVs, while soft X-ray sources are nearby active stars. For the hard sources without NIR counterpart, assuming the average X-ray flux (Table 4) a typical broad-band spectrum of AGN with photon-index of 2 (flat energy spectrum in the $\nu F\nu$ plot), we estimate the expected J, H and K_S magnitudes as 22.7, 22.0 and 21.1, respectively. Taking into account the further reddening $A_K \approx 5$ (Section 2.3), we see that there is almost no hope to detect those background AGNs through the Galactic plane. Even though the above estimate is wrong by a large factor, it is very difficult to see the background AGNs even using the most powerful telescopes. It appears much easier to detect them in hard X-rays.

To understand the properties of the point sources with NIR counterpart, we have made a NIR color-color diagram (Fig. 18). We can see that most soft X-ray sources are along the track of the heavily reddened main sequence stars, which, together with the thin thermal X-ray spectra (Fig. 12), strengthens the stellar origin of the soft X-ray sources. From the X-ray spectral similarities of the soft X-ray sources with and without NIR counterparts, we concluded that soft X-ray sources without NIR counterparts are also likely to be stars (Section 3.5.2). On the other hand, isolated neutron stars can be dim ($\sim 10^{-16}$ ergs cm^{-2} s^{-1}) soft X-ray sources without optical/NIR counterparts (Popov et al. 2000). Popov et al. (2000) estimated expected number of such isolated neutron stars as one per square degree, namely, ~ 0.07 in our *Chandra* field. Therefore, there is hardly a chance that there is an isolated neutron star among our 38 soft X-ray sources without NIR counterparts. Isolated neutron stars should exhibit purely blackbody spectrum, so future high quality X-ray observations of individual sources will distinguish isolated neutron stars and active main sequence stars.

Furthermore, for the X-ray sources with NIR counterpart, we studied the correlation between the X-ray fluxes and the NIR magnitudes (Fig. 19), and correlation between the X-ray spectral hardness and the X-ray to NIR flux ratios (Fig. 20). From Fig. 18 to 20, we notice the following X-ray and NIR characteristics of the sources:

1. On the NIR color-color diagram, the medium and hard X-ray sources are more scattered than the soft X-ray sources that are mostly on the main-sequence track (Fig. 18).
2. Soft X-ray and NIR fluxes are correlated, and the correlation is along the slope expected for the constant luminosity sources at different distances (Fig. 19), though NIR flux variance is large for a given soft X-ray flux. On the other hand, the correlation is not clearly seen between hard X-rays and NIR fluxes.
3. The X-ray spectral hardness and the X-ray to NIR flux ratio show correlations, that is more significant in hard X-ray fluxes than in soft X-rays (Fig. 20).

The above facts (1) and (2) suggest that most soft X-ray sources are active stars, and that variance of both soft X-rays and NIR fluxes is primarily explained by difference of the distance. It is known that CVs are more scattered on the NIR color-color diagram than main sequence stars (Hoard et al. 2002) or AGNs (Cutri et al. 2005). In particular, the distribution of our hard X-ray sources on the NIR color-color diagram (Fig. 18) seems to be similar to that of “uncertain/unclassified” CVs in Hoard et al. (2002). The NIR study thus supports the idea that most of the Galactic hard X-ray sources in our sample are CVs, that is already suggested from X-ray spectral study (Section 4.1). The above fact (3) is presumably indicating intrinsic differences in the hard X-ray fluxes/NIR flux ratio of active stars and CVs, such that CVs are relatively bright hard X-ray sources compared to the NIR fluxes. The new hard X-ray sources we discovered with NIR counterpart have not been previously identified as CVs in optical or any other wavelength (e.g., Downes et al. 2001). Therefore, a hard X-ray observation may be an efficient mean to discover previously unknown or unclassified CVs. Vice versa, those unclassified CVs may be detected in hard X-rays, which may be experimented by *Chandra* and/or *XMM-Newton*.

4.2. Origin of the Galactic Diffuse X-ray emission

We have detected point sources brighter than 3×10^{-15} ergs s^{-1} cm^{-2} (2 – 10 keV) and 2×10^{-16} ergs s^{-1} cm^{-2} (0.5 – 2 keV), and excluded these point sources to study the Galactic diffuse emission spectra. Using the best-fit model (Section 3.6), the observed diffuse emission flux is 6.5×10^{-11} ergs s^{-1} cm^{-2} deg^{-2} (2 – 10 keV) and 8.7×10^{-12} ergs s^{-1} cm^{-2} deg^{-2} (0.5 – 2 keV). Let's consider if this "diffuse" emission may be accounted for by superposition of the still dimmer point sources below our detection limits. In Fig. 8, we show numbers of the hypothetical point sources whose sum would account for 100 % of the Galactic ridge X-ray emission. These numbers are calculated by subtracting the contribution from the detected point sources from the total observed X-ray fluxes, then divided by a given point source flux below our detection limit. So that all the detected diffuse emission is explained by the point sources alone, it is required that the $\log N - \log S$ curves rapidly steepen by an order of magnitude below our sensitivity. No spatial distribution of point sources in the Galactic plane would accommodate such an unusual $\log N - \log S$ curve. Based on similar arguments, Muno et al. (2004) concludes that the Galactic center diffuse emission is either truly diffuse or accounted for by a completely new population of faint sources ($< 10^{31}$ ergs s^{-1}) that are at least 10 times more numerous than any known population. They reserved the point source possibility, because there might be such numerous and exotic sources inhabiting *locally* the Galactic center region that itself is a mystery. However, our observation is a typical Galactic region, and the source population should reflect the *global* X-ray source distribution through the Galactic plane. Hence, we may not expect unusual behavior of the Galactic $\log N - \log S$ curves such as a sudden steepening by an order of magnitude.

Considering the spectral similarity of the diffuse emission on the Galactic plane (Section 3.6) and Galactic center (Muno et al. 2004), we are tempted to conclude that they have similar origins (see also Tanaka 2002). Recent INTEGRAL observations have detected hard X-ray emission above 20 keV in the Galactic center region whose centroid is slightly offset of Sgr A* (Bélanger et al. 2004), but coincides with the center of the diffuse component imaged by *Chandra* (Muno et al. 2004). This suggests that a non-thermal hard-tail of the Galactic center diffuse spectrum is extended above 20 keV. GRXE also has a power-law hard-tail component which extends above ∼20 keV (Yamasaki et al. 1997; Valinia and Marshall 1998). On the other hand, strong diffuse gamma-ray (∼ 100 keV – 1 MeV) emission is observed from the Galactic center and plane region (e.g., Gehrels and Tueller 1993; Skibo et al. 1997; Valinia et al. 2000a; Strong et al. 2003), which is suggested to have a non-thermal origin, as the energy spectrum is represented with a power-law without a thermal cut-off. Intriguingly, the Galactic center and plane diffuse hard X-ray components seem to be smoothly connected to the gamma-ray components, although their physical relationship has not been understood.

We found that GRXE has a truly diffuse origin, then the question is how to produce and maintain such high energetic plasma. There are obvious problems in interpreting GRXE in terms of simple equilibrium thermal plasma, such that the plasma temperature needed to explain the observed spectra, $kT \approx 5 - 10$ keV, is much higher than can be bound by Galactic gravity (Warwick et al. 1985). Also, the energy density of GRXE, ∼10 eV/cm^3, is one or two orders of magnitude higher than those of other constituents in the interstellar space, such as cosmic rays, Galactic magnetic fields, or ordinary interstellar medium (Koyama et al. 1986; Kaneda et al. 1997). Currently there are no accepted theoretical models that can explain the origin of GRXE. Some argue that the interstellar magnetic field is playing a significant role to heat and confine the hot plasma (Tanuma et al. 1999). Others propose that the interstellar medium is mainly responsible for GRXE and gamma-ray emission, via interactions with, for instance, low energy cosmic-ray electrons (Valinia et al. 2000b), in situ accelerated quasi-thermal electrons (Dogiel et al. 2002; Masai et al. 2002), or heavy ions (Tanaka, Miyaji, & Hasinger 1999). Galactic particle acceleration is considered to take place in supernova remnants. Serendipitous discovery of the hard X-ray emitting supernova remnant AXJ 1843.8–0352 in our field (Bamba et al. 2001; Ueno et al. 2003) in fact strongly suggests a close tie between GRXE and supernova remnants.

Various theoretical models of GRXE have to be tested through observations. Different heating or acceleration mechanism of the plasma will result in different plasma conditions, which are reflected in the emission lines. Therefore, from precise measurements of the emission lines in GRXE, we may in principle diagnose the plasma conditions and constrain the theoretical models. In particular, iron line spectroscopy is essential. We have shown that the GRXE iron line central energy is $6.52\pm^{0.08}_{0.14}$ keV (Section 3.6), significantly lower than what expected from thermally equilibrium plasma ($\sim$6.67 keV). Although we could not distinguish if the iron line we detected is a single line or composite of two or three lines, a high signal-to-noise *Chandra* Galactic center diffuse spectrum clearly indicates the three emission lines from low ionized iron, He-like iron and H-like iron (Muno et al. 2004). If we assume similar origins of Galactic center and plane diffuse emission, then the three line interpretation of GRXE iron line emission seems plausible (see also Tanaka 2002). If this is the case, the 6.4 keV line is considered from fluorescence in cool interstellar medium, which may be induced, for instance, by low energy cosmic-ray electrons (Valinia et al. 2000b). Both He-like and H-like lines may be from, for example, the thermal equilibrium plasma, the charge exchange process of iron ions (Tanaka, Miyaji, & Hasinger 1999; Tanaka 2002), or the interaction between in-situ accelerated electrons and cool ($kT < 1$ keV) plasma (Masai et al. 2002). These cases may be distinguished from intrinsic line widths, since in the second case the lines are expected to be significantly broadened by the iron nucleus bulk motion (Tanaka et al. 2000), while on the other hand in the last case the lines are expected to be narrow since the plasma is cold.

We emphasize that the precise iron line diagnostic (including line intrinsic width measurement) is a key to resolve then origin of the Galactic center and Galactic plane diffuse emission. In this context, planned Galactic center observations with Astro-E2 XRS, the first X-ray microcalorimeter in space with $\sim$ 6 eV resolution, will be an enormous help. GRXE may be too dim for Astro-E2 XRS (our simulation suggests that a million second exposure is required), but we believe that the long standing mystery of GRXE will be certainly solved by the future calorimeter observations with higher throughputs and better spectral resolution, expected to be made by *Con-X*, *NEXT* and/or*XEUS*.

5. Conclusion

Using *Chandra* ACIS-I, we have carried out a deep X-ray observation (0.5 – 10 keV) on a typical Galactic region at $(l, b) \approx (28.^\circ 5, 0.^\circ 0)$ within ∼250 arcmin^2, followed by a NIR identification observation with NTT/SOFI at ESO. Main results are summarized below:

1. We have detected 274 new X-ray sources (4 σ confidence) down to $\sim 3 \times 10^{-15}$ erg s^{-1} cm^{-2} in 2 – 10 keV or $\sim 2 \times 10^{-16}$ erg s^{-1} cm^{-2} in 0.5 – 2 keV. Only 26 sources are detected both in the soft and hard bands. In the SOFI field, 83 % of the soft sources are identified in NIR, while only 22 % of the hard sources have NIR conterparts. Most of the soft X-ray sources are considered to be X-ray active stars, while a significant part of the unidentified hard X-ray sources are extragalactic.

2. Only ∼ 10 % of the detected X-ray fluxes in the *Chandra* field is accounted for by the sum of point source fluxes. Hence, we conclude Galactic ridge X-ray emission is truly diffuse emission.

3. Soft X-ray sources exhibit thin thermal spectra, characteristics of active stars. Difference between the soft X-ray sources with and without NIR counterparts is only due for a small part to the source distance. It results to a large extent from differences in their intrinsic NIR luminosities. Small number of the hard X-ray sources with NIR counterpart is considered to be Galactic cataclysmic variables, and exhibits a narrow iron emission line at 6.67 keV expected from hot equilibrium plasma.

4. Removing contamination of point X-ray sources, we have precisely measured the Galactic ridge diffuse X-ray emission. The observed diffuse flux is 2.4×10^{-7} ergs cm^{-2} s^{-1} str^{-1} (0.7 – 10 keV). The energy spectrum can be modeled with a two temperature non-equilibrium ionization model, such that the soft and hard component have different plasma parameters and different amounts of interstellar absorption.

5. We have measured the diffuse iron emission line energy as $6.52\pm^{0.08}_{0.14}$ keV (90 % error). This is significantly lower than what is expected from thermally equilibrium plasma (6.67 keV). This shift of the iron line energy may be explained either by non-equilibrium ionization of the plasma, or hybrid of the 6.4 keV fluorescent line and the 6.67 keV line from equilibrium plasma.

This publication is based on observations made with NASA's *Chandra* observatory (observation ID 949, 1523, and 2298), and ESO Telescopes at the La Silla (under program ID 69.D-0664). Also, this paper makes use of data products from the Two Micron All Sky Survey, which is a joint project of the University of Massachusetts and the Infrared Processing and Analysis Center/California Institute of Technology, funded by the National Aeronautics and Space Administration and the

National Science Foundation. An image used in this paper was produced with Montage, an image mosaic service supported by the NASA Earth Sciences Technology Office Computing Technologies program, under Cooperative Agreement Notice NCC 5-6261 between NASA and the California Institute of Technology. M.T. is financially supported by the Japan Society for the Promotion of Science.

REFERENCES

Bamba, A., Ueno, M., Koyama, K. , & Yamauchi, S. 2001, PASJ, 63, L21

Bélanger, G. et al. 2004, ApJ, 601, L163

Bertin, E. & Arnouts, S. 1996, A&AS, 117, 393

Cox, A. N. 1999, "Allen's Astrophysical Quanties", fourth edition, Springer

Cutri, R. et al. 2005, in preparation

Dame, T. M., Hartmann, D. & Thaddeus, P. 2001, ApJ, 547, 792

Dickey, J. M. & Lockman, F. J. 1990, ARAA, 28, 215

Dogiel, V.A., Inoue, H., Masai, K., Schönfelder, V. & Strong, A. W. 2002, ApJ, 581, 1061

Downes, R., Webbink, R., Shara, M., Ritter, H., Kolb, U., Duerbeck, H. 2001, PASP, 113, 764

Ebisawa, K., Maeda, K., Kaneda, H. & Yamauchi, S. 2001, Science, 293, 1633

Ebisawa, K., Yamauchi, S., Bamba, A., Ueno, M. & Senda, A. 2003, Astron. Nachr. 324, 52

Ezuka, H. & Ishida, M. 1999, ApJS, 120, 277

Forman, W., Jones, C., Cominsky, L., Julien, P., Murray, S., Peters, G., Tananbaum, H. & Giacconi, R. 1978, ApJS, 38 357

Gehrels, N. & Tueller, J. 1993, ApJ, 407, 597

Giacconi, R. et al. 2001, ApJ, 551, 624

Hands, A. D. P., Warwick, R. S., Watson, M. G. & Helfand, D. J. 2004, MNRAS, 351, 31

Harjunpaeae, P. & Mattila, K. 1996, A&A, 305, 920

Hertz, P. & Grindlay, J. E. 1984, ApJ, 278, 137

Hoard, D. W., Wachter, S. Clark, L. L. & Bowers, T. P. 2002, ApJ, 565,511

Ueno, M., Bamba, A., Koyama, K. & Ebisawa, K. 2003, ApJ, 588, 338

Valinia, A. & Marshall, F. E. 1998, ApJ, 505, 134

Valinia, A., Kinzer, R. L. & Marshall, F. E. 2000a, ApJ, 534, 277

Valinia, A. et al. 2000b, ApJ, 543, 733

Vuong, M. H., Montmerle, T., Grosso, N., Feigelson, E. D., Verstraete, L. & Ozawa, H. 2003, A&A, 408, 581

Watson, M. G. 1999, in "Annapolis Workshop on Magnetic Cataclysmic Variables", ASP conference series, vol. 157, p. 291

Warwick, R. S., Turner, M. J. L., Watson, M. G. & Willingale, R. 1985, Nature, 317, 218

Weisskopf, M. C., Brinkman, B., Canizares, C., Garmire, G., Murray, S. & Van Speybroeck, L. P. 2002, PASP, 114, 1

Worrall, D. M., Marshall, F. E., Boldt, E. A. & Swank, J. H. 1982, ApJ, 255, 111

Yamasaki, N. et al. 1997, ApJ, 481, 821

Yamauchi, S. & Koyama, K. 1993, ApJ, 404, 620

Yamauchi, S., Kaneda, H. Koyama, K., Makishima, K., Matsuzaki, K., Sonobe, T. Tanaka, Y. & Yamasaki, N. 1996, PASJ, 48, L15

Yamauchi, S. et al. 2002, in the Proceedings of the IAU 8th Asian-Pacific Regional Meeting, Volume II, Edited by S. Ikeuchi, J. Hearnshaw, & T. Hanawa, the Astronomical Society of Japan, p.81

This preprint was prepared with the AAS LaTeX macros v5.0.

Ueno, M., Bamba, A., Koyama, K. & Ebisawa, K. 2003, ApJ, 588, 338

Valinia, A. & Marshall, F. E. 1998, ApJ, 505, 134

Valinia, A., Kinzer, R. L. & Marshall, F. E. 2000a, ApJ, 534, 277

Valinia, A. et al. 2000b, ApJ, 543, 733

Vuong, M. H., Montmerle, T., Grosso, N., Feigelson, E. D., Verstraete, L. & Ozawa, H. 2003, A&A, 408, 581

Watson, M. G. 1999, in "Annapolis Workshop on Magnetic Cataclysmic Variables", ASP conference series, vol. 157, p. 291

Warwick, R. S., Turner, M. J. L., Watson, M. G. & Willingale, R. 1985, Nature, 317, 218

Weisskopf, M. C., Brinkman, B., Canizares, C., Garmire, G., Murray, S. & Van Speybroeck, L. P. 2002, PASP, 114, 1

Worrall, D. M., Marshall, F. E., Boldt, E. A. & Swank, J. H. 1982, ApJ, 255, 111

Yamasaki, N. et al. 1997, ApJ, 481, 821

Yamauchi, S. & Koyama, K. 1993, ApJ, 404, 620

Yamauchi, S., Kaneda, H. Koyama, K., Makishima, K., Matsuzaki, K., Sonobe, T. Tanaka, Y. & Yamasaki, N. 1996, PASJ, 48, L15

Yamauchi, S. et al. 2002, in the Proceedings of the IAU 8th Asian-Pacific Regional Meeting, Volume II, Edited by S. Ikeuchi, J. Hearnshaw, & T. Hanawa, the Astronomical Society of Japan, p.81

This preprint was prepared with the AAS LaTeX macros v5.0.

– 23 –

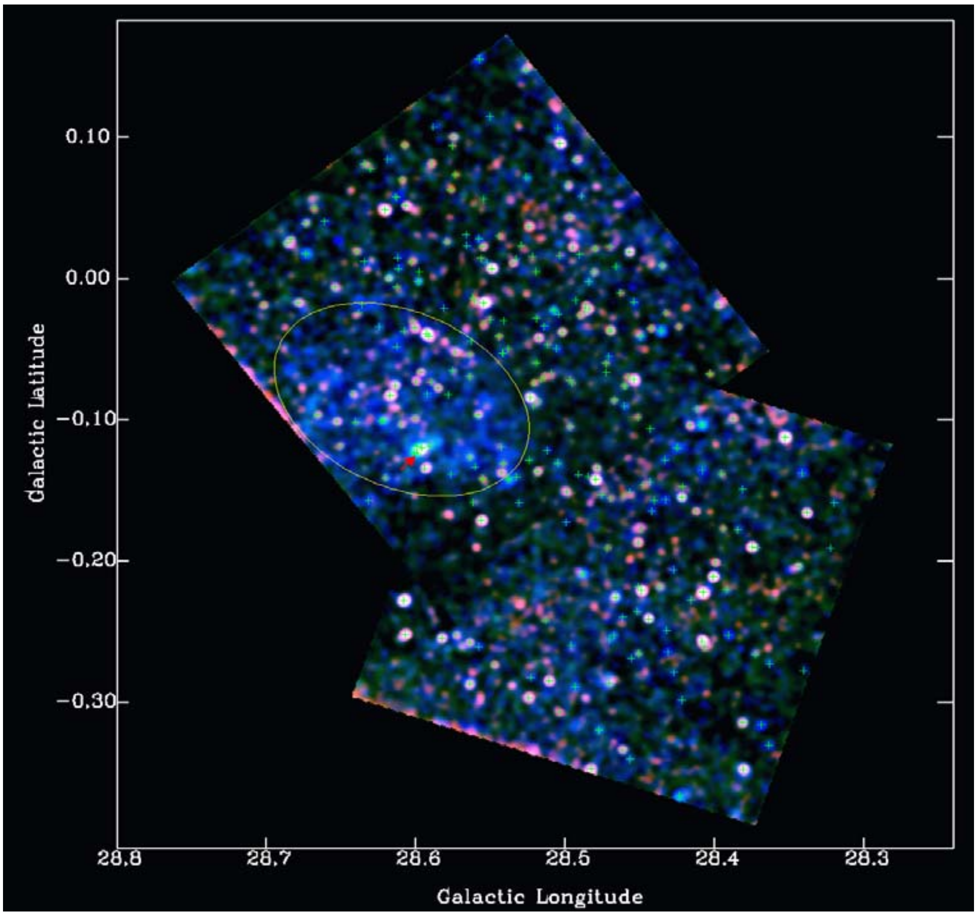

Fig. 1.— Superposed image of the two *Chandra* observations with exposure and vignetting correction (in Galactic coordinates). The upper and lower *Chandra* pointings were made in AO1 and AO2, respectively (each 100 ksec). This is a true-color *Chandra* image where soft X-rays in 0.5 – 2 keV are represented in red, medium X-rays in 2 – 4 keV in green, and hard X-rays in 4 – 8 keV in blue. The image is adaptively smoothed so that both the point sources and the diffuse emission are clearly visible. The 274 detected point sources (Table 1) are marked with crosses. The region including the supernova remnant AX J 1843.8–0352/G28.6–0.1 (Bamba et al. 2001; Ueno et al. 2003) is shown with a yellow ellipse, within which the thermal blob structure CXOU J184357-035441 (Ueno et al. 2003) is marked with a red arrow. Note that the supernova remnant AX J 1843.8–0352/G28.6–0.1, which exhibits non-thermal energy spectrum (Bamba et al. 2001; Ueno et al. 2003), is more prominent in hard X-rays ("bluish" in this representation) than in soft X-rays.

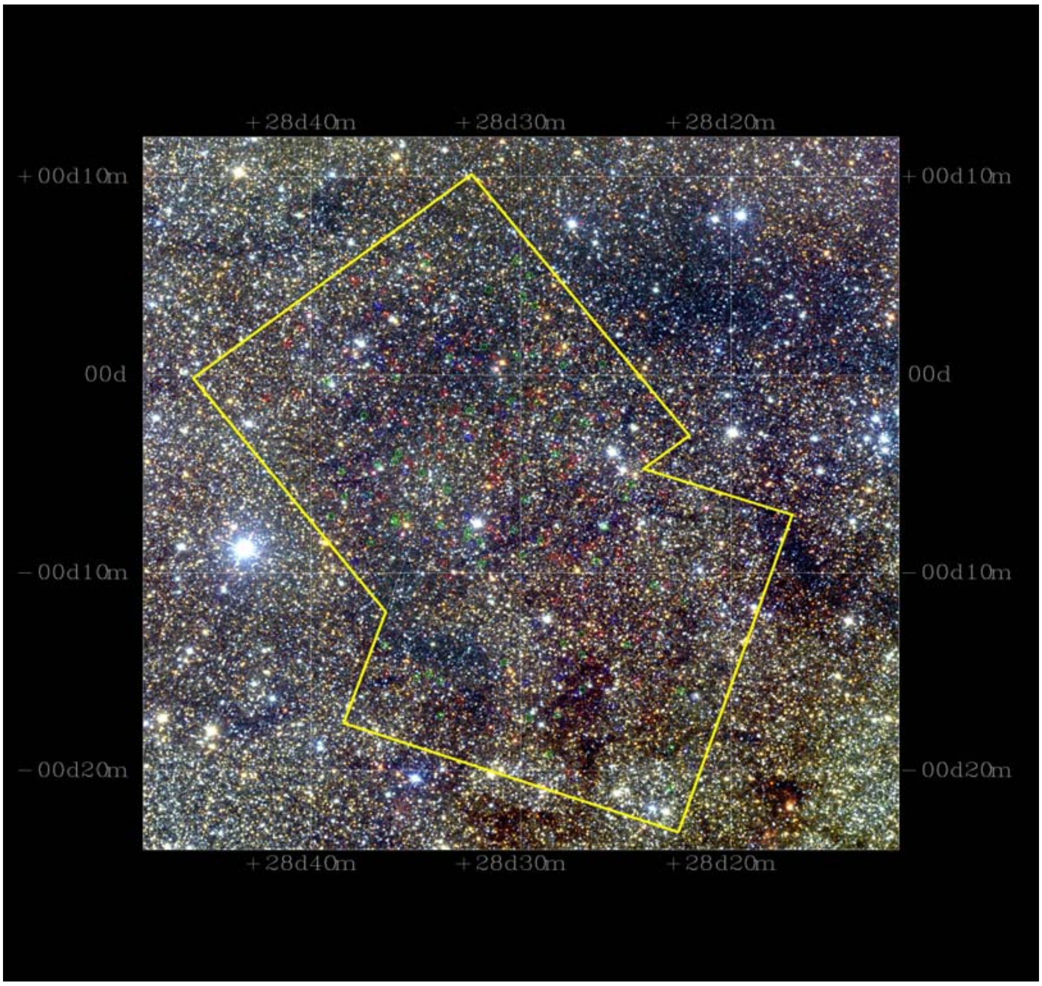

Fig. 2.— 2MASS true color image of the region including our *Chandra* field (in Galactic coordinates). The *Chandra* field of view is drawn, and the *Chandra* sources are marked in red, green or blue, for soft, medium and hard sources, respectively. For the definition of the source spectral hardness, see Section 3.2.

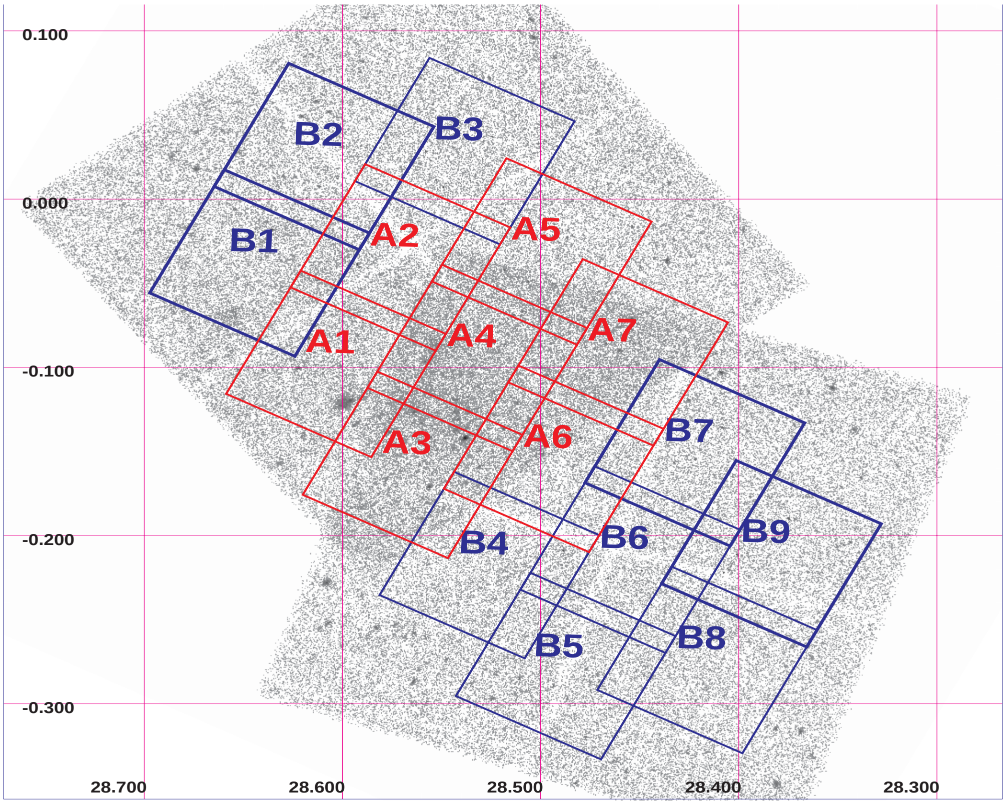

Fig. 3.— SOFI pointing positions on the *Chandra* image (without exposure correction) in Galactic coordinates. Without exposure correction, the AO1 and AO2 overlapping fields and CCD gaps are noticeable (compare with Fig. 1).

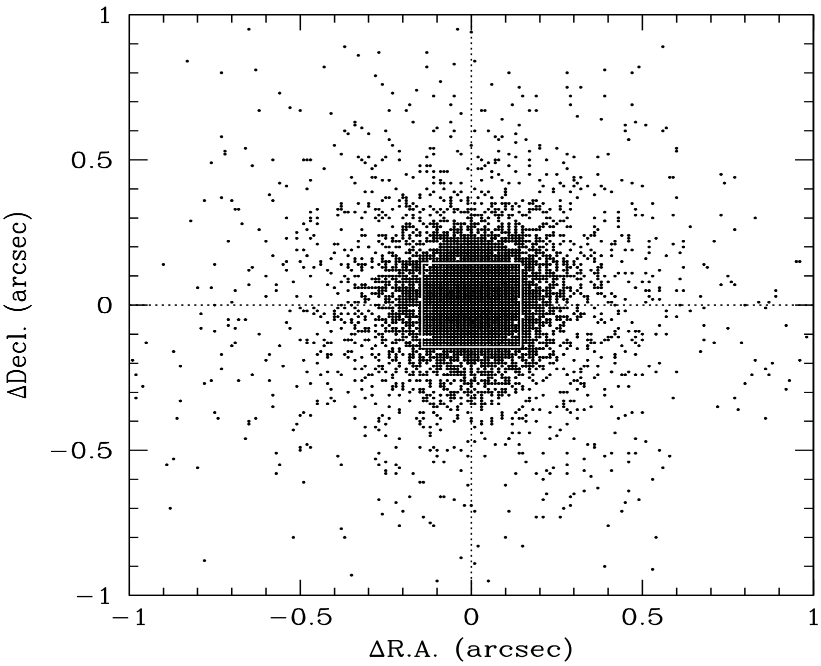

Fig. 4.— For all the 2MASS sources in the SOFI field of view, relative position of the nearest SOFI source (after astrometric correction) is plotted. The central square indicates the SOFI pixel size ($0.''2884 \times 0.''2884$). Standard deviation of the positional shift between 2MASS and SOFI is $0.''2$ in R.A. and Decl.

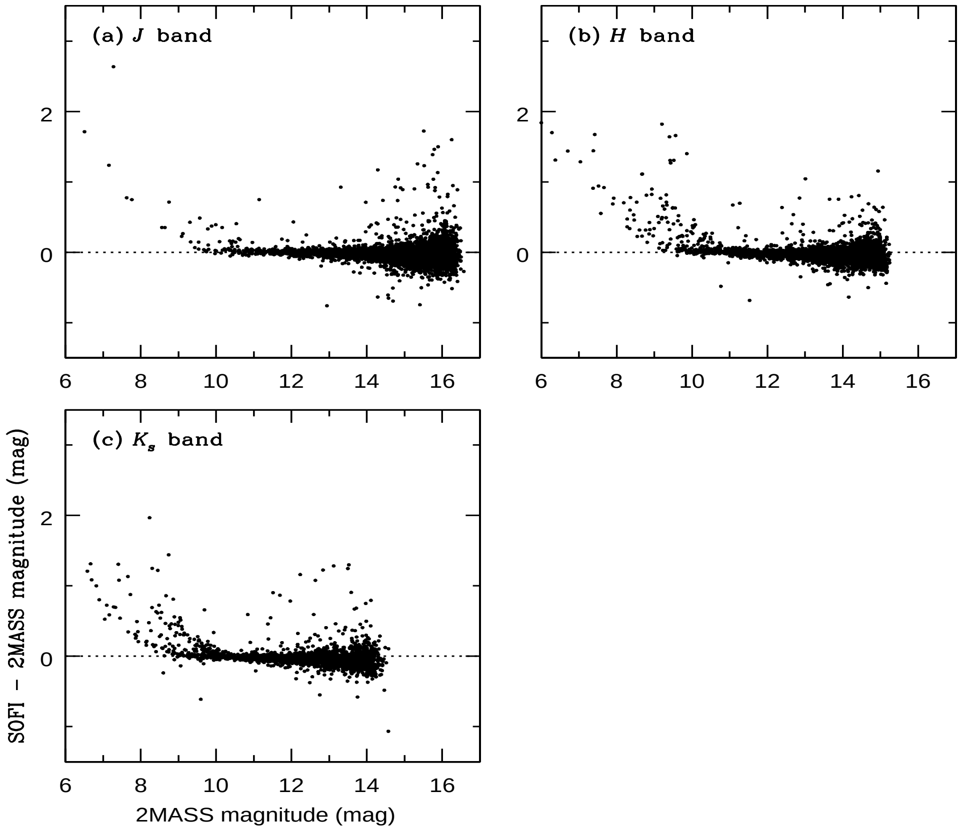

Fig. 5.— Correlation of the J, H and K_S magnitudes of the sources detected by both 2MASS and SOFI. Difference of the magnitudes is plotted as a function of the 2MASS magnitudes.

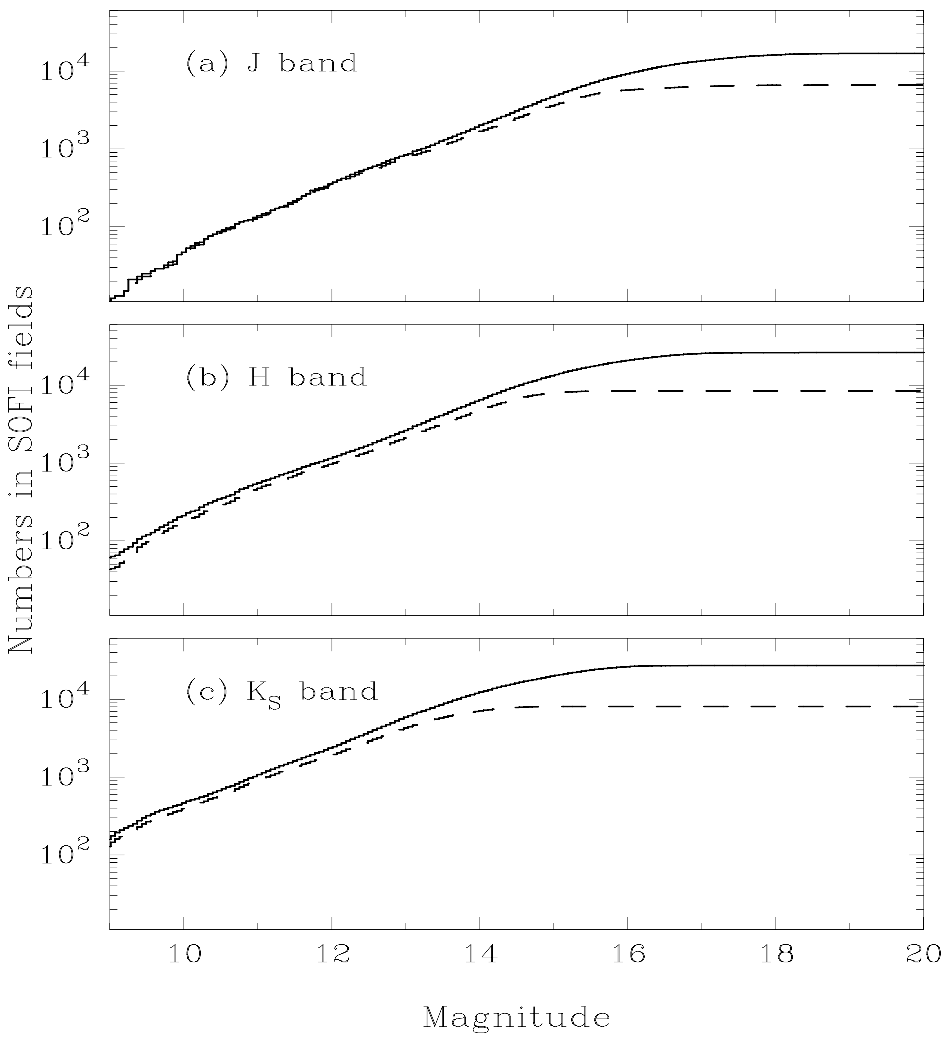

Fig. 6.— Cumulative histograms of the number of SOFI sources (*solid line*) detected in J, H and K_S bands, as a function of the SOFI magnitudes. Number of 2MASS sources in the SOFI fields are also shown with dashed line. Sources detected in two or three bands are counted in each detected band.

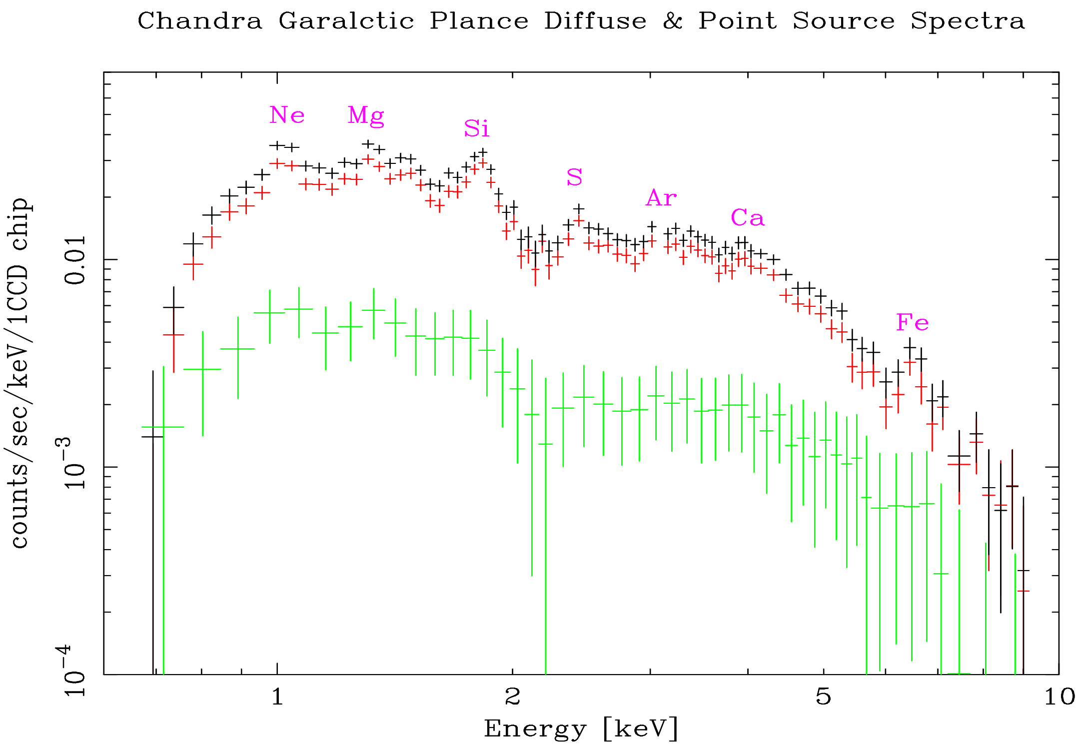

Fig. 7.— Energy spectra of the total X-rays in the field of view (black; the AX J 1843.8–0352/G28.6–0.1 region in Fig. 1 is excluded), of the sum of all the point sources (green), and of their difference, namely, the Galactic diffuse emission (red). It is found that ~ 90 % of the X-ray emission is from the diffuse emission, with which emission lines from highly ionized heavy elements are associated (prominent emission lines are annotated with element names). The ordinate is normalized with the average counting rate per CCD chip.

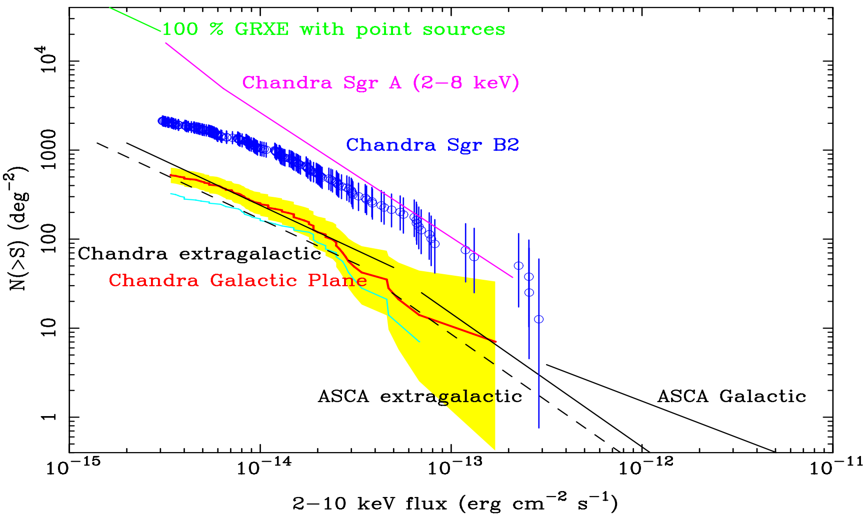

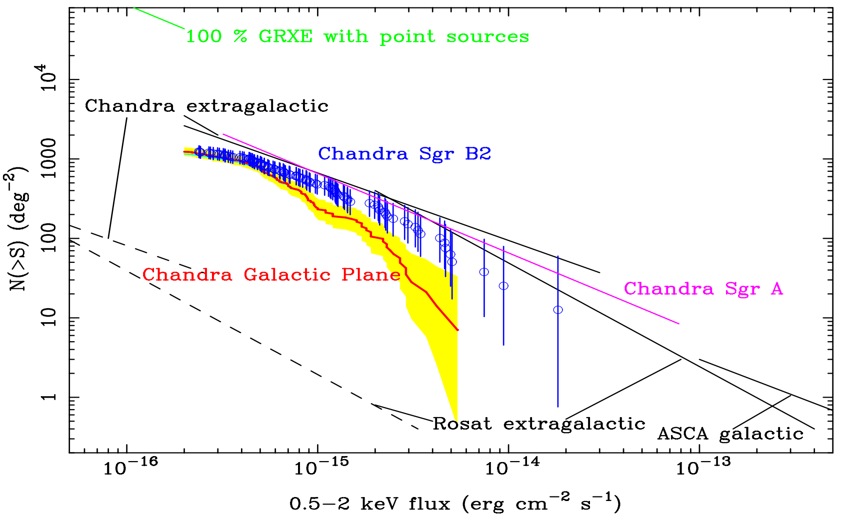

Fig. 8.— The $\log N - \log S$ curves of the point sources detected in our *Chandra* Galactic plane field in 2 – 10 keV (top) and 0.5 – 2 keV (bottom). They are indicated in red lines, and the 90 % error regions are shown in yellow. Also the $\log N - \log S$ curves of only the sources having the near infrared counterparts are shown in cyan (in the soft band, it is almost completely overlapped with red-line, and barely seen only at the lowest flux). In addition, number of the hypothetical point sources whose sum would account for the 100 % of the Galactic ridge X-ray emission at a given point source flux is indicated (in green) below our detection limits. Together, other $\log N - \log S$ relations are shown for the bright *ASCA* Galactic sources (Sugizaki et al. 2001), *Chandra* Galactic center Sgr B2 and Sgr A (Muno et al. 2003), and extragalactic point sources detected with *ASCA* (Ueda et al. 1999), *ROSAT* and *Chandra* (Giacconi et al. 2001). For the extragalactic sources, both the original $\log N - \log S$ curves at high Galactic latitudes (black solid lines) and the ones expected on the Galactic plane after extinguished by a hydrogen column density of 6×10^{22} cm^{-2} (dashed lines) are shown.

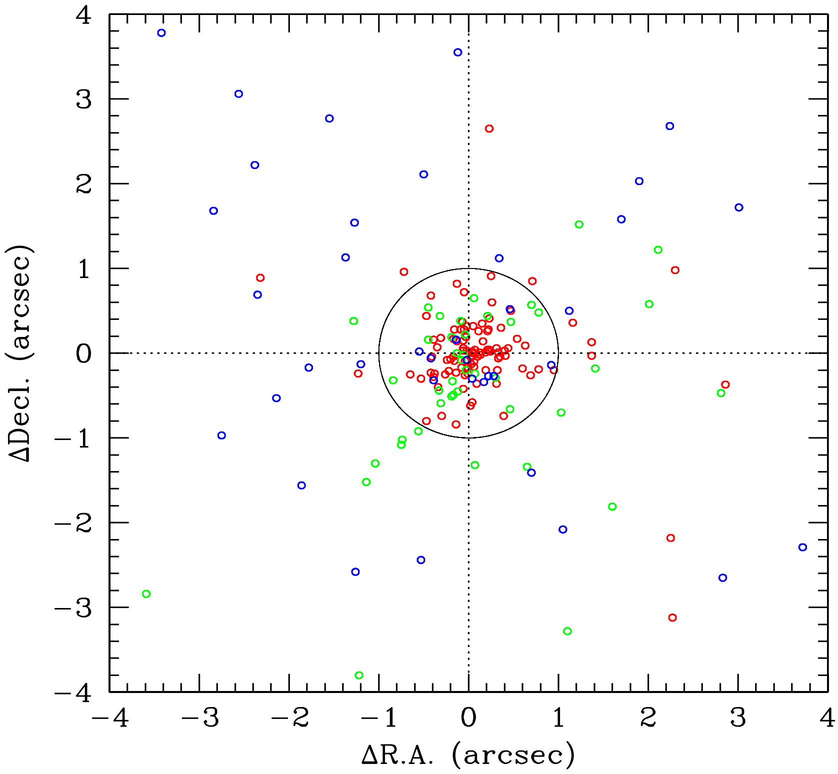

Fig. 9.— For all the *Chandra* sources detected in the fields covered by SOFI, positional offsets of the nearest SOFI sources are plotted. Red, green and blue are soft, medium and hard X-ray sources, respectively. We consider sources within $1''$ (central circle) as the counterparts. It is obvious that soft X-ray sources are more likely to have NIR counterparts than harder X-ray sources (see also Table 3).

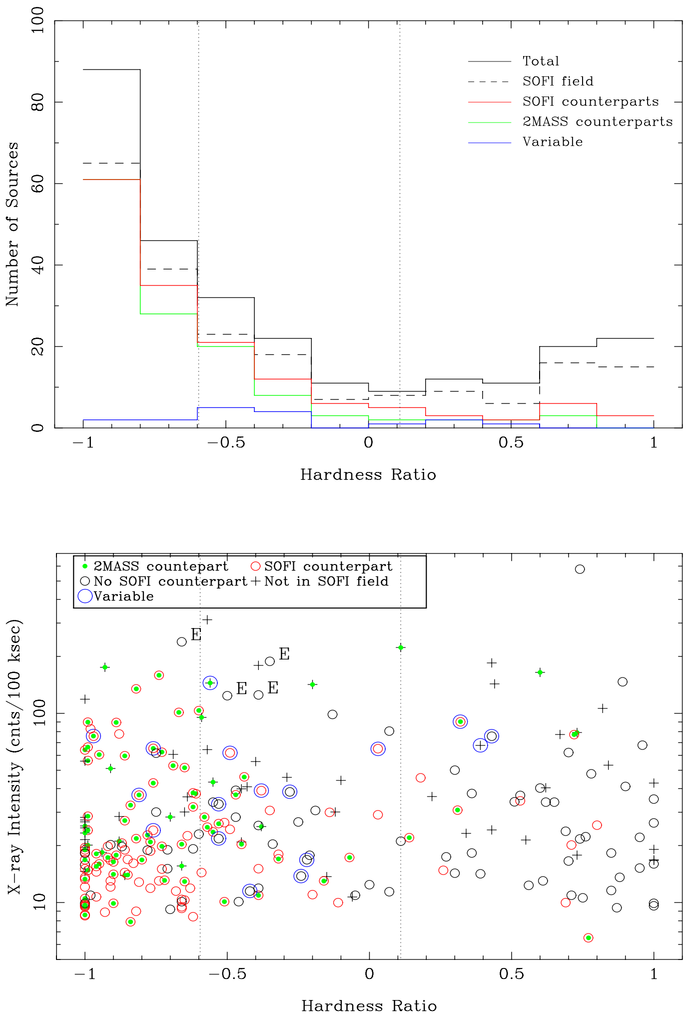

Fig. 10.— Histogram of the number of sources as a function of the spectral hardness ratio (HR) (top) and HR vs. the count rate (bottom). In the top panel, the dashed line indicates the number of sources within the SOFI fields (Fig. 3), and the red line shows the sources having the SOFI near-infrared counterpart. The green line indicates the number of sources having 2MASS counterpart, and the blue line indicates the number of variable sources (Section 3.5.3). In the bottom panel, the sources outside of the SOFI field are shown with crosses, and those inside are with circles: black circles indicate the sources without SOFI counterparts, while red circles are those having the SOFI counterparts. In addition, sources having the 2MASS counterparts are marked with green dots, and variable sources are marked with blue circle. The vertical dotted lines in both figures indicate the boundaries we defined between the soft and medium sources ($HR = -0.595$), and the medium and hard sources ($HR = 0.11$). Source marked with "E" (Sources 208, 210, 213 and 126) in the bottom panel are parts of the extended feature CXOU J184357-035441 (Section 2.2; Ueno et al. 2003).

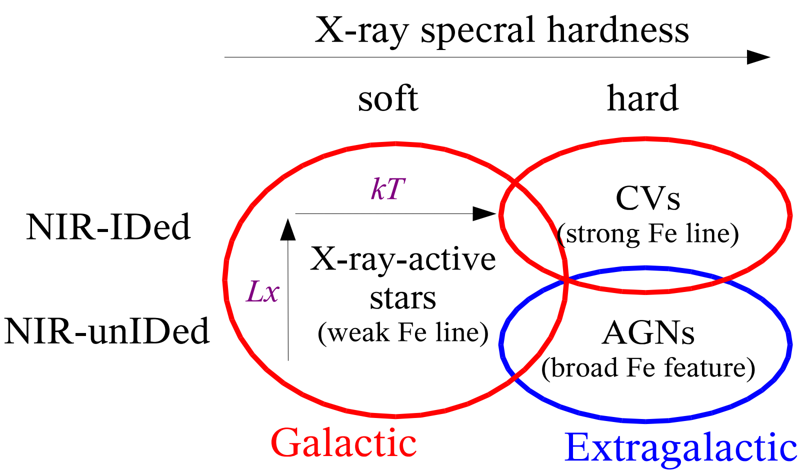

Fig. 11.— Classification of the point X-ray sources according to the X-ray spectral hardness and on the presence or absence of the NIR counterpart.

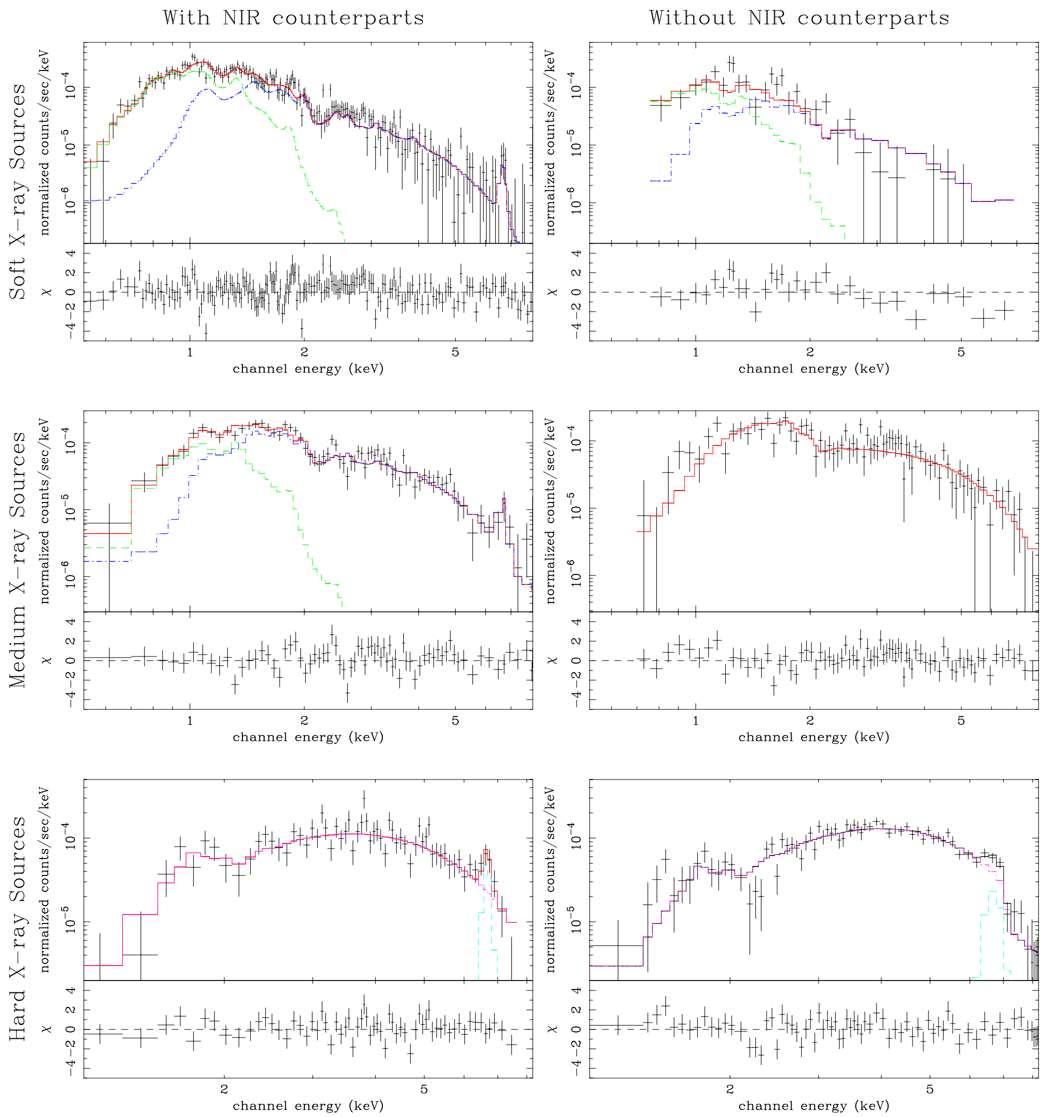

Fig. 12.— Composite energy spectra and model fitting of the point sources grouped by the X-ray spectral hardness and absence or presence of the NIR counterpart. Those having the NIR counterpart are in the left-hand side, and those without the NIR counterpart are in the right-hand side. The top two panels are the soft source spectra, the middle ones are the medium, and the bottom ones the hard. See the text (section 3.5.2) for the fitting models.

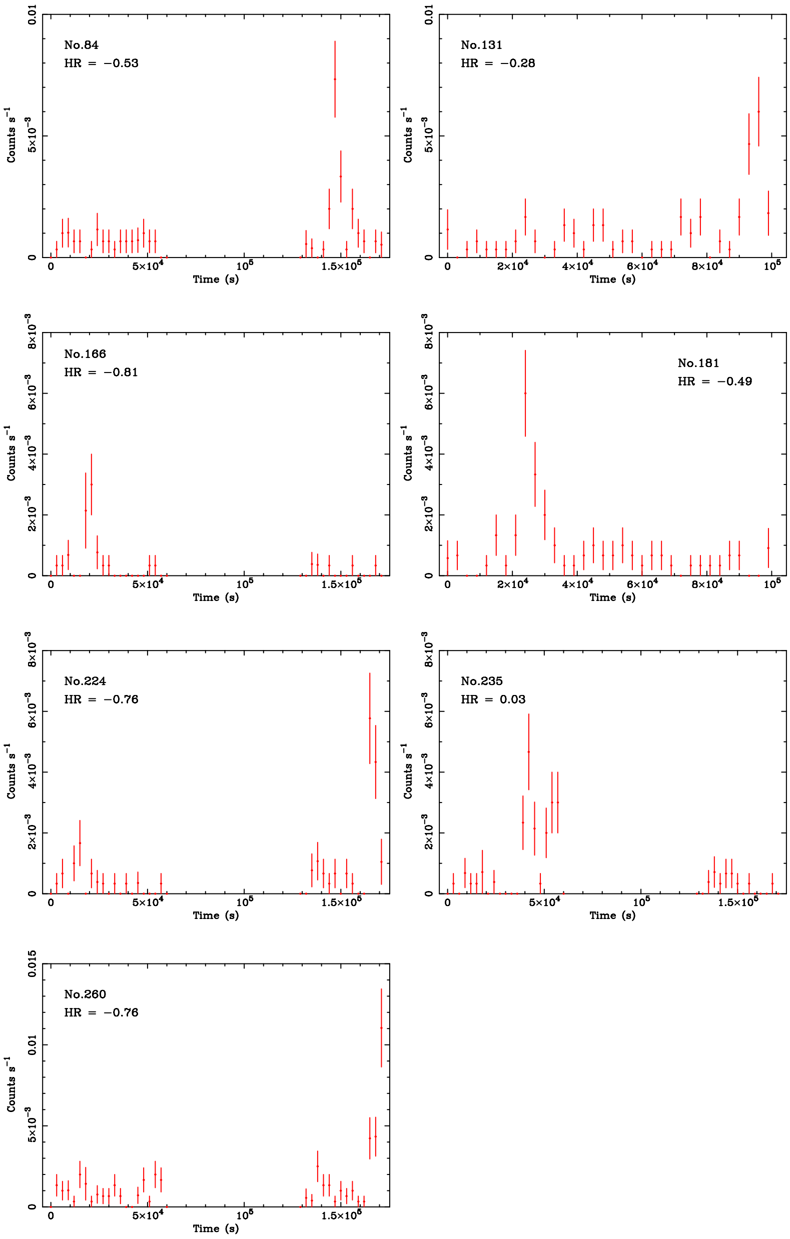

Fig. 13.— Light curves of the seven variable sources exhibiting flare-like phenomena.

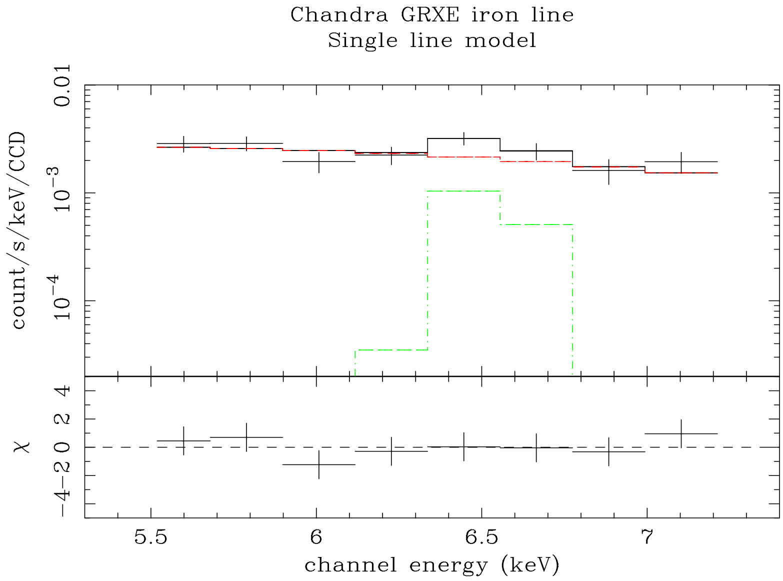

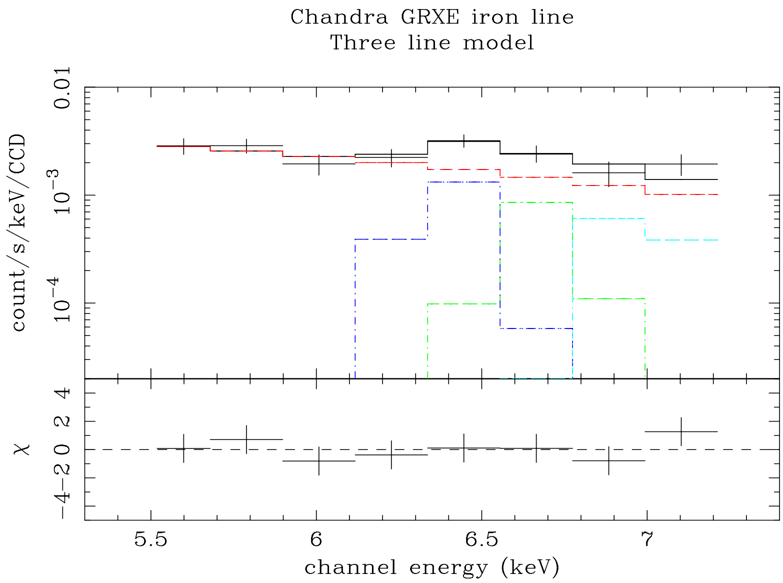

Fig. 14.— The iron line from the Galactic Ridge diffuse X-ray Emission fitted with a single line (top) or three lines (bottom; differentiated with different colors). Both models fit the observed spectrum equally well.

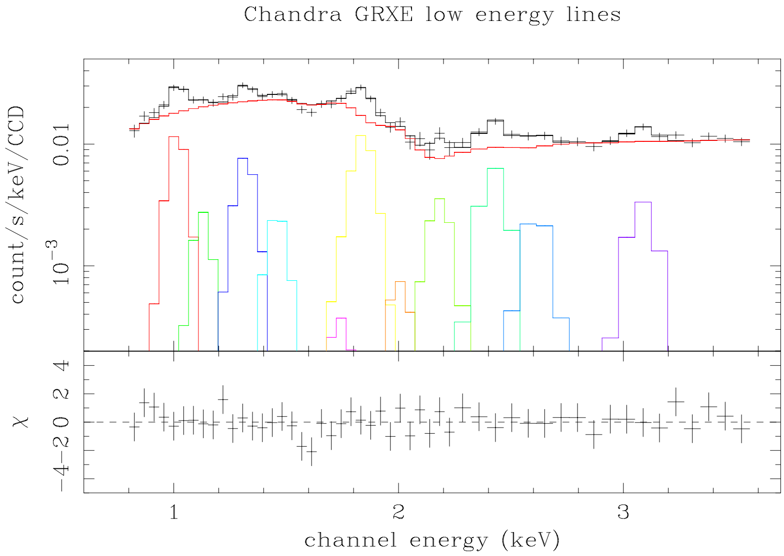

Fig. 15.— Emission lines from the Galactic Ridge diffuse X-ray Emission in the soft energy band. Eleven gaussians (differentiated with different colors) are put with a power-law continuum.

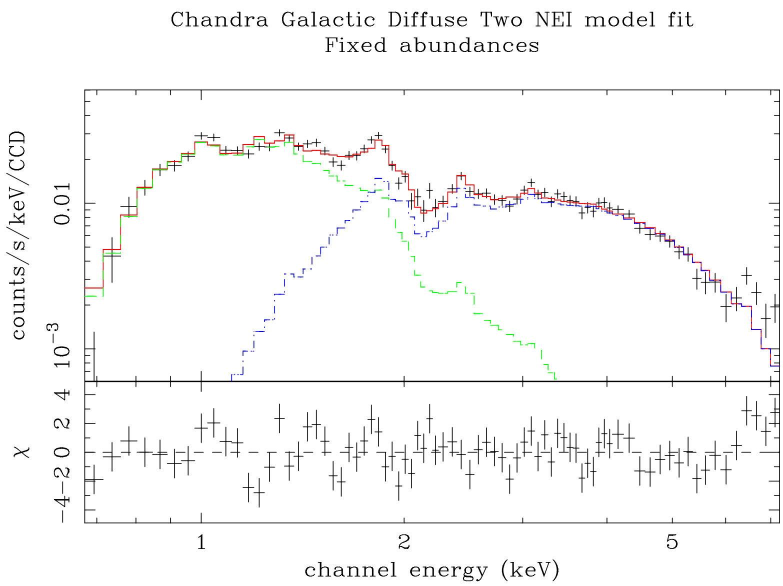

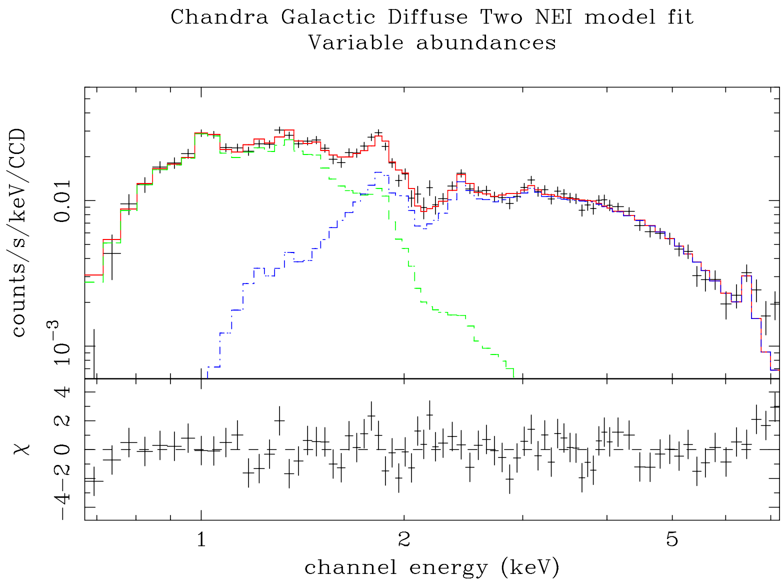

Fig. 16.— Spectral fitting of the Galactic diffuse emission with a two component NEI model (Masai 1984) with fixed abundances for each component (top) or variable abundances (bottom). Note that the iron line ($\sim$ 6.7 keV) and neon line ($\sim$ 1.0 keV) features are fitted in the bottom figure, but not in the top.

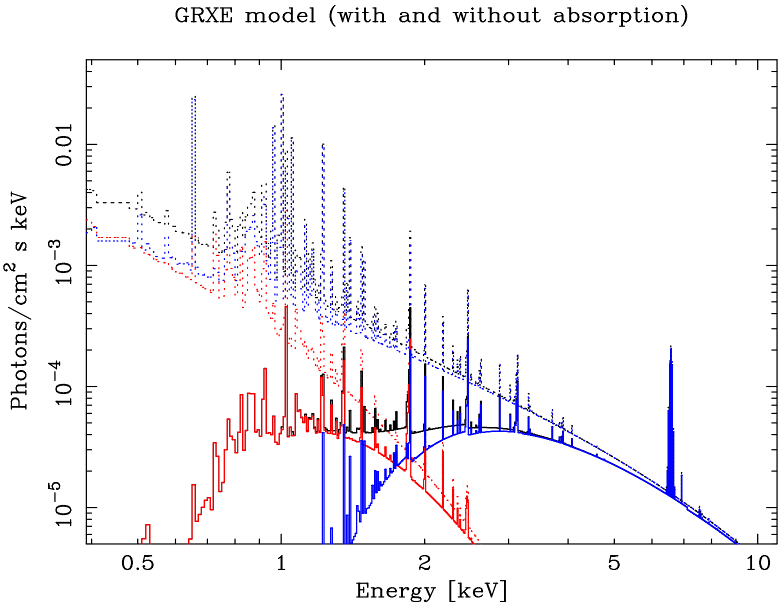

Fig. 17.— Best fit spectral model used in Fig. 16 including interstellar absorption (solid lines) and removing the absorption (dotted lines). Hard component is drawn in blue, soft component is in red, and total is in black.

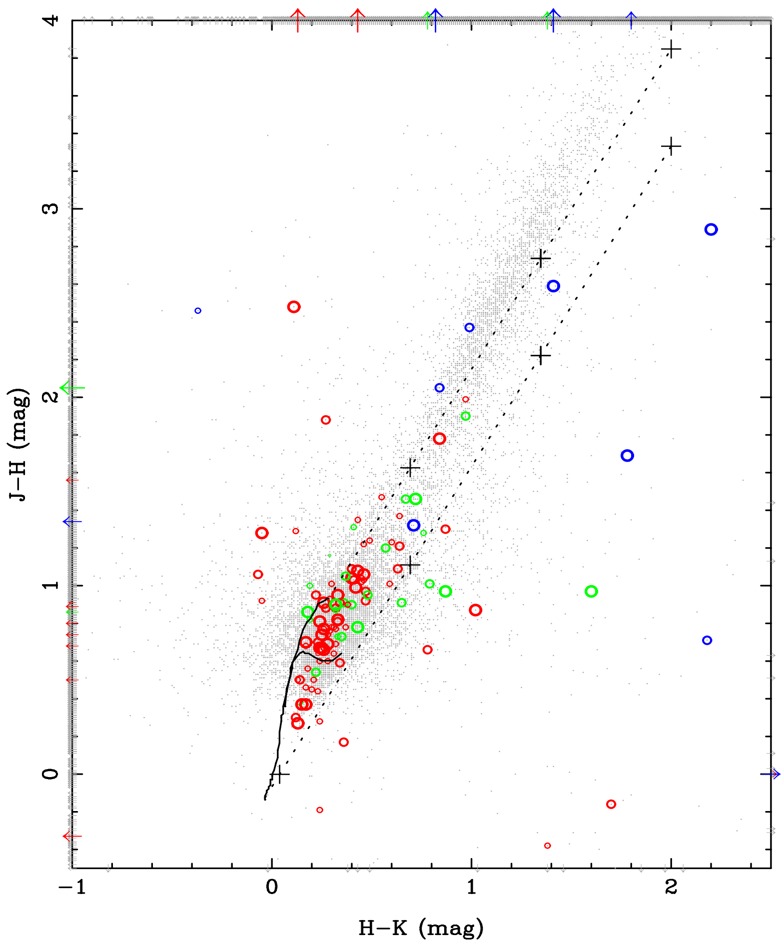

Fig. 18.— NIR color-color diagram of all the SOFI sources (gray) and the *Chandra* sources with NIR counterparts (red, green and blue circles for soft, medium and hard sources, respectively). The symbol size for *Chandra* sources is approximately proportional to the X-ray counting rates. Solid curves indicate the loci for dwarfs (main sequence stars) and giants, and dotted lines show the reddening (towards upper-right), such that distance between the crosses correspond to A_V=10 mag (data taken from Cox 1999). Sources detected only in two bands are marked at the border of the graph. Note that there are significant number of sources which cannot be plotted in this diagram because they are detected only in one band.

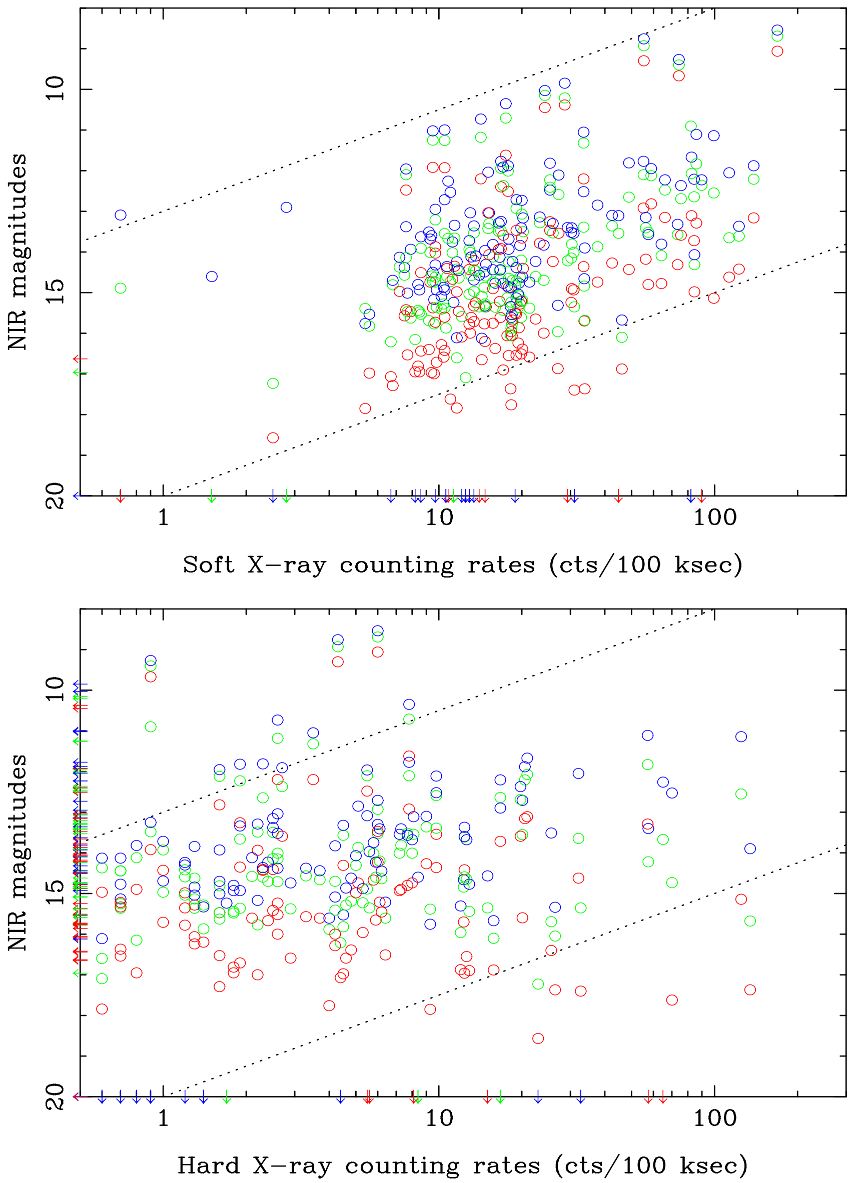

Fig. 19.— Correlation between the X-ray counting rates (top = 0.5 – 2 keV band, bottom= 2 – 10 keV band) and the NIR magnitudes (red=J, green =H and blue = K_S). The black dotted lines indicate the slopes for the sources with the constant luminosities at different distances.

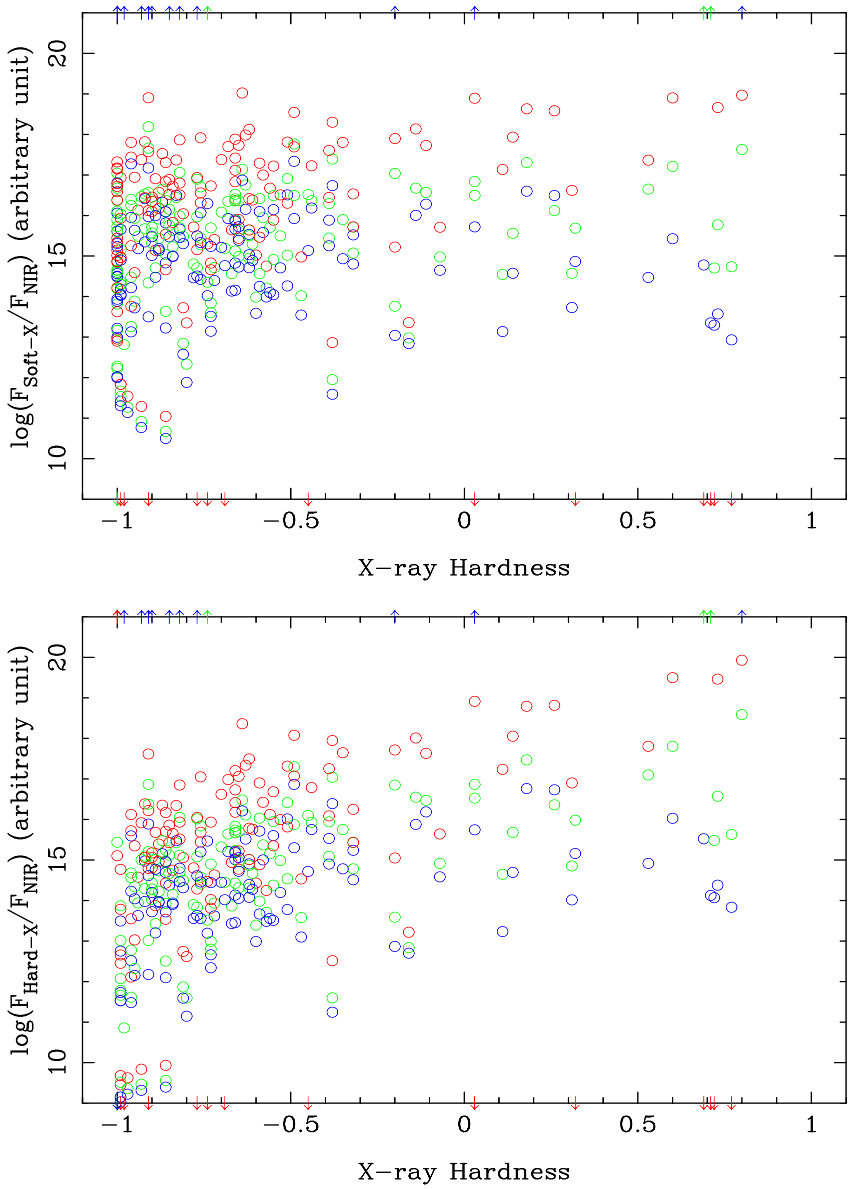

Fig. 20.— X-ray spectral hardness versus the X-ray and NIR flux ratio. Top panel gives the soft X-ray flux over NIR flux ratio, and the bottom is for the hard X-ray flux. Red, green and blue colors indicate J, H and K_S band fluxes, respectively.

Table 1. Detected Source List

ID[a]	AO	R.A. (hh:mm:ss.ss) (J2000)	Dec. (d:mm:ss.s) (J2000)	Error (arcsec)	Significance (σ) Total/Soft/Hard	Normalized counts (cnts/100ks) Total/Soft/Hard	Hardness (H-S)/(H+S)	Flux (ergs s^{-1} cm^{-2}) 0.5-2keV/2-10keV	NIR conterpart ID[b]	seperation (arcsec)	J^c (mag)	H^c (mag)	$K_S{}^c$ (mag)
1	2	18:42:51.77	−3 51 11.2	0.86	5.5/5.1/0.0	27.3/27.1/0.0	-1.00 ± 0.09	4.0E-16/1.6E-16	OoF	···	···	···	···
2^T	2	18:42:53.53	−3 49 19.6	0.93	6.9/3.6/6.3	67.7/21.3/48.8	0.39 ± 0.12	3.5E-16/1.0E-14	OoF	···	···	···	···
3	2	18:42:58.30	−3 53 28.1	0.49	11.3/0.0/11.4	79.2/11.0/70.0	0.73± 0.08	4.2E-17/3.1E-14	J18425832-0353271	1.00	17.62	14.73	12.53
4^T	2	18:43:00.41	−3 53 48.9	0.36	19.0/18.5/6.0	144.7/112.9/32.1	-0.56± 0.07	2.5E-15/1.0E-14	J18430043-0353486	0.36	14.62	13.65	12.05
5	2	18:43:01.50	−3 50 47.3	0.69	5.0/0.0/5.5	17.8/2.5/15.8	0.73 ± 0.20	8.8E-18/6.4E-15	OoF	···	···	···	···
6	2	18:43:01.83	−3 54 42.4	0.48	7.4/6.7/2.0	45.9/29.8/16.3	-0.29 ± 0.15	9.5E-16/3.9E-15	OoF	···	···	···	···
7	2	18:43:06.14	−3 54 54.8	0.43	4.1/4.6/0.0	20.9/15.2/5.8	-0.45 ± 0.21	4.3E-16/1.8E-15	OoF	···	···	···	···
8	2	18:43:06.88	−3 55 37.0	0.35	8.1/6.0/4.0	30.1/17.0/13.2	-0.12 ± 0.19	2.1E-16/6.2E-15	OoF	···	···	···	···
9	2	18:43:07.25	−3 49 55.2	0.55	5.2/8.2/0.0	28.2/28.1/0.0	-1.00 ± 0.08	8.3E-16/3.4E-16	OoF	···	···	···	···
10	2	18:43:07.27	−3 48 58.4	0.75	4.1/0.0/4.0	16.8/0.0/17.2	1.00 ± 0.13	1.1E-17/8.0E-15	OoF	···	···	···	···
11	2	18:43:07.98	−3 53 17.1	0.40	8.1/7.2/0.0	30.6/18.3/12.4	-0.19 ± 0.19	2.3E-16/6.8E-15	No	···	···	···	···
12	2	18:43:08.73	−3 50 01.8	0.53	4.6/3.5/2.4	10.7/6.3/5.7	-0.06 ± 0.32	4.0E-17/1.2E-15	OoF	···	···	···	···
13	2	18:43:10.86	−3 55 35.5	0.38	4.3/6.3/0.0	20.2/19.3/0.9	-0.91 ± 0.10	5.0E-16/2.0E-16	No	···	···	···	···
14	2	18:43:11.41	−3 59 50.1	0.46	8.1/7.6/1.8	39.9/28.9/10.9	-0.45 ± 0.15	7.2E-16/3.0E-15	OoF	···	···	···	···
15	2	18:43:11.81	−3 58 23.7	0.27	7.2/8.8/0.0	26.7/26.7/0.0	-1.00 ± 0.08	7.0E-16/2.8E-16	OoF	···	···	···	···
16	2	18:43:12.15	−3 48 16.2	0.72	3.6/6.0/0.0	21.1/19.7/1.3	-0.88 ± 0.15	7.2E-16/2.9E-16	J18431219-0348167	0.93	15.28	14.62	13.84
17	2	18:43:12.42	−3 57 36.8	0.49	4.3/4.0/0.0	15.6/13.0/2.6	-0.66 ± 0.22	3.8E-16/1.6E-15	J18431239-0357363	0.61	16.00	14.01	13.04
18	2	18:43:12.87	−3 50 42.0	0.55	4.6/4.9/0.0	14.8/14.8/0.0	-1.00 ± 0.15	4.8E-16/1.9E-16	OoF	···	···	···	···
19	2	18:43:12.92	−3 49 36.8	0.49	5.9/6.8/0.0	25.4/25.3/0.0	-1.00 ± 0.09	7.9E-16/3.2E-16	J18431289-0349369	0.36	13.47	12.41	12.48
20	2	18:43:13.36	−4 02 36.1	0.80	5.2/5.5/0.0	29.5/25.3/4.3	-0.71 ± 0.15	8.2E-16/3.4E-15	OoF	···	···	···	···
21	2	18:43:13.77	−3 57 07.4	0.35	6.4/6.9/0.0	20.1/20.0/0.1	-0.99 ± 0.11	5.9E-16/2.4E-16	J18431378-0357073	0.28	13.66	13.07	12.73
22	2	18:43:14.45	−3 52 11.5	0.32	4.2/4.3/0.0	12.7/12.7/0.0	-1.00 ± 0.17	2.6E-16/1.1E-16	No	···	···	···	···
23	2	18:43:14.97	−3 58 12.8	0.45	4.9/3.8/0.0	16.3/10.5/5.8	-0.29 ± 0.26	4.1E-16/1.7E-15	OoF	···	···	···	···
24	2	18:43:15.29	−3 54 19.5	0.17	9.1/9.7/0.0	24.1/24.2/0.1	-0.99 ± 0.08	6.9E-16/2.8E-16	S687/J18431530-0354190	0.38	10.45	10.15	10.03
25	2	18:43:15.29	−3 56 17.2	0.22	10.6/10.7/0.0	30.1/26.3/3.8	-0.75 ± 0.13	8.6E-16/3.6E-15	No	···	···	···	···
26	2	18:43:15.40	−3 50 49.1	0.34	4.5/5.0/0.0	13.9/12.9/1.0	-0.86 ± 0.15	6.1E-16/2.5E-16	J18431539-0350483	0.74	14.43	13.93	13.72
27	2	18:43:15.54	−3 47 58.5	0.67	4.7/0.0/4.9	21.4/4.7/15.9	0.55 ±0.21	1.3E-16/4.0E-15	OoF	···	···	···	···
28	2	18:43:15.81	−3 56 40.4	0.42	4.3/0.0/2.9	13.7/8.5/6.3	-0.15 ±0.28	7.3E-17/2.2E-15	OoF	···	···	···	···
29	2	18:43:17.43	−3 56 00.2	0.22	5.9/3.9/2.8	13.0/7.6/5.5	-0.16 ±0.30	1.3E-16/3.9E-15	S1031/J18431748-0355597	0.90	12.48	12.10	11.96
30	2	18:43:17.43	−3 57 32.7	0.23	7.0/7.4/0.0	19.8/19.1/0.7	-0.92 ±0.11	5.5E-16/2.2E-16	S1018	0.13	16.54	15.25	15.13
31	2	18:43:17.47	−3 48 52.6	0.40	5.3/5.9/0.0	18.4/18.4/0.0	-1.00 ±0.12	4.9E-16/2.0E-16	S1038	0.63	16.06	15.78	15.54
32	2	18:43:17.97	−3 47 14.9	0.82	3.6/4.5/0.0	19.6/19.5/0.0	-1.00 ±0.12	4.5E-16/1.8E-16	OoF	···	···	···	···
33	2	18:43:18.18	−3 47 32.4	0.89	3.0/4.0/0.0	14.6/14.5/0.0	-1.00 ±0.16	4.1E-16/1.7E-16	OoF	···	···	···	···
34	2	18:43:18.41	−4 00 54.9	0.77	3.6/4.1/0.0	9.7/9.7/0.0	-1.00 ±0.23	4.2E-16/1.7E-16	OoF	···	···	···	···
35	2	18:43:18.59	−3 58 52.1	0.35	5.8/6.8/0.0	19.5/19.5/0.0	-1.00 ±0.11	4.6E-16/1.9E-16	S1360	0.36	15.86	15.08	14.77
36	2	18:43:18.73	−3 54 25.2	0.20	5.1/3.3/0.0	11.0/6.7/4.4	-0.20 ±0.31	7.3E-17/2.2E-15	S1398	0.22	17.07	16.21	···
37	2	18:43:18.95	−3 53 27.3	0.24	4.4/4.2/0.0	12.8/11.6/1.2	-0.81 ±0.21	4.3E-16/1.7E-16	S1479	0.74	14.98	14.42	14.24
38	2	18:43:19.01	−3 59 33.4	0.38	8.8/0.0/8.6	33.9/6.4/27.4	0.62 ±0.14	1.8E-17/1.3E-14	No	···	···	···	···
39	2	18:43:19.22	−3 57 31.9	0.28	4.7/4.8/0.0	13.0/11.3/1.7	-0.74 ±0.21	3.4E-16/1.4E-15	S1544	0.73	···	···	15.24
40	2	18:43:19.47	−4 01 36.9	0.73	3.3/5.1/0.0	19.1/19.1/0.0	-1.00 ±0.12	5.5E-16/2.2E-16	OoF	···	···	···	···
41	2	18:43:19.61	−3 55 02.1	0.25	3.8/4.2/0.0	8.9/8.6/0.3	-0.93 ±0.22	2.3E-16/9.2E-17	S1652	0.81	16.44	15.53	···
42	2	18:43:20.55	−3 48 59.9	0.24	8.1/0.0/8.7	26.3/0.0/26.3	1.00 ±0.08	2.1E-17/1.5E-14	No	···	···	···	···
43	2	18:43:20.56	−3 49 03.3	0.31	9.1/0.0/10.1	35.2/0.0/35.3	1.00 ±0.06	2.0E-17/1.5E-14	No	···	···	···	···
44	2	18:43:20.86	−3 52 46.5	0.11	20.6/8.3/14.9	50.2/17.6/32.7	0.30 ±0.14	3.5E-16/1.1E-14	No	···	···	···	···
45	2	18:43:21.10	−3 52 15.0	0.16	4.7/0.0/4.7	9.4/0.6/8.6	0.87 ±0.21	4.7E-18/3.4E-15	No	···	···	···	···
46	2	18:43:21.11	−3 54 30.0	0.20	5.0/0.0/4.2	10.0/1.5/8.4	0.69 ±0.26	6.4E-18/4.6E-15	S2107	0.21	···	···	14.60
47	2	18:43:21.22	−3 49 31.2	0.37	9.0/11.5/0.0	42.8/37.6/5.1	-0.76 ±0.10	9.6E-16/4.0E-15	S2159/J18432128-0349314	0.97	14.74	13.87	12.85
48	2	18:43:21.37	−4 01 02.9	0.27	26.1/12.0/22.0	184.7/52.7/131.9	0.43 ±0.07	1.1E-15/3.4E-14	OoF	···	···	···	···
49	2	18:43:21.62	−3 55 28.0	0.23	4.5/4.8/0.0	9.8/9.7/0.0	-1.00 ±0.22	5.0E-16/2.0E-16	S2284	0.24	14.03	14.62	···

Table 1—Continued

ID[a]	AO	R.A. (hh:mm:ss.ss) (J2000)	Dec. (d:mm:ss.s) (J2000)	Error (arcsec)	Significance (σ) Total/Soft/Hard	Normalized counts (cnts/100ks) Total/Soft/Hard	Hardness (H-S)/(H+S)	Flux (ergs s^{-1} cm^{-2}) 0.5-2keV/2-10keV	NIR conterpart ID[b]	NIR conterpart seperation (arcsec)	J^c (mag)	H^c (mag)	$K_S{}^c$ (mag)
50	2	18:43:21.76	−4 00 39.6	0.53	4.9/5.7/0.0	18.4/17.9/0.5	-0.94 ±0.12	6.1E-16/2.5E-16	J18432180-0400395	0.73	14.88	14.24	13.93
51	2	18:43:21.81	−3 53 03.3	0.19	8.3/8.0/0.0	18.7/16.5/2.2	-0.77 ±0.17	4.0E-16/1.7E-15	S2354/18432182-0353031	0.24	13.94	13.49	13.29
52	2	18:43:22.09	−3 54 26.4	0.17	7.4/7.5/0.0	16.1/14.7/1.4	-0.83 ±0.17	6.1E-16/2.5E-16	S2458	0.34	16.20	15.28	15.33
53	2	18:43:22.82	−3 52 28.6	0.24	4.4/0.0/2.8	10.6/1.3/9.1	0.75 ±0.25	6.2E-18/4.5E-15	No	···	···	···	···
54	2	18:43:22.98	−3 57 53.0	0.19	7.5/7.7/0.0	17.8/16.8/0.9	-0.89 ±0.11	6.0E-16/2.4E-16	S2739/J18432299-0357526	0.47	13.92	13.48	13.25
55	2	18:43:23.03	−3 57 25.3	0.26	5.2/5.0/0.0	11.9/9.6/2.2	-0.63 ±0.27	3.0E-16/1.2E-15	S2749	0.66	17.00	15.77	15.17
56	2	18:43:23.30	−3 48 51.7	0.31	15.3/17.2/0.0	64.1/64.1/0.0	-1.00 ±0.03	2.9E-15/1.2E-15	S2844/J18432331-0348521	0.47	14.78	14.09	13.81
57	2	18:43:23.39	−3 58 05.1	0.21	9.6/10.9/0.0	27.1/25.3/1.9	-0.86 ±0.11	8.1E-16/3.3E-16	S2871/J18432340-0358050	0.19	13.26	12.23	11.82
58	2	18:43:23.62	−3 53 14.1	0.21	4.6/3.4/0.0	10.9/7.5/3.3	-0.39 ±0.30	2.5E-16/1.0E-15	S2932/J18432360-0353138	0.13	15.57	14.57	14.38
59	2	18:43:23.68	−3 51 40.6	0.23	6.6/6.0/0.0	14.4/13.4/1.0	-0.86 ±0.19	5.2E-16/2.1E-16	S2956	0.09	15.71	14.97	14.69
60	2	18:43:23.72	−4 00 26.0	0.42	8.5/5.4/3.1	40.9/28.4/11.4	-0.43 ±0.15	7.5E-16/3.1E-15	OoF	···	···	···	···
61	2	18:43:23.89	−3 53 31.4	0.18	5.4/2.8/4.6	17.4/6.2/10.8	0.27 ±0.25	1.1E-16/3.4E-15	No	···	···	···	···
62[T]	2	18:43:23.96	−3 57 58.9	0.18	13.2/10.7/5.2	39.0/27.0/12.0	-0.38 ±0.15	8.7E-16/3.6E-15	S3040	0.65	16.87	15.96	15.31
63	2	18:43:24.33	−4 03 38.5	1.09	0.0/4.3/0.0	21.5/21.5/0.0	-1.00 ±0.11	2.2E-16/8.7E-17	OoF	···	···	···	···
64	2	18:43:24.47	−3 53 49.8	0.06	42.1/39.3/9.0	101.2/84.3/16.7	-0.67 ±0.07	2.2E-15/9.1E-15	S3203/J18432446-0353495	0.05	13.72	12.64	12.21
65	2	18:43:24.81	−3 59 16.2	0.34	5.6/5.6/0.0	16.7/16.0/0.7	-0.91 ±0.12	5.8E-16/2.4E-16	S3312	0.47	16.37	15.36	14.77
66	2	18:43:25.04	−3 57 51.0	0.22	6.5/6.9/0.0	17.3/16.6/0.7	-0.92 ±0.12	6.2E-16/2.5E-16	S3394/J18432504-0357511	0.17	15.22	14.45	14.13
67	2	18:43:25.25	−3 59 15.3	0.30	6.6/6.4/0.0	23.6/18.3/5.3	-0.55 ±0.19	6.1E-16/2.5E-15	S3450/J18432523-0359150	0.55	15.96	15.23	14.88
68	2	18:43:26.14	−3 56 49.7	0.14	11.2/9.4/2.3	26.4/19.9/6.4	-0.51 ±0.18	7.1E-16/2.9E-15	S3833	0.42	16.51	15.61	15.21
69	2	18:43:26.41	−3 57 05.9	0.17	4.0/0.0/4.2	9.9/0.0/9.8	1.00 ±0.21	6.5E-18/4.7E-15	No	···	···	···	···
70	1	18:43:28.34	−4 07 33.2	0.31	21.3/25.4/0.0	175.1/169.0/6.0	-0.93 ±0.03	4.2E-15/1.7E-15	J18432835-0407331	0.26	9.06	8.69	8.54
71	2	18:43:28.35	−3 46 18.2	0.76	4.0/3.8/0.0	17.4/17.4/0.0	-1.00 ±0.13	6.6E-16/2.7E-16	OoF	···	···	···	···
72	2	18:43:28.67	−3 56 22.8	0.15	4.0/3.4/0.0	8.4/6.8/1.6	-0.62 ±0.30	1.8E-16/7.2E-16	S4885	0.27	17.29	14.81	14.70
73	2	18:43:28.91	−3 57 33.3	0.12	10.8/10.6/0.0	22.7/20.2/2.5	-0.78 ±0.14	5.1E-16/2.1E-15	S4992/J18432891-0357332	0.04	14.41	13.50	13.16
74	2	18:43:29.11	−3 59 42.3	0.39	4.3/0.0/2.5	14.8/5.4/9.3	0.26 ±0.27	8.2E-17/2.5E-15	S5111	0.69	17.85	15.39	15.76
75	2	18:43:29.26	−3 50 50.9	0.25	6.7/7.1/0.0	16.4/15.7/0.8	-0.90 ±0.12	4.7E-16/1.9E-16	S5148/J18432926-0350504	0.16	14.90	14.12	13.82
76	2	18:43:29.32	−3 56 48.7	0.15	8.9/0.0/9.3	22.1/0.5/21.5	0.95 ±0.09	1.5E-17/1.1E-14	No	···	···	···	···
77	1	18:43:29.33	−4 05 19.4	0.48	3.9/5.3/0.0	23.3/23.2/0.0	-1.00 ±0.11	9.2E-16/3.7E-16	J18432934-0405185	0.84	13.78	13.28	13.14
78	2	18:43:29.55	−3 46 56.5	0.52	3.8/0.0/4.0	18.4/0.7/17.7	0.93 ±0.12	1.1E-17/7.7E-15	OoF	···	···	···	···
79	2	18:43:29.70	−3 50 15.1	0.31	5.5/0.0/2.6	20.1/2.8/16.7	0.71 ±0.17	1.2E-17/8.4E-15	S5359	0.30	···	···	12.90
80	2	18:43:30.20	−3 51 18.2	0.21	4.5/4.0/0.0	9.2/7.8/1.4	-0.70 ±0.28	2.8E-16/1.1E-15	No	···	···	···	···
81	2	18:43:30.21	−3 53 44.3	0.17	4.2/4.7/0.0	9.9/9.5/0.5	-0.90 ±0.19	3.4E-16/1.4E-16	S5569/J18433019-0353440	0.33	15.37	14.73	14.50
82	2	18:43:30.27	−3 54 11.4	0.05	49.2/42.1/10.7	103.5/82.4/20.9	-0.60 ±0.08	3.7E-15/1.5E-14	S5602/J18433026-0354110	0.39	13.11	12.07	11.67
83	1/2	18:43:30.35	−3 59 43.3	0.43	0.0/5.0/0.0	15.8/15.8/0.0	-1.00 ±0.11	3.5E-16/1.4E-16	No	···	···	···	···
84[T]	1	18:43:30.52	−4 03 50.3	0.48	6.4/6.0/0.0	33.1/25.5/7.8	-0.53 ±0.17	7.3E-16/3.0E-15	No	···	···	···	···
85	2	18:43:30.63	−3 53 52.0	0.14	5.4/5.8/0.0	10.5/10.5/0.0	-1.00 ±0.18	3.5E-16/1.4E-16	S5758/J18433062-0353515	0.29	11.93	11.26	11.00
86[T]	1/2	18:43:30.75	−4 01 02.5	0.26	16.5/20.5/0.0	75.8/74.2/0.9	-0.97±0.03	2.2E-15/9.0E-16	S5825/J18433077-0401025	0.41	9.67[b]	9.40[b]	9.27[b]
87	1	18:43:30.80	−4 00 45.9	0.65	4.3/4.5/0.0	19.0/18.9/0.0	-1.00 ±0.13	5.6E-16/2.3E-16	S5840/J18433081-0400459	0.35	15.51	14.83	···
88	2	18:43:31.28	−3 50 29.1	0.23	12.6/2.8/9.3	37.7/11.8/25.1	0.36 ±0.16	2.4E-16/7.2E-15	No	···	···	···	···
89	2	18:43:31.30	−3 46 18.0	0.70	6.4/7.6/0.0	34.6/34.8/-0.0	-1.00 ±0.07	9.5E-16/3.8E-16	OoF	···	···	···	···
90	2	18:43:31.47	−3 55 15.8	0.23	4.9/2.9/0.0	10.0/5.6/4.5	-0.11 ±0.33	2.2E-17/6.7E-16	S6146	0.48	16.98	15.82	15.53
91	1/2	18:43:31.59	−3 56 49.4	0.11	14.9/14.0/2.4	32.0/25.9/6.0	-0.62 ±0.11	5.5E-16/2.3E-15	S6217/J18433157-0356492	0.18	14.23	13.53	13.30
92	2	18:43:31.68	−3 48 39.3	0.45	4.3/4.5/0.0	16.8/16.8/0.0	-1.00 ±0.13	5.3E-16/2.1E-16	S6289/J18433170-0348390	0.56	12.40	11.94	11.77
93	2	18:43:31.72	−3 59 56.1	0.48	4.0/0.0/2.7	10.9/5.7/5.2	-0.05 ±0.32	5.0E-17/1.5E-15	No	···	···	···	···
94	2	18:43:31.75	−3 51 26.7	0.15	10.7/9.3/1.9	26.1/19.9/6.1	-0.53 ±0.17	5.7E-16/2.4E-15	S6293/J18433170-0351268	0.55	15.21	14.20	13.41
95	2	18:43:31.76	−3 57 39.3	0.15	13.2/3.7/11.0	34.0/8.3/25.7	0.51 ±0.16	2.4E-16/7.1E-15	No	···	···	···	···
96	2	18:43:31.78	−3 57 17.2	0.20	4.3/3.8/0.0	9.5/7.9/1.6	-0.66 ±0.27	1.7E-16/6.9E-16	S6318	0.07	15.47	15.63	13.93
97	2	18:43:32.27	−3 54 44.7	0.16	6.9/6.2/0.0	16.0/14.6/1.5	-0.81 ±0.17	4.5E-16/1.8E-16	No	···	···	···	···
98	1/2	18:43:32.41	−4 00 50.4	0.39	5.2/5.7/0.0	14.0/12.9/1.2	-0.85 ±0.18	3.9E-16/1.6E-16	S6584/J18433236-0400507	0.70	15.78	15.04	···

Table 1—Continued

ID[a]	AO	R.A. (hh:mm:ss.ss) (J2000)	Dec. (d:mm:ss.s) (J2000)	Error (arcsec)	Significance (σ) Total/Soft/Hard	Normalized counts (cnts/100ks) Total/Soft/Hard	Hardness (H-S)/(H+S)	Flux (ergs s^{-1} cm^{-2}) 0.5-2keV/2-10keV	NIR conterpart: ID[b]	NIR conterpart: seperation (arcsec)	NIR conterpart: J^c (mag)	NIR conterpart: H^c (mag)	NIR conterpart: K^c (mag)
99	1	18:43:32.47	−4 08 49.7	0.51	9.9/0.0/10.1	77.3/13.0/64.7	0.67 ±0.10	3.4E-17/2.5E-14	OoF	···	···	···	···
100	1	18:43:32.58	−4 04 18.7	0.21	31.3/19.7/23.9	222.8/99.3/125.0	0.11 ±0.07	1.6E-15/4.7E-14	J18433257-0404190	0.32	15.14	12.55	11.14
101	2	18:43:32.67	−3 49 07.6	0.37	4.5/0.0/5.1	16.0/0.0/15.7	1.00 ±0.14	8.1E-18/5.9E-15	No	···	···	···	···
102	2	18:43:33.36	−3 54 36.0	0.17	4.6/3.9/0.0	9.3/7.7/1.6	-0.66 ±0.27	2.4E-16/9.8E-16	S7035	0.05	16.53	15.47	15.01
103	2	18:43:33.41	−3 50 19.5	0.20	11.2/11.6/1.8	32.7/30.2/2.6	-0.84±0.10	7.0E-16/2.8E-16	S7055/J18433338-0350200	0.58	15.24	14.15	13.52
104	1	18:43:33.47	−4 03 54.3	0.51	3.6/4.5/0.0	25.2/17.5/7.8	-0.38 ±0.21	6.3E-16/2.6E-15	J18433350-0403541	0.52	11.62	10.71	10.35
105	2	18:43:33.94	−3 52 53.0	0.12	4.7/0.0/3.9	6.5/0.7/5.5	0.77 ±0.30	4.5E-18/3.3E-15	S7294/J18433392-0352529	0.08	···	14.89	13.09
106	2	18:43:34.12	−3 55 23.8	0.15	7.0/7.2/0.0	13.6/13.6/0.0	-1.00 ±0.15	2.8E-16/1.1E-16	S7436	0.45	15.25	14.47	14.10
107	2	18:43:34.13	−3 50 47.5	0.32	3.7/4.3/0.0	9.0/8.2/0.8	-0.82 ±0.21	2.3E-16/9.3E-17	S7413	0.24	16.95	16.15	···
108	1	18:43:34.63	−4 10 32.2	0.92	3.8/0.0/5.0	24.2/7.0/17.3	0.43 ±0.21	1.3E-16/3.8E-15	OoF	···	···	···	···
109	2	18:43:34.79	−3 46 04.2	0.70	4.4/4.5/0.0	28.5/26.8/1.7	-0.88 ±0.11	8.6E-16/3.5E-16	OoF	···	···	···	···
110	1/2	18:43:35.33	−4 00 44.7	0.35	7.1/7.4/0.0	20.3/16.7/3.7	-0.66 ±0.13	5.0E-16/2.1E-15	S8090/J18433529-0400448	0.48	15.61	14.66	14.44
111	2	18:43:35.38	−3 55 56.6	0.13	4.1/4.4/0.0	8.5/8.7/-0.3	-1.00 ±0.03	2.4E-16/9.6E-17	S8139	0.32	16.63	16.96	···
112	2	18:43:35.41	−3 57 14.8	0.25	4.9/5.0/0.0	10.7/10.5/0.2	-0.96 ±0.19	2.5E-16/1.0E-16	S8164	0.08	16.42	15.38	14.93
113	1/2	18:43:35.45	−4 01 12.7	0.34	10.1/1.9/7.9	34.5/9.2/25.6	0.53 ±0.10	1.8E-16/5.4E-15	S8192	0.35	16.40	15.69	13.51
114	2	18:43:35.48	−3 58 46.1	0.29	4.6/3.1/3.3	17.3/9.3/8.0	-0.07 ±0.25	6.4E-17/1.9E-15	S8194/J18433545-0358456	0.27	14.74	14.01	13.68
115	2	18:43:35.59	−3 46 00.8	0.58	6.2/6.0/0.0	60.7/51.5/9.3	-0.69 ±0.10	1.2E-15/5.0E-15	OoF	···	···	···	···
116	2	18:43:35.82	−3 58 54.4	0.29	4.9/4.6/0.0	13.1/11.4/1.9	-0.72 ±0.20	1.5E-16/6.1E-16	S8433/J18433584-0358539	0.68	14.35	13.66	13.34
117	2	18:43:35.84	−3 46 52.7	0.33	20.1/9.5/17.5	143.1/39.9/103.1	0.44 ±0.08	8.9E-16/2.7E-14	OoF	···	···	···	···
118	2	18:43:35.89	−3 57 58.7	0.24	6.1/6.5/0.0	14.8/14.6/0.1	-0.99 ±0.14	2.5E-16/1.0E-16	S8454/J18433588-0357587	0.10	15.77	14.87	14.49
119	1/2	18:43:36.18	−4 01 54.2	0.38	5.6/6.3/0.0	12.1/12.1/0.0	-1.00 ±0.16	4.2E-16/1.7E-16	S8621	0.94	16.09	15.59	···
120	2	18:43:36.39	−3 55 50.1	0.13	5.1/0.0/6.0	9.6/0.0/9.5	1.00 ±0.21	5.9E-18/4.3E-15	No	···	···	···	···
121	2	18:43:36.43	−3 55 53.7	0.15	5.5/1.5/4.8	12.3/2.7/9.5	0.56 ±0.25	1.6E-16/4.8E-15	No	···	···	···	···
122	1/2	18:43:36.74	−3 57 47.9	0.21	7.6/7.8/0.0	21.8/19.1/2.6	-0.82 ±0.11	5.2E-16/2.1E-16	S8957/J18433676-0357478	0.32	15.52	14.71	14.38
123	2	18:43:36.85	−3 54 29.4	0.19	6.6/6.9/0.0	14.5/14.3/0.3	-0.96 ±0.13	4.1E-16/1.7E-16	S9010	0.27	16.65	15.09	16.12
124	1	18:43:37.01	−4 02 34.5	0.45	4.3/2.9/0.0	15.1/13.0/2.2	-0.71 ±0.21	1.9E-16/7.7E-16	No	···	···	···	···
125	2	18:43:37.67	−3 57 44.4	0.28	3.8/4.4/0.0	9.5/9.5/0.0	-1.00 ±0.21	3.1E-16/1.2E-16	S9480/J18433767-0357442	0.29	11.92	11.25	11.02
126[T]	1	18:43:37.87	−4 03 53.2	0.25	16.6/4.7/14.6	75.7/21.8/55.1	0.43 ±0.11	5.8E-16/1.8E-14	No	···	···	···	···
127	1	18:43:38.17	−4 09 46.9	0.37	10.8/12.6/0.0	51.1/48.9/2.3	-0.91±0.07	1.8E-15/7.1E-16	J18433817-0409465	0.39	14.43	12.65	11.81
128	2	18:43:38.28	−3 52 01.1	0.18	4.8/5.6/0.0	9.6/9.7/0.0	-1.00 ±0.20	4.2E-16/1.7E-16	S9809/J18433826-0352012	0.30	15.73	14.74	14.32
129	1	18:43:38.59	−4 05 58.7	0.37	4.8/5.1/0.0	19.2/15.6/3.7	-0.62 ±0.22	5.5E-16/2.3E-15	No	···	···	···	···
130	2	18:43:38.63	−3 57 32.7	0.19	7.9/7.9/0.0	19.0/17.7/1.3	-0.86 ±0.14	3.0E-16/1.2E-16	S10021	0.38	16.06	15.13	14.84
131[T]	2	18:43:38.73	−3 48 34.4	0.35	6.1/3.4/4.9	38.5/24.5/13.9	-0.28 ±0.16	5.7E-16/2.4E-15	No	···	···	···	···
132	2	18:43:39.02	−3 54 44.0	0.14	6.3/6.6/0.0	13.0/12.5/0.6	-0.91 ±0.14	3.6E-16/1.4E-16	S10269	0.19	···	17.09	···
133	2	18:43:39.04	−3 52 45.9	0.06	57.2/56.8/5.8	159.0/138.6/20.5	-0.74 ±0.05	2.9E-15/1.2E-14	S10275/J18433902-0352459	0.25	13.16	12.21	11.88
134	2	18:43:39.04	−3 52 13.6	0.16	7.7/8.5/0.0	18.1/17.8/0.4	-0.96 ±0.11	6.9E-16/2.8E-16	S10271/J18433901-0352138	0.45	12.51	12.01	11.88
135	2	18:43:39.26	−3 52 52.5	0.14	12.0/13.1/0.0	28.6/28.6/0.2	-0.99 ±0.07	9.7E-16/3.9E-16	S10406/J18433923-0352523	0.41	10.38	10.21	9.85[b]
136	1	18:43:39.26	−4 07 02.5	0.46	4.7/0.0/3.8	16.6/2.5/14.1	0.70 ±0.22	1.0E-17/7.5E-15	No	···	···	···	···
137	2	18:43:39.38	−3 49 53.7	0.17	30.1/2.1/34.0	146.5/7.8/135.7	0.89 ±0.04	7.3E-17/5.3E-14	No	···	···	···	···
138	1	18:43:39.51	−4 05 14.2	0.22	15.8/2.0/15.7	62.0/9.4/52.8	0.70 ±0.10	3.5E-17/2.6E-14	No	···	···	···	···
139	2	18:43:39.76	−3 54 08.8	0.15	8.2/8.8/0.0	20.6/19.4/1.3	-0.87 ±0.12	6.3E-16/2.5E-16	S10699	0.42	16.24	15.36	15.04
140	2	18:43:40.34	−3 51 54.3	0.22	4.7/4.6/0.0	12.9/10.7/2.3	-0.65 ±0.24	2.8E-16/1.1E-15	S11045/J18434031-0351544	0.11	14.41	14.60	14.36
141	1	18:43:40.60	−4 03 42.1	0.36	6.8/5.2/1.3	20.4/13.8/6.8	-0.34 ±0.23	3.2E-16/1.3E-15	No	···	···	···	···
142	2	18:43:40.95	−3 49 54.9	0.42	2.7/4.1/0.0	10.9/10.9/0.1	-0.98 ±0.19	2.8E-16/1.2E-16	No	···	···	···	···
143	1/2	18:43:41.02	−3 58 02.3	0.32	3.9/4.3/0.0	16.8/14.2/2.6	-0.80 ±0.18	3.7E-16/1.5E-15	S11475/J18434103-0358024	0.27	12.20	11.18	10.73
144	1/2	18:43:41.13	−3 57 40.6	0.11	36.9/32.7/9.4	62.4/55.2/7.8	-0.73 ±0.08	1.6E-15/6.6E-15	S11523/J18434111-0357404	0.19	12.92	12.10	11.77
145	2	18:43:41.51	−3 50 55.0	0.27	4.5/0.0/2.5	11.4/5.3/6.1	0.07 ±0.32	9.7E-17/2.9E-15	No	···	···	···	···
146	1	18:43:41.81	−4 11 18.6	0.53	4.0/0.0/5.1	16.7/0.0/16.9	1.00 ±0.15	1.1E-17/7.9E-15	OoF	···	···	···	···
147	2	18:43:42.17	−3 57 59.0	0.22	6.3/6.2/0.0	16.9/14.8/1.2	-0.85 ±0.17	2.7E-16/1.1E-16	S12123	0.40	15.35	14.59	14.30

Table 1—Continued

ID[a]	AO	R.A. (hh:mm:ss.ss) (J2000)	Dec. (d:mm:ss.s) (J2000)	Error (arcsec)	Significance (σ) Total/Soft/Hard	Normalized counts (cnts/100ks) Total/Soft/Hard	Hardness (H-S)/(H+S)	Flux (ergs s^{-1} cm^{-2}) 0.5-2keV/2-10keV	NIR conterpart ID[b]	seperation (arcsec)	J^c (mag)	H^c (mag)	$K_S{}^c$ (mag)
148	2	18:43:42.37	−3 55 07.4	0.15	6.0/5.9/0.0	12.1/11.6/0.6	-0.91 ±0.15	3.4E-16/1.4E-16	S12222	0.24	17.84	16.60	16.11
149	1/2	18:43:42.57	−3 59 41.1	0.26	6.0/5.8/0.0	18.0/11.8/6.2	-0.32 ±0.17	4.0E-16/1.6E-15	S12331	0.70	15.46	14.64	14.45
150	2	18:43:42.73	−3 54 24.7	0.16	9.3/8.7/0.0	22.5/18.3/4.0	-0.64 ±0.17	5.1E-16/2.1E-15	S12469	0.21	17.76	15.88	15.61
151	2	18:43:43.26	−3 51 56.9	0.22	12.6/0.0/13.3	47.9/5.1/41.7	0.78 ±0.10	2.6E-17/1.9E-14	No	···	···	···	···
152	1	18:43:43.42	−4 04 51.1	0.27	3.7/4.1/0.0	9.9/9.9/0.0	-1.00 ±0.23	3.6E-16/1.5E-16	No	···	···	···	···
153	2	18:43:43.80	−3 47 33.2	0.48	6.7/7.1/0.0	44.6/36.6/6.9	-0.68 ±0.12	1.0E-15/4.2E-15	OoF	···	···	···	···
154	1	18:43:45.01	−4 03 34.5	0.26	4.8/4.6/0.0	11.9/10.6/1.4	-0.77 ±0.25	4.8E-16/2.0E-15	S14192	0.65	···	15.87	···
155	1	18:43:45.04	−4 05 01.6	0.16	17.2/17.6/2.7	52.9/44.8/8.1	-0.69 ±0.11	1.1E-15/4.5E-15	S14243/J18434503-0405015	0.17	···	13.54	13.[illegible]
156	2	18:43:45.35	−3 53 16.7	0.25	4.6/3.8/0.0	17.0/11.2/5.8	-0.32 ±0.24	3.9E-16/1.6E-15	S14512/J18434537-0353163	0.60	14.67	14.02	13.[illegible]
157	1	18:43:45.87	−4 07 39.6	0.32	4.5/5.1/0.0	14.1/13.4/0.7	-0.90 ±0.16	2.2E-16/8.7E-17	S14852/J18434586-0407387	0.83	15.33	14.44	···
158	2	18:43:46.06	−3 53 51.8	0.17	5.7/6.6/0.0	16.0/15.7/0.4	-0.95±0.12	4.5E-16/1.8E-16	S15011/J18434607-0353521	0.12	15.75	14.74	14.41
159	1	18:43:46.08	−4 03 24.6	0.21	4.0/4.6/0.0	8.6/8.6/0.0	-1.00 ±0.26	2.2E-16/9.0E-17	S15029/J18434610-0403248	0.38	14.51	13.91	13.63
160	1	18:43:46.08	−4 05 48.7	0.23	5.8/6.2/0.0	15.5/15.2/0.3	-0.96 ±0.14	4.7E-16/1.9E-16	S15003/J18434605-0405488	0.49	14.07	13.30	13.04
161	2	18:43:46.43	−3 54 11.6	0.23	5.1/6.2/0.0	13.3/13.4/0.0	-1.00 ±0.15	4.9E-16/2.0E-16	S15282/J18434644-0354117	0.33	14.21	13.53	13.36
162	1	18:43:46.62	−4 04 30.1	0.11	22.9/0.0/25.3	67.8/1.4/66.4	0.96 ±0.05	3.8E-17/2.8E-14	No	···	···	···	···
163	2	18:43:46.66	−3 46 23.8	0.78	3.8/5.6/0.0	24.8/24.7/0.0	-1.00 ±0.09	8.8E-16/3.6E-16	OoF	···	···	···	···
164	2	18:43:46.72	−3 54 43.5	0.21	4.5/3.7/0.0	10.1/7.6/2.5	-0.51 ±0.29	2.0E-16/8.1E-16	S15492/J18434671-0354434	0.06	15.42	14.14	13.38
165[T]	1	18:43:46.79	−4 07 06.3	0.29	7.9/6.9/0.0	21.8/16.7/5.1	-0.53±0.20	4.6E-16/1.9E-15	No	···	···	···	···
166[T]	1	18:43:46.81	−4 01 25.7	0.18	12.2/12.8/0.0	37.0/33.5/3.5	-0.81±0.12	6.5E-16/2.7E-16	S15573/J18434683-0401264	0.83	12.20	11.32	11.05
167	1	18:43:46.96	−4 10 32.7	0.31	9.3/8.8/3.0	37.6/30.3/7.3	-0.61 ±0.15	8.9E-16/3.7E-15	S15657/J18434694-0410326	0.36	14.90	13.81	13.41
168	1	18:43:47.10	−4 08 40.6	0.37	5.8/4.2/0.0	17.8/10.7/7.0	-0.21 ±0.26	1.9E-16/7.7E-16	No	···	···	···	···
169	2	18:43:47.11	−3 53 18.3	0.18	10.3/9.8/0.0	28.3/22.4/5.9	-0.58 ±0.15	7.0E-16/2.9E-15	S15778/J18434709-0353182	0.11	15.65	14.60	14.23
170	1	18:43:47.37	−4 08 30.4	0.17	23.7/27.2/0.0	89.8/89.7/0.2	-0.99 ±0.03	2.3E-15/9.5E-16	S15972/J18434736-0408301	0.32	···	12.36	12.23
171[T]	1	18:43:47.55	−4 04 06.1	0.19	5.2/3.8/1.5	13.8/8.5/5.2	-0.24 ±0.29	2.9E-16/1.2E-15	No	···	···	···	···
172	1/2	18:43:47.63	−3 56 10.3	0.18	13.5/14.4/0.0	46.1/33.7/12.3	-0.44 ±0.12	9.6E-16/3.9E-15	S16177/J18434762-0356105	0.20	15.70	14.84	14.66
173	1/2	18:43:47.79	−3 59 19.0	0.29	6.1/0.0/6.5	18.3/1.3/16.4	0.85 ±0.12	1.1E-17/8.2E-15	No	···	···	···	···
174	2	18:43:48.04	−3 53 57.5	0.26	6.0/0.0/6.8	22.3/2.7/19.3	0.76 ±0.15	1.3E-17/9.3E-15	No	···	···	···	···
175	1	18:43:48.08	−4 03 03.4	0.28	4.4/0.0/4.2	10.9/1.6/9.2	0.71 ±0.27	5.5E-18/4.0E-15	No	···	···	···	···
176	1	18:43:48.67	−4 01 36.1	0.10	37.6/40.3/4.7	134.8/122.4/12.4	-0.82 ±0.05	1.7E-15/6.8E-16	S16952/J18434867-0401362	0.13	14.42	13.61	13.37
177[T]	1	18:43:48.72	−4 01 17.6	0.32	4.5/3.1/0.0	16.8/10.2/6.5	-0.22 ±0.26	1.2E-16/5.0E-16	No	···	···	···	···
178	1/2	18:43:49.03	−3 59 57.1	0.24	7.4/7.1/4.7	30.6/17.9/12.6	-0.35 ±0.12	4.4E-16/1.8E-15	S17276	0.92	16.55	14.65	13.68
179	1	18:43:49.11	−4 02 56.4	0.18	4.3/4.2/0.0	10.4/8.5/1.8	-0.66 ±0.27	3.5E-16/1.4E-15	S17301	0.22	16.95	15.48	14.93
180	1	18:43:49.21	−4 00 54.1	0.30	5.4/2.5/3.8	14.2/4.4/9.8	0.39 ±0.27	5.0E-17/1.5E-15	No	···	···	···	···
181[T]	2	18:43:49.22	−3 52 38.3	0.22	15.2/14.2/3.7	61.8/46.1/15.8	-0.49 ±0.11	1.2E-15/4.9E-15	S17370	0.46	16.88	16.10	15.67
182	1	18:43:49.39	−4 04 13.7	0.18	8.5/4.2/5.1	21.1/9.5/11.7	0.11 ±0.24	1.7E-16/5.1E-15	No	···	···	···	···
183	1	18:43:50.42	−4 02 29.5	0.17	4.0/4.3/0.0	9.7/9.7/0.0	-1.00 ±0.22	2.5E-16/1.0E-16	S18344/J18435042-0402294	0.11	13.87	13.21	12.95
184	1	18:43:50.51	−4 02 07.2	0.17	4.7/4.1/0.0	11.5/9.8/1.9	-0.68 ±0.24	3.1E-16/1.3E-15	S18402	0.19	16.71	15.36	14.93
185	1/2	18:43:50.67	−3 58 52.1	0.31	2.7/4.0/0.0	7.9/7.2/0.6	-0.84 ±0.24	2.6E-16/1.1E-16	S18522/J18435067-0358526	0.62	14.97	14.37	14.13
186	1/2	18:43:50.71	−3 57 38.8	0.33	7.0/0.0/7.3	33.9/6.9/27.0	0.65 ±0.10	1.9E-17/1.4E-14	No	···	···	···	···
187	2	18:43:51.09	−3 52 39.1	0.18	21.4/25.0/0.0	82.9/82.0/0.9	-0.98 ±0.02	2.4E-15/9.8E-16	S18799	0.29	···	10.90	···
188	1/2	18:43:51.81	−3 59 22.3	0.21	13.6/12.6/2.2	38.0/30.8/7.2	-0.62 ±0.10	9.2E-16/3.8E-15	S19355/J18435181-0359222	0.03	14.93	14.01	13.54
189	1	18:43:52.37	−4 07 29.9	0.20	7.4/6.8/0.0	19.0/16.3/2.7	-0.71 ±0.19	5.1E-16/2.1E-15	No	···	···	···	···
190	2	18:43:52.78	−3 53 59.3	0.35	5.8/4.0/0.0	23.0/18.4/4.6	-0.60 ±0.18	4.4E-16/1.8E-15	No	···	···	···	···
191	1/2	18:43:52.78	−4 00 50.1	0.24	7.9/8.6/0.0	24.4/20.1/4.8	-0.49 ±0.13	5.0E-16/2.0E-15	S20105	0.67	16.39	15.19	14.62
192	1	18:43:52.85	−4 04 11.4	0.21	4.4/2.4/0.0	10.1/8.4/1.7	-0.66 ±0.28	3.1E-16/1.3E-15	No	···	···	···	···
193	1/2	18:43:53.11	−3 57 59.8	0.30	5.5/7.2/0.0	25.0/19.1/6.0	-0.57 ±0.14	5.3E-16/2.2E-15	S20390/J18435312-0357594	0.48	13.47	12.93	12.71
194	2	18:43:53.58	−3 51 16.3	0.42	5.0/6.8/0.0	33.9/26.4/7.6	-0.55 ±0.16	8.9E-16/3.7E-15	No	···	···	···	···
195	1/2	18:43:54.18	−3 58 44.0	0.43	0.0/4.9/0.0	14.4/10.2/4.2	-0.59 ±0.18	2.8E-16/1.2E-15	S21144	0.37	16.28	15.41	15.09
196	1/2	18:43:54.56	−3 58 06.3	0.34	6.2/6.2/0.0	39.7/28.0/11.7	-0.41 ±0.11	6.4E-16/2.7E-15	No	···	···	···	···

Table 1—Continued

ID[a]	AO	R.A. (hh:mm:ss.ss) (J2000)	Dec. (d:mm:ss.s) (J2000)	Error (arcsec)	Significance (σ) Total/Soft/Hard	Normalized counts (cnts/100ks) Total/Soft/Hard	Hardness (H-S)/(H+S)	Flux (ergs s^{-1} cm^{-2}) 0.5-2keV/2-10keV	NIR conterpart ID[b]	NIR conterpart seperation (arcsec)	J^c (mag)	H^c (mag)	K_s^c (mag)
197	1/2	18:43:54.61	−3 56 41.5	0.27	14.0/9.9/5.7	80.5/37.6/42.3	0.07 ±0.08	5.2E-16/1.6E-14	No	···	···	···	···
198	2	18:43:54.65	−3 53 36.5	0.43	5.3/5.6/0.0	20.9/18.5/2.4	-0.77 ±0.16	6.0E-16/2.5E-15	S21470/J18435466-0353364	0.34	15.67	14.70	14.23
199	1	18:43:54.83	−4 07 42.0	0.14	22.0/24.4/0.0	77.8/73.4/4.5	-0.88 ±0.06	1.9E-15/7.6E-16	S21566	0.42	14.31	13.57	13.32
200	1/2	18:43:55.10	−3 58 29.6	0.11	90.8/23.3/91.4	577.7/73.8/501.4	0.74 ±0.02	2.3E-16/1.7E-13	No	···	···	···	···
201	1	18:43:55.15	−4 04 20.1	0.15	7.2/7.6/0.0	15.1/15.1/0.0	-1.00 ±0.15	5.0E-16/2.0E-16	S21808	0.36	13.04	13.42	12.04
202	2	18:43:55.42	−3 52 52.9	0.21	21.7/18.8/11.8	98.7/55.3/42.4	-0.13 ±0.10	8.0E-16/2.4E-14	No	···	···	···	···
203	2	18:43:55.69	−3 57 04.3	0.49	4.3/0.0/5.0	25.6/2.5/22.9	0.80 ±0.14	1.2E-17/8.7E-15	S22226	0.39	18.57	17.23	···
204	2	18:43:55.70	−3 52 50.2	0.30	10.1/0.0/8.0	45.6/18.2/26.4	0.18 ±0.15	3.7E-16/1.1E-14	S22272	0.93	17.37	16.05	15.34
205	1	18:43:55.78	−4 08 25.8	0.29	5.2/6.7/0.0	18.9/16.8/2.0	-0.78 ±0.16	4.0E-16/1.6E-15	No	···	···	···	···
206	2	18:43:55.90	−3 55 03.9	0.40	4.4/3.4/0.0	39.2/28.8/10.4	-0.47 ±0.15	5.8E-16/2.4E-15	No	···	···	···	···
207	1	18:43:56.59	−4 06 08.0	0.13	7.2/0.0/6.3	11.6/0.9/10.7	0.85 ±0.18	7.5E-18/5.4E-15	No	···	···	···	···
208[E]	2	18:43:56.68	−3 54 47.8	0.25	16.8/17.4/3.1	238.3/197.9/40.6	-0.66 ±0.05	2.7E-15/1.1E-14	No	···	···	···	···
209	1/2	18:43:56.90	−3 57 33.5	0.37	5.6/7.4/0.0	18.2/18.2/0.0	-1.00 ±0.10	5.5E-16/2.2E-16	No	···	···	···	···
210[E]	2	18:43:56.90	−3 54 37.0	0.30	8.4/0.0/0.0	125.1/86.8/38.4	-0.39 ±0.09	1.6E-15/6.5E-15	No	···	···	···	···
211	1	18:43:57.35	−4 01 23.3	0.21	5.5/2.4/2.8	14.3/4.9/9.2	0.30 ±0.28	1.2E-16/3.5E-15	No	···	···	···	···
212	2	18:43:57.68	−3 51 57.1	0.53	5.3/4.1/0.0	29.9/17.1/12.9	-0.14 ±0.19	2.0E-16/6.0E-15	S23609	0.90	16.90	15.44	14.77
213[E]	2	18:43:57.87	−3 54 45.9	0.31	6.4/0.0/4.2	188.3/126.2/61.1	-0.35 ±0.07	1.8E-15/7.4E-15	No	···	···	···	···
214	1	18:43:57.87	−4 07 37.7	0.10	23.3/24.6/0.0	60.5/58.9/1.6	-0.95 ±0.05	2.7E-15/1.1E-15	S23783/J18435787-0407379	0.37	12.82	12.12	11.95
215	1/2	18:43:57.91	−3 59 19.8	0.34	7.4/3.0/4.9	12.4/6.3/6.2	0.00 ±0.23	1.2E-16/3.7E-15	No	···	···	···	···
216[E]	2	18:43:57.92	−3 54 37.5	0.34	8.5/5.4/0.0	123.9/93.1/30.7	-0.50 ±0.08	1.4E-15/5.9E-15	No	···	···	···	···
217	1	18:43:58.30	−4 03 21.2	0.16	4.5/3.9/0.0	10.3/8.4/1.8	-0.65 ±0.26	2.6E-16/1.1E-15	S24066	0.35	16.81	15.44	14.80
218	1/2	18:43:58.53	−3 56 21.6	0.31	9.4/2.1/9.0	36.8/8.6/28.3	0.53 ±0.12	2.4E-16/7.3E-15	No	···	···	···	···
219	2	18:43:59.02	−3 51 15.7	0.55	6.7/7.2/1.7	26.5/26.2/0.2	-0.98 ±0.08	1.0E-15/4.1E-16	No	···	···	···	···
220	2	18:43:59.28	−3 50 26.2	0.81	4.4/5.1/0.0	36.2/30.7/6.7	-0.64 ±0.13	8.7E-16/3.6E-15	OoF	···	···	···	···
221	2	18:43:59.67	−3 55 18.3	0.41	10.0/10.5/0.0	59.6/55.4/4.3	-0.86 ±0.08	1.7E-15/6.8E-16	S25062/J18435965-0355183	0.21	9.30[b]	8.93[b]	8.76[b]
222	1	18:43:59.92	−4 07 21.5	0.23	5.2/2.4/0.0	11.9/8.2/3.6	-0.39 ±0.30	2.4E-16/1.0E-15	No	···	···	···	···
223	1	18:44:00.31	−4 05 59.2	0.13	8.4/7.6/0.0	19.8/17.1/2.7	-0.73 ±0.17	5.0E-16/2.0E-15	S25554/J18440036-0405594	0.81	13.59	12.37	11.91
224[T]	1	18:44:01.13	−3 57 40.7	0.55	5.8/5.4/0.0	24.1/21.3/2.9	-0.76 ±0.16	2.7E-16/1.1E-15	S26066	0.61	16.59	15.38	14.74
225	1	18:44:01.93	−4 05 11.7	0.19	4.4/3.4/0.0	10.1/7.2/2.7	-0.46 ±0.31	2.1E-16/8.5E-16	No	···	···	···	···
226	1	18:44:02.16	−4 05 23.7	0.11	20.8/22.4/0.0	56.2/56.3/0.4	-0.99 ±0.04	1.7E-15/6.8E-16	S26833/J18440213-0405243	0.93	14.18	13.41	13.15
227	1	18:44:02.44	−4 12 44.8	0.89	4.7/0.0/4.8	19.1/0.0/19.3	1.00 ±0.13	5.6E-18/4.0E-15	OoF	···	···	···	···
228	2	18:44:02.45	−3 51 51.7	0.68	4.0/3.5/0.0	26.7/16.8/10.0	-0.25 ±0.20	4.5E-16/1.8E-15	No	···	···	···	···
229	1	18:44:02.54	−4 09 22.3	0.19	18.5/2.0/19.3	77.2/10.8/65.0	0.72 ±0.09	4.0E-17/2.9E-14	S27070/J18440256-0409228	0.38	···	13.67	12.26
230	1/2	18:44:03.27	−3 58 19.0	0.27	21.0/23.4/0.0	66.3/66.0/0.2	-0.99 ±0.03	1.9E-15/7.8E-16	S27370/J18440331-0358188	0.63	13.15	12.48	12.23
231	1	18:44:03.47	−4 10 41.8	0.50	5.8/2.4/3.2	25.5/17.6/7.8	-0.39 ±0.20	2.8E-16/1.2E-15	No	···	···	···	···
232	1	18:44:03.84	−4 11 23.6	0.70	4.2/0.0/4.4	23.2/7.6/15.5	0.34 ±0.22	1.8E-16/5.4E-15	OoF	···	···	···	···
233[T]	1	18:44:03.95	−4 02 57.6	0.10	31.2/11.8/24.4	90.3/29.3/57.5	0.32±0.11	6.3E-16/1.9E-14	S27641/J18440392-0402577	0.43	···	14.22	13.40
234	2	18:44:03.97	−3 54 06.6	0.73	5.8/6.1/4.7	44.2/24.3/19.9	-0.10 ±0.16	2.8E-16/8.3E-15	OoF	···	···	···	···
235[T]	1	18:44:05.05	−4 04 36.9	0.10	25.2/13.1/15.0	64.9/31.0/32.7	0.03 ±0.13	6.7E-16/2.0E-14	S28081	0.80	17.40	15.35	···
236	1	18:44:05.41	−4 08 32.4	0.14	24.5/25.4/0.0	89.4/84.5/5.0	-0.89 ±0.05	2.3E-15/9.3E-16	S28203/J18440540-0408325	0.17	14.98	14.31	14.07
237	1	18:44:05.56	−4 05 39.1	0.19	6.4/4.8/0.0	15.1/10.4/4.6	-0.39 ±0.26	3.8E-16/1.6E-15	S28248	0.52	16.59	15.28	14.87
238	1	18:44:05.91	−4 06 12.2	0.10	21.0/18.8/3.9	51.6/42.5/9.0	-0.65 ±0.11	1.1E-15/4.6E-15	S28382/J18440589-0406124	0.53	14.27	13.36	13.10
239	1	18:44:06.10	−4 08 43.5	0.22	5.7/6.3/0.0	19.7/18.4/1.3	-0.87 ±0.15	5.2E-16/2.1E-16	No	···	···	···	···
240	1	18:44:06.35	−4 07 04.0	0.20	5.6/0.0/5.6	13.6/0.8/12.5	0.88 ±0.16	8.4E-18/6.1E-15	No	···	···	···	···
241	1	18:44:07.60	−4 05 14.1	0.17	8.5/0.0/6.7	21.7/2.8/18.3	0.74 ±0.17	1.2E-17/8.4E-15	No	···	···	···	···
242	2	18:44:08.59	−3 53 55.8	0.68	6.2/0.0/6.8	53.2/4.5/49.7	0.84 ±0.09	3.0E-17/2.2E-14	OoF	···	···	···	···
243	1	18:44:09.49	−4 07 31.6	0.17	12.8/0.0/11.8	41.0/2.0/37.0	0.90 ±0.08	2.4E-17/1.8E-14	No	···	···	···	···
244	1	18:44:10.98	−4 05 16.8	0.14	12.6/4.3/9.3	30.8/10.5/20.1	0.31 ±0.19	2.4E-16/7.1E-15	S30315/J18441095-0405170	0.51	15.60	13.55	12.71
245	1	18:44:11.89	−4 05 12.6	0.18	14.1/0.9/13.1	40.3/7.9/31.9	0.60 ±0.14	2.3E-17/1.7E-14	No	···	···	···	···

Table 1—Continued

ID[a]	AO	R.A. (hh:mm:ss.ss) (J2000)	Dec. (d:mm:ss.s) (J2000)	Error (arcsec)	Significance (σ) Total/Soft/Hard	Normalized counts (cnts/100ks) Total/Soft/Hard	Hardness (H-S)/(H+S)	Flux (ergs s^{-1} cm^{-2}) 0.5-2keV/2-10keV	NIR conterpart ID[b]	NIR conterpart seperation (arcsec)	J^c (mag)	H^c (mag)	$K_S{}^c$ (mag)
246	1	18:44:11.90	−4 06 30.7	0.23	7.3/4.7/2.3	20.3/14.7/5.6	-0.45 ±0.22	5.9E-16/2.4E-15	S30539/J18441188-0406311	0.55	···	15.35	13.97
247	1	18:44:12.17	−4 08 08.2	0.32	2.3/0.0/4.1	13.0/2.5/10.2	0.61 ±0.27	8.7E-18/6.3E-15	No	···	···	···	···
248	1	18:44:13.16	−4 06 20.2	0.25	5.4/0.0/4.1	15.2/0.3/13.5	0.95 ±0.16	9.1E-18/6.6E-15	No	···	···	···	···
249^T	1	18:44:13.72	−4 02 32.8	0.29	4.0/2.6/0.0	11.5/8.2/3.3	-0.42 ±0.32	2.8E-16/1.1E-15	No	···	···	···	···
250	1	18:44:13.77	−4 12 17.4	0.53	12.9/0.0/14.9	106.2/9.5/97.9	0.82 ±0.06	6.3E-17/4.6E-14	OoF	···	···	···	···
251	1	18:44:14.75	−4 11 34.7	0.44	11.0/11.0/2.0	64.3/50.6/13.7	-0.57 ±0.12	1.4E-15/5.9E-15	OoF	···	···	···	···
252	1	18:44:15.62	−4 03 56.9	0.31	6.5/2.8/4.0	22.0/9.4/12.4	0.14 ±0.24	1.6E-16/4.9E-15	S31107/J18441558-0403569	0.55	16.96	14.59	13.60
253	1	18:44:15.73	−4 08 58.0	0.49	4.6/0.0/4.2	18.3/5.8/12.4	0.36 ±0.25	1.7E-16/5.1E-15	No	···	···	···	···
254	1	18:44:16.25	−4 12 57.0	0.82	5.7/0.0/3.5	40.4/7.7/33.4	0.62 ±0.14	2.4E-17/1.7E-14	OoF	···	···	···	···
255	1	18:44:18.54	−4 06 02.5	0.29	8.3/6.2/3.9	37.1/27.2/9.8	-0.47 ±0.16	8.8E-16/3.6E-15	S31539/J18441855-0406027	0.35	13.54	12.59	12.[illegible]
256	1	18:44:21.13	−3 57 06.3	0.33	26.1/25.6/10.6	312.3/244.1/66.3	-0.57 ±0.05	5.4E-15/2.2E-14	OoF	···	···	···	···
257	1	18:44:21.60	−4 04 53.2	0.40	5.5/3.7/3.3	29.1/14.0/15.0	0.03 ±0.21	3.3E-16/1.0E-14	S31826	0.25	···	15.35	14.57
258	1	18:44:21.77	−4 12 30.1	0.48	14.5/12.7/6.7	179.3/124.8/55.4	-0.39 ±0.08	3.1E-15/1.3E-14	OoF	···	···	···	···
259	1	18:44:22.57	−3 59 39.8	0.57	6.1/7.2/0.0	55.6/39.1/16.5	-0.40 ±0.14	9.8E-16/4.0E-15	OoF	···	···	···	···
260^T	1	18:44:22.61	−4 03 51.0	0.35	11.8/12.4/0.0	65.3/57.5/7.7	-0.76±0.09	1.5E-15/6.2E-15	S31912/J18442259-0403518	0.85	14.80	13.52	13.57
261	1	18:44:22.63	−4 00 40.0	0.50	6.7/0.0/8.2	42.8/0.0/42.9	1.00 ±0.06	2.7E-17/1.9E-14	OoF	···	···	···	···
262	1	18:44:22.67	−4 00 17.4	0.50	6.7/6.5/0.0	43.3/33.5/9.8	-0.55 ±0.15	7.0E-16/2.9E-15	J18442265-0400176	0.30	14.36	13.39	12.52
263	1	18:44:23.45	−4 03 08.5	0.50	5.1/0.0/3.3	23.8/3.7/20.0	0.69 ±0.18	1.1E-17/8.2E-15	No	···	···	···	···
264	1	18:44:24.09	−3 59 11.9	0.57	11.6/11.7/3.6	95.2/75.6/19.8	-0.59 ±0.09	1.8E-15/7.5E-15	J18442406-0359111	0.86	13.59	12.69	12.[illegible]
265	1	18:44:24.24	−4 01 35.1	0.52	5.4/5.2/0.0	28.3/24.0/4.2	-0.70 ±0.16	7.7E-16/3.2E-15	J18442423-0401343	0.72	16.00	14.70	13.[illegible]
266	1	18:44:26.23	−3 57 48.8	0.54	11.8/13.9/0.0	118.7/118.4/0.0	-1.00 ±0.02	2.7E-15/1.1E-15	OoF	···	···	···	···
267	1	18:44:26.45	−4 06 35.5	0.47	5.7/4.7/0.0	28.3/20.8/7.6	-0.47 ±0.19	5.1E-16/2.1E-15	No	···	···	···	···
268	1	18:44:26.66	−4 04 50.1	0.53	4.1/3.5/0.0	15.0/13.1/2.1	-0.73 ±0.21	3.0E-16/1.2E-15	S32241	0.80	15.61	14.58	14.12
269	1	18:44:26.71	−4 03 27.3	0.46	9.8/10.5/0.0	61.5/53.8/7.6	-0.75 ±0.10	1.2E-15/4.8E-15	No	···	···	···	···
270	1	18:44:27.75	−4 07 49.3	0.55	4.3/4.0/0.0	30.1/24.8/5.2	-0.65 ±0.16	8.2E-16/3.4E-15	OoF	···	···	···	···
271	1	18:44:28.51	−4 08 15.3	0.63	6.2/3.8/4.1	36.3/14.3/22.2	0.22 ±0.18	2.9E-16/8.8E-15	OoF	···	···	···	···
272	1	18:44:28.87	−4 01 03.9	0.48	14.3/12.1/8.3	142.0/85.8/57.2	-0.20 ±0.09	8.2E-16/2.5E-14	J18442884-0401033	0.60	13.29	11.83	11.[illegible]
273	1	18:44:30.35	−4 10 44.5	0.50	16.6/7.9/15.6	164.6/33.8/134.5	0.60 ±0.07	9.4E-17/6.8E-14	J18443035-0410445	0.12	17.37	15.68	13.90
274	1	18:44:32.73	−4 07 04.4	0.58	9.2/9.8/0.0	55.9/55.7/0.0	-1.00 ±0.05	1.9E-15/7.6E-16	OoF	···	···	···	···

[a]Sources with T in the ID column show significant time variations, and those with E are extended.

[b]SOFI ID in Table 1 (starts with S) and/or 2MASS ID (starts with J) of the NIR source within $1''$ from the Chandra position. "No" means that the source is in the SOFI field of view, but there are no SOFI counterparts. "OoF" means that the source is out of the SOFI field, and no 2MASS counterparts.

[c]2MASS magnitudes are taken for stars brighter than 10 mag, since SOFI starts to saturate for $<$ 10 mag (see Fig. 5).

Table 2. SOFI NIR source catalog.

ID	R.A. (J2000)	Decl. (J2000)	J (mag)	H (mag)	K_S (mag)	2MASS ID	Chandra ID
1	18:43:08.380	−03:54:34.12	-999	17.64	15.58	...	...
2	18:43:08.382	−03:52:29.29	16.69	15.33	15.09	...	...
3	18:43:08.382	−03:53:46.51	17.37	16.56	16.40	...	...
...							
8	18:43:08.451	−03:54:07.29	-999	16.04	14.56	18430845−0354075	...
...							
687	18:43:15.299	−03:54:19.16	10.45	10.15	10.03	18431530−0354190	24
...							
1018	18:43:17.438	−03:57:32.71	16.54	15.25	15.13	...	30
...							
32397	18:44:28.474	−04:06:50.97	15.72	13.80	12.64	...	...
32398	18:44:28.477	−04:04:33.27	-999	-999	15.18	...	...

Note. — We have detected 32,398 sources from our SOFI fields (Fig. 3). For each source, the position, J, H and K_S magnitudes, and the 2MASS and/or *Chandra* counterparts are given. When not detected, −999 is put for the magnitude. The *Chandra* source identification number is defined in Table 1. The complete version of this table is in the electronic edition of the Journal. The printed edition contains only a sample.

Table 3. Summary of the point source characteristics.

hardness ratio	soft ≤ -0.60	Medium -0.59 to 0.1	Hard ≥ 0.11	Total
All	137	68	69	274
Extended[a]	1	3	0	4
Point Source	136	65	69	270
Time variation[b]	4	10	3	17
	(3 %)	(15 %)	(4 %)	(6 %)
2MASS counterpart[b]	62	17	8	87
	(45 %)	(26 %)	(12 %)	(32 %)
Covered by SOFI[b]	106	47	49	202
	(78 %)	(72 %)	(71 %)	(75 %)
SOFI counterpart[c]	88	25	11	124
	(83 %)	(53 %)	(22 %)	(61 %)
NIR counterpart[d]	98	30	14	142
	(72 %)	(46 %)	(20 %)	(53 %)

[a]Sources associated with the thermal blob-like feature CXOU J184357-035441 (Ueno et al. 2003).

[b]The percentage gives the fraction among all the point sources, excluding the extended sources. Note that the 2MASS covers the entire *Chandra* field, but SOFI does not.

[c]The percentage gives the fraction among the point sources covered by SOFI.

[d]Presence of either 2MASS or SOFI counterparts. The percentage gives the fraction among all the point sources.

Table 4. Spectral fitting results of the average spectra with absorbed power-law model

hardness ratio	Soft ≤ -0.60	Medium -0.59 to 0.1	Hard ≥ 0.11
Sources with NIR counterparts			
N_H (10^{22} cm^{-2})	0.50 ± 0.05	0.9 ± 0.1	3.5 ± 0.4
photon-index	$2.8 \pm^{0.2}_{0.1}$	2.0 ± 0.2	0.90^{d}
N^{a}	1.5 ± 0.2	$1.6 \pm^{0.4}_{0.3}$	1.34 ± 0.11
reduced χ^2 (dof)	1.7 (181)	0.99 (137)	1.2 (62)
observed flux^{b} (0.5 – 10 keV)	2.1	4.7	17
intrinsic flux^{c} (0.5 – 10 keV)	4.8	7.8	23
Sources without NIR counterparts			
N_H (10^{22} cm^{-2})	0.50 ± 0.15	1.6 ± 0.5	5.0 ± 0.8
photon-index	2.8^{d}	2.0^{d}	$0.9 \pm^{0.1}_{0.3}$
N^{a}	0.85 ± 0.2	2.9 ± 0.3	$1.8 \pm^{0.9}_{0.7}$
reduced χ^2 (dof)	1.7 (29)	1.1 (45)	1.27 (170)
observed flux^{b} (0.5 – 10 keV)	1.2	7.1	23
intrinsic flux^{c} (0.5 – 10 keV)	2.7	13	33

[a]Power-law normalization in 10^{-6} photons s^{-1} keV^{-1} cm^{-2} at 1 keV.

[b]Average source flux in units of 10^{-15} ergs s^{-1} cm^{-2}.

[c]Intrinsic source flux in units of 10^{-15} ergs s^{-1} cm^{-2} when hydrogen column density is set to null.

[d]Fixed to the best-fit value obtained for the other group in the same spectral hardness with/without NIR counterpart.

Note. — Errors correspond to 90 % confidence.

Table 5. Spectral fitting results of the average spectra with physical models

	With NIR counterparts	Without NIR counterparts
Soft spectra (two MEKAL model)		
Overall normalization[a]	1.0	0.52
N_H (10^{22} cm^{-2})	1.19 ± 0.15	
kT (keV; soft)	0.25 ± 0.02	
N^{b}(soft)	56	
kT (keV; hard)	2.2 ± 0.5	
N^{b}(hard)	2.8	
reduced χ^2 (dof)	1.35 (179)	1.85 (30)
Medium spectra (two MEKAL model)		
N_H (10^{22} cm^{-2})	1.4 ± 0.3	···
kT (keV; soft)	0.23 ± 0.10	···
N^{b}(soft)	68	···
kT (keV; hard)	3.0 ± 0.4	···
N^{b}(hard)	5.5	···
reduced χ^2 (dof)	1.21 (89)	···
Hard spectra (power-law with iron line and edge)		
N_H (10^{22} cm^{-2})	4.5 ± 0.3	4.8 ± 0.6
photon-index	1.47 ± 0.03	0.77 ± 0.20
N^{c}	3.26	1.57
E_{line} (keV)	6.67 ± 0.08	6.71 ± 0.08
Line intrinsic width (keV)	< 0.05	0.18 ± 0.11
Line equivalent width (eV)	540 ± 200	340 ± 270
E_{edge} (keV)	···	7.11 (frozen)
Edge depth	···	1.2 ± 0.5
reduced χ^2 (dof)	1.06 (59)	1.28 (67)

[a]The same two temperature MEKAL model parameters are used for the soft spectra with or without the NIR counterparts with the exception of the overall normalization. Hydrogen density of the plasma is fixed to $n_H = 1$ cm^{-3}. Parameter errors are for the spectrum with NIR counterparts.

[b]MEKAL model normalization, $10^{-20}/4\pi d^2 \int n_e n_H dV$, where d is distance (cm), n_e and n_H are electron and hydrogen densities (in cm^{-3}), respectively.

[c]Power-law normalization in 10^{-6} photons s^{-1} keV^{-1} cm^{-2} at 1 keV.

Note. — Errors correspond to 90 % confidence. The spectral model for the medium sources without NIR counterpart is given in Table 4.

Table 6. Iron line parameters of the Galactic diffuse emission

	Energy (keV)	Line flux (photons s^{-1} cm^{-2} str^{-1})	Equivalent width (eV)	Identification
Single line model[a]				
	$6.52\pm^{0.08}_{0.14}$	0.55 ± 0.39	170 ± 120	NEI plasma?
Three line model[b]				
	6.40 (fixed)	$0.6\pm^{0.3}_{0.6}$	$100\pm^{50}_{100}$	Fluorescence from low-ionized iron
	6.67 (fixed)	$0.4\pm^{0.8}_{0.3}$	$180\pm^{360}_{140}$	He-like iron
	6.97 (fixed)	$0.5\pm^{0.8}_{0.5}$	$160\pm^{260}_{160}$	H-like iron

[a]Reduced χ^2 = 0.83 with dof=4.

[b]Reduced χ^2 = 1.19 with dof=3.

Note. — Errors correspond to 90 % confidence. Intrinsic line width is fixed to zero, assuming that the lines are narrower than the instrumental width ($\sim$ 100 eV).

Table 7. Low energy line parameters of the Galactic diffuse emission

Energy (keV)	Line flux (photons/s/cm^2/str)	Equivalent width (eV)	Identification
$1.021\pm^{0.009}_{0.002}$	$0.60\pm^{0.14}_{0.11}$	$64\pm^{15}_{12}$	Ne X,Lyα (1.02 keV)
$1.13\pm^{0.07}_{0.03}$	$0.12\pm^{0.12}_{0.09}$	$13\pm^{13}_{10}$	Fe L?
$1.32\pm^{0.02}_{0.01}$	0.32 ± 0.08	36 ± 10	Mg XI, Kα (1.35 keV)
$1.46\pm^{0.04}_{0.03}$	$0.11\pm^{0.11}_{0.08}$	$12\pm^{12}_{9}$	Mg XII, Lyα (1.47 keV)
$1.74\pm^{0.06}_{0.04}$	< 0.32	< 25	Low ionized Si?
$1.849\pm^{0.003}_{0.017}$	$0.87\pm^{0.17}_{0.46}$	$110\pm^{20}_{10}$	Si XIII, Kα (1.86 keV)
2.00 (fixed)	$0.05\pm^{0.11}_{0.05}$	$6\pm^{13}_{6}$	Si XIV, Lyα (2.00 keV)
$2.188\pm^{0.012}_{0.034}$	0.48 ± 0.24	60 ± 30	Si XIII, Kβ (2.18 keV)
2.42 ± 0.02	0.71 ± 0.15	90 ± 20	S XV, Kα (2.45 keV)
$2.61\pm^{0.04}_{0.05}$	0.30 ± 0.14	40 ± 20	S XVI, Lyα (2.62 keV)
3.08 ± 0.03	0.34 ± 0.12	48 ± 17	Ar XVII, Kα (3.12 keV)

Note. — Reduced $\chi^2 = 1.03$ with dof = 27. Errors correspond to 90 % confidence. Intrinsic line width is fixed to zero, assuming it is narrower than the instrumental width (~ 100 eV).

Table 8. Two NEI model fitting of the Galactic diffuse emission

	Fixed abundance model	Free abundance model
Soft Component		
kT (keV)	0.86	0.59 ± 0.09
$\log n_e t$ (cm^{-3} s)	11.1	11.8 ± 0.5
Abundance (except Ne, Mg, Si)	0.11	0.044 ± 0.037
Ne abundance	0.11	0.30 ± 0.2
Mg abundance	0.11	0.14 ± 0.06
Si abundance	0.11	0.25 ± 0.05
N_H (10^{22} cm^{-2})	0.75	0.81 ± 0.12
Observed flux[a] (ergs cm^{-2} s^{-1} str^{-1})	3.1×10^{-8}	2.6×10^{-8}
Intrinsic flux[a] (ergs cm^{-2} s^{-1} str^{-1})	1.0×10^{-7}	1.1×10^{-7}
Hard Component		
kT (keV)	6.52	5.0 ± 0.8
$\log n_e t$ (cm^{-3} s)	10.18	10.6 ± 0.1
Abundance (except Fe)	0.23	0.17 ± 0.04
Fe abundance	0.23	0.9 ± 0.3
N_H (10^{22} cm^{-2})	4.00	3.9 ± 0.4
Observed flux[a] (ergs cm^{-2} s^{-1} str^{-1})	2.1×10^{-7}	2.1×10^{-7}
Intrinsic flux[a] (ergs cm^{-2} s^{-1} str^{-1})	8.1×10^{-7}	7.6×10^{-7}
reduced χ^2 (dof)	1.97 (68)	1.52 (64)

[a]In 0.7 – 10 keV.

Note. — Errors correspond to 90 % confidence.

Fifth part

WORKING AT ISDC

Chapter 10
MORE COLLABORATIONS

This part of the thesis is meant to give an overview of many different topics that have been treated during this PhD thesis, besides the main work presented in the previous parts.

These collaborations came as a natural consequence of the work done on the Observation Simulator as well as on the systematic study of the *INTEGRAL* data for the LMXRB monitoring. This work allowed me to acquire a good level of expertise in the peculiar analysis of the *INTEGRAL* data. This, added to the fact that working at ISDC means meeting many scientists from all over the world, gave rise to many new collaborations.

10.1 A walk through ISDC

The following publications are the result of my involvement in *INTEGRAL* data analysis and ISDC tasks. For each paper the abstract is reproduced.

Most of them are based on *INTEGRAL* Core prgramme data (2 to 5) and were developed in parallel to the LMXRB monitoring programme. They include the monitoring of the Black hole candidate 1E1740.7-2942, the study of IBIS performances on Core programme initial data, and the search for short transient and pulsation events. In paper number 1 we studied the properties of the sources no more in the Galactic plane but in the Large Magellanic Cloud using open time observations.

Finally, papers 6 to 9 are the result of my involvement in the ISDC scientist on duty team.

1. *INTEGRAL observations of the Large Magellanic Cloud region* (Mereghetti S., Götz D., **Paizis A.**, Pellizzoni A., et al., 2004, in: Proceedings of the "5th *INTEGRAL* Workshop - The *INTEGRAL* Universe", Munich, in press)
   Abstract
   We present the preliminary results of the *INTEGRAL* survey of the Large Magellanic Cloud. The observations have been carried out in January 2003 (about 10^6 s) and January 2004 (about 4×10^5 s). Here we concentrate on the bright sources LMC X-1, LMC X-2, LMC X-3 located in our satellite galaxy, and on the serendipitous detections of the Galactic Low Mass X-ray Binary EXO 0748-676 and of the Seyfert 2 galaxy IRAS 04575-7537.

2. *INTEGRAL Monitoring of the Black hole candidate 1E1740.7-2942*, (Del Santo M., Bazzano A., Smith D. M., L. Bassani, **et al.**, 2004, in: Proceedings of the "5th *INTEGRAL* Workshop - The *INTEGRAL* Universe", Munich, in press)
   Abstract
   The brightest persistent Galactic black hole candidate close to the Galactic Centre, 1E 1740.7-2942, has long been observed with *INTEGRAL*. In this paper, we report on the long-term

hard X-ray monitoring obtained during the first year of observations as part of the Galactic Centre Deep Exposure. We discuss the temporal and spectral behaviours in different energy bands up to 250 keV, as well as the hardness-flux correlations.

3. *IBIS performances during the Galactic Plane Scan. I. The Cygnus region* (Del Santo M., Rodriguez J., Ubertini P., Bazzano A., **et al.**, 2003, A&A 411, L369)
   Abstract
   The Plane of our Galaxy is regularly observed by the *INTEGRAL* satellite by means of scheduled scans. We present here results from the IBIS/ISGRI instrument using data from the first two Galactic Plane Scans performed at the end of the Performance Verification phase, while *INTEGRAL* was pointed towards the Cygnus region. Considering the predicted IBIS sensitivity, we expected three persistent sources to be detectable: Cyg X-1, Cyg X-3, Cyg X-2, in order of decreasing intensity in the hard-X energy range ($>$15 keV). In addition to these sources, our analysis revealed two more transient sources, confirming the unprecedented IBIS sensitivity. For each exposure ($\sim$2200 s) of the two scans, we report on detected source fluxes, variabilities and location accuracies.

4. *First results from the IBIS/ISGRI data obtained during the Galactic Plane Scan. II. The Vela region* (Rodriguez J., Del Santo M., Lebrun F., G. Belanger, **et al.**, 2003, A&A 411, L373)
   Abstract
   We report on *INTEGRAL*/IBIS observations of the Vela region during a Galactic Plane Scan (hereafter GPS) presenting the IBIS in-flight performances during these operations. Among all the known sources in the field of view we clearly detect 4U 0836-429, Vela X-1, Cen X-3, GX 301-2, 1E 1145.1-6141, and H0918-549 in the 20-40 keV energy range. Only Vela X-1 and GX 301-2 are detected in the 40-80 keV energy range, and no sources are visible above. We present the results of each individual observation ($\sim$2200 s exposure), as well as those from the mosaic of these scans.

5. *Systematic search for short transients and pulsation events from INTEGRAL survey data* (Ebisawa K., Kretschmar P., Mowlavi N., **Paizis A.**, et al., 2004, in: Proceedings of the "5th *INTEGRAL* Workshop - The *INTEGRAL* Universe", Munich, in press)
   Abstract
   The imaging instruments on board *INTEGRAL* have wide fields of view and high time resolution. Therefore, they are ideal instruments to search for pulsating sources and/or transient events. We are systematically searching for pulsations and transient events from known and serendipitous sources in the Galactic Plane Scan (GPS) and Galactic Center Deep Exposure (GCDE) core programme data. We analyze the standard pipe-line data using ISDC Off-line Science Analysis (OSA) system, so that our results are reproducible by general guest users. In this paper, we describe our system and report preliminary results for the first year of operation.

6. *Scientific Performance of the ISDC Quick Look Analysis*, (Shaw S., Mowlavi N., Ebisawa K., **Paizis A.**, et al., 2004, in: Proceedings of the "5th *INTEGRAL* Workshop - The *INTEGRAL* Universe", Munich, in press)
   Abstract
   The *INTEGRAL* Science Data Centre (ISDC) routinely monitors the Near Real Time data (NRT) from the *INTEGRAL* satellite. A first scientific analysis is made in order to check for the detection of new, transient or highly variable sources in the data. Of primary importance

for this work is the Interactive Quick Look Analysis (IQLA), which produces JEM-X and ISGRI images and monitors them for interesting astrophysical events.

7. *GRB021125: a long GRB localized by INTEGRAL* (Bazzano A. and **Paizis A.**, 2002, GRB Coordinates Network, 1706)

8. *GRB 021125: The first GRB imaged by INTEGRAL* (Malaguti G., Bazzano A., Beckmann V., Bird A. J., **et al.**, 2003, A&A 411, L307)
   Abstract
   In the late afternoon of November 25, 2002 a gamma-ray burst (GRB) was detected in the partially coded field of view (about 7.3 deg from the centre) of the imager IBIS on board the *INTEGRAL* satellite. The instruments on-board *INTEGRAL* allowed, for the first time, the observation of the prompt gamma-ray emission over a broad energy band from 15 to 500 keV. GRB021125 lasted $\sim$24 s with a mean flux of $\sim$5.0 photons/cm^2/s in the 20-500 keV energy band, and a fluence of 4.8×10^{-5} erg/cm^2 in the same energy band. Here we report the analysis of the data from the imager IBIS and the spectrometer SPI.

9. *Possible GRB 030320 localized by INTEGRAL* (Mereghetti S., Götz D., Borkowski J., **Paizis A.**, et al., 2003, GRB Coordinates Network, 1941)

These papers have different aims and have been important to be able to have a glance at other sources with different approaches to the *INTEGRAL* data.

Other collaborations moved along a parallel track with the LMXRB monitoring programme. These include the study of the accreting pulsars and the study of a specific HMXRB, Cyg X-3 described in the next two sections.

10.2 The *INTEGRAL* accreting pulsar monitoring programme

In parallel to the LMXRB monitoring programme discussed in Part III of this thesis, another similar programme has been developed on accreting X-ray pulsars. The aim of this programme is to monitor the spectral and temporal properties of about twenty-four accreting X-ray pulsars. The results of this survey will also be made publicly available with information concerning fluxes in different energy bands, pulse periods and profiles, if possible pulse period derivatives, and broad band spectra.

The first results of this monitoring programme can be seen in Sidoli L., Wilms J., **Paizis A.**, Larsson S., et al., 2004, Nuclear Physics B (Proc.Supll.) 132, 648, *Monitoring programme on Persistent Accreting Neutron Stars observed during the INTEGRAL Galactic Plane Survey*, such as the first images, lightcurves and pulse period estimates based on IBIS/ISGRI data.

In the case of the HMXRB pulsar SAX J2103.5+4545 evidence of a pulse period spin up has been found with respect to previous observations performed with *BeppoSAX* and *RXTE*. This paper is here reproduced (Sidoli L., Mereghetti S., Larsson S., M. Chernyakova,**et al.**, 2004, *First results on the HMXRB Pulsar SAXJ2103.5+4545 with INTEGRAL*, in: Proceedings of the "5th *INTEGRAL* Workshop - The *INTEGRAL* Universe", Munich, in press).

FIRST RESULTS ON THE HMXRB PULSAR SAX J2103.5+4545 WITH INTEGRAL

L.Sidoli[1], S.Mereghetti[1], S.Larsson[2], M.Chernyakova[3], I.Kreykenbohm[4], P.Kretschmar[5], A.Paizis[6], A.Santangelo[7], and C.Ferrigno[7]

[1]IASF Milano, Italy
[2]Stockholm Observatory, Sweden
[3]ISDC Versoix, Switzerland
[4]IAAT/ISDC Versoix, Switzerland
[5]MPE Garching/ISDC Versoix, Switzerland
[6]IASF Milano/ISDC Versoix, Switzerland
[7]IASF Palermo, Italy

ABSTRACT

We report on the preliminary timing and spectral analysis of the High Mass X-ray Binary Pulsar SAXJ2103.5+4545 as observed with INTEGRAL during the Galactic Plan Scan of the Core Program. The source shows a hard spectrum, being detected up to 100 keV. The timing analysis performed on IBIS/ISGRI data shows evidence for a spin-up with respect to previous observations, performed in 1997 with BeppoSAX.

Key words: X–rays; accreting pulsar; individual: SAX J2103.5+4545.

1. INTRODUCTION

SAX J2103.5+4545 is a transient HMXRB pulsar with a ∼358 s pulse period discovered with the WFC on-board BeppoSAX during an outburst in 1997 (Hulleman et al., 1998). Its orbital period of 12.68 days has been found with the RXTE during the 1999 outburst (Baykal et al., 2000). The likely optical counterpart, a Be star with a magnitude V=14.2, has been recently discovered (Reig & Mavromatakis, 2003; Reig et al. 2004).

During the outburst in 1999, Baykal et al. (2002) observed for the first time, with RXTE, the transition from the spin-up phase to the spin-down regime, while the X–ray flux was declining. Indeed, the source underwent a spin-up phase during the initial part of the outburst (during which the pulse period decreased by ∼0.9 s in 150 days), then the flux dropped (and the pulse frequency saturated), and, as the flux continued to decline, a weak spin-down phase started. Moreover, a correlation between spin-up rate and X–ray flux was observed (Baykal et al., 2002), suggestive of the formation of an accretion disk during the periastron passage.

A very preliminary spectral analysis of INTEGRAL public observations of the source region, performed in Dec.2002 during the performance verification phase, has been reported by Lutovinov et al. (2003).

Inam et al. (2004) observed a soft spectral component (blackbody with a temperature of 1.9 keV) and a transient 22.7 s QPO during a XMM-Newton observation performed in Jan, 2003.

SAX J2103.5+4545 has been observed several times during the Galactic Plane Scan (GPS) which INTEGRAL performs every 12 days as part of the Core Program. We report here the timing and spectral analysis of these observations.

An IBIS/ISGRI mosaic of the region of the sky containing SAX J2103.5+4545 is shown in Fig. 1. The source long-term lightcurve, as measured with RXTE All Sky Monitor (ASM) is shown in Fig. 2. The times of the two previous outbursts observed with BeppoSAX (in 1997) and RXTE (in 1999) are indicated, as well as the epoch of the INTEGRAL observations reported here.

2. TIMING RESULTS

We have analysed 20 GPS pointings (duration of about 2000 s each) covering the region of the sky containing the pulsar. This sky region is not covered during the Galactic Center Deep Exposure.

In Fig. 3 we show the IBIS/ISGRI lightcurve of SAX 2103.5+4545, where each point corresponds to the flux from a single pointing.

The data have been reduced using OSA3 release of the analysis software. For each pointing we extracted

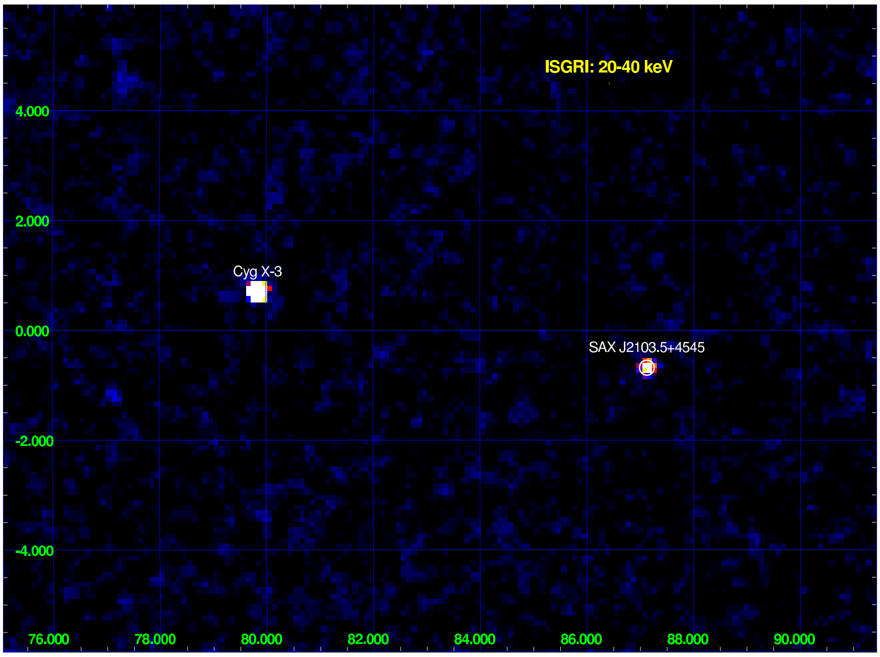

Figure 1. IBIS/ISGRI mosaic of the source field in the 20–40 keV energy range in galactic coordinates

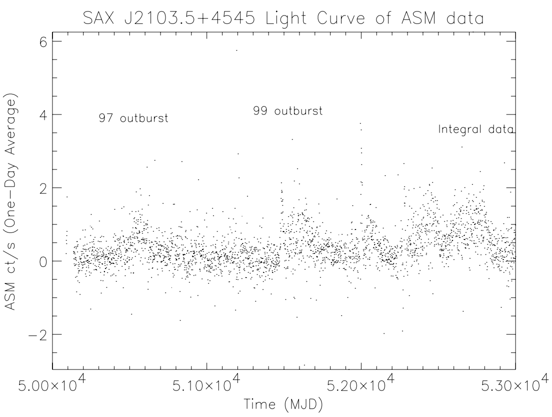

Figure 2. RXTE ASM lightcurve of SAX J2103.5+4545. Times of the INTEGRAL observations have been marked

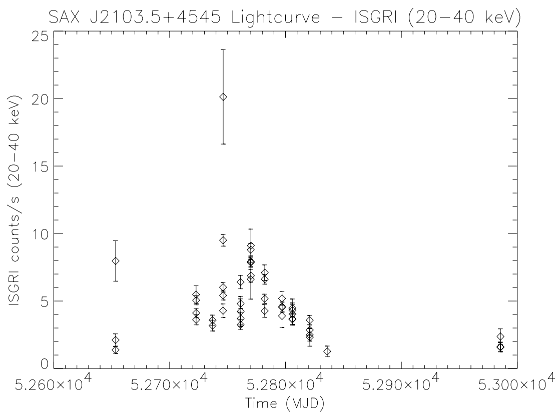

Figure 3. SAX J2103.5+4545 lightcurve with IBIS/ISGRI (20–40 keV). Each point represents the flux during a single observation (~2000 s exposure time)

Table 2. Best determination of the pulse period with IBIS/ISGRI, adding together two consecutive pointings: the first period have been obtained searching for periodicities in the new data-set obtained adding together the two pointings n.3 and 4 in Table 1, while the second one considering the sum of the two observations named n.7 and 8 in Table 1

Start Time MJD	Stop Time MJD	Period s
52746.10	52746.15	353±4
52770.05	52770.10	350±2

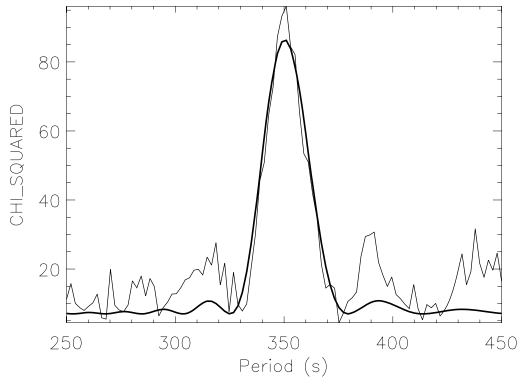

Figure 4. χ^2 distribution for our best measure of the pulse period, obtained summing together two consecutive GPS pointings (see Table 2). The two lines indicate the data (thin line) and the fit with the Leahy function (thick line)

events with a Pixel Illumination Function (pixel fraction illuminated by the source), PIF, equal to 1. After correcting times to the solar system barycenter, we searched for periodicity around the known pulse period. We have found a clear peak in the χ^2 distribution in 10 observations with IBIS/ISGRI, and only in 3 with JEM-X. The estimated pulse periods for each pointing are reported in the Table 1, while in Table 2 we report the measurements of the pulse period obtained adding together two consecutive pointings, and doing the same search for periodicities on the new data-set. The uncertainties on the pulse periods have been estimated from the Leahy function (Leahy 1987).

Our best determination of the pulse period, P, is 350±2 s (ISGRI, 20-40 keV) indicating a clear spin up with respect to RXTE and BeppoSAX estimates (see Figs. 4 and 5 for the χ^2 distribution and the pulse profile, respectively).

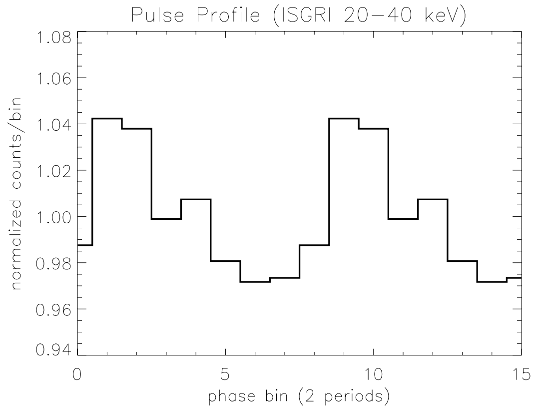

Figure 5. Pulse profile for SAX 2103.5+4545 in the energy range 20–40 keV

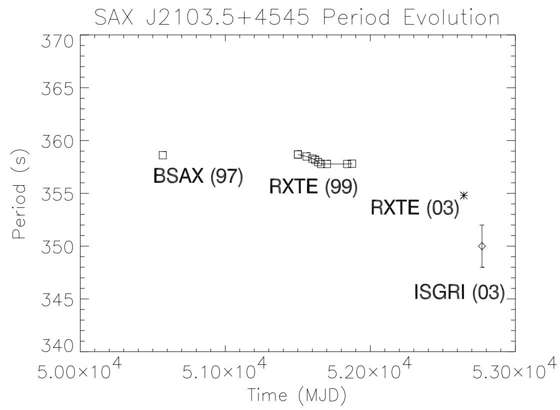

Figure 6. SAX J2103.5+4545 pulse period history; BSAX (97) marks the determination performed by Hulleman et al. (1998); RXTE (99) is from Baykal et al. (2002); RXTE (03) has been taken from the recent measurement performed by Inam et al. 2004; ISGRI (03) is our best measure with IBIS/ISGRI data

A period derivative of about -4×10^{-7} s s^{-1} can be measured with respect to the latest RXTE measurement (P=354.794; Inam et al. 2004) performed in Jan, 2003 indicating an increasing spin-up rate during the last outburst (see Fig. 6). We caution that the pulse period history is poorly sampled (Fig. 6), making the measurement of the period derivative quite uncertain. Anyway, our estimate is compatible with the extrapolation at higher X–ray fluxes ($\sim10^{-9}$ erg cm^{-2} s^{-1}) of the correlation between the period derivative and the X–ray flux, measured by Baykal et al. (2002) during the source outburst in 1999 (see their Fig. 7).

3. SPECTRAL RESULTS

The results on the spectral analysis from the three instruments JEM-X, IBIS/ISGRI and SPI, should be considered very preliminary. Indeed, still large cali-

Table 1. Observations summary and source pulse periods measured with IBIS in each pointing

ID.	ISGRI rate 20-40 keV (s^{-1})	Start Time (MJD)	Pulse Period with ISGRI (s)	Pulse Period with JEM-X (s)
1	5.06 ±0.34	52722.88	349 ±7	334 ±10
2	3.58 ±0.38	52737.07	366 ±10	–
3	6.02 ±0.36	52746.10	341 ±9	–
4	5.41 ±0.33	52746.13	364 ±15	–
5	4.81 ±0.35	52761.29	350 ±10	–
6	8.80 ±0.46	52770.02	360 ±5	–
7	7.85 ±0.34	52770.05	357 ±7	–
8	7.92 ±0.35	52770.08	348 ±6	368 ±13
9	6.61 ±0.36	52782.09	353 ±8	351 ±27
10	7.10 ±0.57	52782.12	369 ±14	–

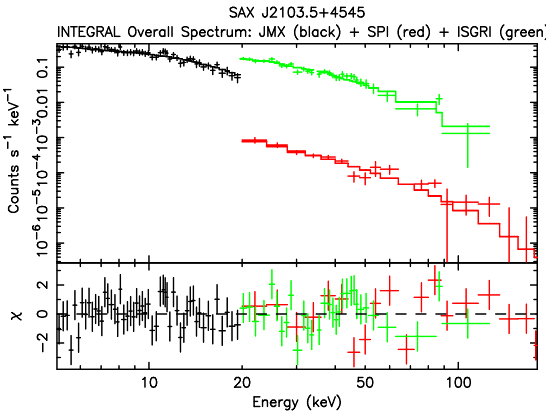

Figure 7. SAX J2103.5+4545 overall spectrum (5–200 keV) extracted from JEM-X (5–20 keV), IBIS/ISGRI (20–100 keV, upper spectrum) and SPI (20–200 keV, lower spectrum) instruments (see text). The residuals displayed in the lower panel are in units of standard deviations

bration and inter-calibration uncertainties exist.

The overall average source spectrum from 5 to 200 keV, obtained combining JEM-X together with IBIS/ISGRI and SPI, is quite hard. We here fitted it with a cut-off powerlaw (including free relative normalizations between the three instruments). The resulting spectral parameters are a photon index of ∼1.1 and a high energy cutoff of 30 keV (see Fig. 7). The 2–100 keV flux is $\sim 1.5 \times 10^{-9}$ erg cm^{-2} s^{-1} (based on JEM-X and SPI response matrices).

The derived spectral parameters are consistent with the WFC/BeppoSAX model (Hulleman et al., 1998).

REFERENCES

Baykal, A., et al., 2000, ApJ, 544, L129.

Baykal, A., et al., 2002, ApJ, 569, 903.

Hulleman, F., in 't Zand, J.J.M., Heise, J., 1998, A&A, 337, L25

Inam, S.C., et al., 2004, astro-ph/0402221, submitted to ApJ

Leahy, D.A., 1987, A&A, 180, 275

Lutovinov, A., et al., 2003, Astron.Lett., 29, 713

Reig, P., Mavromatakis, F., 2003, Atel 173

Reig, P., et al., 2004, A&A in press (astro-ph/0404121)

The two monitoring programmes share the common goal of populating the regularly updated on-line data base on the hard X-ray emission of intrinsically different X-ray binaries. Accreting pulsars are binaries hosting a neutron star and most of them are HMXRBs. Including low mass and high mass binaries in the same database will give a coherent view of the effects in the hard X-ray emission of many intrinsic differences such as the different accretion process (RLO versus wind accretion), magnetic field strength (low in LMXRBs and high in HMXRBs), inclination effects (high mass induced eclipses and dips versus low mass), pulsations (the few low mass cases compared to the high mass cases).

10.3 A particular HMXRB: Cyg X-3

Among the XRB monitoring programme there is Cyg X-3. This is an enigmatic X-ray binary that has evaded simple classification ever since its discovery in 1966 (Giacconi et al., 1967). Its 4.8 hr period is typical for a LMXRB but infrared observations have shown that the donor is a high mass star (e.g. van Kerkwijk et al., 1996). The nature of the compact object is uncertain as well, it may either be a neutron star or a black hole. The system is located at a distance of about 9 kpc and is embedded in a dense wind from the donor star. In X-rays, it exhibits a wide range of variability patterns. On the timescales of months to years, transitions between the hard and soft spectral states occur. The observed lack of ms-timescale variability appears to be due to scattering in the strong wind of the companion (McCollough et al., 1998). Cyg X-3, as an X-ray and γ-ray source, is one of the brightest in our Galaxy and is a good target for *INTEGRAL*. It is also the strongest radio source among X-ray binaries.

It is believed that it shows so many unique properties because it is in a later evolutionary phase of a HMXRB, possibly already in the common envelope phase (Fig. 3.2), which would explain the short orbital period and absorbed spectrum.

In spite of a large number of X-ray observations, the spectrum of Cyg X-3 has mostly been interpreted in terms of phenomenological models (e.g. Nakamura et al., 1993). The first physical interpretation of the broad band spectra of Cyg X-3 was done by Vilhu et al. (2003) based on simultaneous *INTEGRAL-RXTE* observations. The paper is included in this chapter. The *INTEGRAL* data used are taken from observations of the Cygnus region during the performance verification phase (December, 2002).

A collection of spectra from all pointed *RXTE* observations between 1996-2000 was obtained by Szostek and Zdziarski (2004) showing that Cyg X-3 displays many different spectral states, as shown in Fig. 10.1. Two extreme cases are visible: a *high/soft* state in which the spectrum peaks at a few keV with a distinct hard tail with photon index ~ 2 above 30 keV and a *low/hard* state peaking at about 20 keV. The spectra could be well fitted by a model including hybrid (thermal and non thermal) Comptonisation, reflection and absorption, like the one used in Vilhu et al. (2003).

A comparison with the *RXTE* spectra of Szostek and Zdziarski (2004) shows that the *INTEGRAL*la December 2002 observations caught Cyg X-3 in one of its main spectral states, an intermediate one characterised by a medium level of soft X-rays ($\lesssim$10 keV) and a soft extended power law above $\sim$20 keV. In the paper here reproduced we show that this state can be interpreted in terms of thermal Comptonisation of a soft X-ray blackbody with an additional contribution from Compton reflection and a complex absorption.

The monitoring of Cyg X-3 with *INTEGRAL* is mainly aimed to catch the source in most of its spectral states with special attention to the less explored hard X-rays $\gtrsim$50 keV. The soft state, with its high energy tail without cut off below $\sim$ 200 keV requires non thermal Comptonising

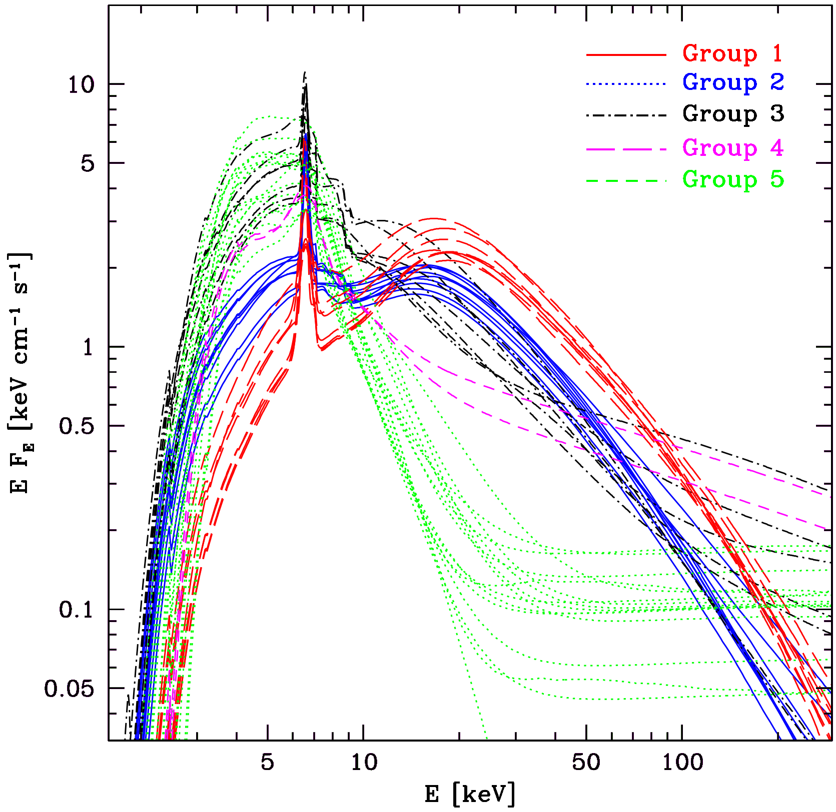

Figure *10.1: Comptonisation model spectra of Cyg X-3 from pointed RXTE observations. Different line styles correspond to the authors' classification of the spectra that show a continuity of spectral shapes. Two extreme states, one with a strong soft X-ray emission followed by a weak hard X-ray tail, and one with a weak soft X-ray emission and hard X-rays peaking around* $\sim 20\,keV$ *are clearly seen. (Szostek and Zdziarski 2004).*

electrons and the search for a cut off (or its absence) at higher energies is particularly interesting for *INTEGRAL* whose imaging and sensitivity capabilities are suited for the hunt of hard tails in XRBs. As already discussed in the first part of this thesis, the presence of a high energy hard tail is not a signature for the presence of a black hole. Nevertheless, apart from the very strong absorption in Cyg X-3, the transitions between the various states resemble those of two well known black hole XRBs GRS 1915+105 and Cyg X-1. This suggest that Cyg X-3 could be a black hole.

The presence of the hard tail appears to be closely related to the level of the flux in the 1.5-12 keV band as measured by *RXTE*/ASM. The soft state has always occurred with an ASM countrate of $\gtrsim$ 25 counts per second (∼300 mCrab). Based on this we have proposed for an *INTEGRAL* observation of Cyg X-3 to be triggered when the source is seen to enter its high soft state by *RXTE*/ASM (Proposal ID: 0220138, PI: Hjalmarsdotter). Unfortunately, although we were awarded 400 ksecs, the source did not enter the soft state. We will submit this proposal again for the *INTEGRAL* AO3 that has been issued at the time of writing (September 2003).

An examination of the archived *RXTE* spectra further shows a lack of observations of the source in a really low/hard state with *RXTE*/ASM count rates below 6 counts per second (∼ 80 mCrab). Due to the anticorrelated behaviour of the hard and soft X-ray emission in the source, a low soft X-ray flux means a high hard-X ray flux and it is therefore in states like this that we would expect to observe the strongest emission between 20-100 keV, where *INTEGRAL* is most efficient. A trigger on this extremely low/hard state of the source has also been proposed for in the aforementioned proposal.

This is one example of the importance of having publically available near real time light-curves for different sources. Today we trigger based on data from *RXTE*/ASM, tomorrow on the *INTEGRAL* XRB monitoring programme.

A&A 411, L405–L410 (2003)
DOI: 10.1051/0004-6361:20031257

Astronomy & Astrophysics

First *INTEGRAL* observations of Cygnus X-3*

O. Vilhu[1,2], L. Hjalmarsdotter[2], A. A. Zdziarski[3], A. Paizis[1,4], M. L. McCollough[5], V. Beckmann[1,6], T. J.-L. Courvoisier[1,7], K. Ebisawa[1,8], P. Goldoni[10], P. Hakala[2], D. Hannikainen[2], P. Kretschmar[1,9], and N. J. Westergaard[11]

1 *INTEGRAL* Science Data Center, Chemin d'Écogia 16, 1290 Versoix, Switzerland
2 Observatory, PO Box 14, 00014 University of Helsinki, Finland
3 Centrum Astronomiczne im. M. Kopernika, Bartycka 18, 00-716 Warszawa, Poland
4 CNR-IASF, Sezione di Milano, via Bassini 15, 20133 Milano, Italy
5 Smithsonian Astrophysical Observatory, 60 Garden Street, MS 67, Cambridge, MA 02138-1516, USA
6 Institut für Astronomie and Astrophysik, Universität Tübingen, Sand 1, 72076 Tübingen, Germany
7 Geneva Observatory, Ch. des Maillettes 51, 1290 Sauverny, Switzerland
8 Laboratory for High Energy Astrophysics, NASA Goddard Space Flight Center, Greenbelt, MD 20771, USA
9 Max-Planck-Institut für Extraterrestrische Physik, Giessenbachstrasse, 85748 Garching, Germany
10 Centre d'Études de Saclay, DAPNIA/Service d'Astrophysique, Orme des Merisiers, 91191 Gif-sur-Yvette Cedex, France
11 Danish Space Research Institute, Juliane Maries Vej 30, 2100 Copenhagen Ø, Denmark

Received 15 July 2003 / Accepted 18 August 2003

Abstract. We present the first *INTEGRAL* results on Cyg X-3 from the PV phase observations of the Cygnus region. The source was clearly detected by the JEM-X, ISGRI and SPI. The *INTEGRAL* observations were supported by simultaneous pointed *RXTE* observations. Their lightcurves folded over the 4.8 hour binary period are compatible with the mean *RXTE*/ASM and *CGRO*/BATSE light curves. We fit our broad-band X-ray/γ-ray spectra with a physical model, which represents the first such published model for Cyg X-3. The main physical processes in the source are thermal Comptonization and Compton reflection with parameters similar to those found for black-hole binaries at high Eddington rates.

Key words. gamma rays: observations – radiation mechanisms: non-thermal – stars: individual: Cyg X-3 – X-rays: binaries – X-rays: general – X-rays: stars

1. Introduction

The bright X-ray binary Cyg X-3 was discovered during an early rocket flight already in 1966 (Giacconi et al. 1967) but it remains still poorly understood. It is a massive system with the donor star and the compact object orbiting each other in a tight orbit. The system is embedded in a dense wind from the donor star, presumably a massive nitrogen-rich Wolf-Rayet star with huge mass loss (van Keerkwijk et al. 1992). The nature of the compact object is not known but recent mass estimates suggest it might be a black hole (e.g. Schmutz et al. 1996).

The system has been observed throughout a wide range of the electromagnetic spectrum (e.g. McCollough et al. 1999). It is one of the brightest Galactic X-ray sources, displaying high and low states and rapid variability in X-rays. It is also the strongest radio source among X-ray binaries, and shows both huge radio outbursts and relativistic jets. The most striking feature in the lightcurve is a 4.8-hr quasi-sinusoidal modulation, present both in X-rays and infrared. The modulation is believed to reflect the orbital motion of the binary with the emission from the X-ray source being scattered by the wind from the companion.

2. Observations and data analysis

On 2002 Dec. 22–23, Cyg X-3 was observed by all the X/γ-ray instruments aboard *INTEGRAL* – the JEM-X (Lund et al. 2003), IBIS/ISGRI (Lebrun et al. 2003), IBIS/PICsIT (Di Cocco et al. 2003) and SPI (Vedrenne et al. 2003). The *INTEGRAL* observations were supported by simultaneous *RXTE*/PCA and HEXTE observations making possible a comparison of the results from the two X-ray telescopes. At the time of the *INTEGRAL* observations, Cyg X-3 was in a relatively high state with the X-ray flux varying between 130 and 330 mCrab, according to the *RXTE*/ASM dwell-by-dwell data. Cyg X-3 was also observed in radio by the RATAN and Ryle telescopes. The results of the radio observations will be presented elsewhere (Hjalmarsdotter et al., in preparation).

Send offprint requests to: O. Vilhu,
e-mail: `osmi.vilhu@helsinki.fi`

* Based on observations with *INTEGRAL*, an ESA project with instruments and science data center funded by ESA and member states (especially the PI countries: Denmark, France, Germany, Italy, Switzerland, and Spain), the Czech Republic, and Poland and with the participation of Russia and the US.

2.1. JEM-X

The observations were performed with the second (JEM-X2) of the two identical X-ray monitors. The data were taken from 43 pointings (science windows), 2200 s each, performed between IJD 1085.6–1087.5 (IJD = fractional number of days since 2000 Jan. 1 00.00 UT, which corresponds to MJD = IJD + 51544) during the 23rd rev. of *INTEGRAL* (2002 Dec. 22–23), which corresponds to 10 binary periods and the net exposure of ~90 ks. In a half of the pointings, Cyg X-3 was in the fully coded field-of-view (FOV, within 2.4° from the FOV center), while in the rest, it was in the partially coded FOV (within 5° from the FOV center). In all the pointings, Cyg X-1 and SAX J2103.5+4545 (an X-ray pulsar, discovered by Hulleman et al. 1998) were >10° from the FOV center and hence the data were not contaminated by those sources. The offsets were rather uniformly distributed as a function of the binary phase.

Source spectra were extracted individually per pointing. Then the average spectrum was obtained from the sum of the individual spectra weighted by the exposure time. The spectral response was Crab-corrected appropriately for this time period (instance 0004). The spectra were implicitly background-subtracted by a deconvolution algorithm assuming a spatially flat background. We used the energy range of 2.6–27 keV for spectral fitting.

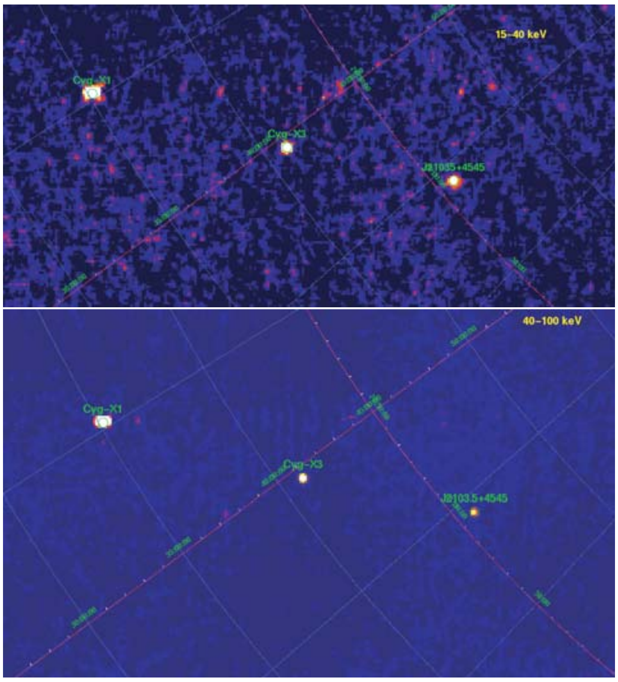

Fig. 1. The ISGRI 15–40 keV (top) and 40–100 keV (bottom) mosaic images showing Cyg X-1 (left), Cyg X-3 (center) and SAX J2103.5+4545 (right).

2.2. IBIS/ISGRI

The ISGRI fully coded FOV is about $9\times9°$, while the partially coded FOV extends up to $29\times29°$. Standard spectral extraction is at present feasible only in the fully coded FOV, therefore we limited ourselves to the science windows where Cyg X-3 was at a distance of <4.5° from the pointing direction. The selected ISGRI data contain about 40 science windows (of an average duration of 2200 s each with exception of two with 500 s duration each) for a total duration of ~79 ks.

Imaging analysis was performed using the current version of the Offline Scientific Analysis (OSA) software, using the procedure described in Goldwurm et al. (2003). Cyg X-3 was detected at a high signal-to-noise in the 15−40 and 40−100 keV energy bands in this as well as in previous ISGRI observations (Goldoni et al. 2003). The source position was obtained with an offset of <1′ with respect to the catalog position. Mosaic images in the 20−40 and 40−100 keV bands are shown in Fig. 1, showing Cyg X-1, Cyg X-3, and SAX J2103.5+4545.

Spectral extraction was performed independently for every science window in 24 channels linearly rebinned in the 13–200 keV range from a 2048-channel response matrix developed at CEA/Saclay. We took the source position as obtained from the imaging procedure and then fitted source and background fluxes in each energy band. The resulting individual spectra were added to obtain the total spectrum. A 5% systematic error was then added in quadrature to each channel.

Cyg X-3 was not detected by the IBIS/PICsIT (Foschini, private comm.), which becomes efficient only at energies ≳250 keV (Di Cocco et al. 2003). Given the low flux from the source above 250 keV, a significantly longer exposure would be required for detection.

2.3. SPI

Out of the 95 dithering pointings taken during the rev. 23 on the Cygnus field, 10 had to be excluded from the SPI analysis as they were either affected by strong solar activity or by the radiation belts. This left 85 dithering pointings with a total exposure of 169 ks for the present analysis. As the SPI data are background-dominated, a careful background substraction is essential in order to get reliable results, especially for weak sources. A time-dependent background model has been applied to the data, based on the saturated events seen by the detector. The image reconstruction was done using the SPI Iterative Removal Of Sources program (SPIROS; Skinner & Connell 2003). To get precise flux values, the source positions of the two brightest sources in the field (Cyg X-1 and Cyg X-3) have been fixed to their catalogue values. No source confusion is expected in the SPI data as there are no other sources visible within 3° around Cyg X-3. The SPI image is shown in Fig. 2.

For spectral extraction, 20 logarithmic bins in the 20−300 keV energy range have been used. The instrumental response function used here has been derived from on-the-ground calibration and then corrected based on the Crab calibration observation. A 5% systematic error has been added to the spectrum.

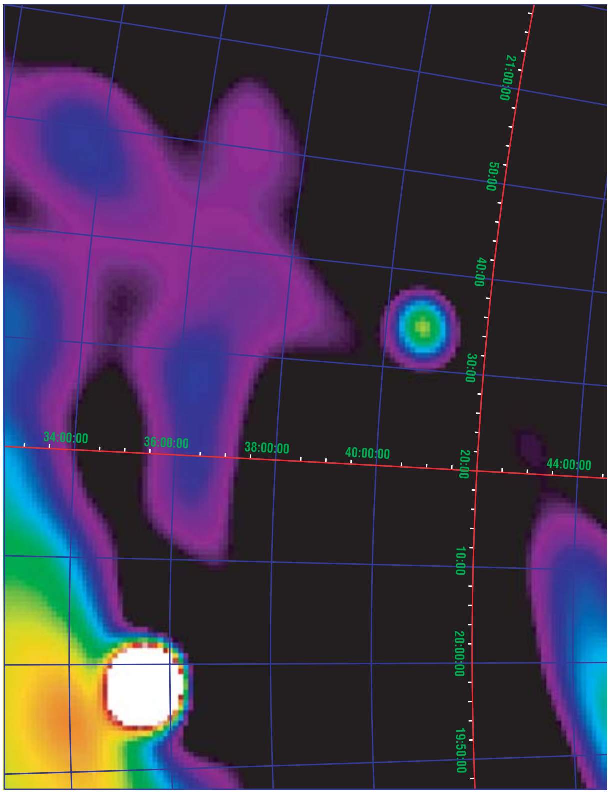

Fig. 2. The SPI 34–52 keV image. The brightest source in the lower left corner is Cyg X-1. Cyg X-3 is the source to the upper right.

2.4. PCA/HEXTE

The *RXTE* data overlapping with the *INTEGRAL* observations are from two pointings on 2002 Dec. 22–23, of duration of 8224 s (data set 1) and 9584 s (data sets 2 and 3), respectively. For the second pointing, there was a change in the number of PCUs used, which required breaking it into two parts, with the lightcurves corrected to the five PCUs. The data sets 1, 2 and 3 then cover the binary phases of (0.86−0.06, 0.16−0.34), 0.47−0.67 and 0.82−1.0, respectively. Hence, data sets 2 and 3 are from around the maximum and minimum phases, respectively. The *INTEGRAL* spectra, accumulated from all phases, should have flux levels in the middle of that from these two sets.

A 1% systematic error has been added to the PCA spectra. The relative normalization of each of the data sets from the two HEXTE clusters with respect to the PCA data has been allowed free in the fits. The response matrices and background files have been obtained using the FTOOLS v. 5.2.

3. Lightcurves

From the JEM-X observations, lightcurves in four energy bands (3–6, 6–10, 10–15 and 15–35 keV) were created. The ISGRI lightcurve was extracted in the 20–40 keV band. The lightcurves were folded using the latest published ephemeris for Cyg X-3 (Singh et al. 2002).

The results are plotted in Fig. 3. Two middle JEM-X bands were used since calibration for the 3−6 and 15−35 keV bands has not been yet consolidated. For comparison, we also plot the folded *RXTE*/ASM (2−12 keV) and *CGRO*/BATSE (20−100 keV) lightcurves from monitoring of the source during 1996−2002 and 1991−2000 respectively. The JEM-X 6−15 keV band shows good agreement with the ASM data and the ISGRI 20−40 keV follows the shape of the BATSE curve. Modelling of the lightcurves will be presented elsewhere (Hjalmarsdotter et al., in preparation).

4. Broad-band spectral modelling

The *RXTE*/PCA-HEXTE, JEM-X, ISGRI and SPI data were fitted using the XSPEC package (Arnaud 1996). We analyze here three *RXTE* spectra and the average *INTEGRAL* spectrum.

We interpret the intrinsic spectra of Cyg X-3 in terms of Comptonization of soft X-ray seed photons, assumed here to be a blackbody with a temperature, T_s. We use a Comptonization model by Coppi (1992, 1999), `eqpair`, described in detail by Gierliński et al. (1999). This model was also used to fit X-ray spectra of GRS 1915+105 and Cyg X-1 by Vilhu et al. (1999), Zdziarski et al. (2001) and by Poutanen & Coppi (1998), Gierliński et al. (1999), Zdziarski et al. (2002b), respectively. In general, the electron distribution in this model can be purely thermal or hybrid, i.e., Maxwellian at low energies and non-thermal at high energies, if an acceleration process is present. This distribution, including the electron temperature, T, is calculated self-consistently from the assumed form of the acceleration (if present) and from the luminosities corresponding to the plasma heating rate, L_h, and to the seed photons irradiating the cloud, L_s. The plasma optical depth, τ, includes a contribution from $e^{\pm}$ pairs. The importance of pairs depends on the ratio of the luminosity to the characteristic size, r, which is usually expressed in dimensionless form as the compactness parameter, $\ell \equiv L\sigma_T/(rm_ec^3)$, where σ_T is the Thomson cross section and m_e is the electron mass. Hereafter, the indices of ℓ have the same meaning as those of L.

We find all the studied spectra compatible with the hot plasma being completely thermal, and with $kT \ll 511$ keV. Then, the $e^{\pm}$ pair production is negligible, and the absolute value of the compactness is only weakly important. Accordingly, we assume a constant $\ell_s = 10$ (which is typical for accreting X-ray sources, e.g., Gierliński et al. 1999).

A complex issue in Cyg X-3 is the structure of its X-ray absorber and the presence of additional spectral components in soft X-rays (e.g. Molnar & Mauche 1986; Nakamura et al. 1993). Given that our data cover energies $\gtrsim 3$ keV only, we neglect any additional soft X-ray components and we use a relatively simple model of the absorber. Namely, we assume that an absorbing medium with the column density, $N_{H,0}$, fully covers the source, and another medium with the column, $N_{H,1}$, covers a fraction, f_1, of the source. A similar model is often used to model the similarly complex absorption of the Seyfert galaxy NGC 4151 (see, e.g. Zdziarski et al. 2002a). We assume the elemental abundances of Anders & Ebihara (1982). We include Compton reflection (Magdziarz & Zdziarski 1995), parametrized by an effective solid angle subtended by the reflector as seen from the hot plasma, Ω, and assuming an inclination of 60°. We also include an Fe Kα fluorescent line,

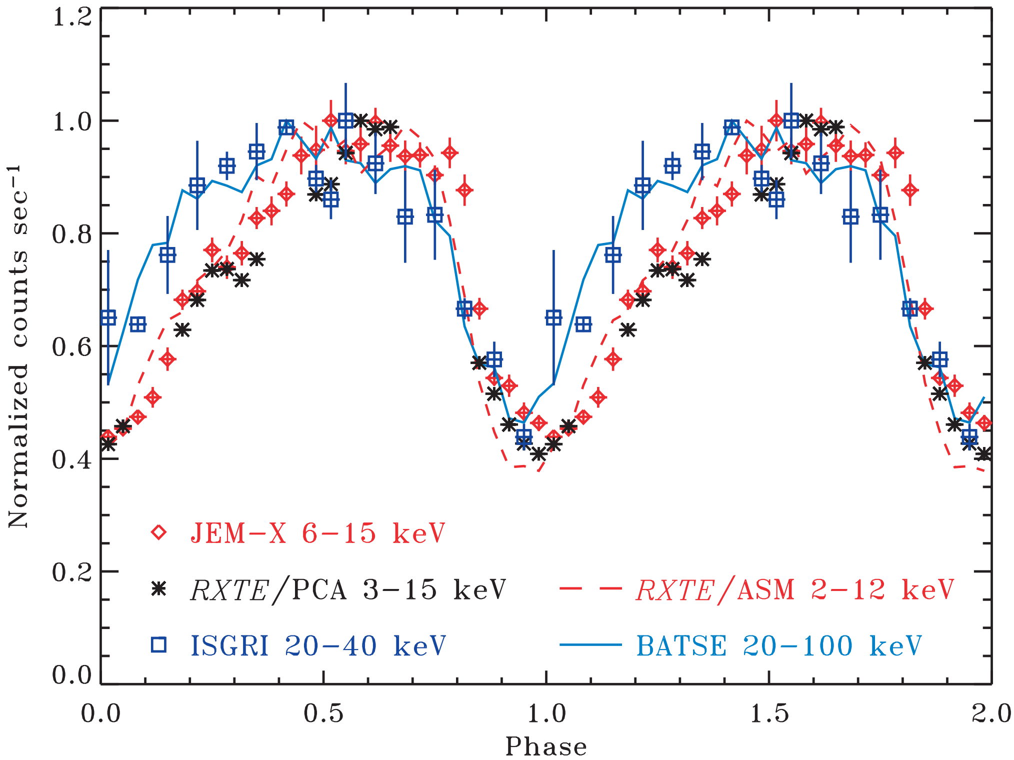

Fig. 3. The JEM-X 6–15 keV (red diamonds) and ISGRI 20–40 keV (blue squares) lightcurves folded over the orbital period. We also show the *RXTE*/PCA 3–15 keV data (black asterisks) from simultaneous observations as well as the *RXTE*/ASM 1.5–12 keV (dashed red curve) and *CGRO*/BATSE 20–100 keV (blue curve) phase dependences averaged over several years of monitoring. The count rates are normalized to the respective maxima.

which we model as a Gaussian (with the physical and equivalent widths of $\sigma_{K\alpha}$ and $W_{K\alpha}$, respectively, and the peak energy at $E_{K\alpha}$). We allow the reflecting medium to be ionized, using the ionization calculations of Done et al. (1992). We define the ionizing parameter as $\xi \equiv 4\pi F_{\rm ion}/n$, where $F_{\rm ion}$ is the ionizing flux and n is the reflector density. Given the simplified treatment of the ionized reflection of Done et al. (1992), we impose a condition of $\xi \leq 10^4$. We assume the temperature of the reflecting medium of 10^6 K.

Given the above approximated treatment of the absorption and ionized reflection, the full description of the part of the spectrum $\lesssim$10 keV is likely to be more complex than that given by our model. However, it provides a statistically satisfactory description of the data, including the absorbed part of the spectrum, and allows us to calculate the broad-band intrinsic spectrum of the source.

During our fits, we have found that the data, covering only photon energies $\gtrsim$3 keV, rather poorly constrain the temperature of the seed blackbody photons. For example, we get 0.3 keV $\lesssim kT_{\rm s} \lesssim$ 0.5 keV within 90% confidence for the *RXTE* data set 1. For simplicity, we fix it at the respective best-fit value for each spectrum when determining the confidence regions of other parameters.

On the other hand, our data yield accurate spectral information only for energies $\lesssim$100 keV. Thus, they poorly constrain possible electron acceleration, which can be present in the plasma in addition to the thermal heating. Nonthermal processes are, in fact, clearly observed in some other spectral states of Cyg X-3 observed by *RXTE* and the *CGRO*/OSSE (work in preparation). However, allowing for the presence of nonthermal electrons improves the fit only weakly, e.g. by $\Delta\chi^2 \simeq -2$ for the *RXTE* data set 1, and thus it is not required in our models statistically. The fraction of the total power supplied to the plasma in electron acceleration is constrained to $\lesssim$0.5, and the power law index, $\Gamma_{\rm acc}$, of the acceleration process is not constrained at all at 90% confidence (typical obtained values are $\Gamma_{\rm acc} \sim$ 2–4). We also note that the presence of nonthermal processes in a very similar state of GRS 1915+105 is required only by the data at $\gtrsim$100 keV (see Fig.3a in Zdziarski et al. 2001).

The Fe Kα line is found to be narrow in all the *RXTE* spectra, with the width much below the instrumental resolution of the PCA. The plasma parameters obtained are given in Table 1, and the spectra for the 3 data sets are shown in Fig. 4.

The *INTEGRAL* spectrum has been found to be rather similar in shape to the *RXTE* ones. However, unlike the PCA, the JEM-X data appear to require the Fe line to be broadened, with the corresponding decrease of $\Delta\chi^2 = -12$. Thus, we have decided to allow for the broadening, but, given the limited resolution of JEM-X, we kept it then frozen at the best-fit value of $\sigma_{K\alpha} \simeq 0.25$ keV. The resulting parameters are given in Table 1, and the spectrum is shown in Fig. 4. We see that the although the fit parameters are similar to those of the *RXTE* fits, the normalization of the JEM-X spectrum is lower than that the avarage of the PCA spectra by a factor of ∼2, which is due to instrumental effects, see below.

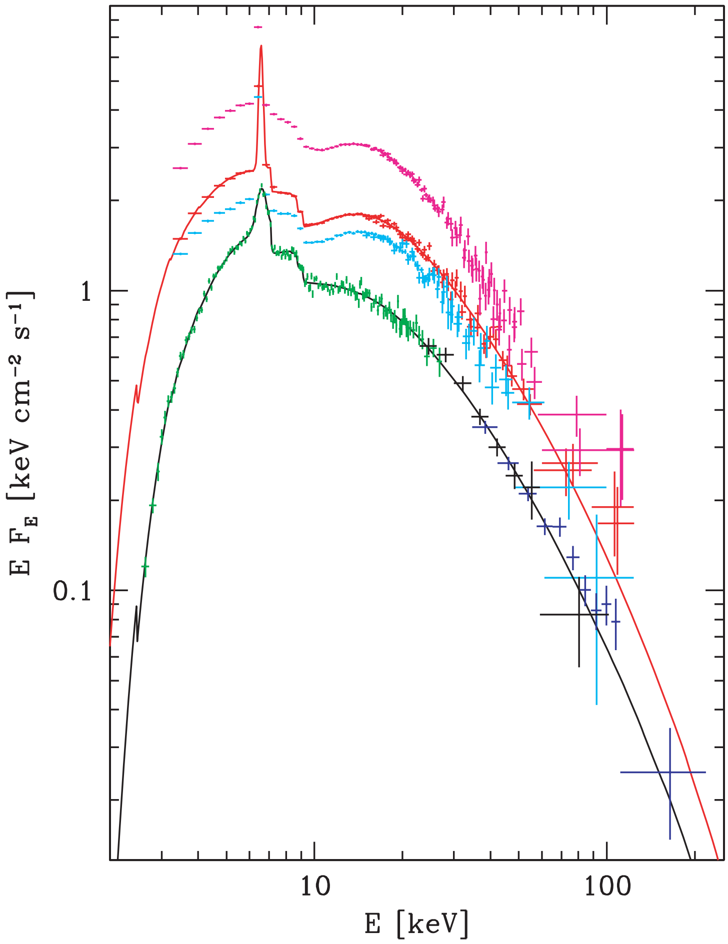

Fig. 4. Deconvoled spectra of Cyg X-3. The red, magenta and cyan spectra correspond to the PCA/HEXTE data set 1, 2, 3, respectively. The HEXTE spectra have been renormalized to the flux level implied by the PCA. The model spectrum is shown only for the middle spectrum (data set 1) for clarity. The green, blue and black spectra are from the JEM-X, ISGRI and SPI, respectively, with the model spectrum shown in the black curve. The ISGRI and SPI spectra have been renormalized to the JEM-X data. The intensity levels of the *INTEGRAL* spectra, which were accumulated over several binary phases, should be close to the mean of the *RXTE* data sets 2 and 3. The proportions of this figure correspond to equal length per decade on each axis.

Table 1. Model parameters[a] for the *RXTE* and *INTEGRAL* spectra. The *RXTE* data sets 1, 2 and 3 are from binary phases (0.86–0.06, 0.16–0.34), 0.47–0.67 and 0.82–1.0, respectively. The *INTEGRAL* spectra were accumulated from all phases.

Data	$N_{\rm H,0}$	$N_{\rm H,1}$	f_1	$kT_{\rm s}$	$\ell_{\rm h}/\ell_{\rm s}$	τ	kT^b	$\Omega/2\pi$	ξ^c	$E_{\rm K\alpha}$	$W_{\rm K\alpha}$	$F_{\rm bol}{}^d$	χ^2/ν
	10^{22} cm^{-2}	10^{22} cm^{-2}		keV			keV		erg cm s^{-1}	keV	eV	erg cm^{-2} s^{-1}	
RXTE(1)	$11.8^{+0.9}_{-0.8}$	256^{+9}_{-17}	$0.61^{+0.02}_{-0.02}$	0.37f	$0.21^{+0.02}_{-0.04}$	$0.23^{+0.03}_{-0.02}$	69	$1.0^{+0.2}_{-0.2}$	$10\,000_{-5000}$	$6.56^{+0.04}_{-0.03}$	400^{+30}_{-30}	8.2×10^{-9}	239/250
RXTE(2)	$12.8^{+1.1}_{-1.0}$	302^{+20}_{-17}	$0.63^{+0.02}_{-0.02}$	0.41f	$0.14^{+0.02}_{-0.01}$	$0.16^{+0.02}_{-0.02}$	71	$1.0^{+0.2}_{-0.2}$	$10\,000_{-5000}$	$6.56^{+0.06}_{-0.02}$	310^{+30}_{-40}	13.5×10^{-9}	250/249
RXTE(3)	$11.1^{+0.3}_{-0.3}$	330^{+13}_{-16}	$0.63^{+0.01}_{-0.01}$	0.45f	$0.17^{+0.02}_{-0.02}$	$0.19^{+0.03}_{-0.02}$	69	$1.4^{+0.3}_{-0.2}$	9000^{+1000}_{-3000}	$6.58^{+0.03}_{-0.03}$	510^{+30}_{-30}	7.0×10^{-9}	174/226
INTEGRAL	$16.2^{+0.6}_{-0.4}$	334^{+36}_{-37}	$0.44^{+0.02}_{-0.02}$	0.38f	$0.18^{+0.05}_{-0.03}$	$0.19^{+0.03}_{-0.02}$	75	$1.1^{+0.2}_{-0.2}$	$10\,000_{-3000}$	$6.58^{+0.04}_{-0.04}$	230^{+20}_{-20}	4.3×10^{-9}	291/186

[a] The uncertainties are for 90% confidence, i.e., $\Delta\chi^2 = 2.71$; "f" denotes a parameter fixed in the fit.
[b] Calculated from the energy balance, i.e., not a free fit parameter.
[c] Assumed $\leq 10^4$ in the fits.
[d] The bolometric flux of the *absorbed* model spectrum.

5. Comparison between individual *INTEGRAL* and *RXTE* spectra

The *INTEGRAL* spectra were accumulated over the entire binary orbit, unlike the three *RXTE* data sets (see Fig. 3). The mean flux levels of the *INTEGRAL* spectra should then correspond closely to the mean of the (extreme) *RXTE* data sets 2 and 3. However, as we see in Fig. 4, the flux level of the JEM-X spectrum is about a half of that. Furthermore, the normalizations of the HEXTE, ISGRI and SPI differ from each other, with the ISGRI spectrum having the flux level about twice of that of the average PCA. Those differences are instrumental. To facilitate appropriate corrections to the fluxes from various instruments, we list the relative normalizations between the instruments in Table 2. The relative ratio between the HEXTE and PCA spectra is consistent with previous results. The coefficients involving the *INTEGRAL* data correspond to the calibration as of 2003 June.

Letter to the Editor

Table 2. The values of the relative normalizations between the flux level from different detectors implied by our data.

Instruments	$E_1 - E_2$ [keV][a]	Ratio[b]
HEXTE 0/PCA(2)	18−120	0.71 ± 0.04
HEXTE 1/PCA(2)	18−120	0.70 ± 0.05
JEM–X/PCA(2)[c]	2.6−27	0.33 ± 0.01
JEM–X/PCA(3)[c]	2.6−27	0.65 ± 0.01
ISGRI/JEM–X	35−220	4.7 ± 0.2
SPI/JEM–X	23−100	2.3 ± 0.1

[a] The energy range of the first of the two compared instruments used to derive the ratio.
[b] The uncertainties are 1-σ.
[c] The JEM-X spectrum should have about the same level as an average of the PCA (2) and (3) spectra, which implies the renormalization factor of ∼0.44.

The slopes of various spectra agree with each other well, as shown in Fig. 4. The ISGRI and SPI data fitted by a power law over the energy ranges given in Table 2 yield the photon index of $\Gamma = 3.6 \pm 0.1$ with $\chi^2/\nu = 34/22, 9/9$, respectively. On the other hand, those data show hardenings at lower energies (not shown in Fig. 4), which appear related to residual inaccuracies of the present response matrices.

6. Conclusions

Cyg X-3 was clearly detected by all three X/γ-ray instruments on board *INTEGRAL*. The JEM-X 6–15 keV lightcurve folded over the orbital period shows good agreement with the *RXTE*/PCA 3−15 keV and *RXTE*/ASM 1.5−12 keV lightcurves. The ISGRI 20–40 keV folded lightcurve matches the *CGRO*/BATSE 20−100 keV one. A difference in the light curve profile between energies above and below ∼15 keV is indicated.

For the first time, we fit Cyg X-3 X/γ-ray spectra with a physical model. The main radiative processes implied by the *INTEGRAL* and *RXTE* data are thermal Comptonization and Compton reflection. The obtained intrinsic spectrum appears similar to that of GRS 1915+105 at a similar Eddington ratio.

At the time of writing, there are apparent differences in the normalizations between the *RXTE*/PCA, JEM-X, SPI and ISGRI spectra. Calibrations and responses at this stage are constantly being improved. Cyg X-3 will be further observed with *INTEGRAL* as a part of the Core as well as the Guest Observer programmes.

Acknowledgements. Authors from the Observatory of the University of Helsinki acknowledge the Academy of Finland, TEKES, and the Finnish space research programme ANTARES for financial support in this research. AAZ has been supported by KBN grants 5P03D00821, 2P03C00619p1,2, PBZ-KBN-054/P03/2001, and the Foundation for Polish Science. We would like to thank M. Revnivtsev for the tools to produce the ISGRI mosaics and J. Poutanen (the referee) for valuable comments. We acknowledge quick-look results provided by the *RXTE*/ASM team.

References

Anders, E., & Ebihara, M. 1982, Geochim. Cosmochim. Acta, 46, 2363
Arnaud, K. A. 1996, in Astronomical Data Analysis Software and Systems V, ed. G.H. Jacoby, & J. Barnes (San Francisco), ASP Conf. Ser., 101, 17
Coppi, P. S. 1992, MNRAS, 258, 657
Coppi, P. S. 1999, in High Energy Processes in Accreting Black Holes, ed. J. Poutanen, & R. Svensson (San Francisco: ASP), ASP Conf. Ser., 161, 375
Di Cocco, G., Caroli, E., Celesti, E., et al. 2003, A&A, 411, L189
Done, C., Mulchaey, J. S., Mushotzky, R. F., & Arnaud, K. A. 1992, ApJ, 395, 275
Hulleman, F., in 't Zand, J. J. M., & Heise, J. 1998, A&A, 337, L25
Giacconi, R., Gorenstein, P., Gursky, H., & Waters, J. R. 1967, ApJ, 148, L119
Gierliński, M., Zdziarski, A. A., Poutanen, J., et al. 1999, MNRAS, 309, 496
Goldoni, P., Bonnet-Bidaud, J. M., Falanga, M., & Goldwurm, A. 2003, A&A, 411, L399
Goldwurm, A., David, P., Foschini, L., et al. 2003, A&A, 411, L223
Lebrun, F., Leray, J. P., Lavocat, P., et al. 2003, A&A, 411, L141
Lund, N., Brandt, S., Budtz-Jørgensen, C., et al. 2003, A&A, 411, L231
McCollough, M. L., Robinson, C. R., Zhang, S. N., et al. 1999, ApJ, 517, 951
Magdziarz, P., & Zdziarski, A. A. 1995, MNRAS, 273, 837
Molnar, L. A., & Mauche, C. W. 1986, ApJ, 310, 343
Nakamura, H., Matsuoka, M., Kawai, N., et al. 1993, MNRAS, 261, 353
Poutanen, J., & Coppi, P. S. 1998, Phys. Scr., T77, 57
Schmutz, W., Geballe, T. R., & Schild, H. 1996, A&A, 311, L25
Singh, N. S., Naik, S., Paul, B., et al. 2002, A&A, 392, 161
Skinner, G. K., & Connell, P. H. 2003, A&A, 123
van Keerkwijk, M. H., et al. 1992, Nature, 355, 703
Vedrenne, G., Roques, G., Schönfelder, V., et al. 2003, A&A, 411, L63
Vilhu, O., Alha, L., Malmivaara, K., et al. 1999, Astrophys. Lett. Comm., 38, 241
Zdziarski, A. A., Grove, J. E., Poutanen, J., Cappi, M., & Mihara, T. 2001, ApJ, 554, L45
Zdziarski, A. A., Leighly, K. M., Matsuoka, M., Rao, A. R., & Vadawale, S. W. 2002a, ApJ, 573, 505
Zdziarski, A. A., Poutanen, J., Paciesas, W. S., & Wen, L. 2002b, ApJ, 578, 357

Sixth part

CONCLUSIONS

CONCLUSIONS

"Le seul vrai voyage de la découverte ne consiste pas à découvrir de nouveaux lieux mais à avoir de nouveaux yeux" (Marcel Proust, 1871 - 1922)

Through the years, many missions have gazed at the sky. Nevertheless, scientists keep trying hard to observe it, designing new missions that could bring answers to longstanding questions. Some missions are aimed to study the sky in less explored energy bands, some others cover well known energy ranges but bring significant improvements in the instrument performances with respect to previous missions. It is always the same sky that we observe but every time with different eyes.

Looking at the X-ray sky we see that (most of) the brightest objects are Galactic X-ray binaries. They are so close to us that they appear much brighter than the very distant, extragalactic, objects, e.g. AGNs that are intrinsically, by far, the brightest persistent objects.

In this thesis we have used *INTEGRAL* to study the less known hard X-ray emission of Galactic X-ray binaries and *Chandra* to discover the nature of newly discovered sources in a deep, source free region.

The *INTEGRAL* survey

With *INTEGRAL* we have developed two parallel monitoring programmes: the LMXRB and the accreting pulsar monitoring programmes.

The aim of these programmes is to monitor the spectral and temporal properties of about seventy-four LMXRBs and twenty-four accreting X-ray pulsars.

With time, while coordinating the LMXRB programme, we realised that there were four main streams to go through, in order to maximise the scientific output of such a work.

The first one is to regularly observe a **large sample** of different sources in the same energy bands and with the same instrumentation. The results are directly comparable, free from extrapolations and/or instrument response differences. Accreting pulsars are binaries hosting a neutron star and most of them are HMXRBs.

Including low mass and high mass binaries in the same database gives a coherent view of the effects in the hard X-ray emission of many intrinsic differences such as the different accretion processes (Roche Lobe overflow versus wind accretion), magnetic field strength (low in LMXRBs and high in HMXRBs), inclination effects (high mass induced eclipses and dips versus low mass), pulsations (the few low mass cases compared to the high mass cases).

A survey of the hard X-ray spectra of neutron stars and black holes candidates over a wide range of luminosities would allow to quantify the differences among these two types of systems for what concerns the dependence of the X-ray spectrum over the luminosity. Furthermore, the presence (or absence) of an exponential cut-off in the power-law hard tail could help investigating the origin (thermal or non thermal) of the hard components.

This comprehensive view is the only way to make a step back from the results and to look at the whole from a distance. Muno et al. (2002) and Gierliński and Done (2002) collected years of data from *RXTE* to actually realise that Atoll sources if observed long enough do display a Z in the colour-colour diagram. Likewise, years of *RXTE* data on Cyg X-3 (Szostek and Zdziarski 2004) gave a more complete view of the different spectral states of this source, allowing us to identify the state in which we have observed it with *INTEGRAL* on much shorter timescales.

This is what we want to achieve with *INTEGRAL*: build a large long-term database in the less known hard X-rays. A database that would not have been possible to implement using individual proposals. Then take a step back. Look at the whole and maybe discover that LMXRBs have a completely different way of locating themselves when looked in this "new" band; that the hard tails and cut-off energy behave in a very definite way with respect to a broad-band or hard X-ray luminosity, or even to hardness ratio history; that black holes and neutron star binaries do show the same dependence of the X-ray spectrum over the luminosity only with different timescales.

INTEGRAL might not give a definite answer to all the above. Actually, it might even add more questions. But a monitoring programme seems a reasonable way to look for the answer to any of these. A large set of data has more chances to catch the sources in all their possible states than single open time observations that go deep in a narrow field rather than giving an overview.

Building such a database is not an easy task given that it involves the time consuming and delicate analysis of *INTEGRAL* data. The data come in at a high pace and keeping step requires developing an infrastructure that analyses automatically the data, extracts the useful information and then displays it in an efficient way. Besides, results of such a programme will appear only in the long run. Nevertheless, it is important to set up all this structure already from the beginning, even if instrument calibration and software validation are still on-going. In this way, along our "overview-quest" we also learnt to deal with *INTEGRAL* data, discovering the limitations and difficulties of the data analysis process, having an idea of the amount of space and time needed to maintain this effort.

As a starting point, among the sources of the database, we made a first selection, focussing on the persistently bright sources and went a bit further in their study. This sample comprises LMXRBs hosting a neutron star, belonging to the Atoll and Z classes.

Our variability study (light-curves, colour-colour and hardness-intensity diagrams) showed that the *INTEGRAL* core programme coverage is sufficient to study the high-energy history and evolution of the sources. We find that Z sources are brighter than Atolls (as expected) and that, with the current data set, there seems to be no important difference in the variability of the sources as a class. If this is confirmed by larger *INTEGRAL* datasets it is an interesting result: Atolls and Z sources are one class when looked at from the variability point of view. The colour-colour and hardness intensity diagrams built in the "traditional" energy bands already display the expected patterns which is an encouraging result for exploring new, *INTEGRAL* defined, energy bands.

Our spectral study showed that Z sources present no evident cut-off until about 50 keV and that they seem to be harder than Atolls ($>$ 20 keV). This is most likely due to the fact that the Atolls of our sample are bright systems mostly in the soft high state, very different with respect to some dim Atoll sources that can be much harder.

We detected a hint for spectral hardening in GX 3+1 and, more obviously, in Sco X-1. The hunt for such hard tails in LMXRBs and understanding their origin are key goals of our monitoring with *INTEGRAL*. They add one more piece to a mosaic that places neutron star binaries next to black holes, for which non-thermal emission was thought to be a prerogative.

In these first results, we performed variability and spectral studies separately. The next step was to merge these two aspects, extracting spectra for a given branch in the colour-colour diagrams, i.e. for well defined spectral states.

This is the way we proceeded in the study of the Z source GX 5-1. In the past, the hard X-ray data of GX 5-1 were contaminated by the nearby (40′) BHC LMXRB GRS 1758-258. Thanks to *INTEGRAL*'s imaging capabilities in combination with its high sensitivity, we were able for the first time to study the energy spectrum of GX 5–1 above ∼30 keV and its spectral variations, free from contamination.

We detected a clear hard emission above ∼30 keV, most likely of the same origin as for the hard tails observed in other Z sources. We favoured the so-called eastern model to study the spectral variability of GX 5–1 since this model provides a physical interpretation for the hard tail.

In our study we interpreted the spectral changes of GX 5–1 along the "Z" pattern in the hardness intensity diagram in terms of Comptonisation of varying soft photons (∼2 keV) by a hot plasma (10 keV). The soft photons were modelled as blackbody emission from the neutron star's hot surface, i.e. the surface heated by the boundary layer. The Comptonising plasma is the boundary layer's optically thin plasma. When GX 5–1 moves downwards in the "Z", the temperature of the hot neutron star surface shows a steady decrease with increasing mass accretion rate. This may be a consequence of the gradual expansion of the boundary layer that we detect in the data, in agreement with theoretical studies that predict the expansion of the boundary layer surface with increasing mass accretion rate (Popham and Sunyaev, 2001).

This study does not bring to a spectral "proof" of the presence of a surface and therefore of a neutron star. The soft varying seed photons culd be coming also from the accretion disc (western model). But indeed this kind of analysis of the poorly known hard X-ray spectral variations could bring us one step closer to finding a signature of the presence of a solid surface in the accreting object and/or closer to finding new differences/similarities among the sources traditionally classified on the basis of the soft X-rays (<20 keV).

We will extend the analysis to the new incoming observations to see if our scenario is confirmed. Moreover, to be able to better constrain the soft emission we have asked for simultaneous *INTEGRAL-RXTE* observations that are being currently performed in the frame of the September-October 2004 *INTEGRAL* GPS and GCDE scans.

This latter point brings us to the second main stream in the study of X-ray binaries: **multiwavelength campains**. Each energy range brings information of one aspect of the source: soft-X rays are likely to give us insight in the accretion disc properties; hard X-rays tell us about the temperature of the plasma surrounding the system; optical data can tell us about the type of the companion; an infra-red counterpart can give hints on the distance of the source; radio observations can help us in finding correlations between the presence of a jet and the hard X- ray emission, etc. We have investigated the possibility of simultaneous observations in the optical, radio and soft X-rays. Interestingly enough, the ground based telescopes are the most difficult to coordinate to *INTEGRAL*. Some attempts were made but in a sporadic way. These attempts will be intensified in the coming months. Much more success came from simultaneous *RXTE* observations. We have obtained 36 ksec of simultaneous observations on the nine persistently bright LMXRBs of our sample. *RXTE* allows to go to softer energies than *INTEGRAL*/JEM-X allowing to better constrain the contribution of the soft part to the spectrum. At the time of writing, October 2004, most of the *RXTE* observations have been performed and the analysis of all this data sets will be soon started.

The richness of the *RXTE* data brings us to the third main stream: **timing analysis**. *RXTE* data will allow to go much deeper, down to the search and study of QPOs, with particular attention to their properties with respect to the hard emission studied by *INTEGRAL*. It is known, for instance that to assess whether a source is an Atoll or Z it is necessary to combine timing and spectral properties as considering only one at a time could be insufficient or misleading. The synergy of spectral and timing properties is most likely the best tool to discriminate among different models that explain the physics of a source. More data mean less possible models, thus finding our way to the most complete one.

The last stream in this whole study consists in **sharing** the results. More scientists accessing the same database means having more ideas, more multiwavelength observations triggered, a higher quality scientific output. The precious information of the *RXTE*/ASM is the best example: we have used it while on shift for *INTEGRAL* to confirm an unusual behaviour of a source; we are using it to monitor e.g. the behaviour of Cyg X-3 to trigger further observations once the source enters its extreme soft and hard states. Bringing *INTEGRAL* results at the same level of visibility would mean making a big step forward in the scientific output of the mission. The results from the monitoring programme will be made publically available on the web and will be updated at every Galactic plane and centre scan. The *INTEGRAL* Bright Source Catalog that was made available on the HEASARC and ISDC web pages is also an effort that goes in this direction.

Sharing the results, makes the difference between our monitoring programme and waiting for large chunks of data to become public. Follow-ups have to be triggered close to the unusual event and the more we are to take care of this, the better.

The *Chandra* survey

The survey project made with *Chandra* was developed on different grounds with respect to *INTEGRAL*. *Chandra* is a well calibrated mission and the analysis software is well beyond the scientific validation phase. The analysis of large amount of data is more straightforward, also because of the technology involved: the *Chandra* operational energy range is softer than *INTEGRAL*, it is still possible to focus soft X-rays with grazing incidence mirrors and analysing data from a CCD is simpler than from coded mask aperture techniques used for *INTEGRAL*.

With *Chandra* we have looked into a region in the Galactic plane that is free from known sources. We have detected 274 point sources (4σ confidence). Thanks to the excellent angular resolution of *Chandra* we were able to disentangle the diffuse emission from the point source contribution and to study them separately.

To identify the point source nature we used the information given by the *Chandra* X-ray spectrum together with follow-up observations performed in the Near Infra Red (NIR) band which is much less absorbed than the optical. We found that most of the hard X-ray point sources of the sample are presumably extragalactic since the number of sources does not significantly exceed the number of expected extragalactic ones (as taken from higher latitute measurements). This conclusion is also confirmed by the NIR results: only $\sim$20% of the hard X-ray sources have NIR counterparts. A significant part of the remaining 80% hard sources with no NIR counterpart is likely to be extragalactic since sources behind the Galactic plane will be completely absorbed in the NIR band. The fewer hard sources with NIR counterpart are likely to be Galactic and possible candidates are quiescent cataclysmic variables that are considered to be numerous in the Galactic plane.

Among the soft sources, $\sim$80% have NIR counterparts. Their X-ray spectrum together with the presence of the NIR counterparts suggest that most of the soft sources are probably nearby active X-ray stars.

Removing the integrated contribution of all these point sources from the overall observed spectrum, leaves us with the spectrum of the observed "diffuse" emission. This resulting "diffuse" emission could still be explained by the superposition of even dimmer point sources below our detection limit ($\lesssim 4\sigma$). A comparison of the number of detected sources above 4σ and the sources that we would need to account for the "diffuse" emission shows that to explain all the detected flux with point sources alone would require that the *log N - log S* curve rapidly steepens by an order of magnitude below our sensitivity limit. This is unlikely, given that no spatial distribution of point sources on the Galactic plane is known to accomodate such an unusual *log N - log S* curve. Thus the observed "diffuse" Galactic emission is likely to be truly diffuse in nature. Below $\sim$10 keV, point sources account only for $\sim$10% of the total observed X-ray flux in the field of view.

One main question was thus answered. But some more rose: how is such a plasma heated at the observed temperature (5-10 keV)? Why is it held within the Galactic plane? Why is its energy density one or two orders of magnitude higher than that of other constituents in the interstellar space?

Here is where I close the circle of the survey projects: "we" build new missions to have some answers. We end up with even more questions. With *Chandra* it is already the case, with *INTEGRAL* it will be soon. The new questions will in turn lead to new missions with which we will keep observing the same sky, but it will always be a different path because *"the only real voyage of discovery consists not in seeking new landscapes but in having new eyes"* (Marcel Proust, 1871 - 1922).

Personal remarks and future work

Making a thesis at the *INTEGRAL* Science Data Centre is a precious experience. *INTEGRAL* launch took place in 2002, right in the middle of my thesis (2000-2004). All this has actively influenced my work.

In the beginning it was difficult to focus on my scientific interests. The project related activities were overwhelming. *INTEGRAL* deadlines always made their way before anything else. Before launch a considerable part of my time was dedicated to taking care of the Observation Simulator and to prepare test data for the instrument specific software. Then came testing the software itself. With the launch date approaching the scientist on duty trainings also took place. The *INTEGRAL* stream was too strong not to be taken away by it. In all this, being able to actually study LMXRBs with "hands-on" data analysis seemed really distant.

After launch things changed. The attention focussed on the incoming data. My work moved from a technical aspect to a more scientific one. It is in this period that I realised how the past software-related work had not only been useful for the project (I hope!) but also for my personal research. It had gained me a good level of expertise in the *INTEGRAL* data analysis. I suddenly found myself in many collaborations, with scientists inside and outside ISDC, on many topics, sometimes even too many to be able to contribute with more than just the data analysis.

Among the different collaborations established, the one on the LMXRB programme with *INTEGRAL* and the *Chandra* survey are certainly the ones with deepest roots.

Coordinating the LMXRB monitoring programme with my PhD advisor has been very enriching. It is a large collaboration on a huge set of interesting data, with an eye towards the wider scientific community. It is a work in progress, much has still to be done in the coming months. The analysis of all the data will be kept up to date with the evolving software and kowledge of the instruments; light curves and hardness ratios will be regularly populating the web pages; based on the incoming results, main parameters will be selected to characterise the sources and detailed studies will be performed on each source; multiwavelength observations will be intensified and the current available *RXTE* data will be analysed introducing the "timing chapter" in this study.

The *Chandra* survey project is already in an advanced stage as it starts bringing new questions. Nevertheless, much more can (and will) be done especially in the direction of making new deep field observations in other regions of the Galactic plane with *Chandra*, and perform follow ups with *XMM-Newton* to better constrain the different components of the lines in the diffuse emission that cannot be resolved by *Chandra*.

With time also *INTEGRAL* will lead to more questions. I used to think that a PhD is the end of a work. Now it looks much more like a beginning.

Seventh part

APPENDICES

Chapter 11
Acknowledgments

ISDC. What a place!! I can't find the words to describe the years I spent here. For me it has been much more than a Ph.D. It has been a wonderful life. So many nice moments, ...rituals! lunch in the garden; scientific discussions ("1001 uses of the microwave: from light-bulbs to the swiss army", I say the sin but not the sinner!); movie nights; Christmas parties; never ending "aperos" (my favourites); software beer meetings; science wine meetings; consortium meetings. Well, hmm, maybe these I enjoyed less. Although the marmitte part on the Christmas consortium meeting has always been quite interesting.... What else? ah! fridge cleaning parties; the simultaneous german-swiss-french-american-russian-italian-polish-japanese-check–etc ways of cooking in the kitchen (more multi-wavelength than ever); the Monday meetings held on every day of the week but on Monday, uff...tough to remember everything.

My Ph.D. is the result of the effort of so many people! I don't have a picture of all of you unfortunately, but I have one with many of you...see next page! Since the picture was taken some people left and some arrived. ISDC will evolve even more in the future but this particular picture depicts ISDC in an important period of its history, during the busy, exciting and AAARRRGGGGHHHHH! weeks before the launch of INTEGRAL.

Sometimes I think of the day of the launch. I remember that the solar panels would not open at the first go when they had to. We even lost telemetry for a short moment. In that short moment, that seemed long then..., I visualised *INTEGRAL* as a stone in space....is this it? Fortunately it wasn't. But it is interesting to see that when you think that you've lost everything, only then you actually realise that it is all worth it.

I know. The above are not strictly scientific acknowledgments. And the non-ISDC people might actually wonder if we even work between parties!

OK. Let me think. YES! we do. But these (and more) are the things that warmed up my path through this Ph. D. so I could not leave them out. As I cannot leave out people who might have not helped me specifically on the topics of my Ph. D. but thanks to whom I managed to go through my days here with a warm ray of light inside of me.

Hum, already more than 20 lines. I am not supposed to make this part longer than the rest of the thesis (a pity!) so I will try to be short. Difficult...

My first personal thought and acknowledgment goes with no doubt to my advisor, Thierry Courvoisier. Thierry, having you as an advisor has enlighted my mind and my days. Seeing how you work and who you are I have understood the scientist I want to be. You have been close to me every day and have been a solid support. Always. In science as well as in my personal life. Thank you. With all my heart.

A special thought and thank you go to the man that made all this possible, my italian boss! Sandro Mereghetti from Milano. Sandro, without you I would have never lived all this. Thank you for choosing me in the first place and for believing in me. Thank you for supporting me here at ISDC for even longer than planned in the beginning. You have changed my life. I hope I have not disappointed you.

To Filippo Frontera, André Maeder, Sandro Mereghetti and Arvind Parmar for accepting to be part of my jury!

I raise my glass to Jerome Rodriguez! Jerome, your enthusiasm, friendship and knowledge have been so important for me. You made my Ph. D. an interesting, stimulating path. Thank you. For your help, for our discussions, for translating all my summary in french!, for the evenings in front of good (?) glass (????????) of red wine, for all the teufs together. "Saluuuuute!". May our friendship and, why not?, collaboration last for long and long and long......Merci mon ami.

A warm thank you to Ken Ebisawa. Ken, working with you has been a really precious experience. I really hope I have taken some of your knowledge, intuition and method. With you, "we" is much more fun than "I".

To Volker Beckmann and Paschal Favre "beasts". Well, what can I say? You made Geneva a home. And Volker, I still don't know if you are a better scientist or dancer. Oh well, one can be sosososososososo good in many fileds, no? Boh! Ciao Caro! Thanks for becoming my alter-ego when I needed help during the A&A special issue and for being always honest in your scientific (and not only...) criticism.

To all my LMXRB and HMXRB collaborators for enriching my Ph. D. path!

To Giorgio Palumbo. For tip-toeing into my thesis in a very difficult moment for me, giving a warm and important help and then discretely walking out of it when I could handle things myself again. Grazie.

To Erik Kuulkers and Joern Wilms, for their patience, for answering to all my LMXRB-HMXRB questions and for being such an up-to-date reference source!

To the ISDC incredible software team and especially to Jurek Borkowski, Bruce O'Neel, Mathias Beck, Mark Gaber and Daniel Rychcik for their efficient and competent help in OSIM, e-mails, latex, NFS, scratch∗, shell, netscape and whatever I managed to crash!

To Mark Gaber! No matter what, we have lunch together. You are such a good friend. Every day, every lunch, a new book, a new movie, a new emotion, a different smile. Thank you.

To Peter Kretschmar, my OSIM boss! And much more, a valid, (party-organiser), friendly, human presence.

To Martine Logossou, for making my stay in Switzerland pleasant and ...legal!

To Nami Mowlavi and Simon Shaw, our great scody coordinators, for all the procedures and effort that allowed me to stay in front of 10 screens without panicking.
Too much.

Again to all the ISDC staff: for the letters, phone calls, post-cards, books, CDs, flowers that you sent me during my convalesence. I really felt your love.

To Barbara and Thierry, Angelika and Reiner, Irina and Mark, Chia-Miao and Nami for being a solid and sort of "mum and dad" presence in the most difficult days of my years in Geneva and of my life.

To Diego Götz, a constant and friendly presence in all my ISDC days...."Ave, come va? a te cosa viene....? senti ma dove hai trovato....? dove hai il file...? tu vai al congresso...? quando vieni a Ginevra?...miiiiiiiii enonmipassapiú. eh sí sí sí."
SEND MAIL? Yes.

To all my friends here for the wonderful dinners, parties, walks, trips, movies. Be it at Flannegans, Shakers, Ferblanterie, Tortellino, Cafe Metis, La trattoria, Chez ma cousine, Chez Beckmann, Chat Noir, Le jardin des crepes...did I forget anything? I am sure I did.. thank you: Volker, Pascal, Jerome, Morag, Simona, Veruska, Joana, Simon. You are such a great group! Thanks to you I know how bad a hangover can be. And you can't deny it... I have shared it all with you.... ;-)

Simona! I am so happy that you came to ISDC. I am looking forward to all our gym-dinner-

movie evenings! I wish you all the best for you Ph.D. and for your new life here in Geneva and especially I wish you to take the opportunity of this swiss adventure to widen your horizon as much as possible, in science, friends, english!, wine, vegetables and fruits. Not necessarily in this order....

Il faut.

A Veruska, ai signori De Meo e a Livio, in questi anni la mia Italia a Ginevra.

To Osmi Vilhu, Diana Hannikainen and Luigi Foschini for the useful discussions and constant encouragement!

To Julia and David for opening a new wonderful door in my life, the door to music.

To Darci for making a room in a foyer feel like home.

To Nicos, Giovanna, Bruna, Roberta, Luisa, Laura, Valentina, Silvia, Christian. My family, school, chess friends. For being always there.

I normally like to leave for the end the most important part....a little bit like having one last glass of good red wine at the end of the meal.... ;–)

To my father and mother. Miiiimmi! Babaka! I would be nothing without you. My strength, my will, my hopes, come from you. Thank you. For giving me a life in which I can choose. And for supporting me in all my choices.

To Mauro. Tutto quello che faccio è più bello perché ci sei tu. Sei la melodia che vorrei sempre suonare, sentire, vivere.

Thank you. Grazie. Merci. In all the languages of ISDC!

You are the book I never want to finish reading.

Chapter 12
List of publications

<u>**2004**</u>

Papers

Paizis A., K. Ebisawa, T. Tikkanen, Rodriguez J., et al., 2004, accepted for publication in A&A (after revision)
Resolving the hard X-ray emission of GX 5-1 with INTEGRAL

Ebisawa K., Tsujimoto M., **Paizis A.**, Hamaguchi K., et al., 2004, submitted to ApJ
Chandra deep X-ray observation of a typical Galactic Plane region and Near-Infrared identification

Rodriguez J., Corbel S., Hanninkainen D., Belloni T., **et al.**, 2004, accepted for publication in ApJ (astro-ph/0407076)
Spectral properties of low frequency quasi-periodic oscillations in GRS 1915+105

Refereed proceedings

Paizis A., Courvoisier T. J.-L., Vilhu O., M. Chernyakova, et al., 2004.
The INTEGRAL LMXRB Monitoring Program. In: Proceedings of the "5th INTEGRAL Workshop - The INTEGRAL Universe", Munich, in press

Ebisawa K., **Paizis A.**, Courvoisier T. J.-L., P. Dubath, et al., 2004.
A Chandra Deep X-ray Exposure on the Galactic Plane and Near Infrared Identification. In: Proceedings of the "5th INTEGRAL Workshop - The INTEGRAL Universe", Munich, in press

Hjalmarsdotter L., Zdziarski A. A., **Paizis A.**, Beckmann V., et al., 2004.
INTEGRAL Observations of Cygnus X-3. In: Proceedings of the "5th INTEGRAL Workshop - The INTEGRAL Universe", Munich, in press

Mereghetti S., Götz D., **Paizis A.**, Pellizzoni A., et al., 2004.
INTEGRAL observations of the Large Magellanic Cloud region. In: Proceedings of the "5th INTEGRAL Workshop - The INTEGRAL Universe", Munich, in press

Shaw S., Mowlavi N., Ebisawa K., **Paizis A.**, et al., 2004.
Scientific Performance of the ISDC Quick Look Analysis. In: Proceedings of the "5th INTEGRAL Workshop - The INTEGRAL Universe", Munich, in press

Ebisawa K., Kretschmar P., Mowlavi N., **Paizis A.**, et al., 2004.
Systematic search for short transients and pulsation events from INTEGRAL survey data. In: Proceedings of the "5th INTEGRAL Workshop - The INTEGRAL Universe", Munich, in press

Piraino S., Santangelo A., Ferrigno C., **et al.**, 2004.
INTEGRAL monitoring of the bright neutron star Low Mass X-ray Binaries: preliminary results on GX 17+2 and Cyg X-2 In: Proceedings of the "5th INTEGRAL Workshop - The INTEGRAL Universe", Munich, in press

Sidoli L., Mereghetti S., Larsson S., M. Chernyakova,**et al.**, 2004.
First results on the HMXRB Pulsar SAXJ2103.5+4545 with INTEGRAL. In: Proceedings of the "5th INTEGRAL Workshop - The INTEGRAL Universe", Munich, in press

Del Santo M., Bazzano A., Smith D. M., L. Bassani, **et al.**, 2004.
INTEGRAL Monitoring of the Black hole candidate 1E1740.7-2942. In: Proceedings of the "5th INTEGRAL Workshop - The INTEGRAL Universe", Munich, in press

Non refereed proceedings

Sidoli L., Wilms J., **Paizis A.**, Larsson S., et al., 2004, Nuclear Physics B (Proc.Supll.) 132, 648
Monitoring Program on Persistent Accreting Neutron Stars observed during the INTEGRAL Galactic Plane Survey.

<u>2003</u>

Papers

Paizis A., Beckmann V., Courvoisier T. J.-L., Vilhu O., et al., 2003, A&A 411, L363
First INTEGRAL observations of eight persistent neutron star low mass X-ray binaries

Vilhu O., Hjalmarsdotter L.,Zdziarski A. A., **Paizis A.**, et al., 2003, A&A 411, L405
First INTEGRAL observations of Cygnus X-3

Malaguti G., Bazzano A., Beckmann V., Bird A. J., **et al.**, 2003, A&A 411, L307
GRB 021125: The first GRB imaged by INTEGRAL

Del Santo M., Rodriguez J., Ubertini P., Bazzano A., **et al.**, 2003, A&A 411, L369
IBIS performances during the Galactic Plane Scan. I. The Cygnus region

Rodriguez J., Del Santo M., Lebrun F., G. Belanger, **et al.**, 2003, A&A 411, L373
First results from the IBIS/ISGRI data obtained during the Galactic Plane Scan. II. The Vela region

Non refereed proceedings

Walter R., Bourban G., Ebisawa K., Kretschmar P., **et al.**, 2003, Astron. Nachr., 324, 160
INTEGRAL surveys

Circulars

Mereghetti S., Götz D., Borkowski J., **Paizis A.**, et al., 2003, GRB Coordinates Network, 1941
Possible GRB 030320 localized by INTEGRAL.

2002

Circulars

Bazzano A. and **Paizis A.**, 2002,GRB Coordinates Network, 1706
GRB021125: a long GRB localized by INTEGRAL

2001

Non refereed proceedings

Ebisawa K., Bamba A., Kaneda H., Maeda Y., **et al.**, 2001
Chandra deep X-ray observation on the Galactic plane. In: Proceedings of the "New visions of the X-ray universe in the XMM-Newton and Chandra Era", The Netherlands

Bibliography

Asai K., Dotani T., Mitsuda K., et al., 1994, PASJ, 46, 479

Asai K., 1994, PhD Thesis

Barret D. and Olive J.-F., 2002, ApJ, 576, 391

Barret D., 2001, Adv. in Space Res., 28, 307

Barret D., van der Klis M., Skinner G. K., et al., 2001, ApSSS, 276, 305

Barret D., Olive J. F., Boirin L., et al., 2000, ApJ, 533, 329

Barret D. and Vedrenne G., 1994, APJSS, 92, 505

Bazzano A. and Paizis A., 2002, GCN, 1706

Bhattacharya D., 1995, Chapter 5 in *X-Ray Binaries*, ed. W. E. G. Lewin, J. van Paradijs and van den Heuvel E. P. J., Cambridge

Bildsten L. 1995, ApJ, 438, 852

Bradt H., Rothschild R. E., Swank, J. H., 1993, A&AS, 97, 355

Bradt H., Naranan S., Rappaport S., et al., 1968, ApJ, 152, 1005

Caroli E., Stephen J. B., Di Cocco G., et al., 1987, SSRv, 45, 349

Carrier F., 2002, *LMXRBs survey with the Euler telescope*, Internal Report

Castro-Tirado A. J., Gorosabel J., Guziy S., et al., 2003, A&A, 411, L315

Church M. J. and Balucinska M., 1995, A & A, 300, 441

Corbet R. H. D., 1986, MNRAS, 220, 1047

Cottam J., Paerels F. and Mendez M., 2002, Natur, 420, 51

Courvoisier T. J.-L., Walter R., Beckmann V., et al., 2003, A&A, 411, L53

Courvoisier T. J.-L., Parmar A. N., Peacock A, et al., 1986, ApJ 309, 265

D'Amico F., Heindl W. A., Rothschild R. E., et al., 2001, ApJ, 547, L147

Del Santo M., Bazzano A., Smith D. M., et al., 2004., Proc. of The 5th INTEGRAL Workshop, *The INTEGRAL Universe*, in press

Del Santo M., Rodriguez J., Ubertini P., et al., 2003, A&A, 411, L369

Di Cocco G., Caroli E., Celesti E., et al., 2003, A&A, 411, L189

Di Salvo T., Farinelli R., Burderi L., et al., 2002, A&A, 386, 535

Di Salvo T. and Stella L., 2002, Proc. of the XXXVIIth Rencontres de Moriond, *The Gamma-Ray Universe*, Ed. A. Goldwurm, D. N. Neumann and J. T. Thanh Van, 67

Di Salvo T., Robba N. R., Iaria R., et al., 2001, ApJ, 554, 49

Di Salvo T., Done C., Zycki P. T., et al., 2001, ApJ, 547, 1024

Di Salvo T., Iaria R., Burderi L., 2000a, ApJ, 542, 1034

Di Salvo T., Stella L., Robba N. R., et al., 2000b, ApJ, 544, L119

Done C., 2004, in *Frontiers in X-Ray Astronomy*, ed. A. C. Fabian, K. A. Pounds, R.D. Blandford (Cambridge: Cambridge U. Press)

Done C. and Gierliński M., 2003, MNRAS, 342, 1041

Ebisawa K., Tsujimoto M., Paizis A., et al., 2004b, ApJ submitted

Ebisawa K., Kretschmar P., Mowlavi N., et al., 2004, Proc. of The 5th INTEGRAL Workshop, *The INTEGRAL Universe*, in press

Ebisawa K., Bourban G., Bodaghee A., et al., 2003, A&A, 411, L59

Ebisawa K., Maeda K., Kaneda H., et al., 2001, Science, 293, 1633

Ebisawa K., Ogawa, M., Aoki T., et al., 1994, PASJ, 46, L141

Farinelli R., Frontera F., Masetti N., et al., 2003, A&A, 402, 1021

Fender R. P., 2001, ‘Proceedings of the Third Microquasar Workshop‘, ed. A. J. Castro-Tirado, J. Greiner and J. M. Paredes

Fender R. P. and Hendry M. A., 2000, MNRAS, 317, 1

Fenimore E. E. and Cannon T. M., 1978, Appl. Opt., 17, 337

Ferguson C., Barlow E. J., Bird A. J., et al., 2003, A&A, 411, L19

Fisher P. C., Jordan W. C., Meyerott A. J., et al., 1968, ApJ, 151, 1

Frank J., King A. and Raine D., 2002, in *Accretion power in Astrophysics*, ed. Cambridge Univ. Press

Frank J., King A. R., and Lasota J.-P., 1987, A&A, 178, 137

Frontera F., et al., 1998, Nuclear Physics B (Proc. Suppl.), 69, 286

Fujimoto M. Y., Hanawa T. and Miyaji S., 1981, ApJ, 247, 267

Giacconi R., Gorenstein P., Gursky H., et al., 1967, ApJ, 148, L119

Giacconi R., et al., 1962, Phys. Rev. Lett, 9, 439

Gierliński M. and Done C., 2002, MNRAS, 331, L47

Grove J. E., Johnson W. N., Kroeger R. A., et al., 1998, ApJ, 500, 899

Hajdas W., Bühler P., Eggel C., et al., 2003, A&A, 411, L43

Hasinger G., van der Klis M., Ebisawa K. et al., 1990, A&A, 235, 131

Hasinger G., and van der Klis M., 1989, A&A, 225, 79

Hynes R. I., Mauche C. W., Haswell C. A., 2000, ApJ, 539, L37

Hoffman J. A., Marshall H. L., and Lewin W. H. G., 1978, Nature, 271, 630

Homan J., Wijnands, R, van der Klis M. et al., 2001, ApJS, 132, 377

Hurley K., Cline T., Barthelmy S., et al., 2001, in *Gamma-Ray Bursts in the Afterglow Era*, ed. E. Costa, F. Frontera, J. Hjorth (Berlin, Heidelberg: Springer), 378

Iaria R., Burderi L., Di Salvo T., et al., 2001, ApJ, 547, 412

Iaria R., Di Salvo T., Burderi L. et al., 2001, ApJ, 548, 883

Jensen P. L., Clausen K., Cassi C., et al., 2003, A&A, 411, L7

Jonker P. G., van der Klis M., Homan J., et al., 2002, MNRAS, 333, 665

Jonker P. G. and van der Klis M., 2001, A&A, 553, L42

Jonker P. G., Fender R., Hambly N. C., et al., 2000, MNRAS, 315, L57

Jonkert H. C. and van der Klis M., 1996, A&A, 310, 474

Kato S., Fukue J. and Mineshige S., 1998, in *Black Hole Accretion Disks*, ed. Kyoto University Press

King A. R.and Ritter H., 1988, MNRAS, 293, L42

King A. R., 1995, Chapter 10 in *X-Ray Binaries*, ed. W. E. G. Lewin, J. van Paradijs and van den Heuvel E. P. J., Cambridge

Kluzniak W., 1993, A&AS, 97, 265

Koyama K., Makishima K., Tanaka Y., et al., 1986, PASJ, 38, 121

Kuulkers E., Homan J., van der Klis M., et al., 2002, A&A, 382, 947

Kuulkers E., van der Klis M., Oosterbroek T., et al., 1994, A&A, 289, 795

X-Ray Binaries, 1995, ed. W. E. G. Lewin, J. van Paradijs and van den Heuvel E. P. J., Cambridge

Lebrun F., Terrier R., Bazzano, A., et al., 2004, Natur., 428, 293

Lebrun F., Leray J. P., Lavocat P., 2003, A&A, 411, L141

Lewin W. H. G., van Paradijs J., and Taam R. E., 1995, Chapter 4 in *X-Ray Binaries*, ed. W. E. G. Lewin, J. van Paradijs and van den Heuvel E. P. J., Cambridge

Lewin W. H. G. and Joss P. C., 1981, SSRv, 28, 3

Liu Q. Z., van Paradijs J., and van den Heuvel E. P. J., 2001, A&A 368, 1021

Lund N., Brandt S., Budz-Jorgensen C., et al., 2003, A&A, 411, L231

Malaguti G., Bazzano A., Beckmann V., et al 2003, A&A, 411, L307

Markoff S. and Nowak M. A., 2004, ApJ, 609, 972

Markoff S., Falcke H., Fender R., 2001, A&A, 372, L25

Mas-Hesse M., Gimènez A., Culhane L., et al., 2003, A&A, 411, L261

McCollough M. L., Robinson C. R., Zhang S. N., et al., 1998, NewAR, 42, 629

Mereghetti S., Götz D., Paizis A., et al., 2004, Proc. of The 5th INTEGRAL Workshop, *The INTEGRAL Universe*, in press

Mereghetti S., Götz D., Beckmann V., et al., 2003, ApJ, 590, L73

Mereghetti S., Götz D., Borkowski J., et al., 2003b, GCN, 1941,1

Mereghetti S., Götz D., Borkowski J., et al., 2003, A&A, 411, L291

Merloni A., Di Matteo T. and Fabian A. C., 2001, 'Proceedings of the Third Microquasar Workshop', ed. A. J. Castro-Tirado, J. Greiner and J. M. Paredes

Mitsuda K., Inoue H., Koyama K, et al., 1984, PASJ, 36, 741

Motch C., Pedersen H., Courvoisier T., et al., 1987, APj, 313, 792

Motch C., Ilovaisky S. A. and Chevalier, C. 1981, IAUC, 3609

Much R., Barr P., Hansson L., et al., 2003, A&A, 411, L53

Muno M. P.,Baganoff F. K., Bautz M. W, et al., 2004, ApJ, 613, 326

Muno M. P., Remillard R. A., and Chakrabarty D., 2002 , ApJ, 568, L35

Nakamura H., Matsuoka M., Kawai N., et al., 1993, MNRAS, 261, 353

Oosterbroek T., Barret D., Guainazzi M., et al., 2001, A&A, 366

Orosz J. A., 2002, Proceedings of the IAU Symposium 212, ed. K. A. van der Hucht, A. Herrero and C. Esteban (astro-ph/0209041)

Paizis A., Ebisawa K., Tikkanen T., et al., 2004a, A&A, submitted

Paizis A., Courvoisier T. J.-L., Vilhu O., et al., 2004, Proc. of The 5th INTEGRAL Workshop, *The INTEGRAL Universe*, in press (astro-ph/0405376)

Paizis A., Beckmann V., Courvoisier T. J.-L., et al., 2003, A&A, 411, L363

Paizis A., Observation Simulator User Manual, distributed in 2001 and later versions. http://isdc.unige.ch/index.cgi?Soft+download

Parmar A. N., Oosterbroek T., Del Sordo S., et al., 2000, A&A, 356, 175

Parmar A. N., White N. E., Giommi P., et al., 1986, ApJ, 308, 199

Paul J., Ballet J., Lebrun F., et al., 1993, AdSpR, 13, 665

Podsiadlowski P., Pfahl E. D., and Rappaport S, 2004, To appear in "Compact binaries in the Galaxy and beyond", in press, (astro-ph/0402024)

Popham R. and Sunyaev R., 2001, ApJ, 547, 355

Psaltis D., 2001, ApJ, 555, 786

Ricker G. R., Atteia J.-L., Crew G. B., et al., 2003, in *Gamma-ray Burst and Afterglow Astronomy*, ed. G. R. Ricker, R. K. Vanderspek, AIP Conf. Proc., 662, 3

Rodriguez J., Corbel S., Hannikainen D., et al., 2004, accepted for publication in ApJ, (astro-ph/0407076)

Rodriguez J., Del Santo M., Lebrun F., et al., 2003, A&A, 411, L373

Rodriguez J., Corbel S. and Tomsick J. A, 2003, ApJ, 595, 1032

Scarsi L., 1993, AdSpR, 13, 369

Shakura N. I. and Sunyaev R. A., 1973, A&A, 24, 337

Shaw S. E., Mowlavi N., Ebisawa K., 2004, Proc. of The 5th INTEGRAL Workshop, *The INTEGRAL Universe*, in press (astro-ph/0405204)

Shimura T. and Takahara F., 1995, ApJ, 445, 780

Sidoli L., Mereghetti S., Larsson S., et al., 2004, Proc. of The 5th INTEGRAL Workshop, *The INTEGRAL Universe*, in press

Sidoli L., Wilms J., Paizis A., et al., 2004, Nuclear Physics B (Proc.Supll.) 132, 648

Smale A. P. and Wachter S., 1999, ApJ, 527, 341

Strohmayer T. and Bildsten L., 2003, in *Compact Stellar X-Ray Sources*, ed. W.H.G Lewin and M. van der Klis (Cambridge U. Press), in press (astro-ph/0301544)

Sunyaev R. A., Arefev V. A., Borozdin, K. N., et al., 1991, SvAL, 17, 409

Schwartz D. A., 2004, Int.J.Mod.Phys. D, 13, 1239

Strong A. W., Bouchet L., Diehl R., et al., 2003, A&A, 411, L477

Sugizaki M., Mitsuda K., Kaneda H., et al., 2001, ApJS, 134, 77

Szostek A. and Zdziarski A. A., 2004, Proceedings of the Conference "X-Ray Timing 2003: Rossi and Beyond", Cambridge, in press (astro-ph/0401265)

Tanaka Y. and Lewin W. H. G., 1995, Chapter 3 in *X-Ray Binaries*, ed. W. E. G. Lewin, J. van Paradijs and van den Heuvel E. P. J., Cambridge

Tauris T. M. and van den Heuvel E. P. J., 2003, in *Compact Stellar X-Ray Sources*, ed. W.H.G Lewin and M. van der Klis (Cambridge: Cambridge U. Press), in press (astro-ph/0303456)

Tavani M. and Barret D., 1997, AIP Conference Proceedings 410, Fourth Compton Symopsium, Ed. C. D. Dermer, M. S. Strickman and J. D. Kurfess, 75

Ubertini P., Lebrun F., Di Cocco G., et al., 2003, A&A, 411, L131

van den Heuvel E. P. J, 1994, in *Interacting binaries*, Saas-Fee Advanced course 22, ed. Springer-Verlag

van der Klis M., 2000, ARA&A, 38, 717

van der Klis M., 1995, Chapter 6 in *X-Ray Binaries*, ed. W. E. G. Lewin, J. van Paradijs and van den Heuvel E. P. J., Cambridge

van der Klis M., Hasinger G., Damen E., et al., 1990, ApJ, 360, L19

van Kerkwijk M. H., Geballe T. R., King D. L., et al., 1996, A&A, 314, 521

van Paradijs J., Penninx W, and Lewin W. H. G., 1988, MNRAS, 233, 437

van Paradijs J., 1996, ApJ, 464, L139

van Paradijs J., McClintock J. E., 1995, Chapter 2 in *X-Ray Binaries*, ed. W. E. G. Lewin, J. van Paradijs and van den Heuvel E. P. J., Cambridge

Vaughan B. A., van der Klis M., Wood K. S., et al., 1994, ApJ, 435, 362

Vedrenne G., Roques J.-P., Schönfelder V., et al., 2003, A&A, 411, L405

Vilhu O., Hjalmarsdotter L., Zdziarski A. A., et al., 2003, A&A, 411, L63

Walter R., Rodriguez J., Foschini L., et al., 2003, A&A, 411, L427

Walter R., Bourban G., Ebisawa K., et al., 2003b, Astron. Nachr., 324, 160

Weisskopf M. C., Brinkman B., Canizares C., et al., 2002, PASP, 114, 1

White N. E., Nagase F. and Parmar A. N., 1995, Chapter 1 in *X-Ray Binaries*, ed. W. E. G. Lewin, J. van Paradijs and van den Heuvel E. P. J., Cambridge

White N. E., Stella L., and Parmar A. N., 1988, ApJ, 324, 363

White N.E., Peacock A., Hasinger G., et al., 1986, MNRAS, 281, 129

White N. E., Parmar A. N., Sztajno M., et al., 1984, ApJ, 283, L9

White N. E., Holt S. S., 1982, ApJ, 257, 318

White N. E. and Swank J., 1982, ApJ, 253, L61

Warwick R. S., Turner M. J. L., Watson M. G., et al., 1985, Natur, 317, 218

Wijnands R., 2004, in The Restless High-Energy Universe, ed. E. P. J. van den Heuvel et al., in press (astro-ph/0309347)

Wijnands R. and van der Klis M., 1998, Nature 235, 37

Winkler C., Courvoisier T. J.-L., Di Cocco G., et al., 2003, A&A, 411, L1

Worrall D. M., Marshall F. E., Boldt E. A. et al., 1982, ApJ, 255, 111

Zdziarski A. A., Poutanen J., Mikolajewska J., et al., 1998, MNRAS, 301, 435.

Zhang S. N., Fishman G. J., Harmon B. A., et al., 1993, Bulletin of the AAS, 25, 921